

NONLINEAR RESPONSE AND BIFURCATIONS ANALYSIS OF ROTOR-FLUID
FILM BEARING SYSTEMS

A Dissertation

by

SITAE KIM

Submitted to the Office of Graduate and Professional Studies of
Texas A&M University
in partial fulfillment of the requirements for the degree of

DOCTOR OF PHILOSOPHY

Chair of Committee,	Alan B. Palazzolo
Committee Members,	Kuang-An Chang
	Pilwon Hur
	Chii-Der Steve Suh
Head of Department,	Andreas A. Polycarpou

December 2016

Major Subject: Mechanical Engineering

Copyright 2016 Sitae Kim

ABSTRACT

Nonlinear response, bifurcations and stability of rotor-fluid film bearing systems are studied using various numerical investigation schemes such as autonomous/non-autonomous shooting, arc-length continuation, direct numerical integrations, Poincaré sections, Lyapunov exponents, etc. Two types of hydrodynamic bearings, a floating ring bearing (FRB) and a tilting pad journal bearing (TPJB), are employed in this study. The nonlinear characteristic of each bearing is analyzed as supports of a rigid rotor system as well as a flexible rotor system. Depending on the existence of the unbalance force on the rotor/disks, autonomous (free vibration) and non-autonomous responses (mass unbalanced excitation) are both identified, and the nonlinear reaction force produced on the lubricant layer is obtained using the finite element method. In addition to isoviscosity lubricants, thermo-hydrodynamic lubricant model is developed to investigate thermal effects on rotordynamic bifurcations; in the procedure, a variable viscosity Reynolds equation and the energy equation are solved simultaneously. For computation efficiency in the analytical bifurcation study, an advanced shooting algorithm, which is combined with the deflation theory and the parallel computing strategy, is proposed for both the autonomous and the non-autonomous cases. In the study with flexible rotors, the finite element based beam models are employed and the model reduction technique such as Component Mode Synthesis is utilized to condense the system degree of freedom.

This dissertation consists of four main discussions regarding: 1) nonlinear response and bifurcations of a rigid rotor supported by FRBs; 2) effects of a thermo-

hydrodynamic (THD) FRB model on rotordynamic bifurcations; 3) nonlinear response and bifurcations of a rigid rotor supported by TPJBs; 4) extension of study to general, complex, multi-mass rotor beam models. In case 1), multiple coexistent solutions and bifurcation scenarios are identified, and those are depended on the ratio of floating ring length to diameter (L/D). Numerical illustrations regarding jumps between two stable limit cycles and quenching large vibrations are demonstrated, and chaos is investigated with the aid of Lyapunov exponent. In case 2), the Hopf bifurcation onset is strongly dependent on thermal conditions, and the saddle node bifurcation points are significantly shifted compared to the isothermal model. In addition, the unbalanced responses stability and bifurcation onsets are highly reliant on the lubricant supply temperature. In case 3), loci of bifurcations are identified, and heavily loaded bearings and/or high unbalance force may induce consecutive transference of response in forms of synchronous to sub-synchronous, quasi-periodic responses and chaotic motions. The periodic doubling bifurcations, saddle node bifurcations and corresponding local stability are reliably determined by selections of pad preload, pivot offset, and lubricant viscosity sets. In case 4), two industrial applications such as a turbocharger supported by FRBs and an eight-stage centrifugal compressor supported by TPJBs are numerically analyzed. The turbocharger shows that torus appears with Neimark-Sacker bifurcation events and the motions are dominant in the high speed ranges ($>60,000\text{rpm}$). In the compressor, sub-/super-synchronous motions are identified other than the $\times 1$ synchronous response, and the appearance of each harmonic is highly depended on the selection of pad preload and pivot offset.

DEDICATION

To my wife

ACKNOWLEDGEMENTS

I would like to thank my committee chair, Dr. Palazzolo for this immeasurable considerations and concerns during my graduate study in Vibration Control Electromechanical Laboratory (VCEL) at Texas A&M University. I also would like to thank Dr. Chang, Dr. Hur and Dr. Suh for their guidance and support throughout the course of this research.

Thanks also go to my VCEL colleagues and the department faculty and staff for making my time at Texas A&M University a great experience. I also want to extend my gratitude to the Turbomachinery Research Consortium who has provided the research funding as well as Republic of Korea Air Force who gave the opportunity to study abroad.

Thanks to my mother, father, mother in law and father in law for their encouragement, patience and love. Finally thanks to my wife, Hyeyoung, for all her hard work at home with my two daughters, Bokyoung and Yukyoung.

NOMENCLATURE

C_b	bearing clearance
C_i, C_o	ring inner and outer clearances
C_p	pad clearance
D	bearing Diameter
\mathbf{I}	identity matrix
I_p	polar moment of inertia of a pad about the pivot
\mathbf{J}_x	jacobian matrix w.r.t states vector \mathbf{x}
\mathbf{J}_τ	jacobian matrix w.r.t time parameter τ
L	bearing Length
$\mathbf{M}, \mathbf{C}, \mathbf{K}$	mass, damping, and stiffness matrices
O_B	bearing center
O_J	journal center
O_R	ring center
O_p	pad center
R	bearing Radius
T	lubricant temperature
e_{imb}	imbalance eccentricity
e_j	static eccentricity of journal position relative to housing

e_{JR}	static eccentricity of journal position relative to ring
e_R	static eccentricity of ring position relative to housing
h	film thickness
p	fluid pressure
t	time parameter
u, v	components of fluid velocity in x, y directions
x_J	x component of journal position relative to housing
x_{JR}	x component of journal position relative to ring
x_R	x component of ring position relative to housing
y_J	y component of journal position relative to housing
y_{JR}	y component of journal position relative to ring
y_R	y component of ring position relative to housing
Γ	torque on ring
Φ_m	Monodromy matrix
ε_D	non-dimensionalized dynamic eccentricity ($\varepsilon_D=e_J/C_b$)
ε_i	non-dimensionalized imbalance eccentricity ($\varepsilon_i=e_{imb}/C_b$)
ζ	Floquet multiplier
η	Gram-Schmidt orthonormalization
θ_i	journal angular position
θ_o	ring angular position

λ	Lyapunov exponent
μ	fluid dynamic viscosity
μ_0	fluid dynamic viscosity at reference temperature
ζ	non-dimensional cross film distance
τ	non-dimensional time parameter
τ_R	journal whirling period
τ_s	journal spin period
ω_J	journal spin speed
ω_R	ring spin speed

TABLE OF CONTENTS

	Page
ABSTRACT	ii
DEDICATION	iv
ACKNOWLEDGEMENTS	v
NOMENCLATURE.....	vi
TABLE OF CONTENTS	ix
LIST OF FIGURES.....	xi
LIST OF TABLES	xvii
CHAPTER I INTRODUCTION	1
Nonlinear Phenomena in Rotor-Fluid Bearing Systems	1
Limitations of Linear and Transient Analyses	2
Multiple Response State Prediction Methods	3
Research Objectives	5
Original Contributions of Research.....	9
CHAPTER II THEORY.....	10
Shooting Method with Deflation Algorithm	10
Arc-length Continuation.....	13
Floquet Theory	16
Lyapunov Exponents.....	18
CHAPTER III NONLINEAR RESPONSE AND BIFURCATIONS OF A RIGID ROTOR SUPPORTED ON FLOATING RING BEARINGS (FRB).....	21
Introduction to Finite FRB Modeling.....	21
A Rigid Rotor Supported by FRB	24
Simulation Results of FRB-RGD	25
Summary of Results	47
CHAPTER IV EFFECTS OF THERMO-HYDRODYNAMIC (THD) FRB MODLE ON ROTORDYNAMIC BIFURCATIONS	49
Introduction to THD FRB Model.....	49

Shooting Method with THD Solutions.....	52
Simulation Results of FRB-RGD with THD Solutions	56
Summary of Results	70
CHAPTER V NONLINEAR RESPONSE AND BIFURCATIONS OF A RIGID ROTOR SUPPORTED ON TILTING PAD JOURNAL BEARINGS (TPJB)	71
Introduction to TPJB-Rotor Systems	71
Finite Element TPJB Modeling.....	73
Model Verification	75
A Rigid Rotor Supported by TPJB.....	79
Simulation Results and Discussion	81
Summary of Results	95
CHAPTER VI NUMERICAL NONLINEAR ANALYSIS OF FLEXIBLE, MULTI MASS ROTOR BEAM MODELS.....	97
Introduction to Large Order Rotor Systems	97
Shooting Method with a Model Reduction Technique	99
Numerical Example 1: Turbocharger Supported by FRBs	103
Numerical Example 2: Eight-Stage Compressor Supported by TPJBs.....	116
CHAPTER IV CONCLUSIONS AND RECOMMENDATIONS	141
Conclusions	141
Recommendations for Further work	146
REFERENCES	151
APPENDIX A	158
APPENDIX B	160
APPENDIX C	169
APPENDIX D	176

LIST OF FIGURES

	Page
Fig. 1. Numerical continuation methods.....	13
Fig. 2. Bifurcation scenarios based on Floquet theory: (a) $(+1,0)$ →symmetry breaking or pitchfork or saddle node bifurcation, (b) $(-1,0)$ →periodic doubling bifurcation, (c) cross the unit circle→Secondary Hopf or Neimark bifurcation.....	17
Fig. 3. Concept of distance change between two neighboring trajectory for finite time interval.....	18
Fig. 4. Block diagram for calculating Lyapunov exponential.....	20
Fig. 5. FRB middle plane and its coordinate system	21
Fig. 6. Layouts of mesh and boundary condition of finite FRB model	23
Fig. 7. Rigid rotor supported by Floating Ring Bearing (FRB).....	25
Fig. 8. Bifurcation diagram ($L/D=0.2, e_{imb}=0.0$)	27
Fig. 9. Identified possible responses using the Shooting Method at 80,000 rpm ($L/D=0.2$): (a) limit cycle #1 (Stable*), (b) limit cycle #2 (Unstable*), (c) limit cycle #3 (Stable*). *the stability of the responses are evaluated by Floquet theory.....	28
Fig. 10. Repelling motion (Journal rel. to housing) of the unstable orbit (LC#2)	28
Fig. 11. Bifurcation diagram ($L/D=0.5, e_{imb}=0.0$)	29
Fig. 12. Stable periodic solutions (journal orbit rel. to ring) among N-S bifurcations	29
Fig. 13. Schematics support excitation to FRB housings	30
Fig. 14. Jump phenomenon between two limit cycles due to bump from FRB base at 80,000 rpm ($L/D=0.2, e_{imb}=0.0$): (a) before: limit cycle #1 (blue) → after: limit cycle #3 (red), (b) before: limit cycle #3 (blue) → after: limit cycle #1 (red).....	31
Fig. 15. Bifurcation ($x_{j\text{-poincaré}}$ vs. journal revolution speed) and corresponding maximum Lyapunov exponents diagrams ($L/D=0.2, e_{imb}=0.4C_i$).....	34

Fig. 16. Nonlinear response evaluation at 10,000 rpm ($L/D=0.2$, $e_{imb}=0.4$): (a~d) for orbits and ring speed, (e~g) for Poincaré maps, (h) for frequency spectrum, (i) for Lyapunov exponents, and (j) for Maximum Lyapunov exponent.....	35
Fig. 17. Nonlinear response evaluation at 16,000 rpm ($L/D=0.2$, $e_{imb}=0.4$): (a~d) for orbits and ring speed, (e~g) for Poincaré maps, (h) for frequency spectrum, (i) for Lyapunov exponents, and (j) for Maximum Lyapunov exponent.....	36
Fig. 18. Nonlinear response evaluation at 20,000 rpm ($L/D=0.2$, $e_{imb}=0.4$): (a~d) for orbits and ring speed, (e~g) for Poincaré maps, (h) for frequency spectrum, (i) for Lyapunov exponents, and (j) for Maximum Lyapunov exponent.....	37
Fig. 19. Nonlinear response evaluation at 40,000 rpm ($L/D=0.2$, $e_{imb}=0.4$): (a~d) for orbits and ring speed, (e~g) for Poincaré maps, (h) for frequency spectrum, (i) for Lyapunov exponents, and (j) for Maximum Lyapunov exponent.....	38
Fig. 20. Responses and synchronization by adding unbalance to the rotor disk at 40,000rpm: (a): responses with no unbalance ($e_{imb}=0.0$), (b): response with $e_{imb}=0.2C_i$, (c): response with $e_{imb}=0.4C_i$, (d): response with $e_{imb}=0.6C_i$	40
Fig. 21. Bifurcation diagrams and associated waterfall diagrams obtained using finite bearing method vs. short bearing approximation ($L/D=0.2$, $e_{imb}=0.4$).....	43
Fig. 22. Comparison of orbits and ring speed ratio which are obtained by finite element method (blue) and short bearing approximation (red) at (a) 10,000rpm, (b) 16,000rpm, (c) 20,000rpm, (d) 35,000rpm, (e) 50,000rpm in case of $L/D=0.2$	44
Fig. 23. Bifurcation diagrams and associated waterfall diagrams obtained using finite bearing method vs. short bearing approximation ($L/D=0.5$, $e_{imb}=0.4C_i$)	45
Fig. 24. Orbits and frequency spectrum at 60,000 rpm from finite and short bearing methods ($L/D=0.5$, $e_{imb}=0.4C_i$).....	46
Fig. 25. Orbits and frequency spectrum at 120,000 rpm from finite and short bearing methods ($L/D=0.5$, $e_{imb}=0.4C_i$).....	47
Fig. 26. Flow chart of THD-shooting method with deflation algorithm.....	54

Fig. 27. Flow chart of steady state THD solution approach.....	56
Fig. 28. Multiple response states (orbits and ring rotational speed ratio) at 65000rpm ($T_{sup}=39^{\circ}\text{C}$). *Stability of the response is determined by the Floquet theory	59
Fig. 29. Temperature distribution of coexistent response #3 at specific time instants	60
Fig. 30. Analytical bifurcation diagrams ($T_{sup}=39^{\circ}\text{C}$): (a) max/min $y_j/(C_i+C_o)$ (b) response period ratio τ/τ_s	61
Fig. 31. Comparison of analytical bifurcation diagrams (THD vs. Isothermal)	62
Fig. 32. Bifurcation (Poincaré) Diagrams w.r.t. Imbalance Eccentricity (isothermal).....	63
Fig. 33. Coexistent responses at 22000 rpm ($e_{imb}=0.3C_i$, $T_{sup}=39^{\circ}\text{C}$).....	65
Fig. 34. Repelling motion from $1\times$ sync to quasi-periodic at 22000rpm ($e_{imb}=0.3C_i$, $T_{sup}=39^{\circ}\text{C}$).....	66
Fig. 35. Time events from $1\times$ sync to quasi-periodic at 22000rpm ($e_{imb}=0.3C_i$, $T_{sup}=39^{\circ}\text{C}$).....	66
Fig. 36. Bifurcation diagrams w.r.t. lubricant supply temperature ($e_{imb}=0.3C_i$)	68
Fig. 37. Bifurcation diagrams: ranges from 15krpm to 34krpm ($e_{imb}=0.3C_i$, $T_{sup}=39^{\circ}\text{C}$).....	69
Fig. 38. Coexisting attractors at 28000rpm ($e_{imb}=0.3C_i$, $T_{sup}=39^{\circ}\text{C}$)	69
Fig. 39. TPJB (5-pad, LOP) schematics and its respective coordinates in x - y plane.....	73
Fig. 40. Finite element TPJB model and an example of pressure distributions on pads	75
Fig. 41. Comparisons of Bearing Coefficients with Someya Table.....	76
Fig. 42. Four-Pad TPJB model in Ref. [28]	77
Fig. 43. Comparison of low unbalance orbits ($e_{imb}=100\mu\text{m}$, $s=0.147$)	78
Fig. 44. Comparison of high unbalance orbits ($e_{imb}=570\mu\text{m}$, $s=0.838$)	78

Fig. 45. Limit cycles of 4 pad TPJB wrt spin speeds	79
Fig. 46. Symmetric TPJB support – rigid rotor system.....	80
Fig. 47. Bifurcation diagrams with regards to rotor mass and imbalance eccentricity - the direct numerical integration	82
Fig. 48. Loci of bifurcation diagram	84
Fig. 49. Bifurcation diagram and coexistent solutions with regard to rotor revolution speed - shooting/continuation ($e_{imb}=0.3C_b$, $m_p=1/2$, $\alpha/\beta=0.5$, $\mu=13.8cP$)	85
Fig. 50. Bifurcation diagram and coexistent solutions with regard to imbalance eccentricity on disc - shooting/continuation (rpm=16000, $m_p=1/2$, $\alpha/\beta=0.5$, $\mu=13.8cP$)	87
Fig. 51. Geometrical schematics of the pad-pivot parameter sets.....	89
Fig. 52. Bifurcation diagrams with regards to pad preloads (m_p) and pivot offset (α/β): (a) case2 ($m_p=1/2$, $\alpha/\beta=0.6$), (b) case3 ($m_p=2/3$, $\alpha/\beta=0.5$), (c) case4 ($m_p=2/3$, $\alpha/\beta=0.6$).....	90
Fig. 53. Bifurcation diagrams with regards to lubricant viscosity: (a) $\mu=27.0cP$, (b) $\mu=10.3cP$	92
Fig. 54. Bifurcation diagram (Poincaré sections) vs. MLE (λ_{max}) with regard to spin speed ($W=19.6kN$, $e_{imb}=0.3C_b$, $\mu=13.8cP$)	94
Fig. 55. Orbits, attractors and frequency spectra: (a) rpm=14.5k, (b) rpm=15.5k, (c) rpm=18.5k	95
Fig. 56. Schematics of turbocharger rotor model in Ref. [56]	103
Fig. 57. F.E. Turbo-charger model with 14 stations	104
Fig. 58. Schematics of floating ring bearing	105
Fig. 59. Orbits comparison at compressor and turbine: Full DOF (62 DOF) vs. CMS (16 DOF)	106
Fig. 60. Whirl Orbits at Compressor and Turbine	108
Fig. 61. Bifurcation diagram: maximum/minimum of vertical displacement at FRB #2.....	109

Fig. 62. Identified journal orbits (rel. to housing) at FRB #2 (106000rpm)	109
Fig. 63. Illustration of a sudden bump	110
Fig. 64. Jump phenomenon between stable orbits: response before bump (blue) → response after bump (red)	111
Fig. 65. Responses at FRB #1 with respect to different imbalance eccentricity (@ 30,000rpm).....	113
Fig. 66. Waterfall diagram w.r.t imbalance eccentricity ($e_{imb}: 0.02C_o \sim 0.12C_o$).....	114
Fig. 67. Bifurcation onset from imbalance eccentricity (@ 30,000rpm)	114
Fig. 68. Chaotic motion in Turbo-charger rotor model ($L/D=0.25$)	115
Fig. 69. Schematic of eight-stage compressor	116
Fig. 70. F.E compressor model supported by two F.E TPJB at the ends.....	118
Fig. 71. Comparison of equilibrium positions between Reduced DOF and Full DOF: without unbalance (imbalance force to bearing load ratio: 0.00)	120
Fig. 72. Comparison of low eccentricity orbits between Reduced DOF and Full DOF: with small unbalance (imbalance force to bearing load ratio: 0.60)	120
Fig. 73. Comparison of high eccentricity orbits between Reduced DOF and Full DOF: with large unbalance (imbalance force to bearing load ratio: 1.60) ...	121
Fig. 74. Bifurcation diagrams wrt spin speed and orbits at specific rpms ($m_p=1/2, \alpha/\beta=0.5$).....	122
Fig. 75. Bifurcation diagrams wrt spin speed and orbits at specific rpms ($m_p=1/2, \alpha/\beta=0.5$).....	123
Fig. 76. Coexistent periodic responses at 13,000rpm ($e_{imb}=1.5C_b$ @ 16 th node and $\mu=13.8cP, m_p=1/2, \alpha/\beta=0.5$)	124
Fig. 77. Bifurcation diagrams with regard to spin speed (using continuation): $e_{imb}=1.5C_b$ (@ 16 th node), $\mu=13.8cP, m_p=1/2$ and $\alpha/\beta=0.5$	125
Fig. 78. Multiple response states at 1300 rad/sec with $e_{imb}=1.5C_b$ (@ 16 th node) $\mu=13.8cP, m_p=1/2$ and $\alpha/\beta=0.5$	126

Fig. 79. Bifurcation diagrams with regard to imbalance eccentricity (13,000rpm, $\mu=13.8\text{cP}$, $m_p=1/2$ and $\alpha/\beta=0.5$).....	128
Fig. 80. Multiple response states at 13,000rpm and $e_{imb}=2.0C_b$ (@16 th node), $\mu=13.8\text{cP}$, $m_p=1/2$ and $\alpha/\beta=0.5$	129
Fig. 81. Bifurcation diagrams with regard to spin speed (using continuation): (a) $m_p=0.5$, $\alpha/\beta=0.5$, (b) $m_p=0.67$, $\alpha/\beta=0.5$, (c) $m_p=0.5$, $\alpha/\beta=0.6$, (d) $m_p=0.67$, $\alpha/\beta=0.6$	132
Fig. 82. Bifurcation diagrams with regard to spin speed (using transient NI): (a) $m_p=0.5$, $\alpha/\beta=0.5$, (b) $m_p=0.67$, $\alpha/\beta=0.5$, (c) $m_p=0.5$, $\alpha/\beta=0.6$, (d) $m_p=0.67$, $\alpha/\beta=0.6$	133
Fig. 83. Bifurcation diagrams with regard to imbalance eccentricity (using continuation): (a) $m_p=0.5$, $\alpha/\beta=0.5$, (b) $m_p=0.67$, $\alpha/\beta=0.5$, (c) $m_p=0.5$, $\alpha/\beta=0.6$, (d) $m_p=0.67$, $\alpha/\beta=0.6$	134
Fig. 84. Bifurcation diagrams with regard to imbalance eccentricity (using transient NI): (a) $m_p=0.5$, $\alpha/\beta=0.5$, (b) $m_p=0.67$, $\alpha/\beta=0.5$, (c) $m_p=0.5$, $\alpha/\beta=0.6$, (d) $m_p=0.67$, $\alpha/\beta=0.6$	135
Fig. 85. Bifurcation diagrams with regard to spin speed (using continuation): (a) $\mu=27.0\text{cP}$, (b) $\mu=13.8\text{cP}$, (c) $\mu=7.0\text{cP}$	137
Fig. 86. Bifurcation diagrams with regard to spin speed (using transient NI): (a) $\mu=27.0\text{cP}$, (b) $\mu=13.8\text{cP}$, (c) $\mu=7.0\text{cP}$	138
Fig. 87. Bifurcation diagrams with regard to imbalance eccentricity (using continuation): (a) $\mu=27.0\text{cP}$, (b) $\mu=13.8\text{cP}$, (c) $\mu=7.0\text{cP}$	139
Fig. 88. Bifurcation diagrams with regard to imbalance eccentricity (using transient NI): (a) $\mu=27.0\text{cP}$, (b) $\mu=13.8\text{cP}$, (c) $\mu=7.0\text{cP}$	140
Fig. 89. The period-double route to chaos in a Logistics map function.....	149
Fig. 90. An example of a rotor-bearing test rig.....	150

LIST OF TABLES

	Page
Table 1. Rotor and FRB parameters	24
Table 2. FRB boundary conditions on finite element fluid film model boundaries..	25
Table 3. Base excitation parameters	31
Table 4. Orbit and associated LEs	32
Table 5. Response characteristics	34
Table 6. Rotor and FRB parameters used for synchronization.....	39
Table 7. Bifurcation onset speed differences between finite and short bearing methods ($L/D=0.5$, $e_{imb}=0.4C_i$).....	46
Table 8. FRB and lubricant parameters	57
Table 9. TPJB specifications in Ref. [28].....	77
Table 10. Unbalance parameters in Ref. [28].....	77
Table 11. TPJB specification and parameter ranges.....	80
Table 12. Bifurcation events for lubricant viscosity.....	92
Table 13. Mechanical models of large order system	98
Table 14. Parameters of the rotor shaft.....	104
Table 15. Parameters of the rigid disks	104
Table 16. Floating Ring Bearing Dimensions	105
Table 17. Sectional data of the eight-stage compressor	117
Table 18. TPJB specification and parameter ranges.....	118
Table 19. Imbalance position and amounts in the eight-stage compressor	118
Table 20. Coordinate values of equilibrium positions.....	119

Table 21. Summary of pad preload (m_p) and pivot offset (α/β) effects on bifurcations	131
--	-----

CHAPTER I

INTRODUCTION

Nonlinear Phenomena in Rotor-Fluid Bearing Systems

Fluid film force may be the most common source of nonlinearities in rotor-bearing systems, since various applications of fluid film bearings such as plain journal bearings, fixed-/tilting-pad journal bearings, squeeze film dampers, floating ring bearings, pressure dam bearings, etc. have been widely used in laboratory and industrial fields. Engineers and researchers who were dealing with turbomachinery supported by fluid film components have observed various nonlinear behaviors of the rotor system such as sub-synchronous whirls, quasi-periodic, aperiodic responses, sub- or super-critical Hopf bifurcation, Neimark-Sacker bifurcation and even chaotic motions [1-6]. In addition, due to the demands of high efficient and high power capacity rotor-machinery, the designs for modern bearings/seals, and squeeze film dampers are facing more drastic specifications. These changes can induce strong nonlinearities, which make difficult to predict system response and stability. These trends demonstrate the importance of nonlinear dynamic analysis; however, today's common analysis methods such as linearization of bearing coefficients or direct numerical integrations have some limitations to thoroughly understand the nonlinear phenomena.

Limitations of Linear and Transient Analyses

In the linear analysis, stiffness and damping coefficients of a bearing are determined by calculating dynamic forces at static equilibrium position. The linearized bearing force terms are utilized to predict instability onset speed of the rotor system. The turbo lab in Texas A&M University is a leading group of measuring/predicting stiffness and damping coefficients of various fluid film bearings [7,8]. The results are still very important to decide system stability, but several nonlinear phenomena cannot be discovered. For instance, the fluid reaction force has obtained with the assumption of absence of imbalance of a rotor, even though it is commonly presented in real machines, so that more stabilized or inaccurate predictions than reality may be provided. Besides, the linear approach gives the stability information in terms of convergence (stable) or divergence (unstable) of the journal motion, thus no other detailed information can be provided after the instability onset speed. This prediction limits the machine's inherent capability such that it is able to operate beyond the onset speed. In addition, the onset speed, which is also called as primary Hopf bifurcation in nonlinear theory, can have different stability characteristics in standpoint of nonlinear dynamics; for instance, Hopf can be divided sub- and super-critical, and each of them exhibits different patterns of oil whirls.

For better understanding, nonlinear analysis based on the direct numerical integration schemes are widely used in recent studies. The transient, numerical integration to steady states (TNISS) is a solution approach based on initial condition problems for nonlinear equations, so that the response of a dynamic system is obtained

consecutively in time domain from the initial moment. This numerical procedure extends that the user can predict response states beyond the instability onset speed and the orbital motions induced by unbalance force. Even though vast numbers of the research rely on the numerical procedure [1-6, 9-14], TNISS has some limitations such that excessive computation time is often required to get a steady state response, especially near bifurcation points. In addition, users need to specify an initial condition for all degrees of freedom (e.g. positions and velocities) and important response states may miss on the initial conditions. This produces that a totally different response state may exist for the same speed and imbalance distribution than predicted by TNISS. In particular, unstable limit cycles can never obtained even though they are required for a complete picture of the bifurcation characteristics of the system (e.g., repelling/attracting orbital motion).

Multiple Response State Prediction Methods

Multiple response states prediction (MRSP) for rotordynamics is another approach based on nonlinear dynamics theory. MRSP employs an algorithm directed search to determine all possible coexistent response states and their stability. MRSP algorithm can be roughly categorized into two solution approaches.

In the frequency based approach, the harmonic balance method (HBM) was applied to find synchronous/sub-synchronous response state of rotor system with stator rubs and squeeze-film dampers, respectively [15,16]. Some research shows that HBM is able to be combined with the arc-length continuation to extend solution branches over a varying system parameter in a rotor/stator contact problem in Ref. [17]. Trigonometric

collocation method (TCM) along with component mode synthesis (CMS) was used to calculate the periodic response of multi disk rotor system with squeeze film damper [18,19]. The solution approach in the frequency domain methods can be explained as an assumed response or nonlinear force is defined in terms of harmonics of frequency components then substituted into the original system equation. This approach inherently generates more nonlinear algebraic equations than the number of system equation whenever users attempt to define more precise solution form with supplementary frequency components. Besides, these methods may be hard to apply if nonlinear force model in a system is highly complicated.

In the time domain based approach, the shooting method, which is a numerical approach to solve two point boundary value problems, has been used to predict response states of a rotor system. Here, the known boundary conditions are the beginning and the end states of a limit cycle, and each state contains the information of position and velocity at the moment. This algorithm is capable of determining stability of response, bifurcation scenarios and multiple response states in operations, but it also requires amounts of computation resources and time to obtain Jacobian matrix in the algorithm routines. Sundararajan and Noah developed non-autonomous shooting and arc-length continuation codes combined with CMS scheme for flexible rotor systems supported by squeeze film dampers and plain journal bearings [20,21]. Chu and Tang applied non-autonomous shooting to a rotor-bearing system with pedestal looseness and determined response stability by Floquet theory [22].

So far, however, most research on MRSP for rotordynamics has dealt with nonlinear behaviors of single fluid film applications such as a plain journal bearing and a squeeze film damper, and fluid film force is obtained by employing infinitely short-/long-bearing approximation. The Ocvirck and Sommerfeld models are able to reduce computation time due to their closed form expressions of isoviscosity Reynolds equation, but it is known that the prediction is only reliable for short-/long-bearing length to diameter ratio (L/D) and low eccentricity cases [23,24]. Besides, the assumption of isothermal condition of the lubricant layer restricts to investigate thermal effects on nonlinear response and bifurcations. Another limitation is that an extended application to various practical bearings such as pressure dam, fixed-, tilting-pad bearings may not be appropriate with the simplified force model.

Research Objectives

The present research try to understand nonlinear response and bifurcations of rotor-fluid film bearing systems with aids of various numerical analysis tools such as shooting/arc-length continuation, a direct numerical integration, Poincaré sections, Lyapunov exponents, etc. In this study, however, some advanced numerical algorithms and more accurate rotor and bearing models are applied to overcome the described limitations of the current other research. For case study, two types of fluid film bearings are selected as floating ring bearing and tilting pad journal bearing, and each bearing is to be combined with a rigid rotor as well as a flexible rotor.

Floating ring bearing (FRB) is a special type of journal bearing and has strong nonlinearity due to its double-layered fluid film on inner and outer ring surfaces. Though it is a source of instability, cost-effectiveness and high functionality for lightly loaded high speed rotor system provide that the FRB has been widely used for automotive turbochargers (TCs) and aircraft accessory equipment. Since FRB can be operated in extremely high speed range (e.g., 150krpm-350krpm) [9], various nonlinear phenomena have been reported from a number of research in terms of TNISS scheme. However, analytical study for the nonlinear behaviors of FRB was not thoroughly conducted compared to the single fluid film applications. Recently, a few works began to analyze FRB's nonlinear behaviors with a MRSP method. Boyaci et al. utilized both numerical continuation software packages, AUTO and MATCONT, and center manifold reduction techniques to analyze FRB supported rotors [25,26]. They investigated bifurcations, coexistent solutions, and total instability with nonlinear force model based on the short bearing approximation.

Tilting pad journal bearings (TPJB) are one of the most popular bearing applications in modern turbomachinery due to their stabilizing effects on rotor-bearing systems. The tilting motions of pads lead the cross-coupled stiffness terms of the bearings become negligible, so the bearing has stable performance than plain/fixed-pad journal bearings. Though considerable numerical study has been conducted to predict the responses and characteristics of TPJB rotor systems by means of the linear and TNISS approaches with the finite length of TPJB models [27-30], the analytical bifurcation

studies have been seldom reported yet. Thus the nonlinear behaviors related to multiple response states, bifurcations, repelling/attracting motions, etc. are still in vague.

In this paper, an improved autonomous/non-autonomous shooting method for a rotor system is introduced to determine multiple response states of a rigid/flexible rotor supported by fluid film bearings. Here, the shooting is combined with the deflation algorithm and the parallel computing strategy. Deflation is a mathematical algorithm to determine solutions in a multiple roots problem [31-33]. The idea of this approach is to reduce needless computation time by avoiding previously found solutions while a nonlinear solver is seeking a new solution. To achieve the purpose, the original system equation is redefined once a unique solution is identified. Parallel computing has been increasingly adopted in recent years to reduce computation time through the full use of multicore processors [34]. Parallel computing strategy is also suitable to shooting and continuation algorithms, since the routines for obtaining of Jacobian matrix from perturbed initial conditions are independent procedures, so each segment of the solution routine can be executed simultaneously. In this work, both accelerating methods have significantly enhanced computation efficiency in theoretical and practical manners.

This appears to be the first work to apply the deflation and the parallel computing to the MRSP technique for finding multiple responses and bifurcations in rotor dynamics. The solution obtained from the numerical method contains phase state and period of limit cycle so that the bifurcation diagram can provide orbit and period information along with system parameters. Since multiple orbits can coexist at the same operation speed and imbalance amount, response jump between two limit cycles is

simulated with a sudden base excitation during operation. In addition, other nonlinear aspects such as chaos and synchronization in the rotor-bearing systems are presented. Referring to the work from Adiletta et al. in Ref [4], chaotic motion is shown for the non-autonomous, heavily loaded case. Lyapunov exponent, strange attractor, bifurcation diagram, and frequency spectrum, were used to evaluate the chaos as in Ref. [35]. Quenching oil whirls using intentional imbalance (i.e., synchronization) is useful treatment in industrial fields [36]. A numerical investigation for synchronization is demonstrated.

As introduced, due to the computational burden of shooting/continuation, all the previous work has used infinitely short bearing approximation [20-22, 25,26]. In contrast, the present research utilizes the finite element based bearing models by enduring the computational overloads with aids of the acceleration techniques: deflation and parallel computing. This makes possible to determine lubricant pressure distributions, velocity profiles and viscosity distributions during the solution routines. This approach is eligible to investigate thermal effect on bifurcations in a fluid film bearing. In order to proceed the analytical study, the finite element based variable viscosity Reynolds equation is coupled with the energy equation, and then it is dragged into the shooting and the arc-length continuation algorithms.

The format of the dissertation is as follows. In the next chapter, mathematical backgrounds of the numerical analysis methods for the nonlinear rotor-bearing system are introduced. In Chapter 3, nonlinear response and bifurcations of a rigid rotor supported by FRBs are presented. Chapter 4 describes effects of thermo-hydrodynamic

FRB model on rotordynamic bifurcations. In Chapter 5, nonlinear characteristics of a rigid rotor supported by TPJBs are analyzed. Chapter 6 extends the rotor applications to general, flexible, multi-mass beam models. Finally, the conclusions are reached in Chapter 7.

Original Contributions of Research

Advanced nonlinear dynamics algorithms are proposed:

- Shooting combined with the deflation algorithm and the parallel computing
- Steady state thermal solutions are included in the shooting method
- Autonomous and non-autonomous codes are developed

Precise computational bearing models are utilized for bifurcation study:

- Finite element based fluid film bearing models (e.g, floating ring bearing, tilting pad journal bearing) in analytical study
- Lubricant temperature distributions and viscosity are updated

Practical/industrial rotor models are applied:

- Turbo-charger (62 DOF) and compressor rotor (150 DOF)

CHAPTER II

THEORY

Shooting Method with Deflation Algorithm

The shooting method is a numerical approach to solve two-point boundary value problems for identifying a periodic solution in autonomous/non-autonomous systems. In non-autonomous system, the period of the solution subjected to external excitation is assumed to be a known such as forcing period τ_F or a rational multiple of τ_F . On the other hand, the period is an unknown value in autonomous system since it is depended on the internal state of system. Then the system needs an additional constraint condition to remove the arbitrariness. There exists several techniques to set up the condition and Mees' approach are used in this work [37,38].

Let \mathbf{x}_0 be an initial condition for a periodic solution and $\mathbf{x}_T(\mathbf{x}_0, \tau_0)$ is the state vector after τ_0 period. If \mathbf{x}_0 is a value of \mathbf{x} on an orbital equilibrium state of period τ_0 , it is true that

$$\mathbf{f}(\mathbf{x}_0, \tau_0) = \mathbf{x}_T(\mathbf{x}_0, \tau_0) - \mathbf{x}_0 = 0 \quad (1)$$

Let \mathbf{x}_0^i, τ_0^i be a first guess of the function \mathbf{f} in Eq. (1), and expand in the Taylor series and remain the first order term in $\Delta\mathbf{x}_0$ and $\Delta\tau_0$ within a tolerance limit,

$$\mathbf{f}(\mathbf{x}_0^i, \tau_0^i) + \left. \frac{\partial \mathbf{f}(\mathbf{x}_0, \tau_0)}{\partial \mathbf{x}_0} \right|_i \delta \mathbf{x}_0^i + \left. \frac{\partial \mathbf{f}(\mathbf{x}_0, \tau_0)}{\partial \tau_0} \right|_i \delta \tau_0^i \approx 0 \quad (2)$$

where $\delta \mathbf{x}_0^i = \mathbf{x}_0^{i+1} - \mathbf{x}_0^i$ and $\delta \tau_0^i = \tau_0^{i+1} - \tau_0^i$.

Substitute Eq. (1) into Eq. (2) to obtain,

$$\mathbf{x}_T(\mathbf{x}_0^i, \tau_0^i) - \mathbf{x}_0^i + [\mathbf{J}_{x_0}^i - \mathbf{I}] \delta \mathbf{x}_0^i + \mathbf{J}_{\tau_0}^i \delta \tau_0^i = 0 \quad (3)$$

where, $\mathbf{J}_{x_0}^i = \frac{\partial \mathbf{x}_T(\mathbf{x}_0^i, \tau_0^i)}{\partial \mathbf{x}_0}$, $\mathbf{J}_{\tau_0}^i = \frac{\partial \mathbf{x}_T(\mathbf{x}_0^i, \tau_0^i)}{\partial \tau_0}$, and \mathbf{I} is identity matrix

Since n number of system equations have $n+1$ unknowns in terms of \mathbf{x}_0 and τ_0 , it is necessary to define an additional constraint equation. Here, Mee's approach is,

$$\dot{\mathbf{x}}_0^T \delta \mathbf{x}_0 = 0 \quad (4)$$

This assumption specifies the correction vector $\delta \mathbf{x}_0$ to be orthogonal to the vector field $\dot{\mathbf{x}}_0$. When Eq. (4) is included, the following Newton-Raphson (N-R) iteration form can be obtained for the solution search,

$$\begin{Bmatrix} \mathbf{x}_0^{i+1} \\ \tau_0^{i+1} \end{Bmatrix} = \begin{Bmatrix} \mathbf{x}_0^i \\ \tau_0^i \end{Bmatrix} + \begin{bmatrix} \mathbf{J}_{x_0}^i - \mathbf{I} & \mathbf{J}_{\tau_0}^i \\ \dot{\mathbf{x}}_0^{iT} & 0 \end{bmatrix}^{-1} \begin{Bmatrix} \mathbf{x}_0^i - \mathbf{x}_T(\mathbf{x}_0^i, \tau_0^i) \\ 0 \end{Bmatrix} \quad (5)$$

This paper employs a deflation algorithm to enhance the computational efficiency of the shooting method. The general concept of the deflation approach is to avoid previously found solutions while a nonlinear solver is seeking further solutions in a multiple roots problem. This can be achieved by modifying the original system equations using “deflated” functions once a new solution is found. The deflated function has all of the same roots as the original function with the exception that roots that have already been located no longer are roots of the deflated function. The deflation function employed is a series product of Euclidean norms of deviations away from the initial states of periodic solutions previously obtained by the shooting approach. In the case of an autonomous system, the periods (τ_0) of solution are independent of each other as well as the phase states (x_0). In this study, for computation simplicity, the period of solution is selected to define the deflated function h ,

$$h(\tau_0) = \prod_{j=1}^p \|\tau_0^i - \tau_{0j}\| \quad (6)$$

where, $\|\cdot\|$ denotes Euclidean norm and $\tau_{0j}, j=1,2,\dots,p$ is the previously found periods of solutions. This function is updated every time a new (unique) solution is found. The original system equation is modified with h appearing in the denominator in Eq. (7) so that previously found roots are no longer roots of the modified function.

$$\hat{\mathbf{f}}(\mathbf{x}_0, \tau_0) = \frac{\mathbf{f}(\mathbf{x}_0, \tau_0)}{h(\tau_0)} = \frac{\mathbf{x}_T(\mathbf{x}_0, \tau_0) - \mathbf{x}_0}{\prod_{j=1}^p \|\tau_0^i - \tau_{0j}\|} = 0 \quad (7)$$

Using Eq. (7), the first order Taylor series as in Eq. (2, 3) are redefined as in Eq. (8, 9) such as

$$\hat{\mathbf{f}}(\mathbf{x}_0^i, \tau_0^i) + \left. \frac{\partial \hat{\mathbf{f}}(\mathbf{x}_0, \tau_0)}{\partial \mathbf{x}_0} \right|_i \delta \mathbf{x}_0^i + \left. \frac{\partial \hat{\mathbf{f}}(\mathbf{x}_0, \tau_0)}{\partial \tau_0} \right|_i \delta \tau_0^i \simeq 0 \quad (8)$$

$$\begin{aligned} \frac{\mathbf{x}_T(\mathbf{x}_0^i, \tau_0^i) - \mathbf{x}_0^i}{h(\tau_0)} + h(\tau_0)^{-1} \left\{ \left. \frac{\partial \mathbf{x}_T(\mathbf{x}_0, \tau_0)}{\partial \mathbf{x}_0} \right|_i - \mathbf{I} \right\} \delta \mathbf{x}_0^i + \\ \left\{ -h(\tau_0)^{-2} \left. \frac{\partial h}{\partial \tau_0} \right|_i \{ \mathbf{x}_T(\mathbf{x}_0^i, \tau_0^i) - \mathbf{x}_0^i \} + h(\tau_0)^{-1} \left. \frac{\partial \mathbf{x}_T}{\partial \tau_0} \right|_i \right\} \delta \tau_0^i = 0 \end{aligned} \quad (9)$$

If Mees correction vectors are included, the N-R iteration form with deflation technique yields,

$$\begin{aligned} \begin{Bmatrix} \mathbf{x}_0^{i+1} \\ \tau_0^{i+1} \end{Bmatrix} = \begin{Bmatrix} \mathbf{x}_0^i \\ \tau_0^i \end{Bmatrix} + \\ \begin{bmatrix} h(\tau_0)^{-1} \{ \mathbf{J}_{x_0}^i - \mathbf{I} \} & -h(\tau_0)^{-2} \left. \frac{\partial h}{\partial \tau_0} \right|_i \{ \mathbf{x}_T(\mathbf{x}_0^i, \tau_0^i) - \mathbf{x}_0^i \} + h(\tau_0)^{-1} \mathbf{J}_{\tau_0}^i \\ \hline \dot{\mathbf{x}}_0^{iT} & 0 \end{bmatrix}^{-1} \begin{Bmatrix} \frac{\mathbf{x}_0^i - \mathbf{x}_T(\mathbf{x}_0^i, \tau_0^i)}{h(\tau_0)} \\ 0 \end{Bmatrix} \end{aligned} \quad (10)$$

Arc-length Continuation

As can be seen in Fig. 1, numerical continuations can be followed a shooting method to explore solution manifolds of a nonlinear system. A simple numerical continuation scheme such as the sequential continuation sets the previous solution vector as an initial guess for next step. This is intuitive and simple to use, but it may fail the solution guess procedure when it faces a high curvature region.

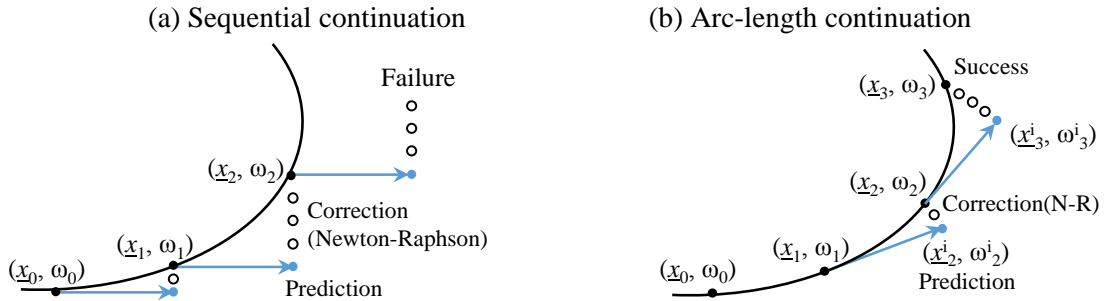


Fig. 1. Numerical continuation methods

In contrast, the arc-length continuation scheme produces an initial guess for next step in the tangential direction with regard to the current solution curve. Thus, it is capable of the succession of solution search even in the middle of the high curvature. In order to pass the inflection point, the arc-length continuation defines the trajectory of solution curves as a function of arc-length (Δs). Then Eq. (1) has an additional unknown, ω , for the arc-length function, $f(x, \omega)$, and to constrain the parameter, an additional function is introduced by employing Euclidean arc-length normalization.

$$\zeta \left\| \frac{d\mathbf{x}}{ds} \right\|_2^2 + \left(\frac{d\omega}{ds} \right)^2 = 1 \quad (11)$$

where $\zeta = 1$ (tuning parameter).

If the initial point (\mathbf{x}_0, ω_0) of the continuation was pre-defined by the shooting method, the prediction for next step in the tangential direction can be expressed as,

$$(\bar{\mathbf{x}}_1^i, \omega_1^i) = (\bar{\mathbf{x}}_0, \omega_0) + (\dot{\bar{\mathbf{x}}}_0, \dot{\omega}_0) \Delta s \quad (12)$$

where, $(\dot{\bar{\mathbf{x}}}_0, \dot{\omega}_0) = (d\mathbf{x}_0/ds, d\omega_0/ds)$

It should be noted that there is no previous point at the very beginning of prediction. Thus, a procedure for defining the first tangent should be needed, and it can be expressed as follows,

$$\frac{d}{d\omega} (\mathbf{f}(\mathbf{x}_0, \omega_0)) = \frac{d}{d\mathbf{x}} \mathbf{f} \frac{d\mathbf{x}}{d\omega} \Big|_{n=0} + \frac{d\mathbf{f}}{d\omega} \Big|_{n=0} = \mathbf{J}_0 \frac{d\mathbf{x}}{d\omega} \Big|_{n=0} + \mathbf{f}_{\omega_0} = 0 \quad (13)$$

$$\frac{d\mathbf{x}}{d\omega} \Big|_{n=0} = -\mathbf{J}_0^{-1} \cdot \mathbf{f}_{\omega_0} \quad (14)$$

Using Eq. (11) to obtain,

$$\zeta \left\| \frac{d\mathbf{x}}{d\omega} \frac{d\omega}{ds} \right\|_2^2 + \left(\frac{d\omega}{ds} \right)^2 = 1 \Rightarrow \left(\zeta \left\| \frac{d\mathbf{x}}{d\omega} \right\|_2^2 + 1 \right) \left(\frac{d\omega}{ds} \right)^2 = 1 \quad (15)$$

$$\frac{d\omega}{ds} = 1 / \sqrt{\zeta \left\| \frac{d\mathbf{x}}{d\omega} \right\|_2^2 + 1} \quad (16)$$

Using Eqs. (14, 16),

$$\frac{d\mathbf{x}}{ds} = -\mathbf{J} \cdot \mathbf{f}_\omega / \sqrt{\zeta \left\| \frac{d\mathbf{x}}{d\omega} \right\|_2^2 + 1} \quad (17)$$

Then the next point (\mathbf{x}_1, ω_1) can be obtained as,

$$\begin{Bmatrix} \mathbf{x}_1 \\ \omega_1 \end{Bmatrix} = \begin{Bmatrix} \mathbf{x}_0 \\ \omega_0 \end{Bmatrix} + \begin{Bmatrix} d\mathbf{x}/ds \\ d\omega/ds \end{Bmatrix}_0 \Delta s \quad (18)$$

Equations (13-17) are only used for the first prediction of the continuation. Once the two solution points (e.g., (\mathbf{x}_0, ω_0) , (\mathbf{x}_1, ω_1)), are obtained, the first tangential prediction $(\mathbf{x}^i_2, \omega^i_2)$ for next solution can be defined as,

$$\begin{aligned} \mathbf{x}^i_2 &= \mathbf{x}_1 + \frac{\mathbf{x}_1 - \mathbf{x}_0}{\Delta s} \Delta s = 2\mathbf{x}_1 - \mathbf{x}_0 \\ \omega^i_2 &= \omega_1 + \frac{\omega_1 - \omega_0}{\Delta s} \Delta s = 2\omega_1 - \omega_0 \end{aligned} \quad (19)$$

In most cases, the first guess in the tangential direction suggests an uncorrected solution. Thus, a correction procedure should be incorporated, and it can be achieved by employing Newton's method as in the shooting algorithm. Eq. (11) can be linearized by backward difference approximation such that

$$\zeta \left\| \frac{\mathbf{x}_n^i - \mathbf{x}_{n-1}}{\Delta s} \right\|_2^2 + \left(\frac{\omega_n^i - \omega_{n-1}}{\Delta s} \right)^2 = 1 \quad (20)$$

where, $(\mathbf{x}_{n-1}, \omega_{n-1})$ is the found solution for previous step $(n-1)$ and $(\mathbf{x}_n^i, \omega_n^i)$ is guess for current step (n) .

A function q can be defined from Eq. (11)

$$q(\mathbf{x}, \omega, s) = \zeta \left\| \mathbf{x}_n^i - \mathbf{x}_{n-1} \right\|_2^2 + (\omega_n^i - \omega_{n-1})^2 - (\Delta s)^2 = 0 \quad (21)$$

Using Taylor's series in first order form, the functions \mathbf{f} and q (i.e., eqns. (1), (21)) are given by

$$\begin{bmatrix} \mathbf{f}(\mathbf{x}_n, \omega_n) \\ q(\mathbf{x}_n, \omega_n, s) \end{bmatrix} = \begin{bmatrix} \mathbf{f}(\mathbf{x}_n^i, \omega_n^i) \\ q(\mathbf{x}_n^i, \omega_n^i, s) \end{bmatrix} + \begin{bmatrix} \frac{\partial \mathbf{f}_n^i}{\partial \mathbf{x}} & \frac{\partial \mathbf{f}_n^i}{\partial \omega} \\ \frac{\partial q_n^{iT}}{\partial \mathbf{x}} & \frac{\partial q_n^i}{\partial \omega} \end{bmatrix} \begin{Bmatrix} \mathbf{x}_n^{i+1} - \mathbf{x}_n^i \\ \omega_n^{i+1} - \omega_n^i \end{Bmatrix} = 0 \quad (22)$$

where $\partial \mathbf{f} / \partial \mathbf{x}_n$ is $p \times p$ matrix, $\partial \mathbf{f} / \partial \omega_n$ is $p \times 1$ vector, $\partial q / \partial \mathbf{x}_n$ is $1 \times p$ vector and $\partial q / \partial \omega_n$ is scalar. The detailed expressions for $\partial q_n / \partial \mathbf{x}$ and $\partial q_n / \partial \omega$ are,

$$\frac{\partial q_n^i}{\partial \mathbf{x}} = 2\zeta (\mathbf{x}_n^i - \mathbf{x}_{n-1}^i), \quad \frac{\partial q_n^i}{\partial \omega} = 2(\omega_n^i - \omega_{n-1}^i) \quad (23)$$

Then the iterative form of Newton's method

$$\begin{aligned} \begin{Bmatrix} \mathbf{x}_n^{i+1} \\ \omega_n^{i+1} \end{Bmatrix} &= \begin{Bmatrix} \mathbf{x}_n^i \\ \omega_n^i \end{Bmatrix} + \begin{bmatrix} \mathbf{J}_n^i & \mathbf{f}_{\omega,n}^i \\ \frac{\partial q_n^{iT}}{\partial \mathbf{x}} & \frac{\partial q_n^i}{\partial \omega} \end{bmatrix}^{-1} \begin{bmatrix} -\mathbf{f}(\mathbf{x}_n^i, \omega_n^i) \\ -q(\mathbf{x}_n^i, \omega_n^i, s) \end{bmatrix} \\ &= \begin{Bmatrix} \mathbf{x}_n^i \\ \omega_n^i \end{Bmatrix} + \begin{bmatrix} \mathbf{J}_n^i & \mathbf{f}_{\omega,n}^i \\ 2\zeta (\mathbf{x}_n^i - \mathbf{x}_{n-1}^i) & 2(\omega_n^i - \omega_{n-1}^i) \end{bmatrix}^{-1} \begin{bmatrix} \mathbf{x}_n^i - \mathbf{x}_{TR}(\mathbf{x}_n^i, \omega_n^i) \\ -\zeta \|\mathbf{x}_n^i - \mathbf{x}_{n-1}^i\|^2 - (\mathbf{x}_n^i - \mathbf{x}_{n-1}^i)^2 + (\Delta s)^2 \end{bmatrix} \end{aligned} \quad (24)$$

The Jacobian matrices \mathbf{J}_n and \mathbf{f}_ω can be obtained numerically from perturbed initial condition with respect to \mathbf{x} and ω .

Floquet Theory

The shooting and continuation procedures provide a periodic solution which may be a result of limit cycle or harmonically forced steady state responses in a nonlinear system. The local stability of the periodic solution is explicitly determined by Floquet theory. If a dynamic equilibrium of the system is described with a set of n nonlinear, ordinary differential equations,

$$\mathbf{x}' = \mathbf{g}(\mathbf{x}, \tau) \quad (25)$$

By obtaining an approximate, time varying, periodic solution $\mathbf{x}_0(\tau)$, and solving the matrix differential equation

$$\frac{d}{d\tau}\Phi_m = \mathbf{J}(\mathbf{x}_0, \tau)\Phi_m \quad (26)$$

with the initial condition $\Phi_m(0)=\mathbf{I}_n$. The solution is called the matrizant matrix.

$$\Phi_m(0)=\mathbf{I} \quad (27)$$

Evaluate Φ_m at τ_{\min} =minimum period of \mathbf{J}

$$\mathbf{H} = \Phi_m(\tau_{\min}) = \text{Monodromy matrix} \quad (28)$$

Eigenvalues (ζ_{mk}) of the monodromy matrix are Floquet multipliers, also called as characteristic numbers, which indicate system stability and bifurcation scenario as described in Fig. 2.

- asymptotically stable if $|\zeta_{mk}| < 1$ for all k
- asymptotically unstable if $|\zeta_{mk}| > 1$ for all k
- marginally stable if $|\zeta_{mk}| = 1$ for all k and $|\zeta_{mj}| < 1$ for all $j \neq k$

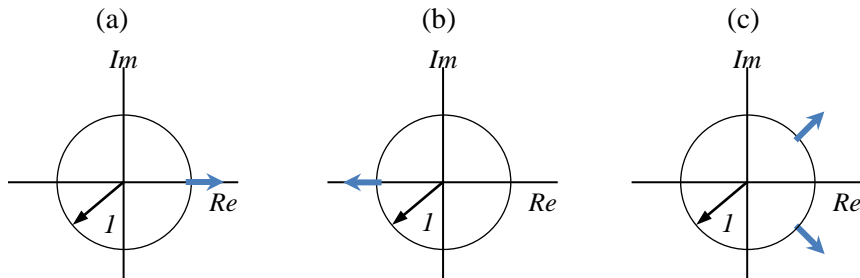


Fig. 2. Bifurcation scenarios based on Floquet theory: (a) $(+1,0)$ →symmetry breaking or pitchfork or saddle node bifurcation, (b) $(-1,0)$ →periodic doubling bifurcation, (c) cross the unit circle→Secondary Hopf or Neimark bifurcation

Lyapunov Exponents

In some circumstances successive bifurcations leads to chaos. Various techniques are used to identify the presence of chaos by implicit and explicit approaches. Lyapunov exponents provide a quantitative indicator by obtaining averaged rate of divergence or convergence of two infinitesimally close trajectories onto an attractor in state space (Fig. 3). The neighboring solutions exhibit exponential growth or exponential decay (i.e., $d(t) \sim d_0 e^{\lambda t}$). Since n number of independent initial vectors in n dimensional space is tested to calculate the rate of the separation, there is a spectrum of Lyapunov exponents λ_i ($i=1,2,\dots,n$), the maximum value of the Lyapunov spectrum λ_{\max} can be a critical indicator to determine stability of local responses.

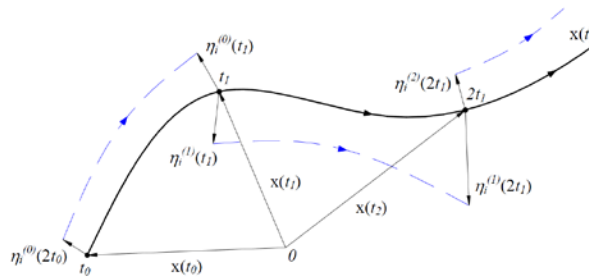


Fig. 3. Concept of distance change between two neighboring trajectory for finite time interval

- $\lambda_{\max} < 0$: system attracts to a fixed point or stable limit cycle (asymptotic stability)
- $\lambda_{\max} = 0$: system is neutrally stable (Lyapunov stability)
- $\lambda_{\max} > 0$: system is chaotic and unstable

The distance $\Delta(t)$ to be measured between actual attractor $\mathbf{x}(t)$ and perturbed trajectories $\mathbf{x}'(t)$ is defined,

$$\Delta(t) = \|\mathbf{x}'(t) - \mathbf{x}(t)\| = \|\delta\mathbf{x}(t)\| = \sqrt{\delta\mathbf{x}_1^2 + \delta\mathbf{x}_2^2 + \dots + \delta\mathbf{x}_n^2} \quad (29)$$

The perturbations are determined using the linearized form of the nonlinear governing differential equations along with initial conditions for the perturbations.

- Governing differential equations: $\dot{\mathbf{x}} = \mathbf{f}(\mathbf{x})$ (30)

- Linearized form of Eq. (29): $\boldsymbol{\eta}' = \mathbf{A}(\boldsymbol{\eta})$, where \mathbf{A} is $n \times n$ matrix of partial derivatives of $\mathbf{f}(\mathbf{x})$ (31)

Equations (30) and (31) need to be simultaneously integrated until the LEs of the nonlinear system has reached steady state. However, numerical integration for large t may cause numerical error, the integration need to be carried out in appropriate time interval t_f and newly perturbed orthonormal vectors should be defined every time step. This set of orthonormalized perturbed vector can be produced using Gram-Schmidt procedure,

$$\hat{\boldsymbol{\eta}}_1 = \frac{\boldsymbol{\eta}_1(t_f)}{\|\boldsymbol{\eta}_1(t_f)\|}, \hat{\boldsymbol{\eta}}_2 = \frac{\boldsymbol{\eta}_2(t_f) - (\boldsymbol{\eta}_2(t_f) \cdot \hat{\boldsymbol{\eta}}_1)\hat{\boldsymbol{\eta}}_1}{\|\boldsymbol{\eta}_2(t_f) - (\boldsymbol{\eta}_2(t_f) \cdot \hat{\boldsymbol{\eta}}_1)\hat{\boldsymbol{\eta}}_1\|}, \text{ and } \hat{\boldsymbol{\eta}}_m = \frac{\boldsymbol{\eta}_m(t_f) - \sum_{i=1}^{m-1} (\boldsymbol{\eta}_m(t_f) \cdot \hat{\boldsymbol{\eta}}_i)\hat{\boldsymbol{\eta}}_i}{\|\boldsymbol{\eta}_m(t_f) - \sum_{i=1}^{m-1} (\boldsymbol{\eta}_m(t_f) \cdot \hat{\boldsymbol{\eta}}_i)\hat{\boldsymbol{\eta}}_i\|} \quad (32)$$

After repeating the integrations in Eqs. (30, 31) and Gram-Schmidt orthonormalizations in Eq.(32) for r times, the Lyapunov exponent is obtained from

$$\lambda_i = \frac{1}{rt_f} \sum_{k=1}^r \ln(\Delta_i^{(k)}(t_k)) \quad (33)$$

where superscript k denotes the k th time step and the subscript i denotes i th vector element. Figure 4 shows the block diagrams for calculating Lyapunov exponents.

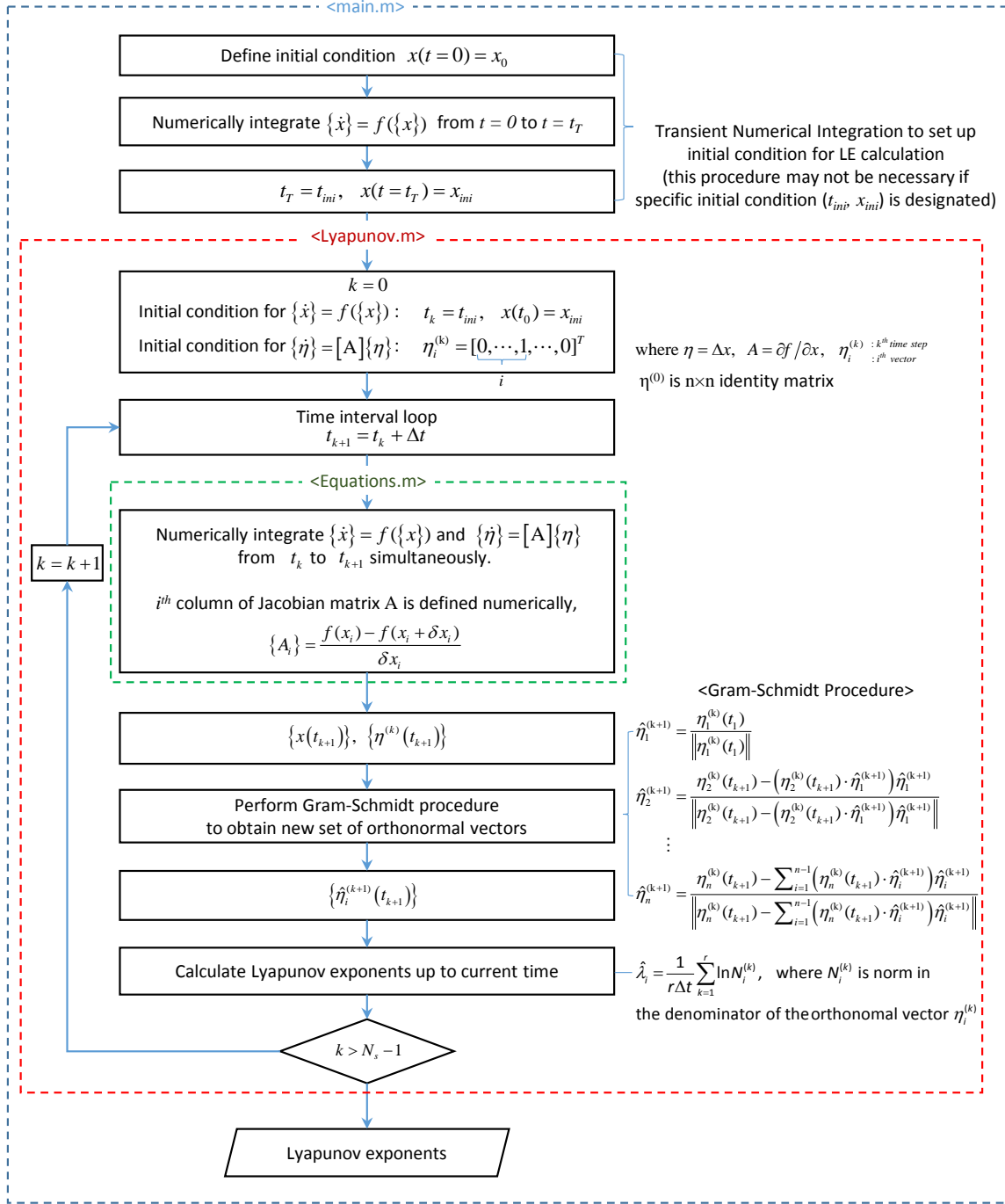


Fig. 4. Block diagram for calculating Lyapunov exponential

CHAPTER III

NONLINEAR RESPONSE AND BIFURCATIONS OF A RIGID ROTOR SUPPORTED ON FLOATING RING BEARINGS (FRB)*

Introduction to Finite FRB Modeling

FRBs have two fluid film layers on inner and outer ring surfaces. Fig. 5 depicts the middle plane in axial direction (z -axis) of a FRB model and its coordinate system used in this paper. O_B , O_J , and O_R denote the center of bearing housing, the journal center, and the ring center, respectively. e_J and e_R indicate the vector to the journal center and the ring center in reference coordinate O_{Bxyz} , and e_{JR} represents the journal position relative to the ring center O_R .

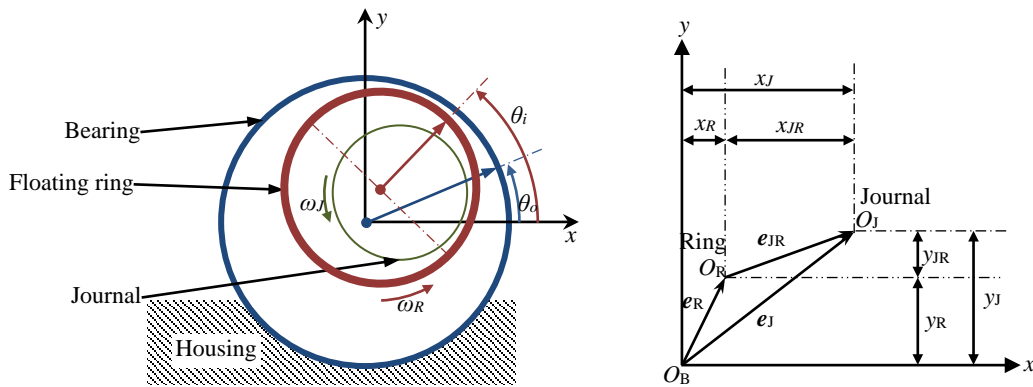


Fig. 5. FRB middle plane and its coordinate system

* Part of this chapter is reprinted with permission from “Shooting with deflation algorithm based nonlinear response and Neimark-Sacker bifurcation and chaos in floating ring bearing system” by Kim, S., and Palazzolo, A. B., 2016, Journal of Computational and Nonlinear Dynamics, doi: 10.1115/1.4034733, Copyright 2016 by ASME.

The hydrodynamic pressures acting on the inner and outer fluid film, i.e., p_i and p_o , of the ring can be described by Reynolds equation for incompressible and iso-viscosity lubricating oil, as follow,

$$\frac{\partial}{\partial \theta_i} \left(\frac{h_i^3}{12\mu_i} \frac{\partial p_i}{\partial \theta_i} \right) + \frac{\partial}{\partial z} \left(\frac{h_i^3}{12\mu_i} \frac{\partial p_i}{\partial z} \right) = \frac{R_j \omega_j + R_{Ri} \omega_R}{2} \frac{\partial h_i}{\partial \theta_i} + \frac{\partial h_i}{\partial t} \quad (34a)$$

$$\frac{\partial}{\partial \theta_o} \left(\frac{h_o^3}{12\mu_o} \frac{\partial p_o}{\partial \theta_o} \right) + \frac{\partial}{\partial z} \left(\frac{h_o^3}{12\mu_o} \frac{\partial p_o}{\partial z} \right) = \frac{R_{Ro} \omega_R}{2} \frac{\partial h_o}{\partial \theta_o} + \frac{\partial h_o}{\partial t} \quad (34b)$$

where R_j and R_{Ro} represent radius of journal and floating ring. ω_j and ω_R denotes the rotational speed of journal and ring, the subscripts i and o indicate the region of inner fluid film and outer fluid film, respectively. The thicknesses of inner and outer fluid film (h_i , h_o) and their time derivatives ($\partial h_i / \partial t$, $\partial h_o / \partial t$) can be expressed as follow,

$$h_i = C_i - x_{jR} \cos \theta_i - y_{jR} \sin \theta_i \quad (35a)$$

$$h_o = C_o - x_{rR} \cos \theta_o - y_{rR} \sin \theta_o \quad (35b)$$

$$\frac{\partial h_i}{\partial t} = -(\dot{x}_{jR} \cos \theta_i - \dot{y}_{jR} \sin \theta_i) \quad (35c)$$

$$\frac{\partial h_o}{\partial t} = -(\dot{x}_{rR} \cos \theta_o - \dot{y}_{rR} \sin \theta_o) \quad (35d)$$

$$\mathbf{e}_j = x_j \hat{i} + y_j \hat{j}, \quad \mathbf{e}_R = x_R \hat{i} + y_R \hat{j}, \quad \mathbf{e}_{jR} = x_{jR} \hat{i} + y_{jR} \hat{j} = (x_j - x_R) \hat{i} + (y_j - y_R) \hat{j} \quad (35e)$$

$$\dot{\mathbf{e}}_j = \dot{x}_j \hat{i} + \dot{y}_j \hat{j}, \quad \dot{\mathbf{e}}_R = \dot{x}_R \hat{i} + \dot{y}_R \hat{j}, \quad \dot{\mathbf{e}}_{jR} = \dot{x}_{jR} \hat{i} + \dot{y}_{jR} \hat{j} = (\dot{x}_j - \dot{x}_R) \hat{i} + (\dot{y}_j - \dot{y}_R) \hat{j} \quad (35f)$$

where C_i and C_o represent radial clearance of inner and outer fluid film. θ_i and θ_o indicate circumferential position of inner and outer fluid film. In this paper, the oil pressures on floating ring surfaces are calculated using a finite element model. Three node simplex, triangular type mesh is generated on the half of fluid film layer in axial direction with an assumption of symmetrical pressure state. The boundary conditions include an ambient pressure p_{amb} at the side end, zero flow at the symmetric end, and

continuous pressure and continuous pressure gradient at the cut ends. Fig. 6 depicts the typical layout of the outer/inner film meshes and boundary conditions.

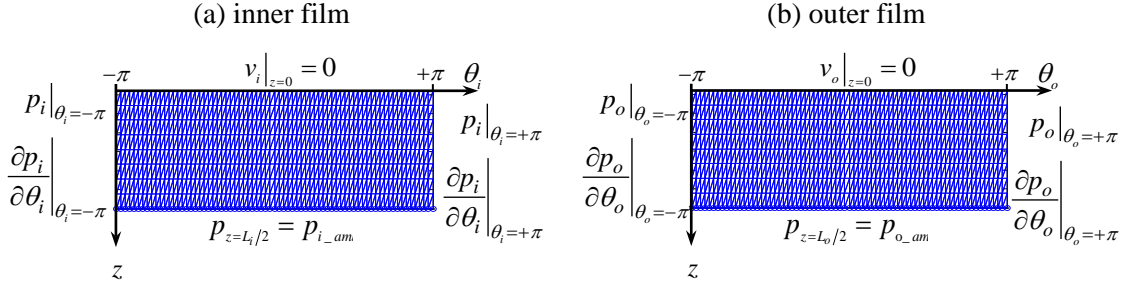


Fig. 6. Layouts of mesh and boundary condition of finite FRB model

Fluid film forces acting on the journal and ring can be obtained by integrating the nodal pressures throughout the inner and outer floating ring meshes and multiplying by 2 to account for the other half.

$$F_i = \begin{Bmatrix} F_{ix} \\ F_{iy} \end{Bmatrix} = 2 \int_0^{L_i/2} \int_{-\pi}^{+\pi} p_i \begin{Bmatrix} \cos \theta_i \\ \sin \theta_i \end{Bmatrix} d\theta_i dz \quad (36a)$$

$$F_o = \begin{Bmatrix} F_{ox} \\ F_{oy} \end{Bmatrix} = 2 \int_0^{L_o/2} \int_{-\pi}^{+\pi} p_o \begin{Bmatrix} \cos \theta_o \\ \sin \theta_o \end{Bmatrix} d\theta_o dz \quad (36b)$$

The equations of motion for the journal and ring can be written as

$$M_J \ddot{e}_J = F_i + W_{Js} + W_{Jd} \quad (37a)$$

$$M_R \ddot{e}_R = -F_i + F_o + W_{Rs} + W_{Rd} \quad (37b)$$

$$I_R \ddot{\omega}_R = \Gamma_o - \Gamma_i \quad (37c)$$

where M_J and M_R are journal mass and ring mass. W_{Js} , W_{Jd} and W_{Rs} , W_{Rd} are static and dynamic load on the journal and ring, respectively. The static force can be the weight of each component or a side load, and the dynamic force is usually due to unbalance force from dynamic eccentricity of the each component. The term I_R is the ring mass moment

of inertia, and Γ_i and Γ_o are the torques applied on the inner and outer films on the floating ring surfaces which determine the ring rotational speed ω_R .

$$\Gamma_i = \int_0^{L_i} \int_{-\pi}^{\pi} \left\{ -\frac{h_i}{2} \frac{\partial p_i}{\partial \theta_i} + \frac{\mu_i}{h_i} (\omega_j - \omega_R) R_i \right\} R_i d\theta_i dz \quad (38a)$$

$$\Gamma_o = \int_0^{L_o} \int_{-\pi}^{\pi} \left\{ \frac{h_o}{2} \frac{\partial p_o}{\partial \theta_o} + \frac{\mu_o}{h_o} \omega_R R_o \right\} R_o d\theta_o dz \quad (37b)$$

A Rigid Rotor Supported by FRB

A symmetric rigid rotor supported by two identical floating ring bearings as shown in Fig. 7 is utilized as test model to apply the presented numerical method. The rotor and FRB parameters used in this study are described in Table 1 and the boundary condition for FRB is defined in Table 2. In order to analyze the response characteristics with respect to amounts of fluid film surfaces and external force states, bearing L/D ratio and imbalance eccentricity (e_{imb}) were varied in the study.

Table 1. Rotor and FRB parameters

Rigid Rotor Parameters	Values	
Mass (kg)	$m/2=1.63$	
Young's modulus (GPa)	$E=207$	
Diameter of rotor section (mm)	$d=11.490$	
Bearing Length (mm)	$L_{brg}=3.56, 8.90$	
Bearing Diameter (mm)	$D_{brg}=17.8$	
L/D ratio	0.2, 0.5	
FRB Parameters	Inner film	Outer film
Viscosity (cp)	$\mu_i=13.5$	$\mu_o=13.5$
Clearance (μm)	$C_i=26.5$	$C_o=42.5$
Diameter (mm)	$ID=11.543$	$OD=17.722$
Length (mm)	$L_R=2.49$	$L_B=3.56$
Ring mass (g)	$m_R=3.38, 8.45$	
Ring's polar moment of inertia (10^{-6}kgm^2)	$I_R=18.89, 47.23$	

Table 2. FRB boundary conditions on finite element fluid film model boundaries

	Ambient Pressure on Pad	Ambient Pressure on Ring
Finite FRB	0 kPa	0 kPa

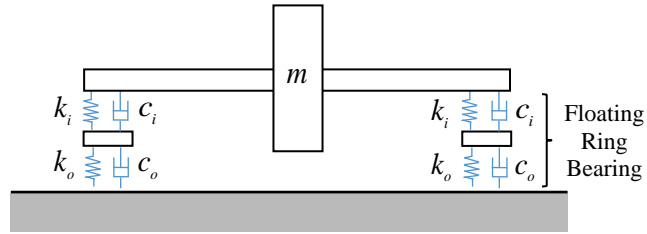


Fig. 7. Rigid rotor supported by Floating Ring Bearing (FRB)

Simulation Results of FRB-RGD

Bifurcations

The nonlinear behavior of the self-excited nature in FRBs, is demonstrated by considering the autonomous system (i.e., $e_{imb}=0.0$), and two different areas of the fluid layer (i.e. $L/D=0.2, 0.5$). Floquet theory determines the response stability through the entire numerical procedure. A commercial mathematical routine for numerically integrating stiff equations, MATLAB[®] ode15s[©], was utilized to obtain the Jacobian matrix in the correction step.

As shown in Fig. 8, the numerical method provides two bifurcation diagrams such as non-dimensionalized maximum and minimum vertical displacements of the rotor center (i.e., \max/\min of $y_j C_o / (C_i + C_o)$) as in Fig. 8 (a) and non-dimensionalized period of the limit cycle (i.e., τ/τ_s , where τ_s is spinning period, 2π) as in Fig. 8 (b) with respect to bifurcation parameters (i.e., rpm). As the rotor speed increased, the equilibrium position

(EP) loses its linear stability at Hopf bifurcation and turns to a periodic (limit cycle) response (PS#1). PS#1 maintains stable and small amplitude before encountering the first saddle-node bifurcation, but the amplitude is drastically shifted along the saddle to saddle section (PS#2). After the second saddle-node bifurcation, the vertical motion is gradually increased and the high amplitude state is sustained. The numerical scheme also provides the exact period solution manifold associated with orbital motion as can be seen in Fig. 8(b). The period ratio of the response is located on 11 to 19, the range of which corresponded to the 30% ~ 40% of ring rotational speed. In addition, it is noted that the ring rotational speed highly depends on amplitude of orbits, since high amplitude whirl motion induces more shear stress on ring surfaces. Multiple steady state responses coexist in the saddle-saddle section; they can be either equilibrium position-limit cycle or two limit cycles depending on whether the revolution speed is located before or after the Hopf bifurcation. In addition, unstable limit cycles exist along with the stable responses (See Fig. 9 (b)); this cannot be obtained from TNISS, and it gives information about how the orbit repels away from the unstable state towards other attractors as shown in Fig. 10. Thus PS#2 acts as a border manifold which helps define the convergence route in phase space.

In the $L/D=0.5$ case, the system has a N-S bifurcation after undergoing Hopf bifurcation. Since the first N-S bifurcation appears as a sub-critical type, closed orbit and torus orbit coexist in the overlapped range. After the first N-S bifurcation, the response frequently undergoes another N-S bifurcations so that additional frequency components are removed or emerge at each N-S. Fig. 12 depicts closed orbits at rpms among the N-S

bifurcations. When the orbit has another form of periodic response (i.e., closed orbit), the corresponding period of the solution is disconnected from the previously found periodic solution as in Fig. 11(b).

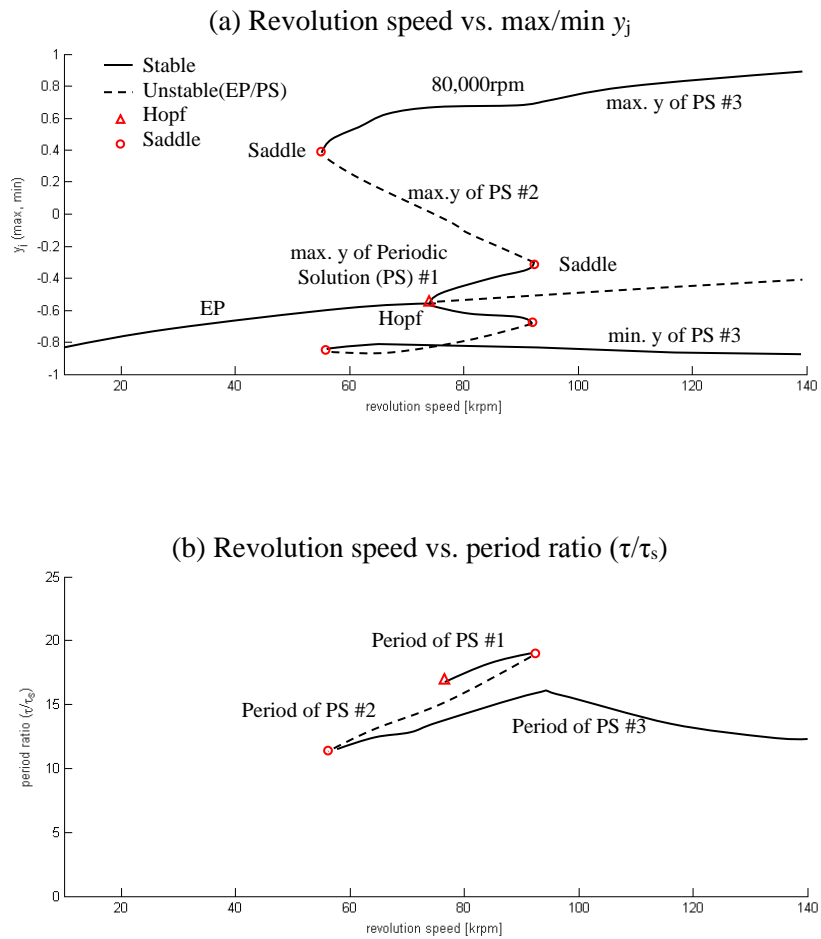


Fig. 8. Bifurcation diagram ($L/D=0.2$, $e_{imb}=0.0$)

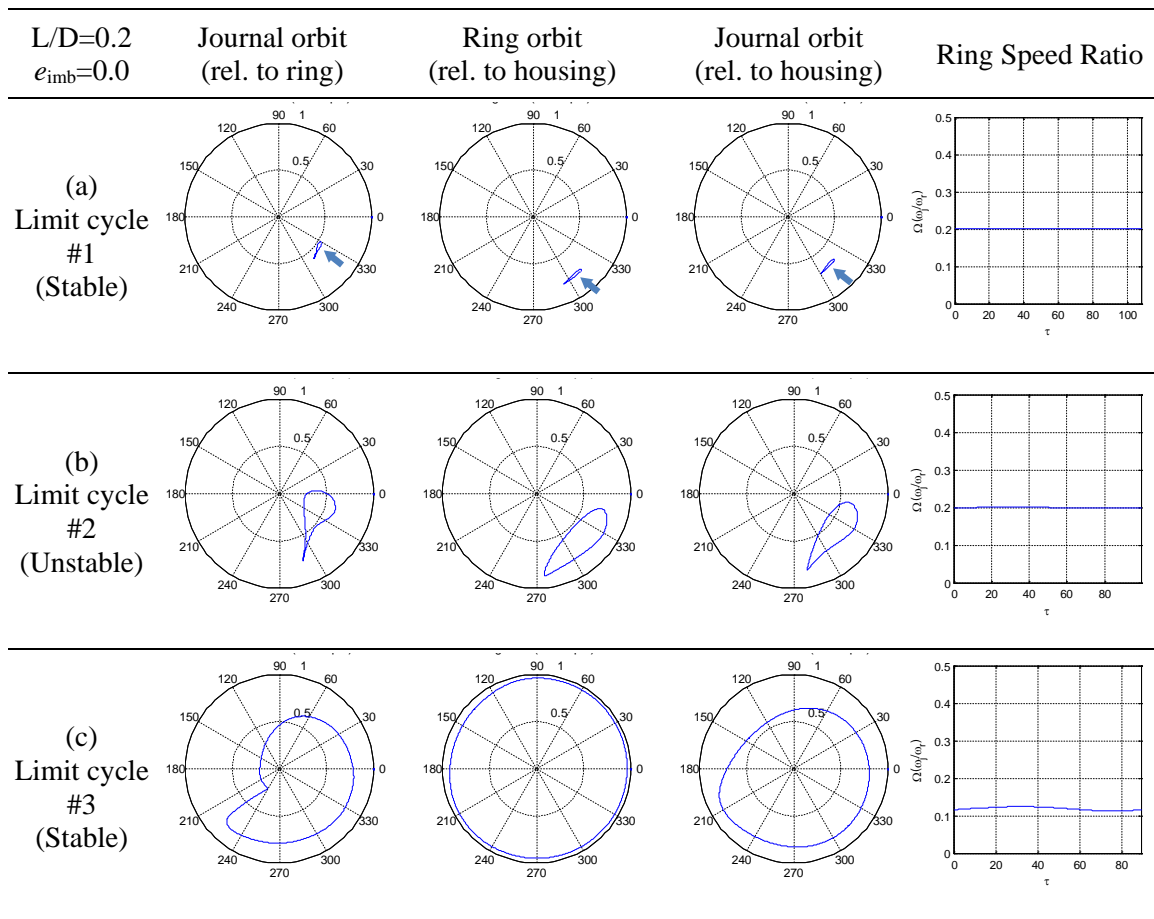


Fig. 9. Identified possible responses using the Shooting Method at 80,000 rpm ($L/D=0.2$): (a) limit cycle #1 (Stable*), (b) limit cycle #2 (Unstable*), (c) limit cycle #3 (Stable*). *the stability of the responses are evaluated by Floquet theory.

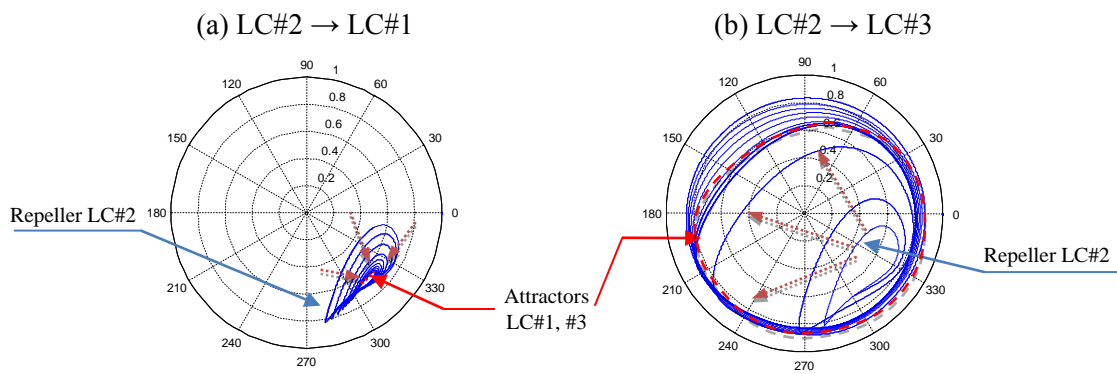


Fig. 10. Repelling motion (Journal rel. to housing) of the unstable orbit (LC#2)

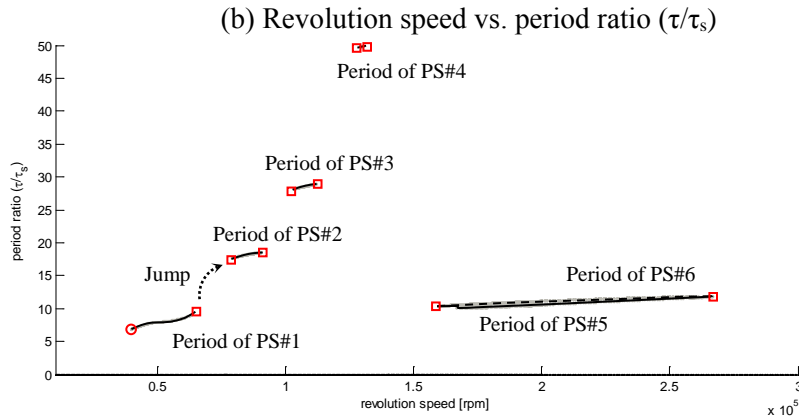
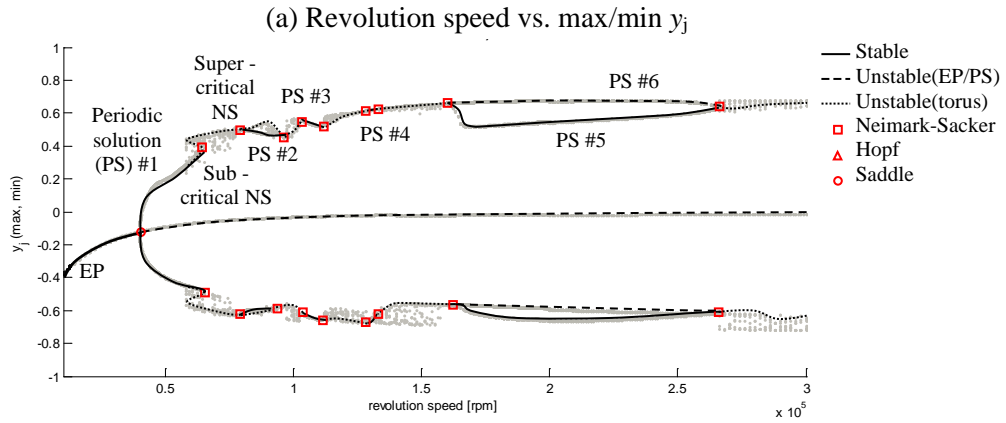


Fig. 11. Bifurcation diagram ($L/D=0.5, e_{imb}=0.0$)

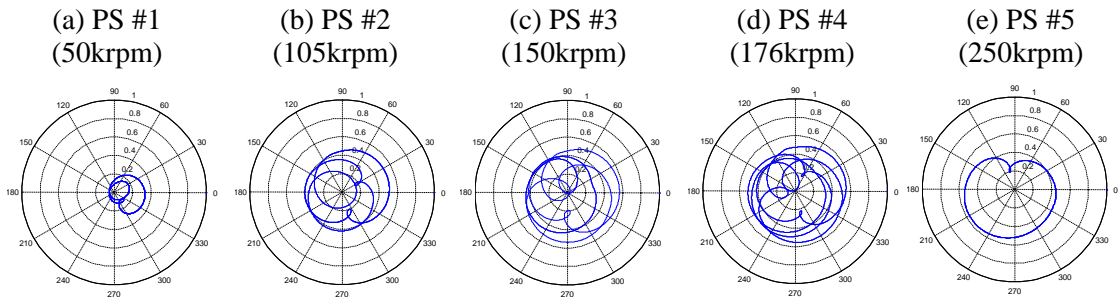


Fig. 12. Stable periodic solutions (journal orbit rel. to ring) among N-S bifurcations

Jump between coexistent orbits

Since multiple steady state responses can coexist at the same rpm, and the same imbalance amount; it may be speculated that one response state could potentially switch to the other if a disturbance is sufficiently strong to force the original state to jump out of its current basin of attraction (BOA). In reality, FRBs are used in automotive turbochargers and aircraft accessory equipment so that a sudden disturbance, for instance, speed bumps on roads or turbulences in airflow, may induce response jumps in operation. It would be beneficial for developers/operators to anticipate the response uncertainty. In order to simulate this phenomenon, an impulsive, vertical base excitation is applied to the FRB housing over a very short period while the FRB-rotor system is operating within one steady state orbital state. The displacement of the FRB housing can be expressed with a characteristic frequency of base motion and its harmonics.

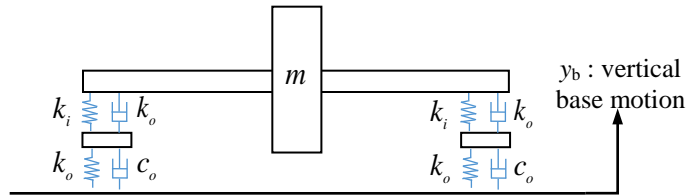


Fig. 13. Schematics support excitation to FRB housings

In the study, the maximum harmonic excitation component, n , in Eq. (39) is selected as 100 to establish an impulse function. And other parameters such as pulse amplitude Y_o , pulse period T_f , and pulse time τ_p are described in the Table 3.

$$y_b(t) = Y_o \left\{ \frac{\tau_p}{T_f} + \sum_{n=1}^{\infty} \frac{2}{n\pi} \sin\left(\frac{n\pi\tau_p}{T_f}\right) \cos\left(\frac{2n\pi}{T_f}t\right) \right\} \quad (39)$$

Table 3. Base excitation parameters

	Y_o [μm]	T_f [ms]	τ_p [ms]
LC#1→LC#2	8.5	0.150	0.0375
LC#2→LC#1	17.85	0.075	0.0187

The sudden base movements cause external force term to the outer film, and if the force is enough to escape the current BOA in phase space, the orbit may converge to another response state. Fig. 14(a) depicts the jump phenomenon from the small amplitude limit cycle (LC#1 in Fig. 9 (a)) to the large amplitude limit cycle (LC#3 in Fig. 9 (c)) from a sudden base excitation. The jump can also occur in the opposite direction as shown in Fig. 14 (b).

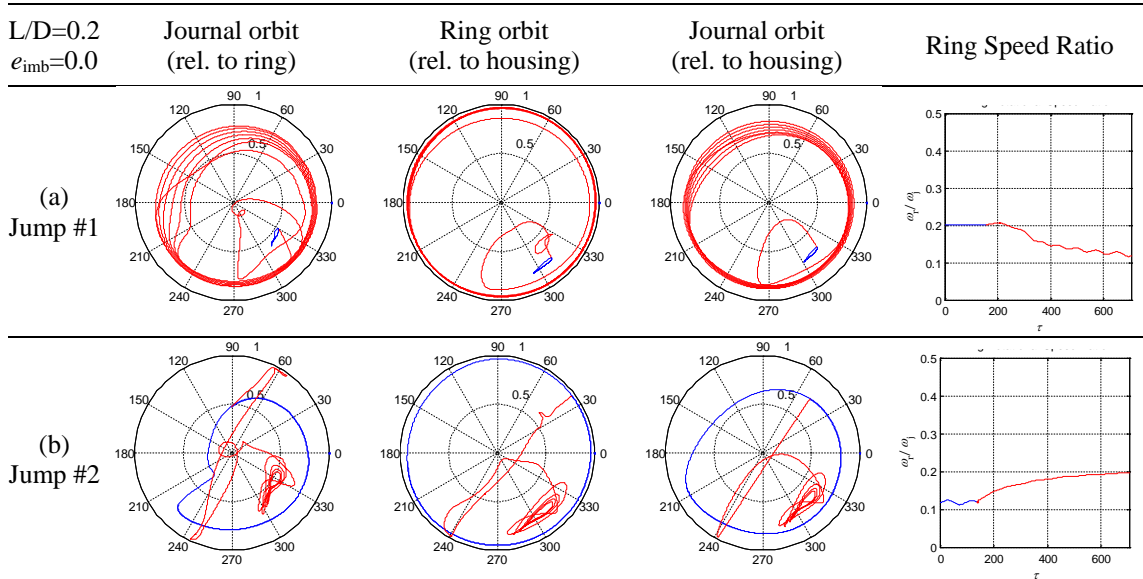


Fig. 14. Jump phenomenon between two limit cycles due to bump from FRB base at 80,000 rpm ($L/D=0.2$, $e_{imb}=0.0$): (a) before: limit cycle #1 (blue) → after: limit cycle #3 (red), (b) before: limit cycle #3 (blue) → after: limit cycle #1 (red)

Chaos

Nonlinear dynamic systems occasionally undergo chaotic motion. The response is highly random, so it is not categorized in periodic or quasi-periodic. The associated Poincaré map may consist of strangely patterned dots; which is referred to as a strange attractor. Along with the implicit method, Lyapunov exponents (LEs) provide an explicit approach to determine chaos. In order to confirm the nonlinear characteristics, this paper employed additional techniques such as frequency spectrum, bifurcation diagram, and orbital motion along with the implicit/explicit methods.

Table 4. Orbit and associated LEs

Orbit	LEs
Fixed point	all LEs are negative
Limit cycle	an LE is zero and other LEs are all negative
n -frequency quasi-periodic (n -torus)	The first n LEs are zeros and remaining LEs are negative
Chaotic motion	at least one LE is positive

Chaos tends to occur in non-autonomous system so that a dynamic eccentricity $e_{imb}=0.4C_i$ is applied to the FRB-rotor system. For the sake of reference, the dynamic differential equations are integrated by MATLAB[®] routine ode15s[®] for 600 revolution periods from 5,000 rpm to 50,000 rpm. Steady state is assumed to be subjected to the response was collected for the last 100 revolution. As can be seen in Fig. 15 (a), a bifurcation diagram, which consisted of samplings of the non-dimensional vertical journal motion relative to housing (x_j) recorded at each revolution period with respect to revolution speed, shows that $\times 1$ synchronous and $\times 1/3$ sub-synchronous responses are

identified in certain operation ranges (e.g, 6krpm~12krpm, 23krpm~26krpm, 28.5krpm~50krpm). However, the character of the other responses is somewhat ambiguous to be interpreted either as quasi- or aperiodic. On the other hand, LEs do provide further clarification as described in section 2 by means of 600 time intervals with 0.25 revolution per interval. As shown in the Fig. 15 (b), maximum Lyapunov exponents (MLEs) are determined with respect to rpm and clearly distinguish the chaos emerged sections from the undetermined ranges. In order to confirm the response characteristics, the orbital motion, Poincaré map, and frequency spectrum are added up for selected operation speeds such as 10krpm, 16krpm, 20krpm, and 40krpm. In Fig. 15, the Poincaré maps and frequency spectrum indicate $\times 1$ synchronous response. The calculated LEs are all negative. In Fig. 17, the orbits look keep wandering and corresponding Poincaré maps show closed limit cycles, so the motion is two period quasi-periodic response. Though the first two LE components remain in very small values (i.e, 0.004, -0.005), those are assumed to be converged to marginal value (i.e, zero) after all. In Fig. 18, the orbits and ring rotational speed are obviously aperiodic response, and the corresponding Poincaré maps have not a simple shapes such as points, close curves, or torus but instead have peculiar shapes like humming birds, Fig. 18 (e), (g) or a flower, Fig. 18 (f); The sampling dots are collected for 2000 revolution periods to make sure the chaotic behavior. This kind of Poincaré map is apparently a strange attractor. In frequency domain, broadband components are observed as in Fig. 18 (h). LE spectrum and positive MLE indicate the motion characteristics as chaos. In Fig. 19, the orbits show large amplitude whirls and corresponding Poincaré maps and frequency

spectrum confirm the response as $\times 1/3$ sub-synchronous response. LE spectrum and negative MLE confirm the motion has periodicity.

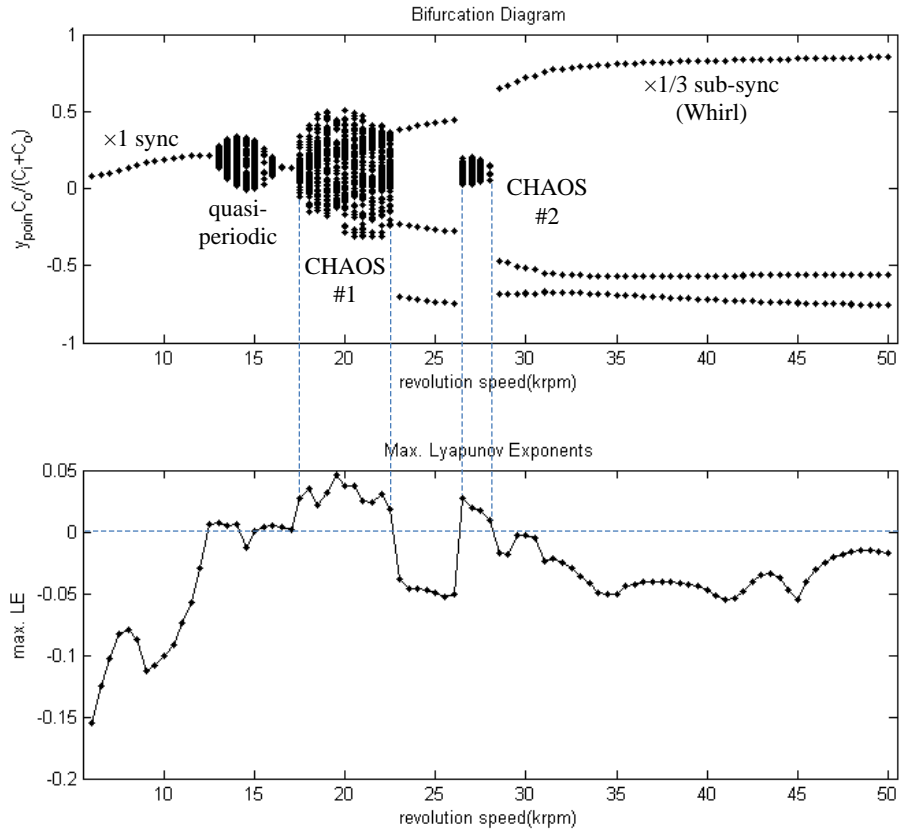


Fig. 15. Bifurcation (x_j -poincaré vs. journal revolution speed) and corresponding maximum Lyapunov exponents diagrams ($L/D=0.2$, $e_{imb}=0.4C_i$)

Table 5. Response characteristics

Revolution speed	Poincaré map (Attractor)	Max. Lyapunov exponent	Frequency Spectrum
10,000rpm	1 fixed point	-0.1007 (Stable)	$\times 1$ synchronous
16,000rpm	Limit cycle (closed curve)	0.004 (Marginal)	Multi components
20,000rpm	Strange attractor	0.0244 (Chaos)	Broad band components
40,000rpm	3 fixed points	-0.0482 (Stable)	$\times 1/3$ sub-synchronous

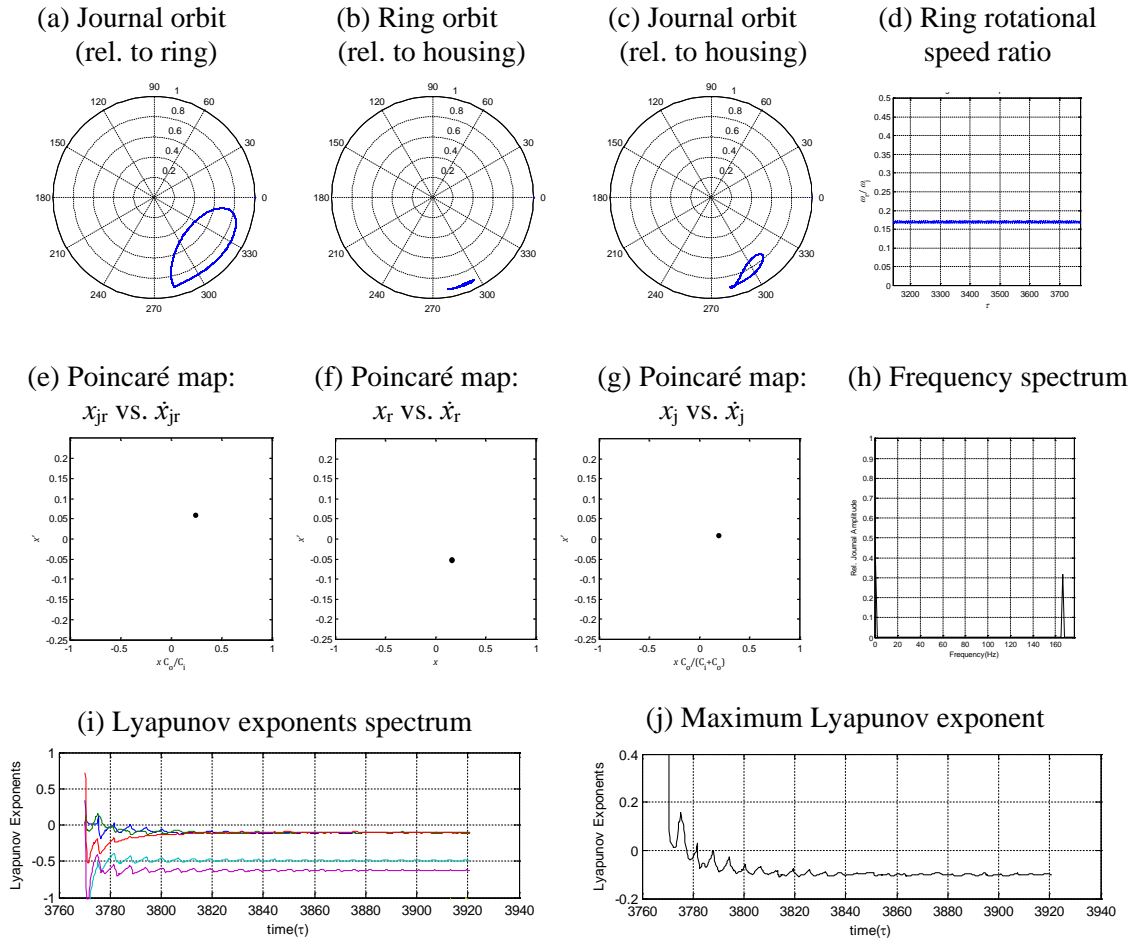


Fig. 16. Nonlinear response evaluation at 10,000 rpm ($L/D=0.2$, $e_{imb}=0.4$): (a~d) for orbits and ring speed, (e~g) for Poincaré maps, (h) for frequency spectrum, (i) for Lyapunov exponents, and (j) for Maximum Lyapunov exponent

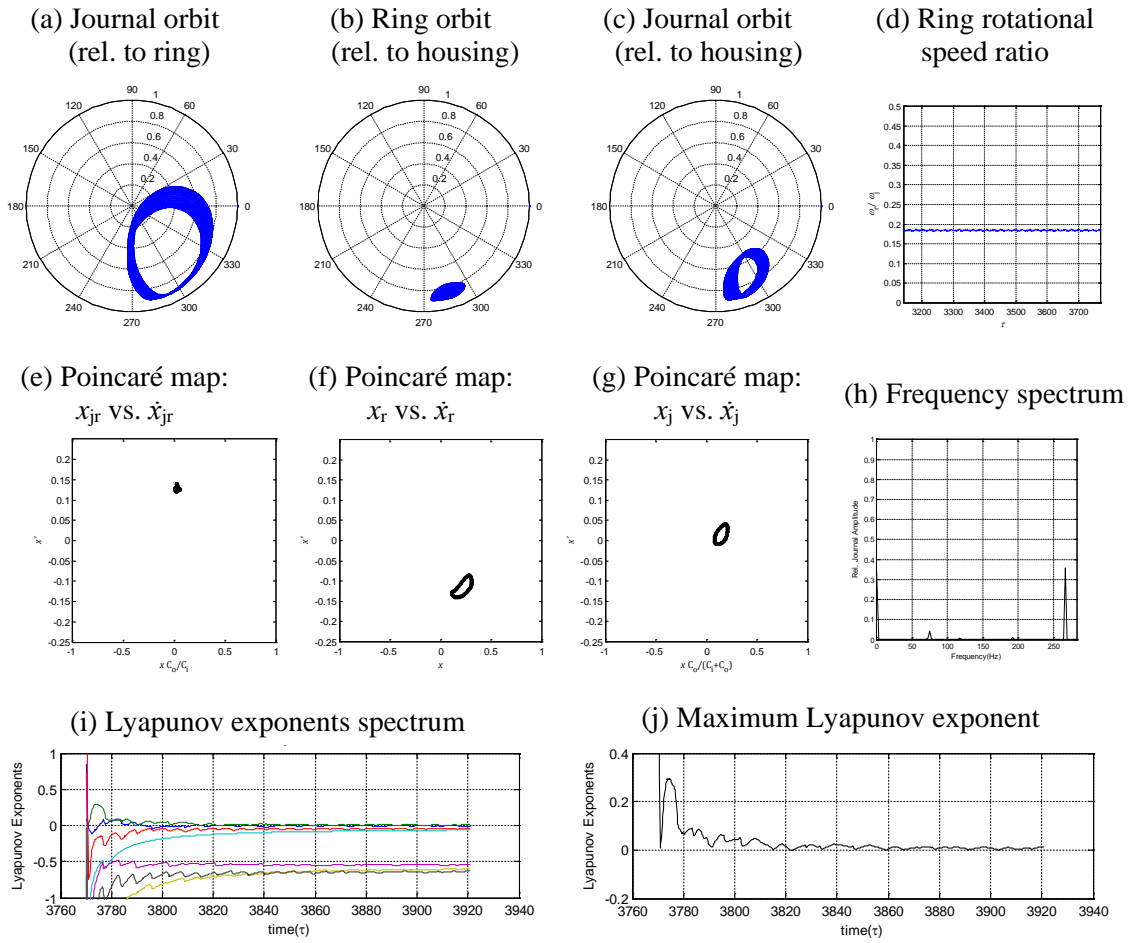


Fig. 17. Nonlinear response evaluation at 16,000 rpm ($L/D=0.2$, $e_{imb}=0.4$): (a~d) for orbits and ring speed, (e~g) for Poincaré maps, (h) for frequency spectrum, (i) for Lyapunov exponents, and (j) for Maximum Lyapunov exponent

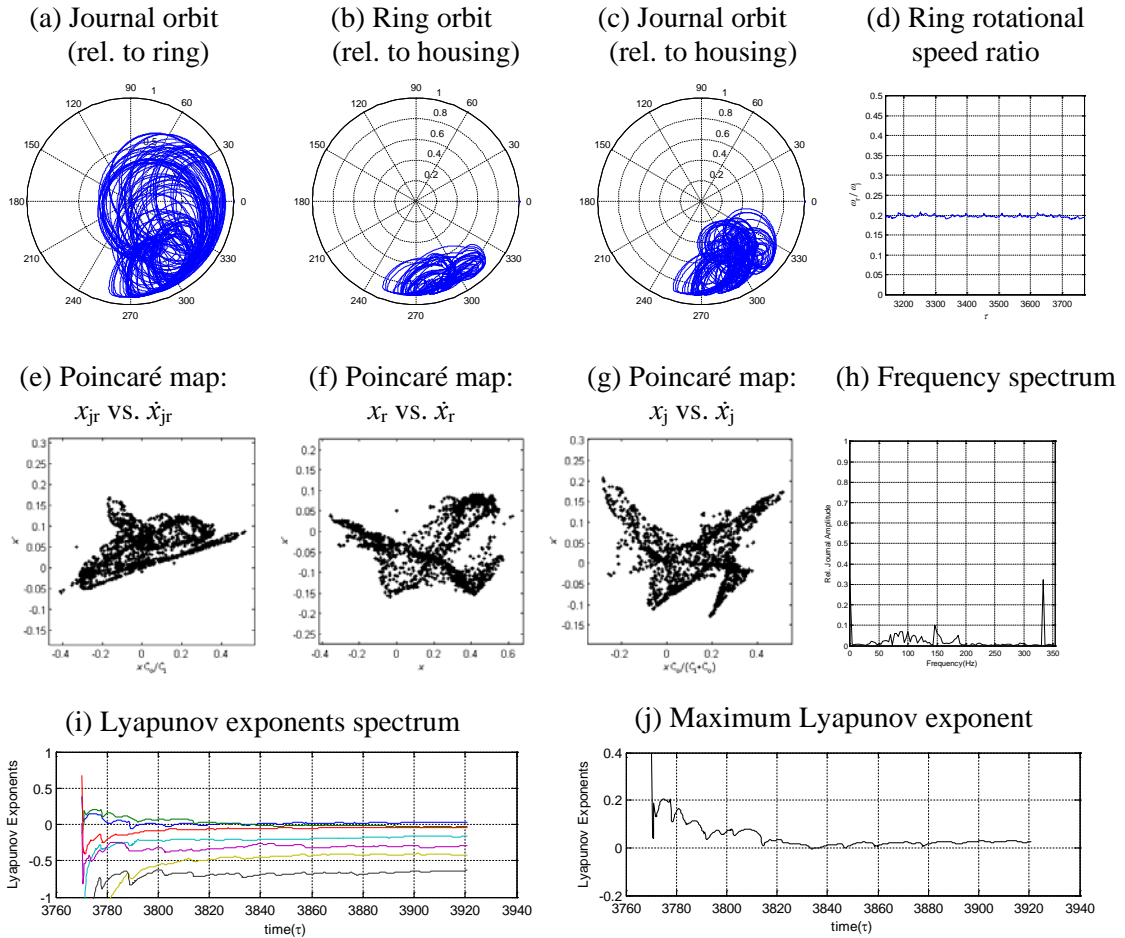


Fig. 18. Nonlinear response evaluation at 20,000 rpm ($L/D=0.2$, $e_{imb}=0.4$): (a~d) for orbits and ring speed, (e~g) for Poincaré maps, (h) for frequency spectrum, (i) for Lyapunov exponents, and (j) for Maximum Lyapunov exponent

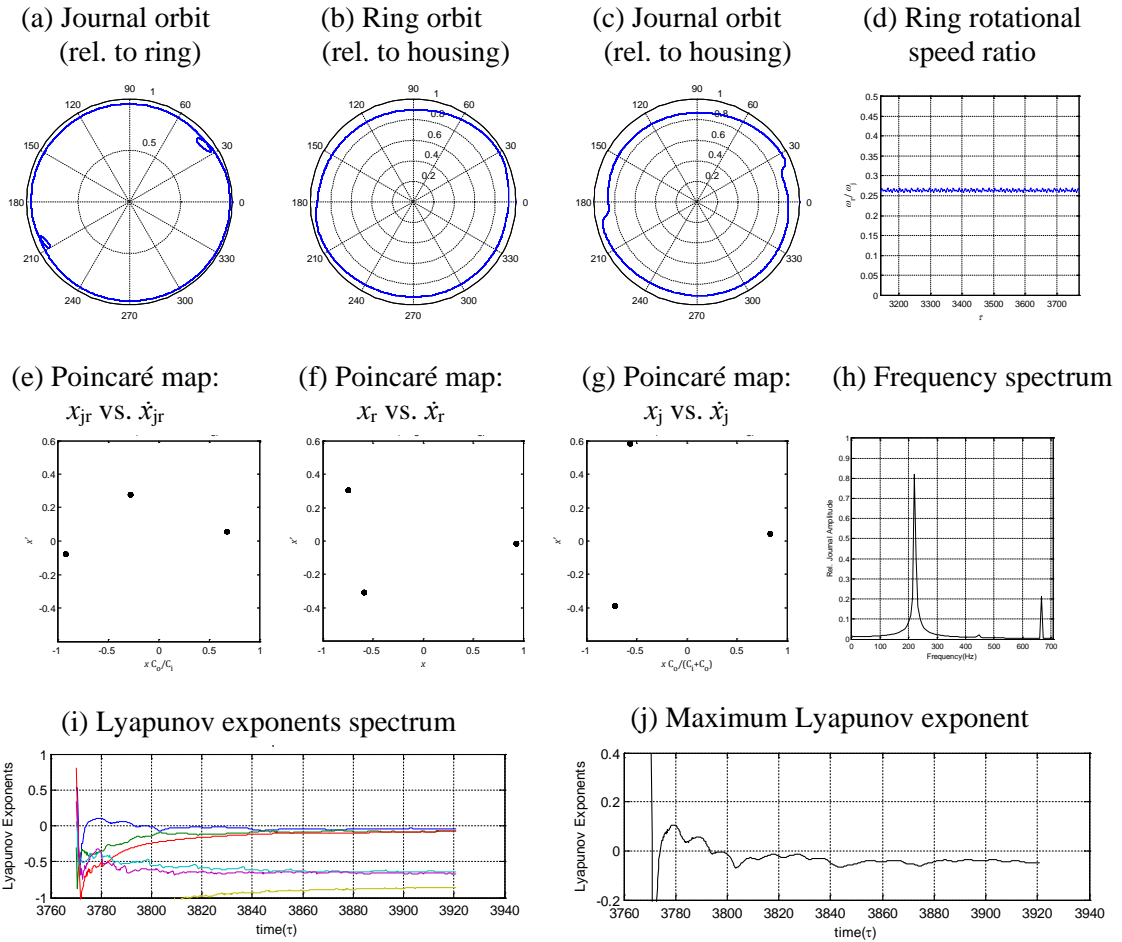


Fig. 19. Nonlinear response evaluation at 40,000 rpm ($L/D=0.2$, $e_{imb}=0.4$): (a~d) for orbits and ring speed, (e~g) for Poincaré maps, (h) for frequency spectrum, (i) for Lyapunov exponents, and (j) for Maximum Lyapunov exponent

Synchronization

In industry, engineers have observed oil/gas whirls due to the self-excited nonlinear characteristics of fluid film bearings. One useful treatment for the problem is that properly added intentional imbalance can quench the large sub-synchronous orbit, i.e., synchronization. A numerical investigation of the synchronization is conducted for the rigid rotor supported by FRB. The unbalance force amount is added with various eccentricities. Table 6 lists the rotor/FRB parameters used in the simulation. Fig. 20 depicts the orbital motion and corresponding frequency spectrum for each e_{imb} amount. As the imbalance eccentricity increases until $e_{imb}=0.4C_i$, low frequency components are suppressed and the $\times 1$ frequency component is getting extruded. After the critical point, the responses are returned to large amplitude sub-synchronous as shown in the Fig. 20 (d).

Table 6. Rotor and FRB parameters used for synchronization

Rigid Rotor Parameters	Values	FRB Parameters	Inner film	Outer film
Bearing Length (<i>mm</i>)	$L_{brg}=14.24$	Length (<i>mm</i>)	$L_R=2.49$	$L_B=3.56$
Bearing Diameter (<i>mm</i>)	$D_{brg}=17.8$	Ring mass (<i>g</i>)	$m_R=13.51$	
L/D ratio	0.8	Ring's polar moment of inertia (10^{-6}kgm^2)	$I_R=75.578$	

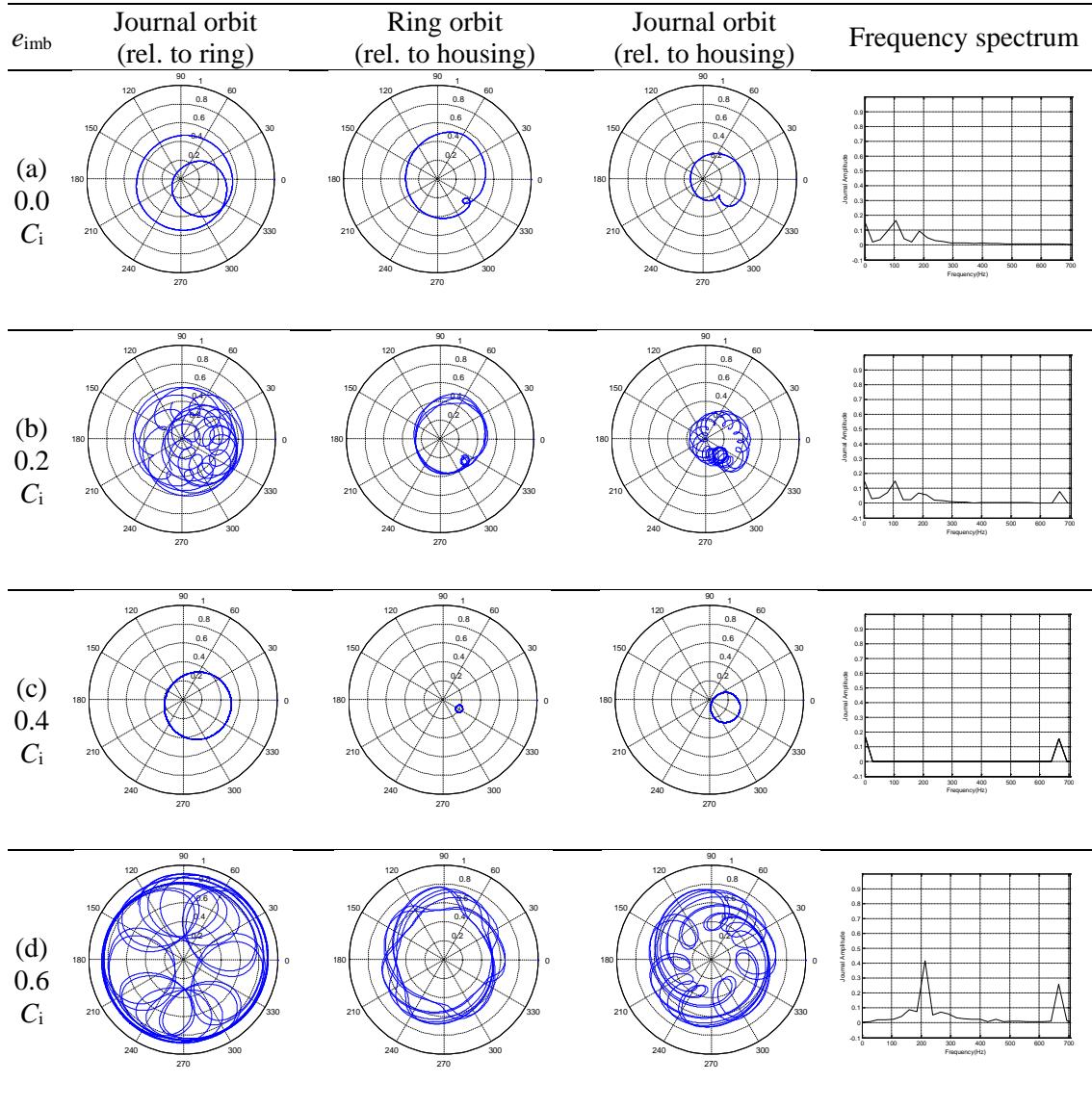


Fig. 20. Responses and synchronization by adding unbalance to the rotor disk at 40,000rpm: (a): responses with no unbalance ($e_{imb}=0.0$), (b): response with $e_{imb}=0.2C_i$, (c): response with $e_{imb}=0.4C_i$, (d): response with $e_{imb}=0.6C_i$

Finite element FRB vs. infinitely short approximated FRB

The infinitely short approximation, Ocvirk solution, assumes that the pressure gradient in the z direction is significantly larger than that in the x direction (i.e., $\partial p/\partial x \ll \partial p/\partial z$). Pressure distribution in radial direction is negligible so that the Reynolds equation Eq. (40a) and Eq. (40b) become simplified as,

$$\frac{\partial}{\partial z} \left(\frac{h_i^3}{12\mu_i} \frac{\partial p_i}{\partial z} \right) = \frac{R_j \omega_j + R_{Ri} \omega_R}{2} \frac{\partial h_i}{\partial \theta_i} + \frac{\partial h_i}{\partial t} \quad (40a)$$

$$\frac{\partial}{\partial z} \left(\frac{h_o^3}{12\mu_o} \frac{\partial p_o}{\partial z} \right) = \frac{R_{Ro} \omega_R}{2} \frac{\partial h_o}{\partial \theta_o} + \frac{\partial h_o}{\partial t} \quad (40b)$$

The fluid forces on inner and outer surface can be expressed by direct integration of the simplified Reynolds equation for each surface,

$$\begin{Bmatrix} F_{ix} \\ F_{iy} \end{Bmatrix} = \mu_i (\omega_j + \omega_R) R_j L_i \left(\frac{R_j}{C_i} \right)^2 \left(\frac{L_i}{2R_j} \right)^2 \begin{Bmatrix} f_{ix} \\ f_{iy} \end{Bmatrix} \quad (41a)$$

$$\begin{Bmatrix} F_{ox} \\ F_{oy} \end{Bmatrix} = \mu_o \omega_R R_{ro} L_o \left(\frac{R_{ro}}{C_o} \right)^2 \left(\frac{L_o}{2R_{ro}} \right)^2 \begin{Bmatrix} f_{ox} \\ f_{oy} \end{Bmatrix} \quad (41b)$$

where f_{ix} , f_{iy} , f_{ox} , and f_{oy} are non-dimensional fluid forces. The detailed process of the derivation is well described in studies from Adiletta et al. and Tian et al. [4,39]. This approach has given reasonable fluid film forces for relatively small bearing length and diameter ratios (L/D) below 0.25. Most recent papers related to bifurcation and stability analysis of FRBs are based on this approximation. However, though there are many papers which compared responses from the short bearing approximation and the finite element method for journal bearing operations, very few studies has done for FRBs. This study tried to compare nonlinear responses between the two FRB modeling methods for two different bearing length and diameter ratio (e.g. L/D=0.2, 0.5).

Fig. 21 (a) and (b) are bifurcation diagrams in case of $L/D=0.2$ ($e_{imb}=0.4$), which consists of the journal displacement relative to housing samplings per revolution period in x direction (x_j) vs. journal revolution speed (rpm) obtained from finite bearing method and short bearing approximation. Fig. 21 (c) and (d) represent the associated waterfall diagrams. In the diagrams, response types, bifurcations, and frequency components from the two methods agree with each other in the overall traversing speed range, but some misaligns in terms of bifurcation onset and stability are observed. In the results from finite element method, bifurcation from chaos to $1/3$ sub-synchronous response is occurred at 23,000rpm, then the response goes back to chaos at 26,500rpm. However, results from short bearing approximation has such turning points at 23,000rpm and 27,500rpm, respectively. The other difference of bifurcation point that while the responses from finite bearing theory is showing only $1/3$ sub-synchronous at traversing speed range from 28,500rpm to 50,000rpm, the response from short bearing method undergoes a N-S bifurcations at 45,500rpm which is transition between periodic and quasi-periodic orbits.

As can be seen in Fig. 22, journal and ring orbits and ring rotational speed ratio obtained from the two methods are compared at specific operation speeds. The result from finite element method (blue) are overlaid with the results from short bearing approximation (red). In overall traversing speed range, the two orbits and ring rotational speed ratios show good agreement, though the orbit stability from short bearing approximation has difference when it undergoes extremely large amplitude vibration.

In Fig. 23, response data obtained from the two force models is compared for the case of $L/D=0.5$ ($e_{imb}=0.4$). Although the results show a good agreement in low speed range (5krpm ~ 40krpm), recognizable differences in terms of bifurcation onset speed can be observed as the rotor goes into high speed range after 55krpm.

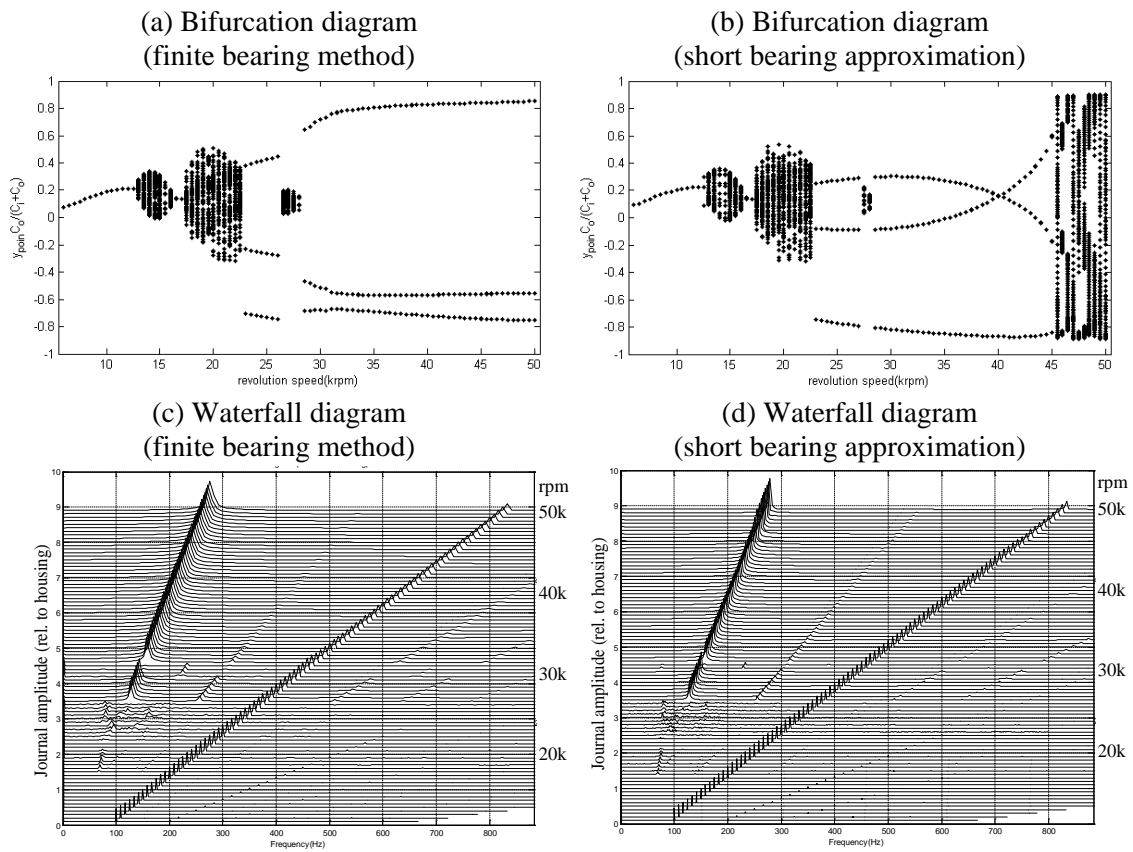


Fig. 21. Bifurcation diagrams and associated waterfall diagrams obtained using finite bearing method vs. short bearing approximation ($L/D=0.2$, $e_{imb}=0.4$)

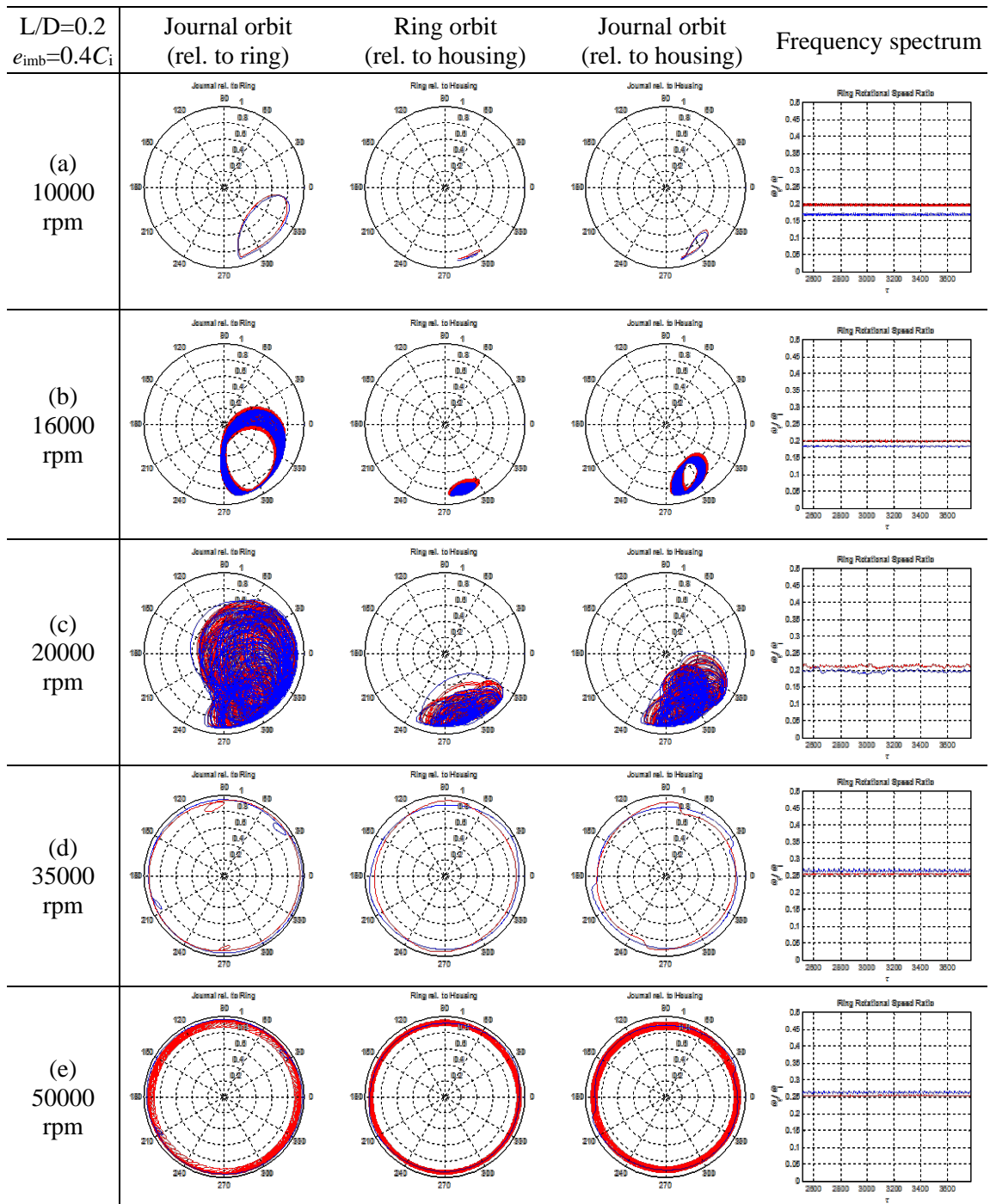


Fig. 22. Comparison of orbits and ring speed ratio which are obtained by finite element method (blue) and short bearing approximation (red) at (a) 10,000rpm, (b) 16,000rpm, (c) 20,000rpm, (d) 35,000rpm, (e) 50,000rpm in case of $L/D=0.2$

As described in Table 7, bifurcation onsets, the entries of the limit cycle #1 and #2, are different from the two methods. In addition, N-S bifurcation can be clearly observed in the finite element model so that the response lose/obtain an additional frequency component at 159krpm and 171krpm. Due to the difference of onset, amplitudes at certain speed range show big difference from short approximation. For example, Fig. 24 and Fig. 25 represent the orbit and frequency spectrum from the two methods at 60krpm and 120krpm, respectively. And the results show significantly different orbital motion and frequency components.

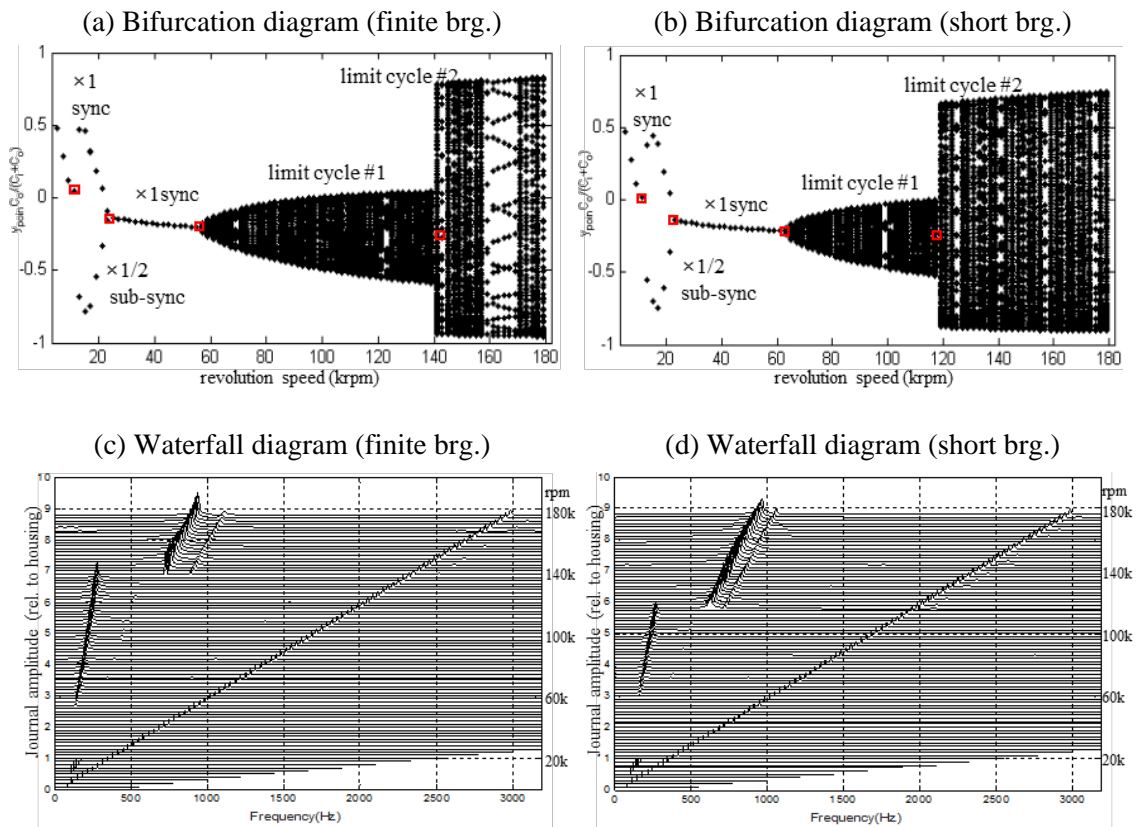


Fig. 23. Bifurcation diagrams and associated waterfall diagrams obtained using finite bearing method vs. short bearing approximation ($L/D=0.5$, $e_{imb}=0.4C_i$)

Table 7. Bifurcation onset speed differences between finite and short bearing methods
 ($L/D=0.5, e_{imb}=0.4C_i$)

Differences		Finite	Short
Response types		×1 sync, ×1/2 sync, Limit cycle #1, Limit cycle #2	
Bifurcation onset speeds	×1 sync → ×1/2 sync	11,000 rpm	11,000 rpm
	×1/2 sync → ×1 sync	24,000 rpm	23,000 rpm
	×1 sync → limit cycle #1	55,000 rpm	61,000 rpm
	limit cycle #1 → limit cycle #2	141,000 rpm	119,000 rpm

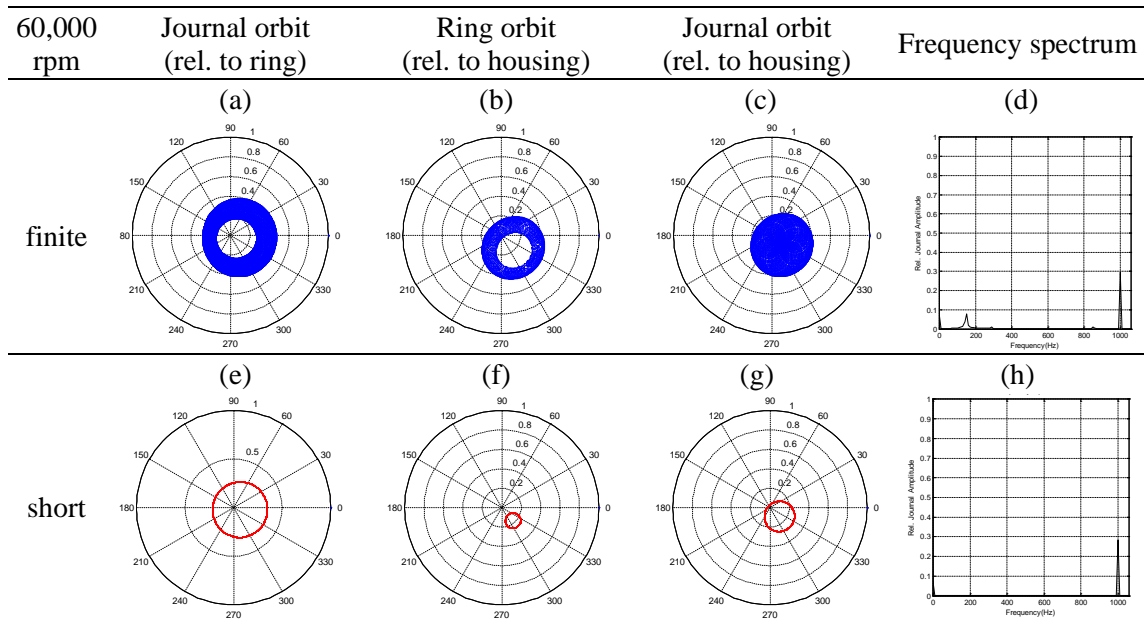


Fig. 24. Orbits and frequency spectrum at 60,000 rpm from finite and short bearing methods ($L/D=0.5, e_{imb}=0.4C_i$)

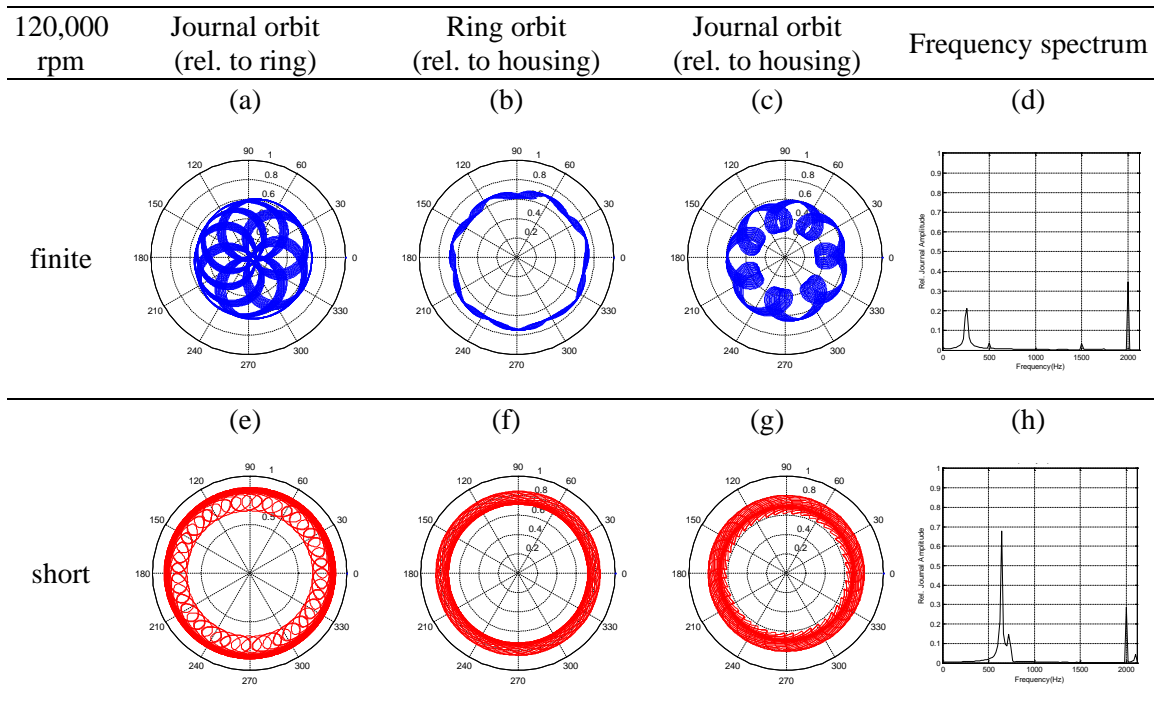


Fig. 25. Orbits and frequency spectrum at 120,000 rpm from finite and short bearing methods ($L/D=0.5$, $e_{imb}=0.4C_i$)

Summary of Results

The improved numerical shooting/arc-length continuation approach is developed by including a deflation algorithm. Nonlinear behaviors of the autonomous FRB-rigid rotor system has been analyzed with the numerical scheme, and phase states and periods of the solution manifold are obtained. In the FRB-rotor system, primary Hopf, and secondary Hopf (i.e., N-S) bifurcations are identified depending on L/D ratio of the FRB. Higher L/D ratio tends to have N-S bifurcation in low rpm, and the response repeatedly switches between periodic and quasi-periodic following N-S bifurcations. It is confirmed that two coexistent steady state responses can jump to each other in identical

operation condition upon a sudden base excitation. This has an important consequence for machinery that encounters sudden base motions, since response amplitude and ring rotational speed can drastically jump at the event. Chaos was quantitatively confirmed for a non-autonomous case, with low L/D ratio in the FRB-rotor system. A positive LE component and strange attractor confirm the characteristics in explicit and implicit manners. It was also confirmed that an appropriate intentional imbalance suppressed high amplitude sub-synchronous frequency components and entrained the response to synchronous. In this numerical study, fluid film forces on FRB were calculated using finite element method. From the comparison with short bearing approximation, it was shown that predictions of bifurcation onset speed can differ significantly as L/D ratio increased.

CHAPTER IV
EFFECTS OF THERMO-HYDRODYNAMIC (THD) FRB MODLE ON
ROTORDYNAMIC BIFURCATIONS

Introduction to THD FRB Model

The literature provides many examples of fluid film bearing force induced nonlinear behavior such as bifurcations, sub-synchronous whirl, and quasi-periodic, aperiodic, and coexistent responses in rotor-bearing systems [1,4,5]. Computational advancement has enabled more accurate modeling by including thermal effects in the lubricant film. Gadangi et al. [28,29] utilized a nonlinear, time transient approach, including a variable viscosity Reynolds and static energy equation fluid film model, to predict the response of a rotor supported on tilting pad journal bearings to a sudden mass balance, such as a blade or deposit loss occurrence. Suh and Palazzolo [30] developed a high fidelity, nonlinear Morton effect (i.e., thermal induced synchronous instability) simulation incorporating 3D structural finite elements for the shaft and pads, and variable viscosity Reynolds fluid film model with a transient energy equation. Clarke et al. presented a steady state thermal model with π oil films for floating ring bearings (FRBs) systems. They considered a heavily loaded power generating system and compared the results with isothermal cases [40]. San Andres et al. proposed an advanced lumped parameter thermal model for a lightly loaded turbocharger rotor to improve modeling accuracy, and compared their predictions with experimental data [41].

The majority of the previous thermo-hydrodynamic (THD) bearing literature focused on improving the accuracy of rotordynamic response prediction obtained with direct, transient numerical integration. In contrast, the THD bearing – rotordynamic response literature is paucal for treatment with numerical algorithms that directly obtain coexisting, steady state nonlinear responses and bifurcation occurrences and types. Some methods that are typically used for this objective include harmonic balance, shooting and continuation. This approach replaces “brute force” numerical integration with selected initial conditions, with more complex search-based numerical approaches that repeatedly evaluate Jacobian matrices. Limitations in computational resources have restricted earlier modeling efforts to rotorbearing systems of small order supported by bearings that were modeled with isoviscous and short bearing approximations [20,21,25,26].

An objective of the present study is to identify the effects of lubricant film temperature distribution on rotordynamic bifurcation. A finite element based variable viscosity Reynolds equation is simultaneously solved with the energy equation and viscosity-temperature relation to obtain a thermohydrodynamic based pressure distribution in the lubricant film. The integrated pressure forces are transferred into the rotor governing equations during the shooting and arc-length continuation based solution procedure. The computational task is accelerated by employing efficient numerical approaches including deflation and parallel computing.

Deflation is a mathematical approach that is utilized in solving multiple root problems [31-33]. The function that is being searched for roots is redefined each time a root is located in the deflation procedure. The benefit deflation provides is the avoidance

of previously located roots while searching for all roots, which accelerates the root finding process. Parallel computing has been increasingly adopted in recent years to reduce computation time through the full use of multicore processors [34]. Parallel computing strategy is suitable for shooting and continuation algorithms, since the routines for obtaining Jacobian matrices from perturbed initial conditions are independent procedures, so each segment of the solution routine can be executed simultaneously. Deflation and the use of parallel computing both play significant roles in accelerating the computationally intensive search for coexisting steady state solutions and bifurcation points for rotordynamic systems with THD modeled floating ring bearings.

A rigid rotor model is employed to illustrate how the double layered fluid films on the inner and outer ring surfaces of a FRB may induce strongly nonlinear behavior. This situation is exacerbated by the very high speed range that turbochargers supported by FRBs operate over, providing greater possibilities for bifurcation, whirl and coexisting response events [25,26].

General contributions of this paper include:

- A comparison of the effects of iso-viscosity vs. variable viscosity lubricant models on bifurcation and response behaviors
- A development of the autonomous and non-autonomous shooting and arc-length continuation algorithms with THD solutions for fluid film bearings
- Flow diagram for computationally based solution and simulation based response results for a FRB rotordynamic system

Shooting Method with THD Solutions

An overall flow chart of the combined THD - “shooting with deflation” process is shown in Fig. 26. It follows the framework of the conventional shooting method, i.e. the solver generates n guesses for finding initial conditions of orbital equilibrium states (i.e., periodic responses) and the Newton-Raphson based updating procedure is performed for each guess. However, the Jacobian matrices are obtained based on a steady state THD-rotordynamics solution in the iterative solution search, which is detailed in the next section. The computation flow also contains both parallel computing and deflation to accelerate completion of execution as indicated by the shaded portions in Fig. 26.

Thermo-hydrodynamic solution for temperatures, viscosities and pressures in the thin fluid layer is governed by the variable viscosity Reynolds equation and the energy equation. The two equations are coupled with each other since the Reynolds equation provides the pressure and velocity distributions to the energy equation which in turn provides the updated viscosity information to the Reynolds equation.

The variable viscosity Reynolds equation is a statement of mass conservation expressed in terms of pressures via use of the momentum equations, and has the form;

$$\nabla \cdot (C_1 \nabla p) + (\nabla C_2) \cdot \mathbf{u} + \frac{\partial h}{\partial t} = 0 \quad (42)$$

where,

$$C_1 = \int_0^h \int_0^z \frac{\zeta}{\mu} d\zeta dz - \frac{\int_0^h \frac{\zeta}{\mu} d\zeta}{\int_0^h \frac{1}{\mu} d\zeta} \int_0^h \int_0^z \frac{1}{\mu} d\zeta dz \quad (43)$$

$$C_2 = \frac{\int_0^h \int_0^z \frac{1}{\mu} d\zeta dz}{\int_0^h \frac{1}{\mu} d\zeta}$$

The Reynolds equation is solved by using simplex, three node finite elements to interpolate pressure. Reynolds cavitation boundary conditions are employed in the model for sake of illustration. The pressure distributions in the inner and outer films are integrated over the ring and bearing areas to obtain the fluid reaction forces, F_i , F_o . The viscosity in each lubricant layer may vary strongly with film temperature, and is determined from the empirical formula

$$\mu = \mu_o e^{-\beta(T-T_o)} \quad (44)$$

The temperature distribution in each fluid layer is determined by solving the energy equation, which is a statement of conservation of energy and is given by

$$\nabla \rho C_p \frac{\mathbf{D}T}{\mathbf{D}t} = \nabla \cdot (k \nabla \mathbf{T}) + \mu \left[\left(\frac{\partial u}{\partial y} \right)^2 + \left(\frac{\partial w}{\partial y} \right)^2 \right] \quad (45)$$

where the total derivative is defined as

$$\frac{\mathbf{D}T}{\mathbf{D}t} = \frac{\partial T}{\partial t} + \mathbf{u} \cdot \nabla T \quad (46)$$

Numerical experiments conducted by the authors revealed that the temporal term ($\partial T / \partial t$) is negligible due to the small thermal mass. This converts Eq. (46) into essentially a steady state problem.

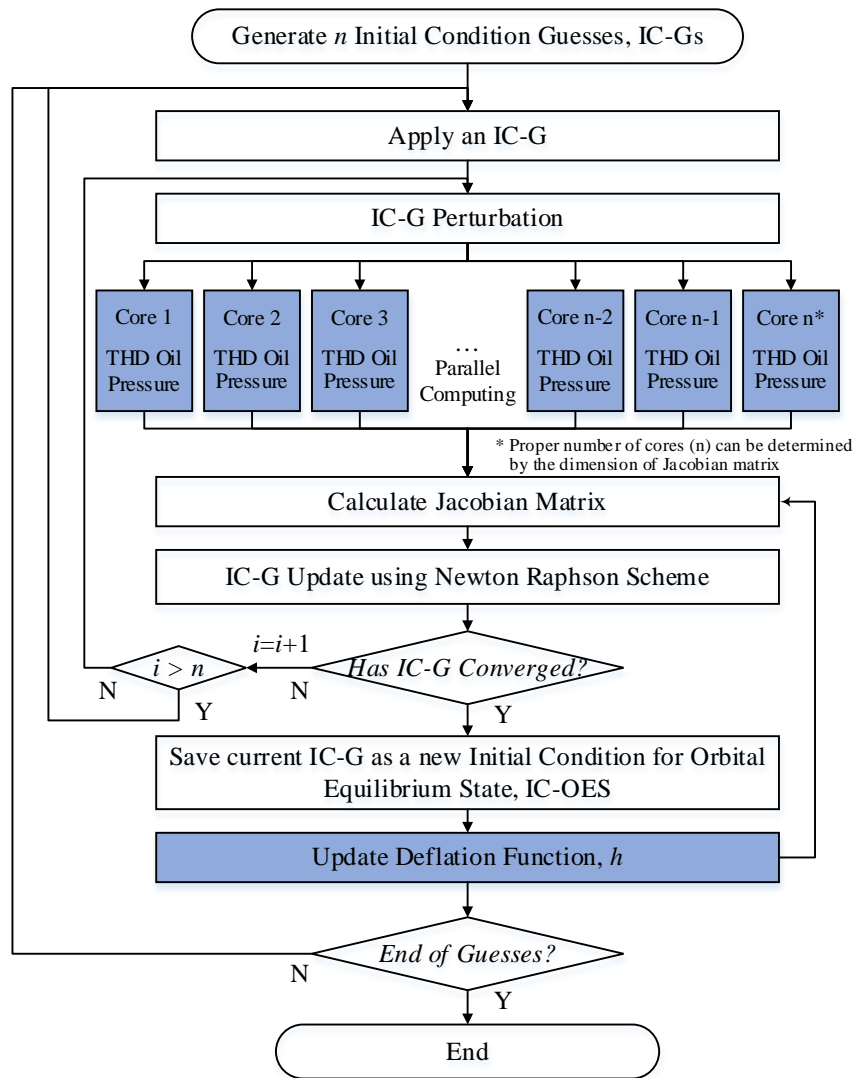


Fig. 26. Flow chart of THD-shooting method with deflation algorithm

The energy equation for the inner and outer lubricant films is further simplified to a one dimensional form to further reduce the computation time. The shaft and bearing temperatures are assumed to be constant and equal to the lubricant supply temperature for sake of illustration (i.e. $T_s=T_h=T_{sup}$). The heat conduction equation is solved with

appropriate boundary conditions to obtain the temperature distribution in the floating ring.

$$\nabla \cdot \nabla T = 0 \quad (47)$$

Lubricant temperatures at discrete locations around the circumference are obtained by utilizing the Trigonometric Collocation Method TCM, which is a numerical solution method for nonlinear differential equations with periodicity boundary conditions [42]. The assumed form of the solution has harmonics of sinusoidal functions that exhibits continuity of the temperature and the heat flux at the connected nodes in circumferential direction (i.e, beginning and end nodes on the inner and the outer lubricant layers).

$$T = \sum_{n=1}^m a_n \cos n\xi + \sum_{n=1}^m b_n \sin n\xi \quad (48)$$

Fig. 27 shows a flow chart of the steady state THD solution approach which was utilized in [28,29].The temperature distributions for the lubricants are determined through iterative calculations between the Reynold equation and the energy equation for a certain time segment Δt , where the time segment is set equal to 1/30 of the shaft whirling period (τ_R). The journal position and velocity are confirmed once the temperature distributions and the corresponding lubricant viscosity distributions are converged. These conditions are then utilized as initial condition for the next time segment iteration.

The steady state THD solution procedure is embedded in the shooting algorithm (Fig. 26), and is simultaneously solved along n paths in the parallel computing approach.

The parameter n is the number of states in the model, and therefore the number of perturbations required to form the Jacobian matrix in the shooting method.

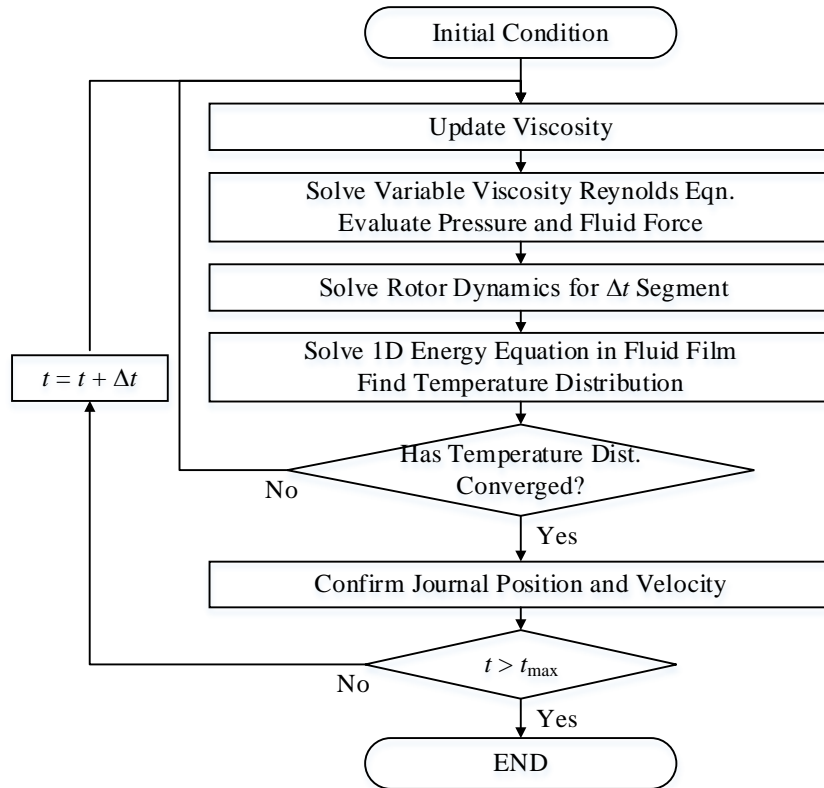


Fig. 27. Flow chart of steady state THD solution approach

Simulation Results of FRB-RGD with THD Solutions

A symmetry rigid rotor supported by two identical FRBs is considered as mechanical model to apply the THD numerical algorithms for analytical bifurcation study, and the detailed parameters for the FRB and the lubricant are defined in Table 8.

The non-autonomous case corresponds to an imbalanced rotor which causes a periodic force with frequency equal to the spin frequency. The imbalance eccentricity is set equal to ($\varepsilon=0.3C_i$) for the non-autonomous case. In the autonomous case, the rotor is considered to be fully balanced, Three different lubricant supply temperatures ($T_{\text{sup}}=29^\circ\text{C}, 39^\circ\text{C}, 49^\circ\text{C}$) are used to analyze thermal effects on nonlinear phenomena and stability. The responses from the current FE based THD bearing model are compared with those from a simplified bearing model (isothermal solutions from short bearing theory) which was widely utilized in related studies.

Table 8. FRB and lubricant parameters

FRB Parameters [Units]	Values
Clearance [μm]	$C_i=26.5, C_o=42.5$
Diameter [mm]	$D_i=11.543, D_o=17.722$
Length [mm]	$L_i=2.493, L_o=3.561$
Rotor mass [g]	$M_I/2=814.9$
Ring mass [g]	$M_R=3.38$
Ring polar moment of inertia [10^{-6}kgm^2]	$I_R=18.89$
Ring thermal conductivity [$\text{W}/\text{m}^\circ\text{C}$]	$k_{\text{lub}}=0.13$
Lubricant Parameters [Units]	Values
Supply temperature [$^\circ\text{C}$]	$T_{\text{sup}}=29, 39, 49$
Viscosity exponent [$1/^\circ\text{C}$]	$\beta=0.0155$
Viscosity @ $29^\circ\text{C}, 39^\circ\text{C}, 49^\circ\text{C}$ [cP]	$\mu=12.0, 10.3, 8.8$
Specific heat [$\text{J}/\text{kg}^\circ\text{C}$]	$C_p=2000$
Thermal conductivity [$\text{W}/\text{m}^\circ\text{C}$]	$k_{\text{lub}}=0.13$
Convection coefficient [$\text{W}/\text{m}^2^\circ\text{C}$]	$h_{\text{lub}}=500$
Density [kg/m^3]	$\rho=860$

Autonomous systems

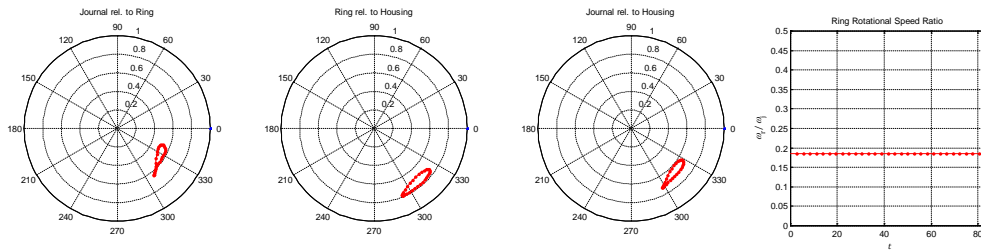
Multiple response states

Fig. 28 shows the coexisting multiple steady state responses determined by the autonomous shooting method at a speed of 65 krpm with the lubricant supply temperature $T_{\text{sup}}=39^{\circ}\text{C}$. The three periodic solutions (PS) are identified using the THD-autonomous shooting method, and the equilibrium position (EP) is obtained with a Newton-Raphson search. The stability of each response is determined utilizing the Floquet theory, i.e. a monodromy matrix eigenvalue magnitude greater than 1 implies instability. These results imply that the two unstable solutions (PS 2 and EP) will ultimately be attracted to one of the stable solutions (PS 1 or PS 3). Fig. 29 represents temperature distributions of FRB in cross section plane at specific time instants of PS 3, which include temperature variations of inner and outer films as well as the ring area.

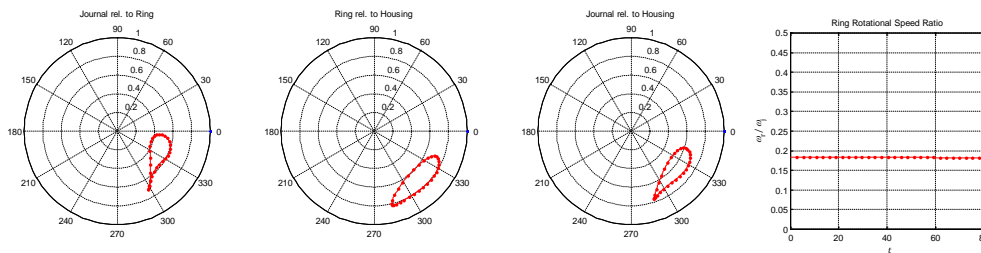
Bifurcation diagram

The arc-length continuation algorithm is applied to determine the THD case response manifold and stability in traversing a speed range (e.g, 10krpm to 100krpm). Fig. 30 shows the maximum and minimum values of the non-dimensionalized vertical displacements, $y_j/(C_i+C_o)$, as well as the corresponding non-dimensionalized response periods, τ/τ_s , of the autonomous system with $T_{\text{sup}}=39^{\circ}\text{C}$ are plotted on the bifurcation diagrams.

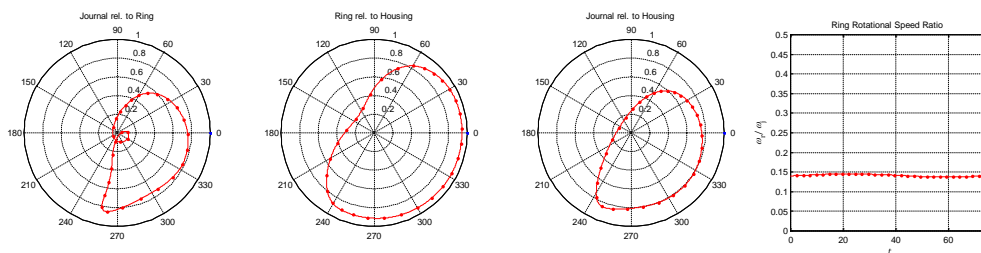
(a) Coexistent Response #1 (PS, $\tau_R=13.246\tau_S$, Stable*)



(b) Coexistent Response #2 (PS, $\tau_R=12.859\tau_S$, Unstable*)



(c) Coexistent Response #3 (PS, $\tau_R=11.805\tau_S$, Stable*)



(d) Coexistent Response #4 (EP, Unstable*)

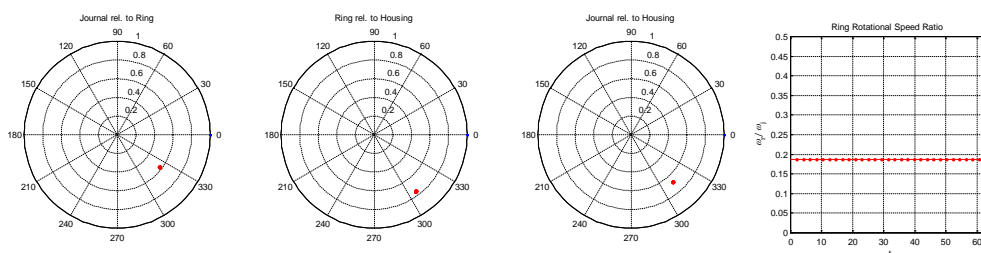


Fig. 28. Multiple response states (orbits and ring rotational speed ratio) at 65000rpm ($T_{sup}=39^\circ\text{C}$). *Stability of the response is determined by the Floquet theory

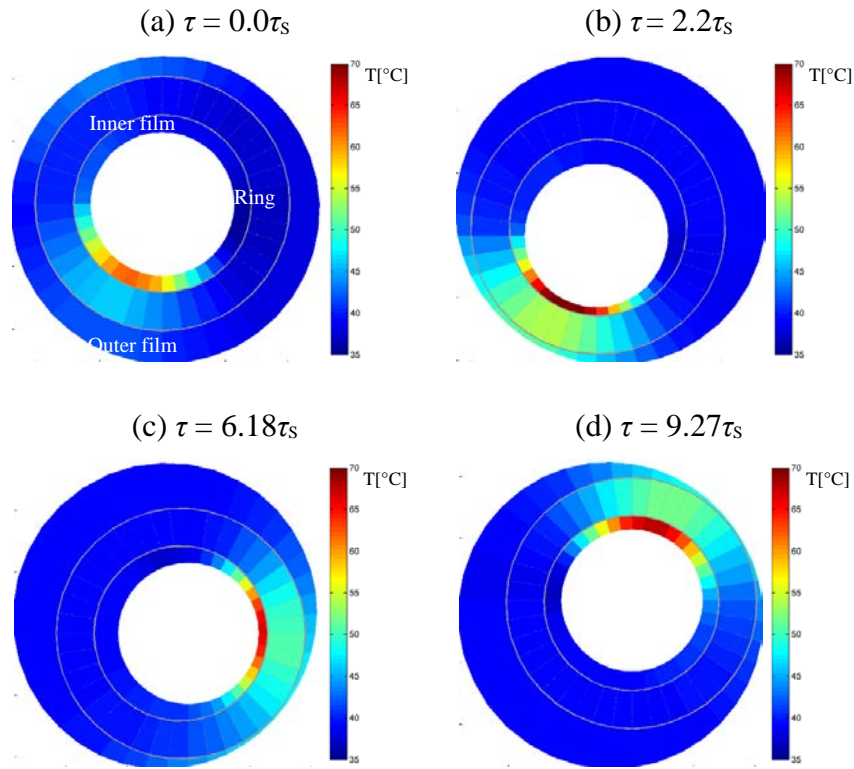


Fig. 29. Temperature distribution of coexistent response #3 at specific time instants

In Fig. 30(a), the stable equilibrium position, EP, which is dominant in low revolution speeds, becomes unstable after crossing the Hopf bifurcation near 60 krpm. At that point, a stable periodic solution (PS 1) emerges in the arc length continuation and enlarges in orbit size with increasing rpm to the first saddle node (SN 1). The arc length continuation then identifies an unstable orbit (PS 2), which rapidly expands as rpm decreases until it reaches the second saddle node (SN 2). The response (PS 3, stable) then slowly approaches the clearance limit as rpm increases. Multiple coexisting response states exist in the speed range between the two saddles (i.e, 53krpm to 70krpm). The repeller limit cycle forces the response away from itself while a pair of competing attractors determine the final steady state limit cycle depending on initial

conditions. This exhibits a potentially dangerous operating condition of the machine since an impulse load may cause the system to jump from the small limit cycle to the large limit cycle while operating at a fixed speed.

The corresponding period ratios of the responses are represented in Fig. 30 (b) where τ is the limit cycle period and τ_s is the shaft spin period. The EP is a fixed equilibrium point so it does not have a period, and therefore only the periods for PS 1-3 are shown in the diagram. The periods for all PS fall in the range between 10 and 14. This range corresponds to 30% ~ 50% of the ring rotational frequency, which is in the expected range for oil whirl of the ring in the FRB system.

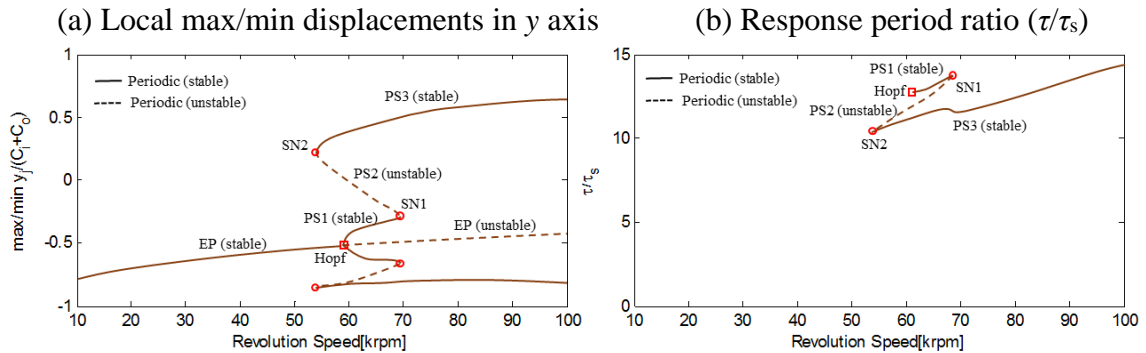


Fig. 30. Analytical bifurcation diagrams ($T_{sup}=39^\circ\text{C}$): (a) max/min $y_j/(C_i+C_o)$ (b) response period ratio τ/τ_s

A comparison of Figures 31(a), 31(b) and 31(c) reveals that the speed range between the saddle nodes is enlarged and shifted with the THD model as compared to the isothermal lubricant model ($\mu_o=8.8\text{cP}$, 10.3cP , 12.0cP) results. This implies a wider speed range of coexistent solutions and uncertainty of jumps from possibly benign to

potentially destructive vibration levels, between the bifurcation speeds. The THD based, autonomous solutions also exhibit a much higher sensitivity to the lubricant supply temperature than the assumed isoviscous model results.

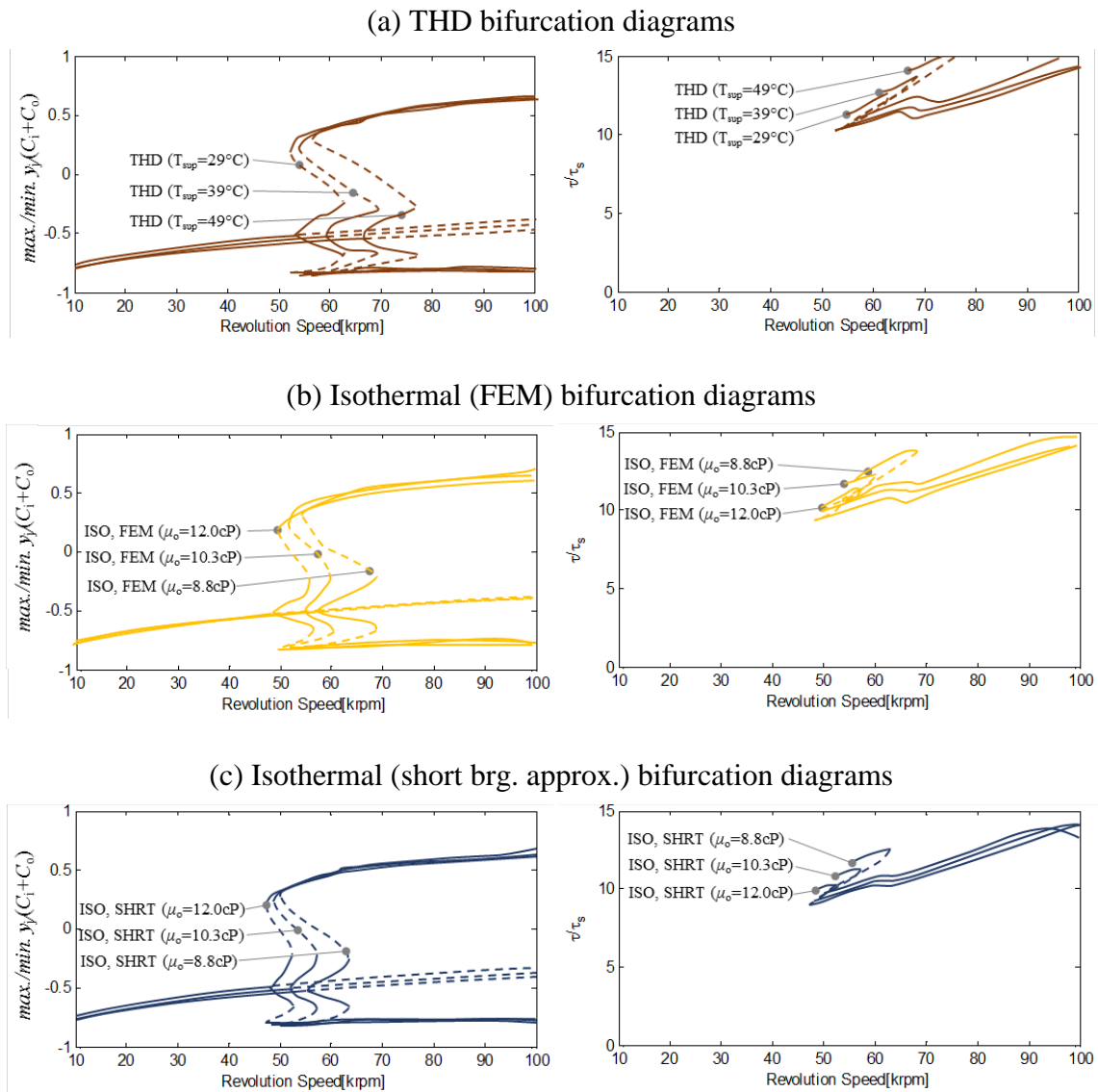


Fig. 31. Comparison of analytical bifurcation diagrams (THD vs. Isothermal)

Non-Autonomous Systems

A transient numerical integration (TNI) study was performed with varying levels of imbalance to aid in discerning appropriate levels of disk mass imbalance to utilize in the non-autonomous coexistent solution/ bifurcation point search. Fig. 32 shows some results of this study in the form of bifurcation diagrams, constructed from a series of Poincaré sections vs. rpm, for imbalance eccentricity ranging from $0.02C_i$ to $0.3C_i$. The response with small unbalance is similar to the autonomous ($0.0C_i$) results, though the instability onset shifts slightly higher with the small added imbalance.

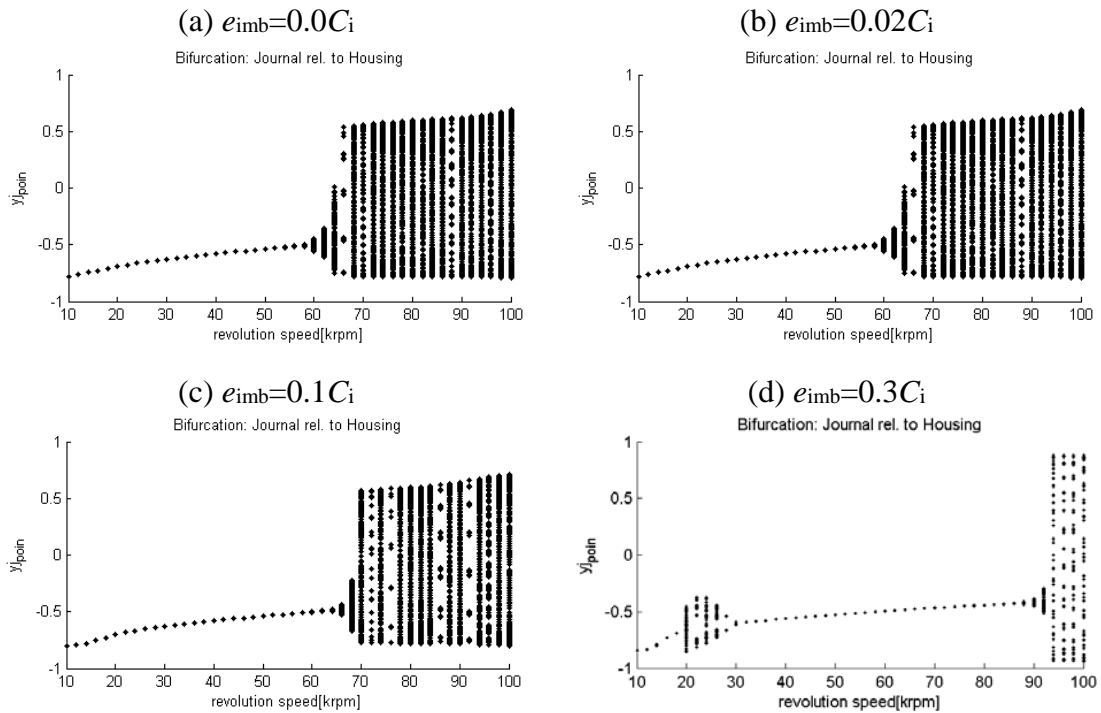


Fig. 32. Bifurcation (Poincaré) Diagrams w.r.t. Imbalance Eccentricity (isothermal)

In contrast, the Poincaré sections with large unbalance, for example $e_{imb}=0.3C_i$ shows the oil whirl type bifurcation onset is significantly raised in rpm level. This quenching effect of the subsynchronous whirl is referred to as synchronization, and has been reported in large industrial machinery [36].

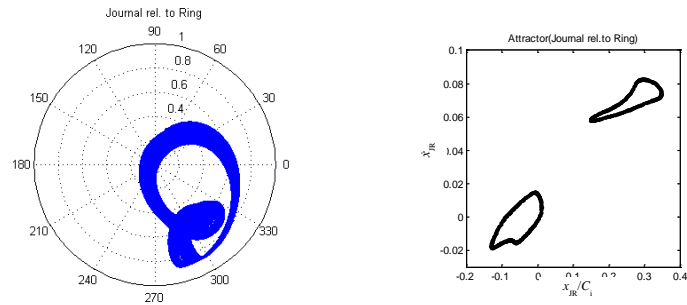
The larger imbalance also causes the emergence of a small amplitude subsynchronous whirl over a short range of lower speeds (i.e, 20kpm ~ 30krpm). As expected the larger imbalance case shows a greater distinction with the autonomous case and is thus examined in the coexistent response/bifurcation study.

Multiple response states

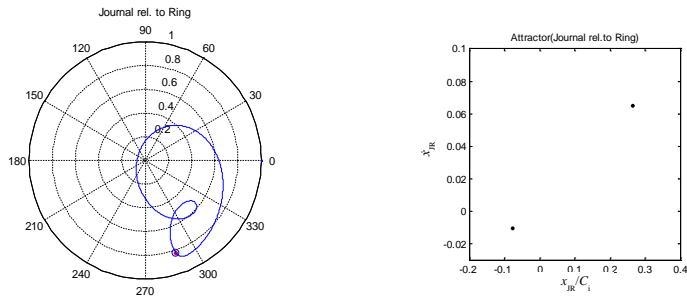
The THD non-autonomous shooting algorithm is employed in searching for $n\tau$ periodic responses for each lubricant temperature ($T_{sup}=29^\circ\text{C}$, 39°C , 49°C), and the TNI method is utilized for obtaining possible quasi periodic responses. Fig. 33 shows the predicted multiple response states when the algorithm is applied at 22000 rpm with $T_{sup}=39^\circ\text{C}$. The journal orbits relative to the ring and the corresponding Poincaré sections are shown for each response state: $1\times$ synchronous, $1/2\times$ sub-synchronous, and quasiperiodic. The Floquet monodromy matrix eigenvalues determine that the two periodic responses are unstable repellers, so that trajectories slightly perturbed from these response states diverge and evolve into a quasi-periodic response. Transient numerical integration is utilized to demonstrate this evolution from the $1\times$ synchronous state to the quasi-periodic state at a speed of 22000rpm. Fig. 34 shows the trajectory initially repelled from the $1\times$ state to the $1/2\times$ state and ultimately progressing to full

quasiperiodic motion, as evidenced by the closed locus Poincare maps. Fig. 35 shows the transition event in time domain.

(a) Quasi-periodic



(b) $1/2\times$ sub-synchronous (unstable)



(c) $1.0\times$ synchronous (unstable)

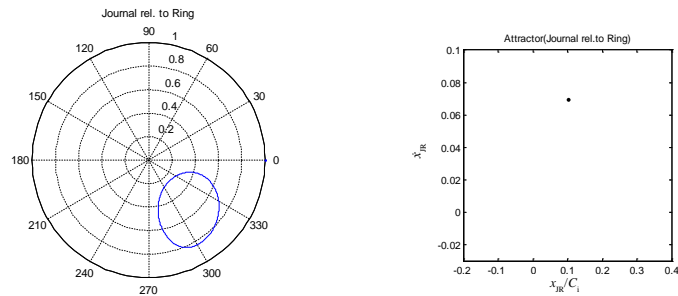


Fig. 33. Coexistent responses at 22000 rpm ($e_{imb}=0.3C_i$, $T_{sup}=39^\circ\text{C}$)

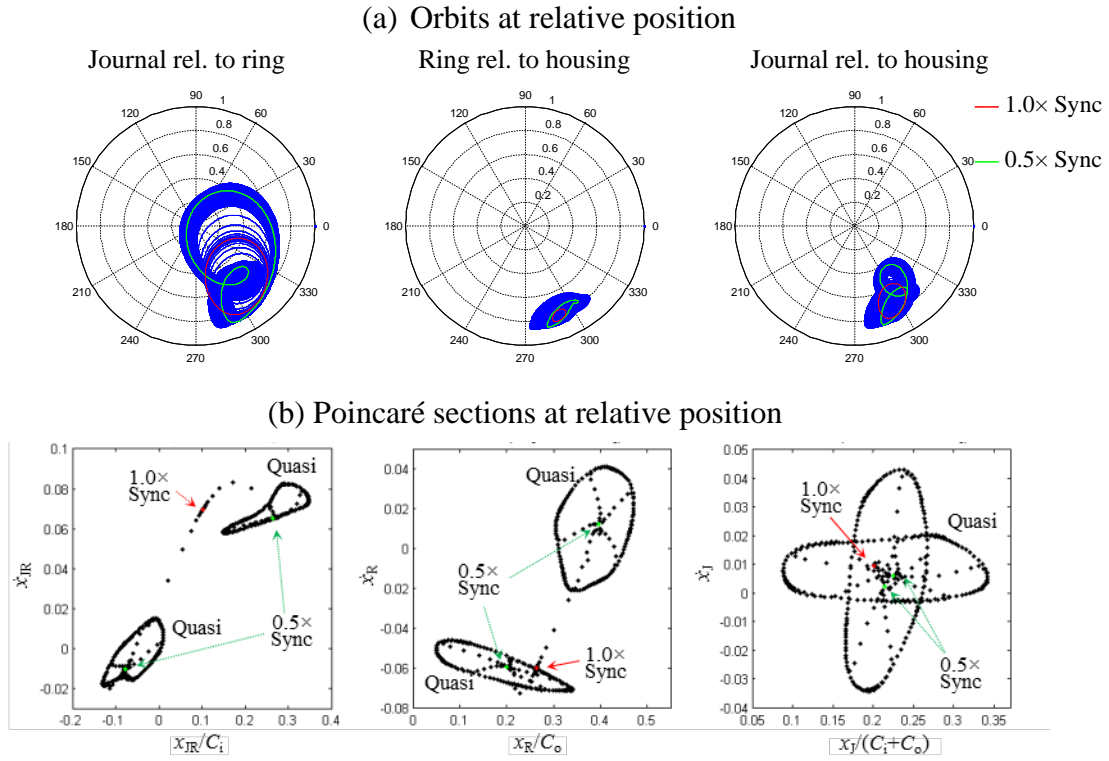


Fig. 34. Repelling motion from $1\times$ sync to quasi-periodic at 22000rpm ($e_{imb}=0.3C_i$, $T_{sup}=39^\circ\text{C}$)

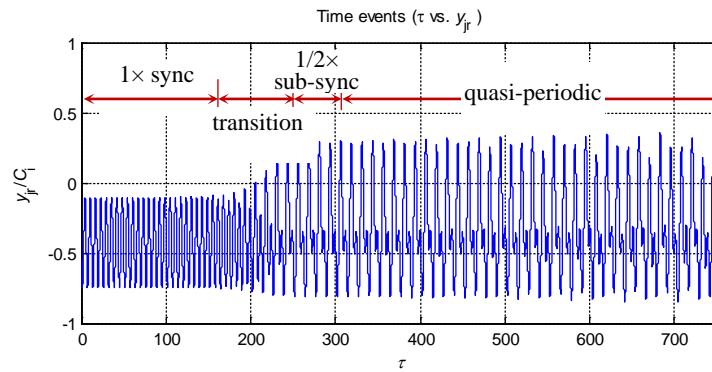


Fig. 35. Time events from $1\times$ sync to quasi-periodic at 22000rpm ($e_{imb}=0.3C_i$, $T_{sup}=39^\circ\text{C}$)

Bifurcations

The bifurcation diagrams in Fig. 36 are obtained by applying the method of THD, non-autonomous, arc-length continuation. The maximum and minimum vertical displacements of journal relative to ring, $\max./\min. |x_{jr}/C_i|$, are plotted vs. the spinning speed for 3 lubricant temperatures. The emergence of the $1/2\times$ sub-synchronous response occurs between 18 krpm and 30 krpm independent of the lubricant temperature. The high speed range (70krpm ~ 100krpm) instability onset speed increases markedly with oil supply temperature. This also occurs in the autonomous system. Fig. 37 shows a zoomed segment of the THD model's bifurcation diagram in Fig. 36 for $T_{sup}=39^\circ\text{C}$ and its counterpart from the isothermal case model. In these figures, for conciseness, the maximum amplitudes of journal relative to ring, $\max. e_{jr}/C_i$, are plotted vs. the spinning speed. The figure shows that the stable $1\times$ synchronous becomes unstable at BF 1, and two additional response states emerge; an unstable $1/2\times$ sub-synchronous response and a quasi-periodic response. The $1/2\times$ sub-synchronous response becomes stable at BF 2, and the large amplitude quasi-periodic response is emerged near the bifurcation point. The periodic response bifurcates again at BF 3, with the $1/2\times$ sub-synchronous disappearing and a stable $1\times$ synchronous returning. Fig. 38 (a) shows the coexisting attractors at 27000rpm for both the quasi-periodic and $1/2\times$ sub-synchronous, and its respective orbits can be seen in Fig. 38 (b).

The THD and isothermal cases have very similar responses in the spin speed range studied. The isothermal amplitudes are slightly smaller and the bifurcations occur at a slightly lower speed than in the THD results. This similarity can be explained since

the dynamic eccentricities (ϵ_D) are relatively small ($0.2 < \epsilon_D < 0.4$), so that the viscosity is not significantly changed from the isoviscosity value.

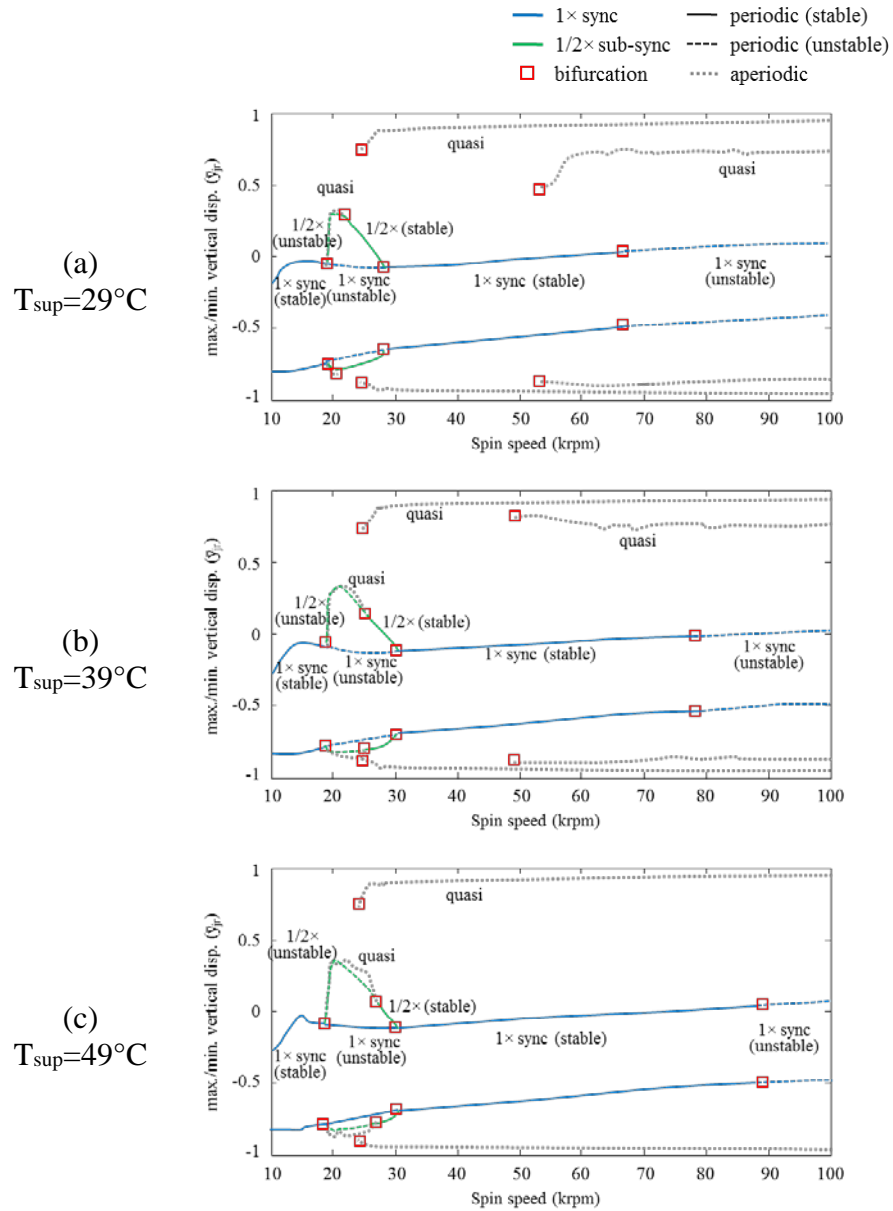


Fig. 36. Bifurcation diagrams w.r.t. lubricant supply temperature ($e_{imb}=0.3C_i$)

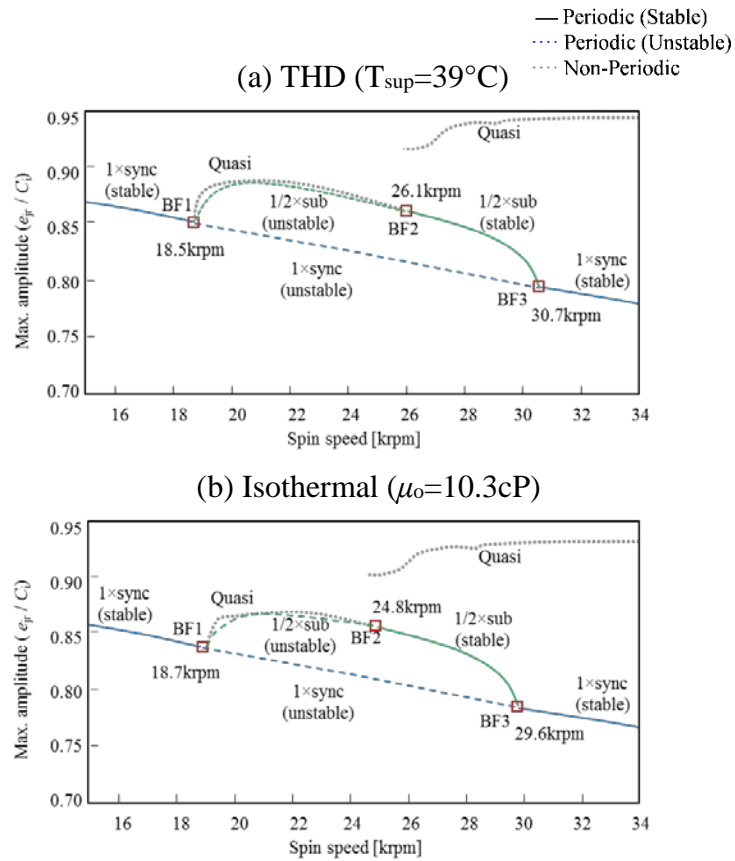


Fig. 37. Bifurcation diagrams: ranges from 15krpm to 34krpm ($e_{imb}=0.3C_i$, $T_{sup}=39^{\circ}\text{C}$)

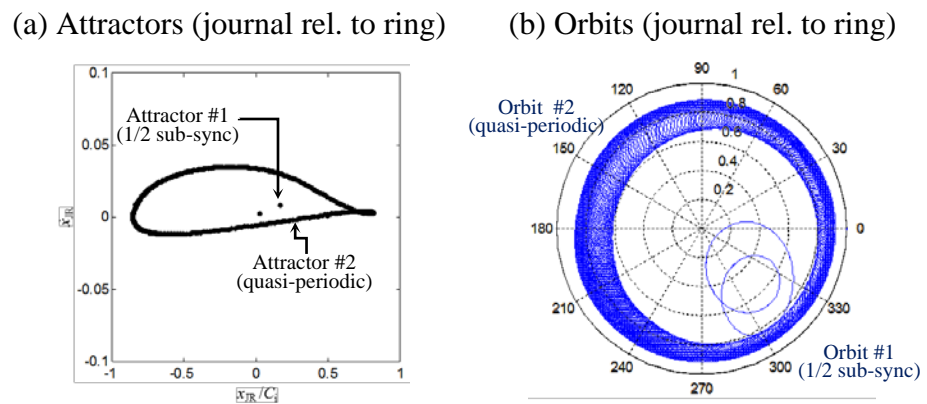


Fig. 38. Coexisting attractors at 28000rpm ($e_{imb}=0.3C_i$, $T_{sup}=39^{\circ}\text{C}$)

Summary of Results

The THD shooting/arc-length continuation algorithm for analyzing thermal effects on bifurcations of fluid film bearings was developed and illustrated for FRBs. Both free vibration (autonomous) and imbalance excited (non-autonomous) cases are examined and illustrated for a FRB-rigid rotor system. The autonomous case results showed the co-existence of multiple response states and the presence of Hopf and two saddle node bifurcations. Although increasing the lubricant supply temperature delays the onset of a Hopf bifurcation with increasing speed, it adversely widens the speed range over which a sudden jump from a benign limit cycle to a large limit cycle may occur. In general the THD bifurcation curves are seen to be more sensitive with regard to changes in speed and supply temperature than the isothermal responses.

The non-autonomous system results clearly indicate significant increase in the oil whirl onset speed as the level of imbalance is increased. This is a good example of synchronization in nonlinear dynamical systems. The quenching effect of this synchronization extends the stability of the upper spin speed range, however it also results in a bifurcation from synchronous response to a small amplitude whirl in the lower speed range. The stability of the $1/2\times$ sub-synchronous and quasi-periodic responses in the low speed ranges are strongly dependent on the lubricant supply temperature. Comparison of the THD and isothermal models show good agreement for small dynamic eccentricities as expected. Future work in THD bearing modelling for coexistent steady state solutions and bifurcations include flexible, multi mass rotor models and other bearing types such as pressure dam, tilting pad, etc.

CHAPTER V
NONLINEAR RESPONSE AND BIFURCATIONS OF A RIGID ROTOR
SUPPORTED ON TILTING PAD JOURNAL BEARINGS (TPJB)

Introduction to TPJB-Rotor Systems

Modern rotating machinery, such as gas/steam turbines, generators, compressors, gearboxes, pumps, etc. experience higher performance and efficiency as the number of stages and speed increase. However this change tends to increase the propensity of the machines for rotordynamic instability. Tilting pad journal bearings (TPJBs) have been selected in such machines due to their stabilizing effects on the rotor systems; the tilting motions of pads greatly suppress the cross-coupled stiffness coefficients and thus enhance rotor stability. Nonetheless, a survey of the literature reveals that TPJBs do not always perform successfully.

Pagano et al. [43] and Brancati et al. [44] used numerical integration to determine that an unbalanced rotor supported by TPJBs may experience sub-synchronous motions with one-half or one-quarter components under certain operating conditions. Abu-Mahfouz and Adam [6] used numerical integration to determine that an unbalanced rotor supported by three-pad TPJBs may experience quasi-periodic and chaotic responses. Cao, Dimond, and Allaire [45] used numerical integration to determine that a complex flexible rotor, 8-stage centrifugal compressor, supported by TPJBs, exhibited strong nonlinear behaviors such as sub- and super-synchronous responses. Gadangi, Palazzolo, et al. [28,29] indicated that large, multi-harmonic orbital motions occur in TPJB

supported machines with high levels of unbalance, and are affected by pad deformations and fluid thermal effects. Suh and Palazzolo [30] investigated thermally induced synchronous instability, i.e, Morton effect, in TPJBs using 3D structural finite elements models for the shaft and pads, a variable viscosity Reynolds equation and the 3D energy equation. So far, a considerable amount of numerical studies have been conducted to predict instability and nonlinear dynamic characteristics of TPJB-rotor systems, most of them rely on transient numerical integrations.

Steady state, nonlinear dynamics, search-based approaches such as harmonic balance, trigonometric collocation, shooting/continuation, etc. have seldom been used for the analyzing the nonlinear response of TPJB supported rotors. These approaches use numerical integration to iteratively determine initial states of all coexistent periodic responses, their local stability, and bifurcation onsets. However, the use of this approach requires an extensive amount of computations to evaluate Jacobian matrices iteratively in the solution procedure. This limited previous studies to considering Jeffcott type rotor models supported on simple geometry bearings [17-21, 25-26, 46], for instance, floating ring bearings, squeeze film dampers and plain journal bearings, which are suitable for providing fluid film forces obtained from infinitely short-/long- bearing theories.

In the present paper, an improved non-autonomous shooting/arc-length continuation method is employed to analyze nonlinear behaviors of rotors supported on TPJBs. An objective of this research is to identify bifurcations and coexistent responses including both stable and unstable solutions. In addition, effects of pad preload, pivot offset, and lubricant viscosity on rotordynamic bifurcations are investigated. Due to the

geometrical and dynamical complexity of TPJBs, simplified fluid film models have limitation to evaluate fluid film pressure on the pads so that a finite element based TPJB model with rigid rocker pivots is developed for the bifurcation study. Efficient execution algorithms such as deflation and parallel computing are employed in order to reduce the corresponding computation time.

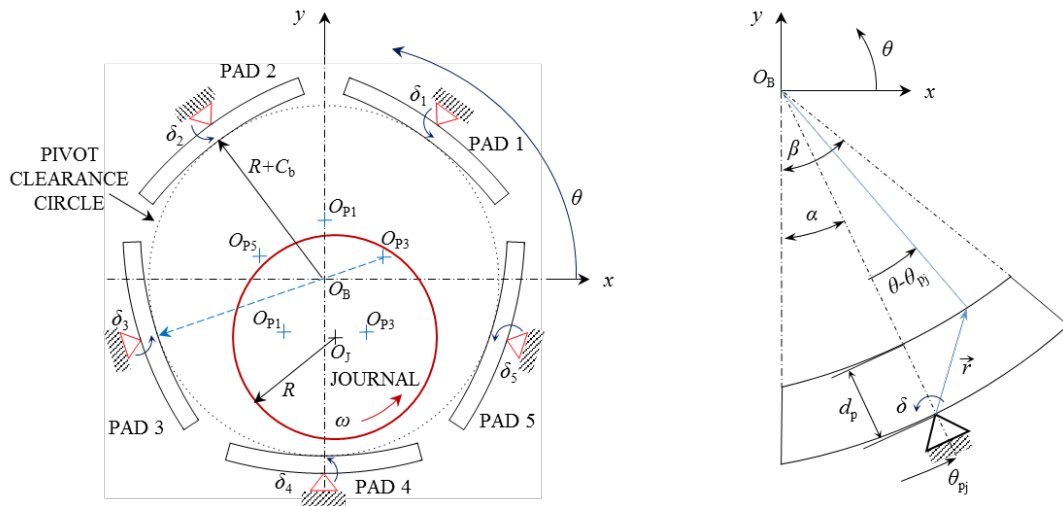


Fig. 39. TPJB (5-pad, LOP) schematics and its respective coordinates in x - y plane

Finite Element TPJB Modeling

Fig. 39 depicts the middle plane in the axial direction of a TPJB model and its coordinate system. The film thickness distribution for a given pad is dependent on the x and y components of the journal center and on the pad angle δ_j , as given by the formula:

$$h(\theta) = C_{pj} - X \cos(\theta) - Y \sin(\theta) - (C_{pj} - C_B) \cos(\theta - \theta_{pj}) - \delta_j R \sin(\theta - \theta_{pj}) \quad (49)$$

where $h(\theta)$ is film thickness at angular location θ , C_{Pj} is the radial pad clearance of pad j , C_B is the radial bearing clearance, X, Y are x and y components of the journal's displacement relative to bearing center O_B , δ_j is the rotation angle of pad j , R is the journal radius and θ_{Pj} is value of θ at the pivot of pad j .

The hydrodynamic pressure on the fluid film of each pad, p , can be determined from Reynolds equation for an incompressible and iso-viscosity lubricating oil model, as follows,

$$\frac{\partial}{\partial \theta} \left(\frac{h^3}{12\mu} \frac{\partial p}{\partial \theta} \right) + \frac{\partial}{\partial z} \left(\frac{h^3}{12\mu} \frac{\partial p}{\partial z} \right) = \frac{R\omega}{2} \frac{\partial h}{\partial \theta} + \frac{\partial h}{\partial t} \quad (50)$$

where z is the axial direction of the bearing, μ is dynamic viscosity and ω denotes the rotational speed of journal. The solution of Reynolds equation is obtained using a finite element model, which consists of a three-node simplex, triangular type mesh generated on half of fluid film layer in the axial direction with an assumption of a symmetrical pressure state. Fluid reaction force between a pad and the journal is obtained by integrating the pressure throughout the mesh and multiplying by 2 to account for the other half of the bearing.

$$\begin{Bmatrix} F_{xj} \\ F_{yj} \end{Bmatrix} = 2 \int_0^{L/2} \int_{\theta_{Bj}}^{\theta_{Ej}} p_j(\theta, y) \begin{Bmatrix} -\cos(\theta) \\ -\sin(\theta) \end{Bmatrix} d\theta dz \quad (51)$$

The total, lubricant film force on the journal is

$$\begin{Bmatrix} F_x \\ F_y \end{Bmatrix} = \sum_{j=1}^{N_p} \begin{Bmatrix} F_{xj} \\ F_{yj} \end{Bmatrix} \quad (52)$$

The pressure distribution on pad j induces a moment on the pad about its pivot;

$$M_{P_j} = 2 \int_0^{L/2} \int_{\theta_{Bj}}^{\theta_{Ej}} P_j(\theta, y) \vec{r} \times \begin{Bmatrix} \cos(\theta) \\ \sin(\theta) \end{Bmatrix} R d\theta dz \quad (53)$$

where \vec{r} is the vector from the pivot contact point on pad j to the location of the differential force on pad j . Fig. 40 shows the finite element TPJB model used in this study and an example of pressure distributions on pads.

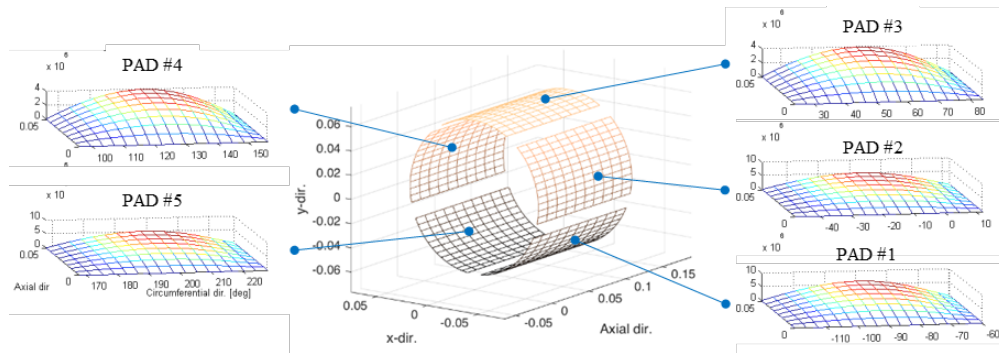


Fig. 40. Finite element TPJB model and an example of pressure distributions on pads

Model Verification

Code verification works are conducted with two previous studies on TPJBs: Gadangi et al. in Ref. [28] and Someya et al. in Ref. [47]. The calculated pressure fields on pads of the TPJBs are used to solve dynamic and static states of the rotors whether the existence of unbalance force.

Comparison with Someya Table (without unbalance)

Static state results from two specific bearing geometries in Someya table, e.g. No.49 and No.50, are compared with those from the developed TPJB codes and the equilibrium positions, altitude angles and respective synchronized reduced bearing coefficients agrees well with each other as in Fig. 41.

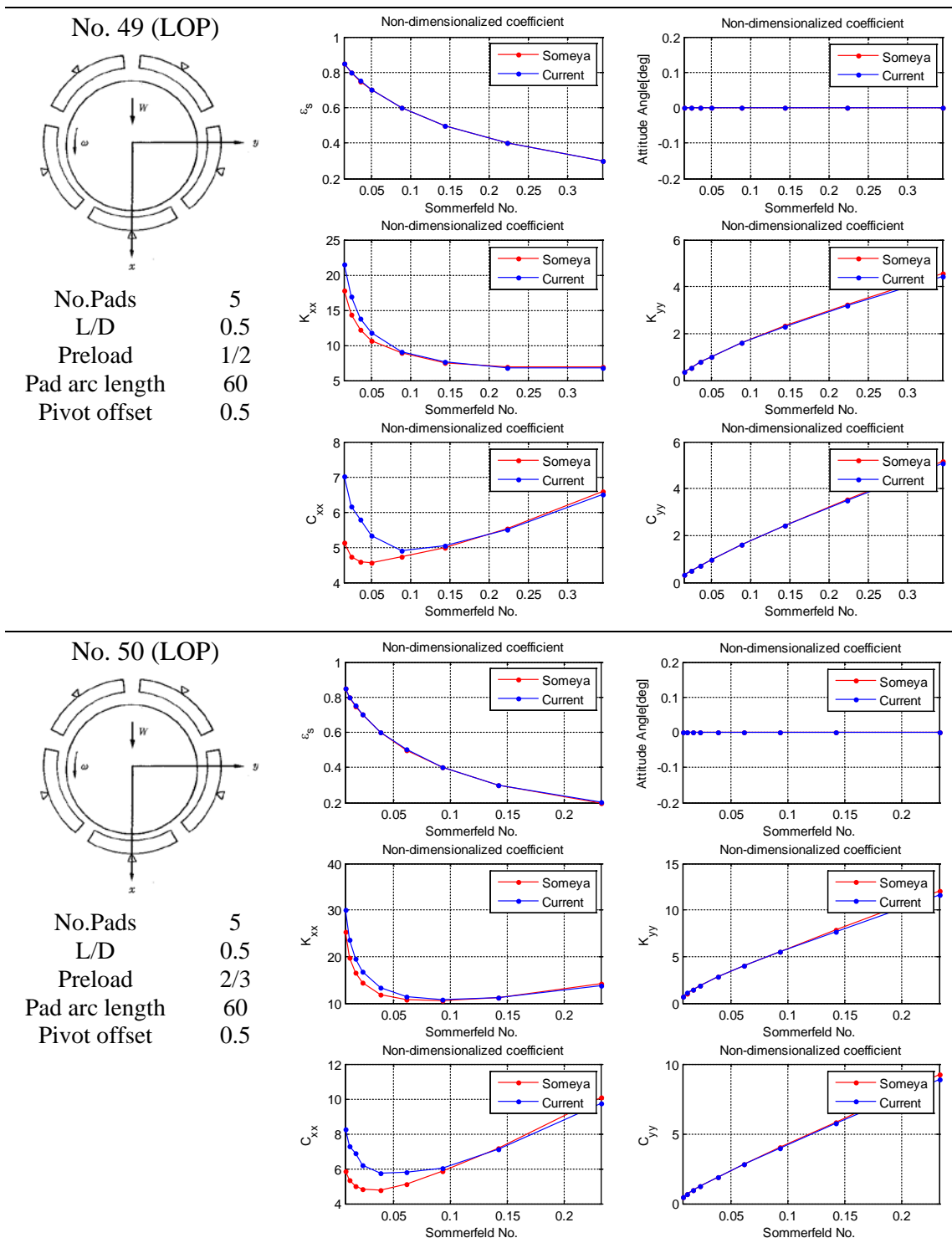


Fig. 41. Comparisons of Bearing Coefficients with Someya Table

Comparison with Gadangi's results (with imbalance)

Gadangi et al. [28] investigated dynamics of a TPJB-rotor system under sudden unbalance forces those are assumed to be induced by blade loss events. The detailed TPJB parameters in the study are listed in the Table 9, and a schematic view for the pad position (LBP) and clearances are shown in Fig. 42. Table 10 describes amounts of imbalance eccentricities in the study; two different unbalance force (low and high) are applied to the rotor system.

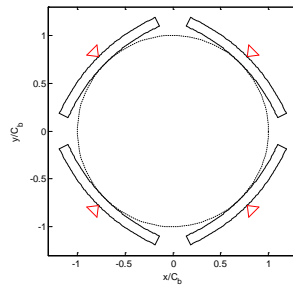


Fig. 42. Four-Pad TPJB model in Ref. [28]

Table 9. TPJB specifications in Ref. [28]

Bearing parameter	Value [unit]	Pad parameter	Value [unit]
Journal diameter	0.1 m	Num. of pads (arclength)	4 (75°, LBP)
Bearing length	0.07 m	Preload	0.47
Rotor speed	209.44 rad/s	Offset	0.5
Rotor mass	1000 kg	Pad clearance	148 μm
Static load	20 kN	Pad thickness	0.02 m

Table 10. Unbalance parameters in Ref. [28]

spin speed 209.44 rad/s (2000rpm)	imbalance eccentricity (e_{imb})	ratio between dynamic and static loads (F_d/F_s)
Low unbalance case	100 μm (1.27 C_b)	$s=0.147$
High unbalance case	570 μm (7.26 C_b)	$s=0.838$

As can be seen in Fig. 43 and Fig. 44, the orbits from the current code agree well with the Gadangi's results.

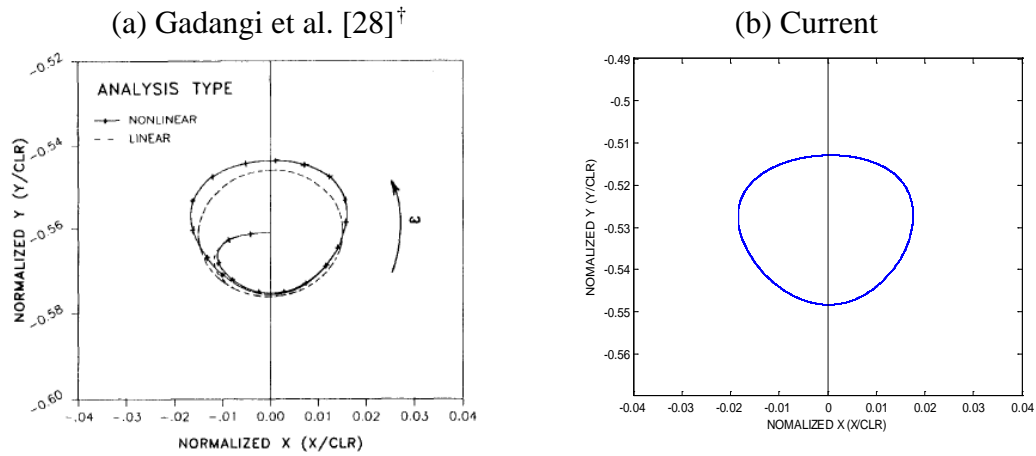


Fig. 43. Comparison of low unbalance orbits ($e_{imb}=100\mu\text{m}$, $s=0.147$)

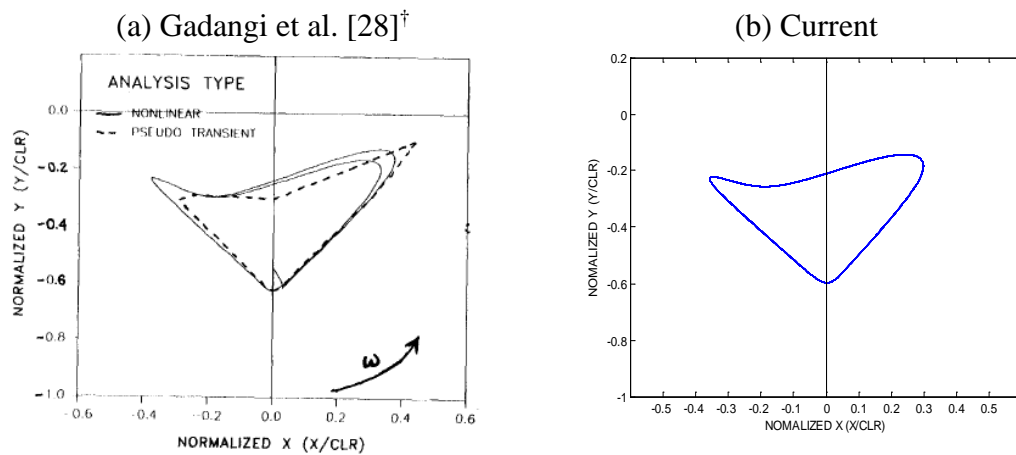


Fig. 44. Comparison of high unbalance orbits ($e_{imb}=570\mu\text{m}$, $s=0.838$)

† Fig. 43 (a) and Fig. 44 (a) are reprinted with permission from “Transient analysis of plain and tilt pad journal bearings including fluid film temperature effects” by Gadangi, R.K., and Palazzolo, A. B., 1996, Journal of Tribology, doi: 10.1115/1.2831319, Copyright 1996 by ASME.

In the Gadangi's paper, only one spin speed is assigned to the investigation (e.g. 209rad/s or 2000rpm). To see how the response changes with regard to the spin speed, increased rpms are applied to the system as show in the Fig. 45. As results, the responses do not have much of a variety, but the response keeps expanding to the catastrophic limit as rpm increased.

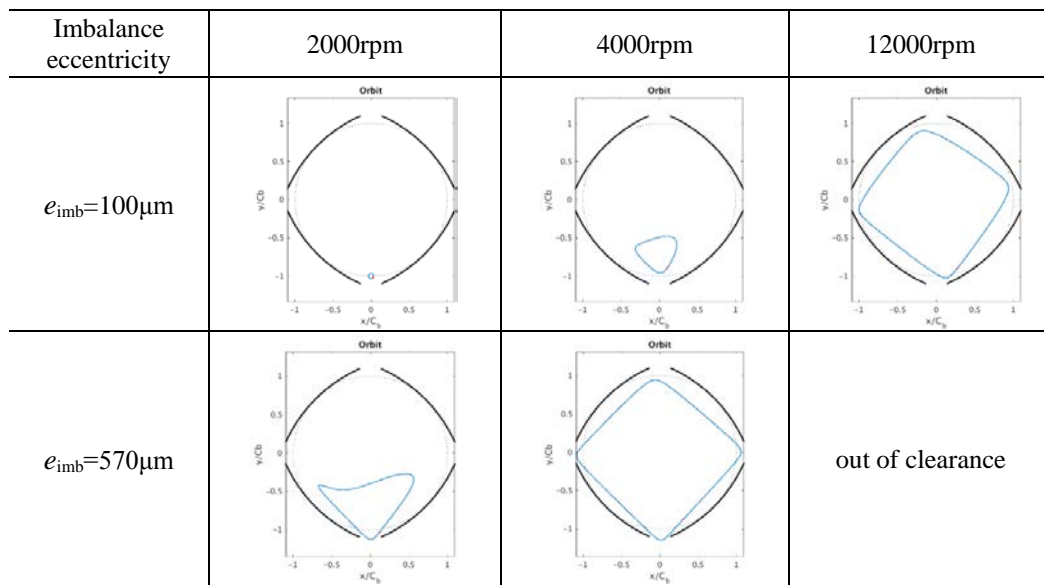


Fig. 45. Limit cycles of 4 pad TPJB wrt spin speeds

A Rigid Rotor Supported by TPJB

A “Jeffcott” type symmetric rigid rotor supported by 5-pad tilting pad journal bearings (TPJB-RGD) is set to as a mechanical model for investigation of nonlinear response and bifurcation behaviors as can be seen in Fig. 46. The bearing specification and parameter ranges are specified in Table 11. Spin speeds and rotor mass are varied in the TPJB-RGD system model for the parametric study.

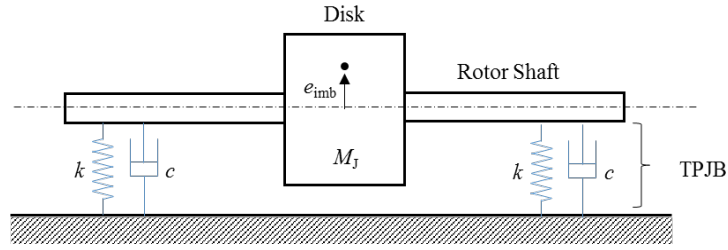


Fig. 46. Symmetric TPJB support – rigid rotor system

The equations of motion for the journal and pads can be written as,

$$\begin{aligned}
 M_J \ddot{x} &= F_x + W_{dx} + W_{sx} \\
 M_J \ddot{y} &= F_y + W_{dy} + W_{sy} \\
 I_{pj} \ddot{\delta}_{pj} &= M_{pj}
 \end{aligned} \tag{54}$$

where M_J is the journal mass, I_p is the pad inertia, W_s , W_d are static and dynamic load on the journal, M_p is the integrated moments on pad. The static force can be the weight of rotor/disc or side loads, and the dynamic force is usually due to unbalance force, F_{imb} , from imbalance eccentricity, e_{imb} , on rotor/disc.

Table 11. TPJB specification and parameter ranges

Bearing Parameter	Value [unit]	Pad parameter	Value [unit]
Journal diameter (D)	0.1016 [m]	Num. of pads (arclength)	5 (60°, LOP)
Bearing length (L)	0.0508 [m]	Preload (m_p)	1/2, 2/3
Spin speed	1 ~ 20 [krpm]	Offset (α/β)	0.5, 0.6
Bearing load (W)	4.9, 9.8, 19.6 [kN]	Bearing clearance (C_b)	88 [μm]
Lubricant viscosity (μ)	10.3, 13.8, 27.0 [cP]	Pad clearance (C_p)	162 [μm]
Amounts of imbalances on disc (e_{imb})	$0.05C_b \sim 0.3C_b$	Pad thickness	0.02 [m]

Simulation Results and Discussion

In order to investigate bifurcations and nonlinear behaviors of TPJB-RGD system, both the direct numerical integration (NI) and shooting/arc-length continuation are applied with various operation conditions.

Bifurcation analysis with Direct NI

Use of direct NI can provide bifurcation diagrams consisting of consecutive collections of Poincaré dots with regard to an operation control parameter. Although this method provides only an incomplete picture regarding multiple, coexisting responses and their stability, it is still useful for providing a “brute force” means to view some possible responses and rotordynamic bifurcations. For the transient responses, the dynamic differential equations are integrated using the MATLAB[®] routine ode15s, for 300 revolution periods, and steady state is assumed to occur during the last 100 revolutions. As can be seen in Fig. 47, a bifurcation diagram, which shows the non-dimensional vertical journal motion, y/C_b , at each spin period, is plotted vs. rpm. This presentation is conducted for different parameters of imbalance eccentricity and bearing load.

As a result, lightly loaded and low unbalance cases generally show stabilized vibrations such as synchronous response over all the traversed speed range. In contrast, heavily loaded and high unbalance cases exhibit period doubling bifurcations and sub-synchronous responses at high speed ranges; all the sub-synchronous responses emerge after the dynamic unbalance force exceeds the static force (i.e., $F_{imb}/W > 1$).

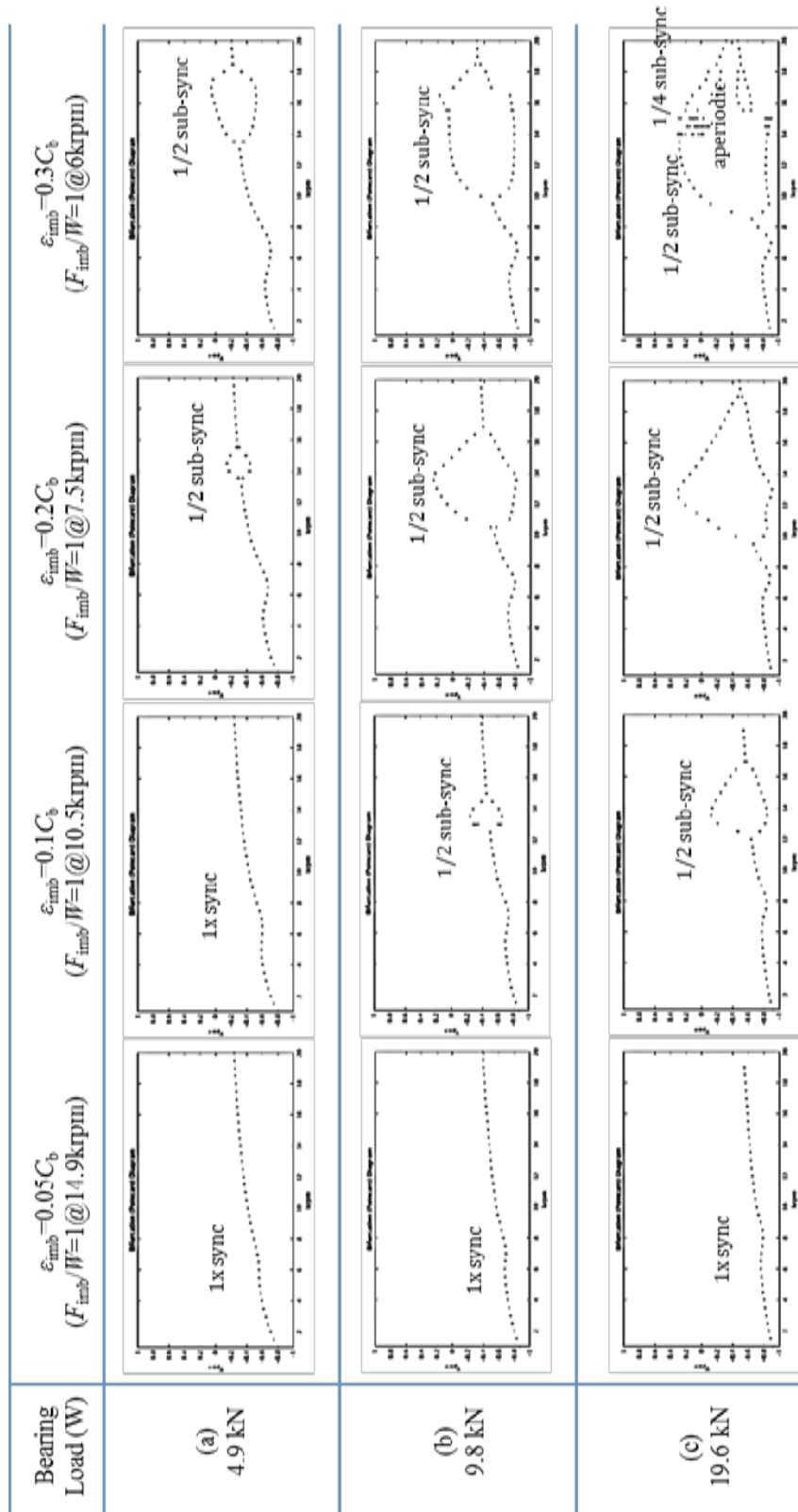


Fig. 47. Bifurcation diagrams with regards to rotor mass and imbalance eccentricity - the direct numerical integration

The cases of Fig. 47 (c), with $W=19.6\text{kN}$, have various response types such as synchronous, sub-synchronous and quasi-/aperiodic motions. For this reason, this bearing load is selected to conduct further analyses such that the bifurcation diagrams are made with different imbalance amounts ranging from $0.02C_b$ to $0.4C_b$.

Combining all the bifurcation diagrams with regards to imbalance eccentricity and spin speed yields the loci of bifurcations diagram in Fig. 48. In the diagram, it can be seen that the rotor system has only 1τ periodic response under 8krpm regardless of the amount of imbalance on the rotor. In contrast, various responses are expected at operation speeds above 8krpm . For instance, if the rotor system has a constant operating speed of 15krpm , and it accumulates unbalance due to deposits on the rotor, the system may exhibit various responses in the consecutive forms of $1\tau \rightarrow 2\tau \rightarrow 4\tau \rightarrow$ quasi-periodic/aperiodic as the accumulated unbalance force increases.

It should be noted that this result is obtained from the direct NI method so that multiple responses near the bifurcation locus are not considered. This means that the loci of bifurcations in the figure are not the only solution map for this system, but only one of the multiple possible solution maps. On the other hand, bifurcation diagrams from the shooting/arc-length continuation may provide further regions such as coexistent solutions, response stability and bifurcation scenarios.

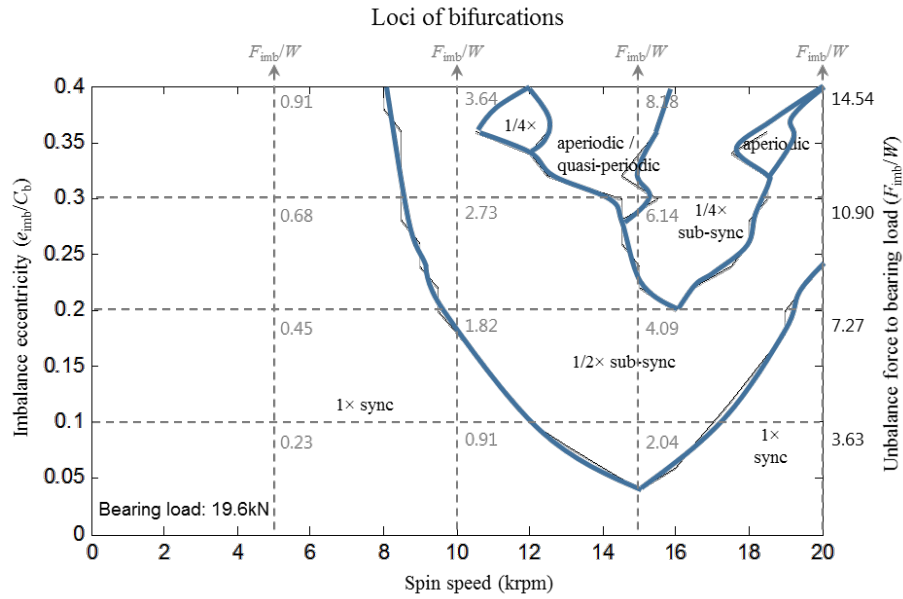


Fig. 48. Loci of bifurcation diagram

Bifurcations on run-up/run-down

The introduced shooting/arc-length continuation methods are applied to the TPJB-RGD system. The control parameter of the numerical continuation is the rotor revolution speed (rev/min), and it is incremented for each harmonic solution that is identified by the shooting method.

To illustrate the results, the maximum and minimum values of the non-dimensional vertical displacements, y/C_b , of the periodic solutions are plotted in Fig. 49. Here, the imbalance eccentricity of the disc (e_{imb}) is set as $0.3C_b$. The small windows connected to the bifurcation diagram show the orbital states of solutions at the specific sections. In case coexistent solutions are identified, all the solution states are plotted, and the stability of each solution is determined by the Floquet theory.

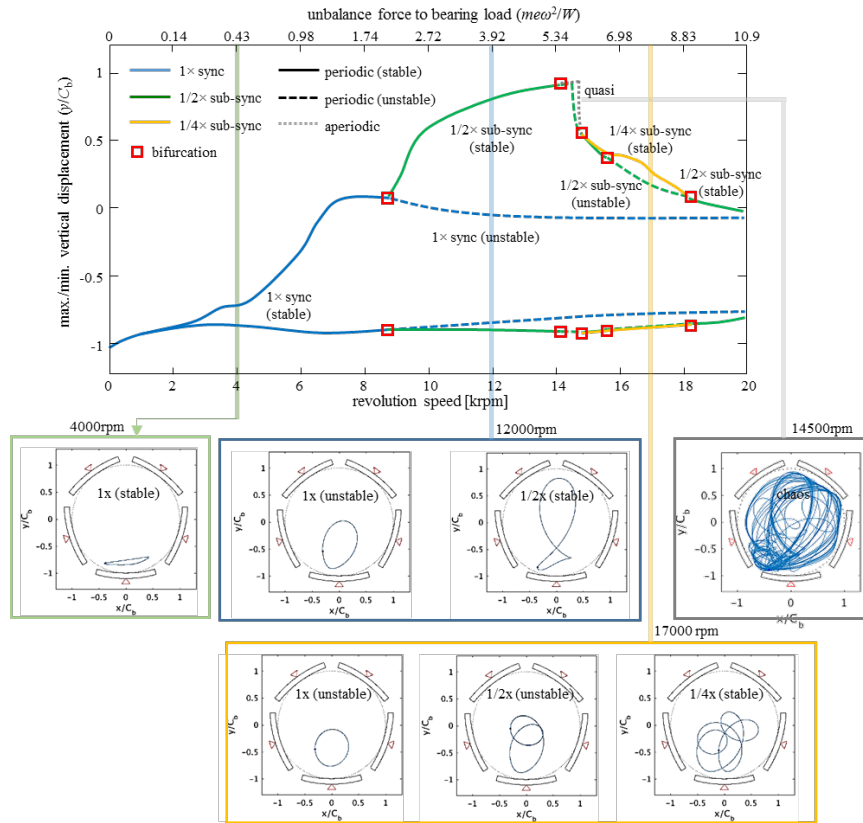


Fig. 49. Bifurcation diagram and coexistent solutions with regard to rotor revolution speed - shooting/continuation ($e_{imb}=0.3C_b$, $m_p=1/2$, $\alpha/\beta=0.5$, $\mu=13.8cP$)

Over the low spin speed range, the journal maintains a stable $1\times$ synchronous response and is statically located near the minimum clearance area. A periodic doubling bifurcation occurs at 8.7krpm, and at the same time the $1\times$ synchronous response loses its stability and a stable $1/2$ sub-synchronous response appears. The orbit of $1/2$ sub-synchronous gradually enlarges as rpm increases until 14.1krpm. Stability of the $1/2$ sub-synchronous changes to unstable with the appearance of aperiodic motion, but it returns at 14.8 krpm and the aperiodic motion disappears. Then a stable $1/4$ sub-synchronous emerges with the $1/2$ sub-synchronous (unstable), and the states last up to 18.2krpm.

Eventually, the two motions converge at 18.2krpm, and a stable $\frac{1}{2}$ sub-synchronous orbit emerges. The unstable $1\times$ sync persists over the entire speed range above the 1st bifurcation.

Bifurcations on accumulating imbalance of rotor

The balance condition of a rotor system may change over time of operation due to blade erosion or distortion, shaft bowing, misalignment, etc. [36][48]. Stopping the operation of a plant in order to balance a machine is always a very costly decision in terms of lost product. On the other hand, failure of a machine due to excessive vibration may lead to an even costlier scenario. Prediction of responses with accumulating unbalance force, during long-term operation, can provide a valuable tool for deciding if a machine should be immediately balanced or repaired.

In order to understand bifurcation scenarios with respect to accumulated imbalance eccentricity, the control parameter of the numerical continuation is set to imbalance eccentricity on the disc with the spin speed fixed at 16000rpm. Fig. 50 shows the responses in the low imbalance eccentricity ($e_{imb} < 0.06C_b$) range maintain a stable $1\times$ sync state, and then bifurcate into a new $\frac{1}{2}$ sub-synchronous response with the stability of the $1\times$ sync switched to unstable. The orbital motion of $\frac{1}{2}$ sub-synchronous gradually enlarges as imbalance increases until $0.21C_b$, which is the onset of a stable $\frac{1}{4}$ sub-synchronous. The $\frac{1}{2}$ sub-synchronous response has several saddle node bifurcations in the high imbalance condition ($e_{imb} > 0.27C_b$) so that additional orbital equilibrium states are generated. For example, when the imbalance eccentricity become $e_{imb} = 0.28C_b$, six

periodic responses: one $1\times$ sync (unstable), four $1/2$ sub-synchronous (stable/unstable) and one $1/4$ sub-synchronous (stable) coexist at the identical operating condition. The sub-synchronous responses bifurcate into an aperiodic motion after $0.38C_b$, and the unstable $1\times$ sync persists throughout the unbalance range, following the 1^{st} bifurcation.

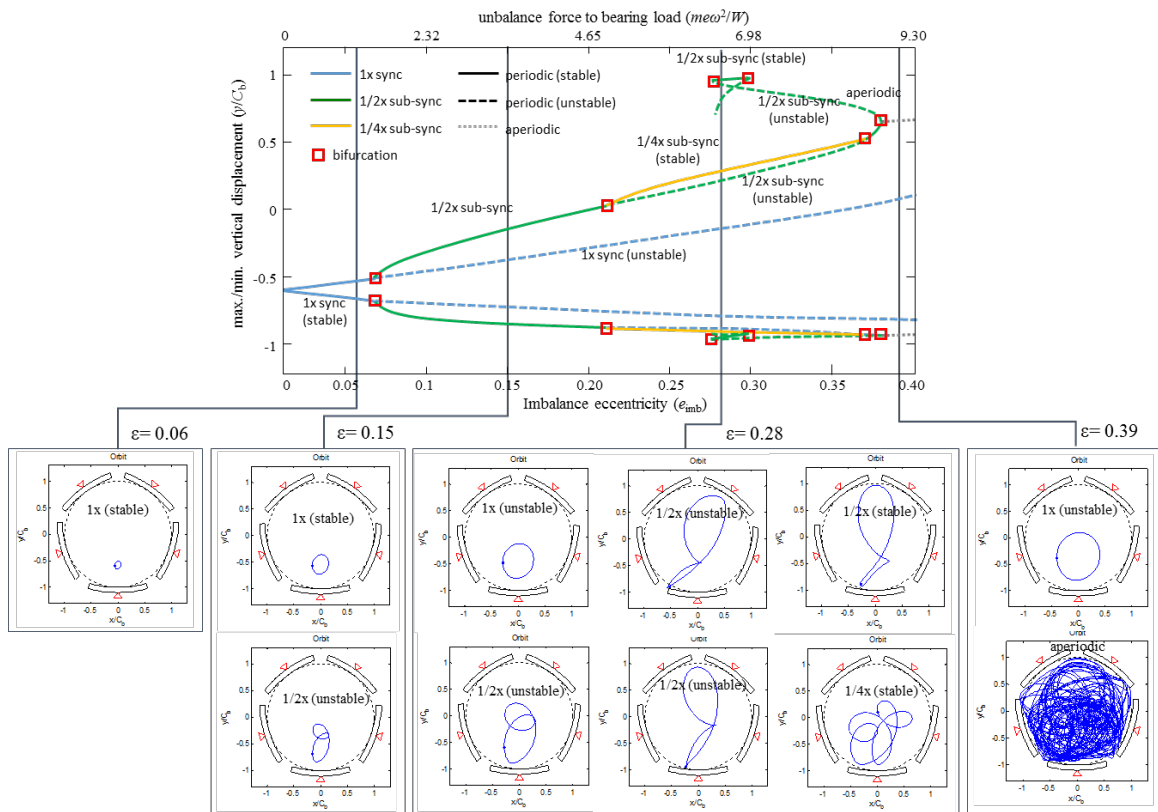


Fig. 50. Bifurcation diagram and coexistent solutions with regard to imbalance eccentricity on disc - shooting/continuation (rpm=16000, $m_p=1/2$, $\alpha/\beta=0.5$, $\mu=13.8cP$)

Effects of pad preload and pivot offset on bifurcations

In addition to the current pad preload and pivot offset parameters, i.e, case1: $m_p=1/2$, $\alpha/\beta=0.5$, three pad-pivot geometrical sets: case2: $m_p=1/2$, $\alpha/\beta=0.6$, case3: $m_p=2/3$, $\alpha/\beta=0.5$, case4: $m_p=2/3$, $\alpha/\beta=0.6$, are chosen for investigating their effects on bifurcations of TPJB-RGD system. Fig. 51 depicts the geometry of the respective pad preload and pivot offset cases.

Fig. 52 represents the results of the shooting/continuation with the pad-pivot parameter sets. In case2 ($m_p=1/2$, $\alpha/\beta=0.6$) shown in Fig. 52 (a), it is observed that significant delay of bifurcation onset to the oil whirl ($1/2$ sub-synchronous), which occurred at $0.07C_b$ with the original set, i.e. case 1, moves to $0.14C_b$. In addition, the emergence of a $1/4$ sub-synchronous response that came out of the $1/2$ sub-synchronous with periodic doubling bifurcation at $0.21C_b$, disappears over the entire unbalance range. In case3 ($m_p=2/3$, $\alpha/\beta=0.5$) shown in Fig. 52 (b), it can be seen that the bifurcation onset to oil whirl shifts only by a small amount, i.e, from $0.07C_b$ to $0.085C_b$, so the increased preload over $1/2$ seems to have only a minor stabilizing effect. However, the $1/4\times$ sub-synchronous response is observed over an extended range of unbalance, and the high vibration region of $1/2$ sub-synchronous, which was located from $0.275C_b$ in the original set, occurs at a lower amount of imbalance eccentricity. In case 4 ($m_p=2/3$, $\alpha/\beta=0.6$) shown in Fig. 52 (c), the overall bifurcation scenarios are very similar with parameter set 2, but the high vibration states of the $1/2$ sub-synchronous response is close to the results from parameter set 3. In that regard case 4 appears to act qualitatively similar to a combination of sets 2 and set 3.

Based on this overview, the pivot location plays a major role in determining the system's response states and bifurcation behavior, The preload has a significant effect on the location and existence of stable, high vibrations of the $1/2$ sub-synchronous near $e_{imb}=0.25 \sim 0.3C_b$.

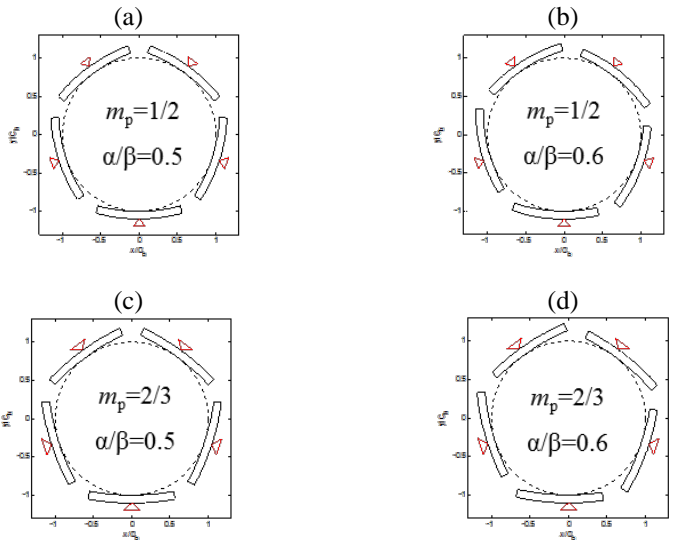


Fig. 51. Geometrical schematics of the pad-pivot parameter sets

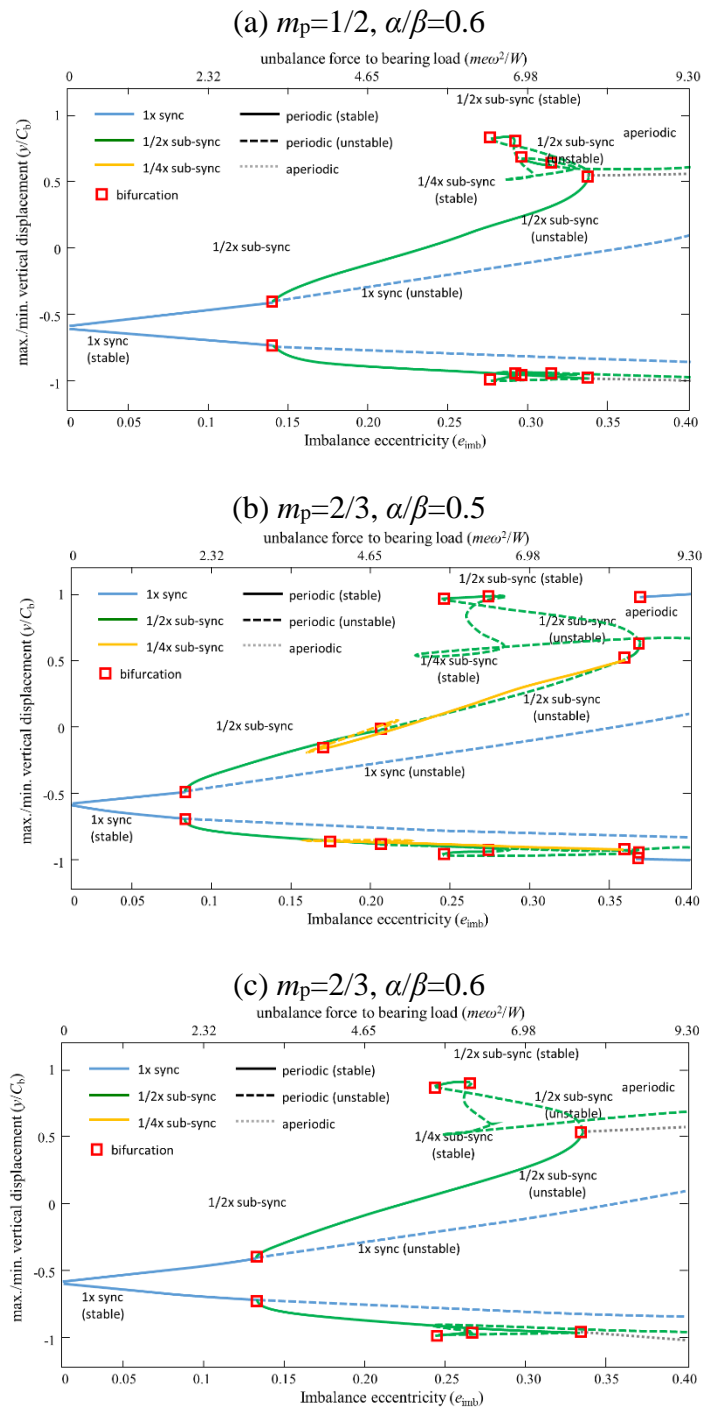


Fig. 52. Bifurcation diagrams with regards to pad preloads (m_p) and pivot offset (α/β): (a) case2 ($m_p=1/2, \alpha/\beta=0.6$), (b) case3 ($m_p=2/3, \alpha/\beta=0.5$), (c) case4 ($m_p=2/3, \alpha/\beta=0.6$)

Effects of lubricant viscosity

In addition to the lubricant viscosity parameter, $\mu=13.8\text{cP}$, utilized for all previous cases two additional viscosity values $\mu=27.0\text{cP}$ and 10.3cP , are utilized for investigating the lubricant viscosity effect on the TPJB-RGD system. The oil is assumed to be ISO VG 22 and a corresponding temperature is 45°C ($@ \mu=27.0\text{cP}$), 65°C ($@ \mu=13.8\text{cP}$) and 75°C ($@ \mu=10.3\text{cP}$), respectively. Fig. 53 shows the bifurcation diagrams with the viscosity parameters; here, $\text{rpm}=16\text{k}$.

The result with high viscosity, i.e., $\mu=27.0\text{cP}$ shown in Fig. 53 (a), shows a more stabilized response behavior over all the unbalance operation range, such that the $\frac{1}{4}$ sub-synchronous responses have disappeared, and only $1\times$ synchronous and $\frac{1}{2}$ sub-synchronous remain. In addition, the period doubling bifurcation from $1\times$ synchronous to $\frac{1}{2}$ sub-synchronous is significantly delayed from $0.07C_b$ to $0.155C_b$. The appearance span of the $\frac{1}{2}$ sub-synchronous is also reduced. In contrast, the low viscosity case holds the $\frac{1}{4}$ sub-synchronous response and extends its appearance span. The stability of the $\frac{1}{4}$ sub-synchronous turns to unstable after $0.18C_b$, and at the same unbalance level the other periodic solutions, $1\times$ synchronous and $\frac{1}{2}$ sub-synchronous, also become unstable even up to high imbalance eccentricity (although a stable $\frac{1}{2}$ sub-synchronous is identified in short range from $0.31C_b$ to $0.33C_b$). This means that a quasi-periodic response dominates above the imbalance amount ($0.18C_b$). Table 12 compares the responses for the 3 viscosity cases.

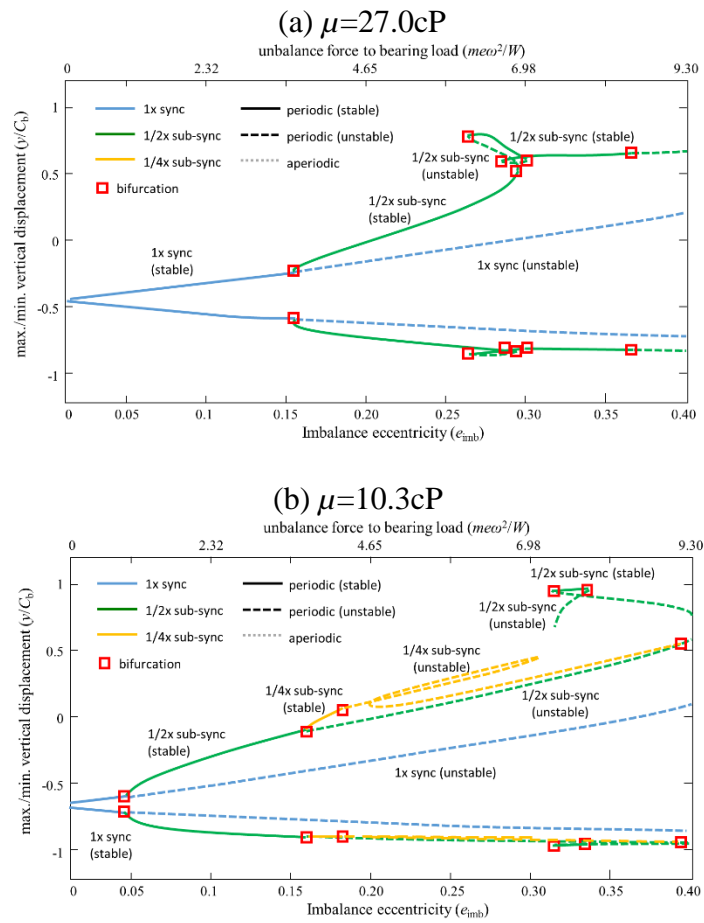


Fig. 53. Bifurcation diagrams with regards to lubricant viscosity:
(a) $\mu=27.0\text{cP}$, (b) $\mu=10.3\text{cP}$

Table 12. Bifurcation events for lubricant viscosity

Bifurcation events	$\mu=27.0\text{cP}$	$\mu=13.8\text{cP}$	$\mu=10.3\text{cP}$
onset $1 \times \text{sync} \rightarrow \frac{1}{2} \text{ sub-sync.}$	$0.155C_b$	$0.07C_b$	$0.045C_b$
appearance of $\frac{1}{4}$ sub- sync.	- (disappeared)	$0.21C_b \sim 0.37C_b$ (net: $0.16C_b$)	$0.16C_b \sim 0.395C_b$ (net: $0.235C_b$)
1 st saddle node of $\frac{1}{2}$ sub- sync.	$0.295C_b$	$0.38C_b$	$0.41C_b$

Quasi-periodic / aperiodic motions

As indicated by the above results the rotor-bearing system response may lose its periodicity and the response becomes either quasi-periodic or aperiodic. Shooting and arc-length continuation are numerical algorithms for identifying the periodic solutions, so a separate device such as Lyapunov exponents is needed to quantitatively determine the existence of quasi-periodic or chaotic motions. Based on the bifurcation diagram from the direct numerical integrations of the heavily loaded and high unbalance force in Fig. 47 (c) with $e_{imb}=0.3C_b$, the system loses its solution periodicity at high spin speed ranges, which is revealed through the accumulated Poincaré dots on the bifurcation diagram (not shown as single or a few numbers). To examine the character of the aperiodic motions, the maximum Lyapunov exponents (MLEs) are compared with the bifurcation diagram as can be seen in Fig. 54. Here, steady state is assumed to occur after 600 revolution periods, after which the MLEs are obtained by means of 600 time intervals with 0.25 revolution per interval. The MLEs are negative values for $\times 1$ synchronous and $\times 1/2$ sub-synchronous responses. Figure 13 shows that in certain operating ranges (e.g., 14.5krpm~15.5krpm and 18.5krpm), the MLEs exceed or are very close to the stability limit and the values provide further clarification to be interpreted either as quasi- or aperiodic.

Three samples at 14.5krpm, 15.5krpm, and 18.5krpm are examined in Fig. 55, which displays orbital motions, frequency spectra and Poincaré maps along with Lyapunov exponent spectra as in Ref. [35]. This approach is very helpful for identifying the response types. As can be seen in Fig. 55 (a), which was selected as a chaotic state

based on the MLE ($\lambda_{\max} = +0.008$), the orbit is obviously an aperiodic response, the corresponding Poincaré dots form a strange shape, and broadband components are observed in the frequency spectrum. In Fig. 55 (b) though the MLE is slightly above the critical boundary; $\lambda_{\max} = +0.0008$ and which implies very low chaos. It is assumed that the MLE eventually converge to zero, since the respective orbit and Poincaré represent a quasi-periodic motion. In Fig. 55 (c), the response which has $\lambda_{\max} = -0.005$ represents periodic motion, and it is also confirmed as an n-periodic response by the other response displays.

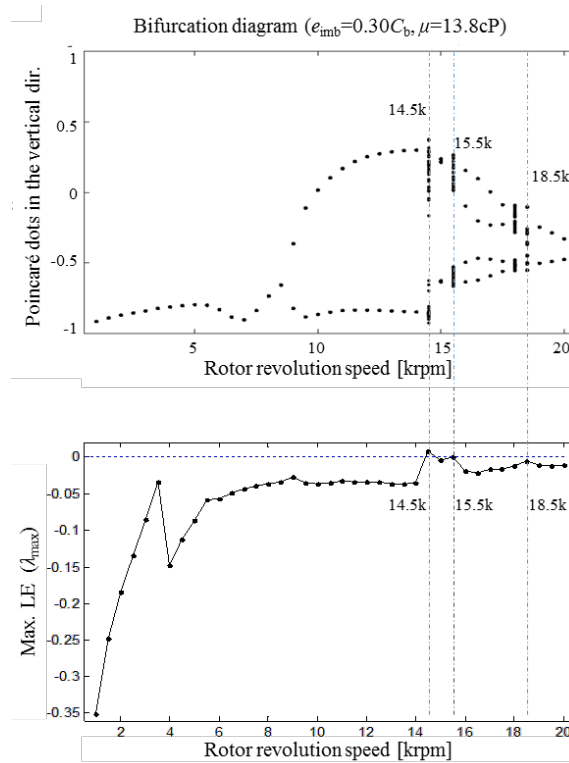


Fig. 54. Bifurcation diagram (Poincaré sections) vs. MLE (λ_{\max}) with regard to spin speed ($W=19.6kN, e_{imb}=0.3C_b, \mu=13.8cP$)

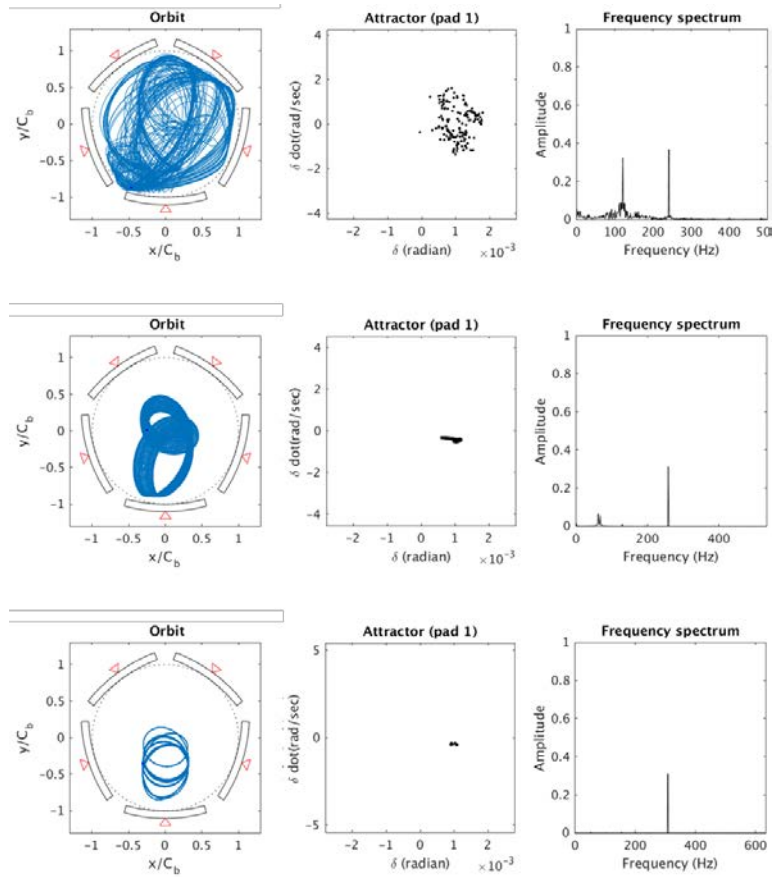


Fig. 55. Orbits, attractors and frequency spectra: (a) rpm=14.5k, (b) rpm=15.5k, (c) rpm=18.5k

Summary of Results

The nonlinear response and bifurcations of a rotor supported by five-pad TPJBs are examined utilizing highly efficient computational algorithms. TPJBs are well known as highly stable when vibration responses are small, but the numerical study shows sub-synchronous-, aperiodic- motions, bifurcations and coexistent solutions can occur under heavily statically loaded and highly dynamically unbalanced conditions. Application of

non-autonomous shooting/continuation algorithms implemented with deflation and parallel computing for execution acceleration, exhibited various nonlinear behaviors with regards to imbalance eccentricity and spin speed variations. A parametric study with pad geometry confirmed that the pivot location significantly influences nonlinear aspects such that periodic doubling bifurcations and high vibration states are suppressed by locating the pivot point a little after the mid-plane of the pads (i.e., $\alpha/\beta > 0.5$). On the other hand, the pad preload influences onsets of stable high amplitude $1/2$ sub-synchronous responses. Simulations confirmed that lubricant viscosity has a major role on overall response behavior such that higher viscosity tends to suppress the appearance of sub-synchronous responses and lower viscosity tends to cause quasi-periodic motion. Lyapunov exponents can explicitly differentiate n -periodic-, quasi-periodic, chaotic responses in TPJBs. Future investigation for analytical bifurcations and nonlinear behaviors in TPJB systems will include a flexible, multi mass rotor models with a modal reduction technique.

CHAPTER VI
NUMERICAL NONLINEAR ANALYSIS OF FLEXIBLE, MULTI MASS ROTOR
BEAM MODELS

Introduction to Large Order Rotor Systems

Most of the rotating machineries in industry are not sample as a “Jeffcott” rotor but are consisted of multiple shafts and multiple discs, therefore, the structural vibrations and gyroscopic effects should be taken into consideration for the motions of the machine. The finite element based rotor beam model with lumped masses and lumped rotational inertias in the finite nodes is typical approach to illustrate the general, flexible, multi-mass rotor shaft for numerical analysis. Nonlinear analysis of large-order systems usually demands lots of computation time and resources to incorporate the large number of state condition in both the rotor-beam and bearing models. Hence, it becomes necessary to combine with a model condensation technique such as real-/complex-eigenvector modal reduction, component mode synthesis and Guyan reduction, which give computational advantages by choosing important modes out of total degree of freedom (DOF).[7]

Component Mode Synthesis (CMS) method has been introduced as one very suitable model reduction scheme for nonlinear system with the sense that 1) CMS lends itself for transient analysis, 2) it can be directly applied to multiple shafts with multiple interconnections, 3) it can be associated with the finite element method [49]. In the procedure, it remains nonlinear associated dynamic components (i.e. constrained normal

modes) in physical coordinate and transfer the other components (i.e. static modes) to modal coordinate and substantially reduce degree of freedom of the modal elements. In a series of research from Nelson et al. [50-52] and Craig et al. [53,54], CMS had been proven as an accurate dimension reduction method for stability and transient analysis. Meanwhile, Sundararajan and Noah [21] first attempted to combine CMS and shooting/continuation methods to analyze a large order nonlinear rotor-bearing system. In their study, a six-node shaft beam model supported on plain journal bearings was used as a mechanical model; the model has 24 DOF and the fluid film pressures on supports are obtained using the short bearing approximation. They obtained the results of unbalance response amplitude with respect to spin speed and determined local stability based on Floquet theory. Although they have introduced the algorithm that is capable of identifying multiple response states and their stability analysis, another related research, which is following their approach, is seldom reported yet. The objective of this study is to extend the capability of the introduced numerical algorithms (shooting/continuation with Deflation and the parallel computing) to industrial applications such as turbochargers and steam turbine compressors as described in Table 13.

Table 13. Mechanical models of large order system

	Example 1	Example 2
Rotor beam	F.E. turbocharger rotor with 14 nodes	F.E. eight-stage compressor with 35 nodes
Bearing	F.E. Two floating ring bearings	F.E. two tilt pad journal bearings
Total DOF	$56 + 6 = 62$ DOF	$140 + 10 = 150$ DOF
Total state element	$112 + 10 = 122$ state elements	$280 + 20 = 300$ state elements

Shooting Method with a Model Reduction Technique

In this research, fixed-interface CMS is employed to condense the large-order systems. The CMS is applied to both the numerical integration and the shooting and continuation methods. The followings are mathematical formulations for model reduction steps prior to apply the shooting method; the mathematical derivations widely refers to Sundararajan's dissertation [49].

Step 1: System Condensation

From finite element formulation, rotor system may have an equation in a form of,

$$\mathbf{M}\ddot{\mathbf{x}} + \mathbf{C}\dot{\mathbf{x}} + \mathbf{K}\mathbf{x} = \mathbf{F} \quad (55)$$

Equation (55) can be divided and re-ordered with boundary (nonlinear) coordinate \mathbf{x}_b , and interior (static) coordinate, \mathbf{x}_i

$$\begin{bmatrix} \mathbf{M}_{bb} & \mathbf{M}_{bi} \\ \mathbf{M}_{ib} & \mathbf{M}_{ii} \end{bmatrix} \begin{Bmatrix} \ddot{\mathbf{x}}_b \\ \ddot{\mathbf{x}}_i \end{Bmatrix} + \begin{bmatrix} \mathbf{C}_{bb} & \mathbf{C}_{bi} \\ \mathbf{C}_{ib} & \mathbf{C}_{ii} \end{bmatrix} \begin{Bmatrix} \dot{\mathbf{x}}_b \\ \dot{\mathbf{x}}_i \end{Bmatrix} + \begin{bmatrix} \mathbf{K}_{bb} & \mathbf{K}_{bi} \\ \mathbf{K}_{ib} & \mathbf{K}_{ii} \end{bmatrix} \begin{Bmatrix} \mathbf{x}_b \\ \mathbf{x}_i \end{Bmatrix} = \begin{Bmatrix} \mathbf{F}_b \\ \mathbf{F}_i \end{Bmatrix} + \begin{Bmatrix} \mathbf{F}_{ns,b} \\ \mathbf{F}_{ns,i} \end{Bmatrix} \quad (56)$$

where \mathbf{x}_b is boundary (nonlinear) coordinate, \mathbf{x}_i is interior (static) coordinate, F_b is nonlinear force, F_i is force acting at interior coordinate (e.g. unbalance force). $F_{ns,b}$ and $F_{ns,i}$ are non-symmetric element forces from bearing, seal, damping, and other properties at boundary and interior coordinate, respectively. Since real mode CMS is utilized in this study, any non-symmetric terms in matrix \mathbf{C} and \mathbf{K} are located in right hand side of Eq. (56).

By selecting interior coordinate components and then obtaining the free-vibration problem.

$$\mathbf{M}_{ii}\ddot{\mathbf{x}}_i + \mathbf{C}_{ii}\dot{\mathbf{x}}_i + \mathbf{K}_{ii}\mathbf{x}_i = 0 \quad (57)$$

Note that all element in \mathbf{M}_{ii} , \mathbf{C}_{ii} , \mathbf{K}_{ii} matrices are symmetric, and \mathbf{C}_{ii} is zero since system does not have linear damping component.

The normal modes of interior coordinates can be represented with eigenvector matrix \mathbf{A} and modal vector \mathbf{q} ,

$$\mathbf{x}_{i_normal} = \mathbf{A}\mathbf{q}_i \quad (58)$$

The static modes of interior coordinates can be represented as,

$$\mathbf{x}_{i_static} = -\mathbf{K}_{ii}^{-1}\mathbf{K}_{ib}\mathbf{x}_b \quad (59)$$

Then, transformation of the coordinates can be expressed as,

$$\begin{Bmatrix} \mathbf{x}_b \\ \mathbf{x}_i \end{Bmatrix} = \begin{bmatrix} \mathbf{I}_{bb} & \mathbf{O}_{bi} \\ \mathbf{B}_{ib} & \mathbf{A}_{ii} \end{bmatrix} \begin{Bmatrix} \mathbf{x}_b \\ \mathbf{q}_i \end{Bmatrix} = \mathbf{D} \begin{Bmatrix} \mathbf{x}_b \\ \mathbf{q}_i \end{Bmatrix} \quad (60)$$

Using a transformation matrix \mathbf{D} in Eq. (59) and pre-multiplying \mathbf{D}^T , the system equation yields,

$$\begin{bmatrix} \mathbf{M}_{11} & \mathbf{M}_{12} \\ \mathbf{M}_{21} & \mathbf{M}_{22} \end{bmatrix} \begin{Bmatrix} \dot{\mathbf{x}}_b \\ \dot{\mathbf{q}} \end{Bmatrix} + \begin{bmatrix} \mathbf{C}_{11} & \mathbf{C}_{12} \\ \mathbf{C}_{21} & \mathbf{C}_{22} \end{bmatrix} \begin{Bmatrix} \dot{\mathbf{x}}_b \\ \dot{\mathbf{q}} \end{Bmatrix} + \begin{bmatrix} \mathbf{K}_{11} & \mathbf{K}_{12} \\ \mathbf{K}_{21} & \mathbf{K}_{22} \end{bmatrix} \begin{Bmatrix} \mathbf{x}_b \\ \mathbf{q} \end{Bmatrix} = \begin{Bmatrix} \mathbf{F}_1 \\ \mathbf{F}_2 \end{Bmatrix} \quad (61)$$

$$\bar{\mathbf{M}}\ddot{\mathbf{x}}_q + \bar{\mathbf{C}}\dot{\mathbf{x}}_q + \bar{\mathbf{K}}\mathbf{x}_q = \bar{\mathbf{F}} \quad (62)$$

By selecting important modes, which is normally low natural frequency related modes, total degree of freedom of the system equation can be remarkably reduced. The reduced DOF consists of number of nonlinear forces and retained number of modes.

First order form can be expressed as,

$$\begin{bmatrix} 0 & \bar{\mathbf{M}} \\ \bar{\mathbf{M}} & \mathbf{C} \end{bmatrix} \dot{\mathbf{h}} + \begin{bmatrix} -\bar{\mathbf{M}} & 0 \\ 0 & \bar{\mathbf{K}} \end{bmatrix} \mathbf{h} = \begin{bmatrix} 0 \\ \bar{\mathbf{F}} \end{bmatrix}, \text{ where } \mathbf{h} = \begin{bmatrix} \dot{\mathbf{x}}_q \\ \mathbf{x}_q \end{bmatrix} = \begin{bmatrix} \dot{\mathbf{x}}_b \\ \dot{\mathbf{q}}_b \\ \mathbf{x}_b \\ \mathbf{q}_b \end{bmatrix} \quad (63)$$

$$\mathbf{A} \dot{\mathbf{h}} + \mathbf{B} \mathbf{h} = \tilde{\mathbf{F}} \quad (64)$$

For numerical integration of Eq. (64), it can be re-written as,

$$\dot{\mathbf{h}}(\ddot{\mathbf{x}}_b, \ddot{\mathbf{q}}, \dot{\mathbf{x}}_b, \dot{\mathbf{q}}) = -\mathbf{A}^{-1} \mathbf{B} \mathbf{h}(\dot{\mathbf{x}}_b, \dot{\mathbf{q}}, \mathbf{x}_b, \mathbf{q}) + \mathbf{A}^{-1} \tilde{\mathbf{F}}(t, \mathbf{x}, \dot{\mathbf{x}}, \dot{\theta}) \quad (65)$$

Step 2: Non-dimensionalization

Non-dimensionalize Eq. (65) along with,

$$\bar{\mathbf{x}}_b = \mathbf{x}_b / C_b, \quad \bar{\mathbf{q}} = \mathbf{q} / C_b, \quad \frac{d}{dt} = \omega_j \frac{d}{d\tau}$$

to obtain,

$$\begin{Bmatrix} C_b \omega_j^2 \bar{\mathbf{x}}_b'' \\ C_b \omega_j^2 \bar{\mathbf{q}}'' \\ C_b \omega_j \bar{\mathbf{x}}_b' \\ C_b \omega_j \bar{\mathbf{q}}' \end{Bmatrix} = -\mathbf{A}^{-1} \mathbf{B} \begin{Bmatrix} C_b \omega_j \bar{\mathbf{x}}_b' \\ C_b \omega_j \bar{\mathbf{q}}' \\ C_b \bar{\mathbf{x}}_b \\ C_b \bar{\mathbf{q}} \end{Bmatrix} + \mathbf{A}^{-1} \tilde{\mathbf{F}}(t, \mathbf{x}, \dot{\mathbf{x}}, \dot{\theta}) \quad (66)$$

$$\left[\begin{array}{c|c} C_b \omega_j^2 & 0 \\ \hline 0 & C_b \omega_j \end{array} \right] \begin{Bmatrix} \bar{\mathbf{x}}_b'' \\ \bar{\mathbf{q}}'' \\ \bar{\mathbf{x}}_b' \\ \bar{\mathbf{q}}' \end{Bmatrix} = -\mathbf{A}^{-1} \mathbf{B} \left[\begin{array}{c|c} C_b \omega_j & 0 \\ \hline 0 & C_b \end{array} \right] \begin{Bmatrix} \bar{\mathbf{x}}_b' \\ \bar{\mathbf{q}}' \\ \bar{\mathbf{x}}_b \\ \bar{\mathbf{q}} \end{Bmatrix} + \mathbf{A}^{-1} \tilde{\mathbf{F}}(t, \mathbf{x}, \dot{\mathbf{x}}, \dot{\theta})$$

$$\begin{Bmatrix} \bar{\mathbf{x}}_b'' \\ \bar{\mathbf{q}}'' \\ \bar{\mathbf{x}}_b' \\ \bar{\mathbf{q}}' \end{Bmatrix} = - \left[\begin{array}{c|c} C_b \omega_j^2 & 0 \\ \hline 0 & C_b \omega_j \end{array} \right]^{-1} \mathbf{A}^{-1} \mathbf{B} \left[\begin{array}{c|c} C_b \omega_j & 0 \\ \hline 0 & C_b \end{array} \right] \begin{Bmatrix} \bar{\mathbf{x}}_b' \\ \bar{\mathbf{q}}' \\ \bar{\mathbf{x}}_b \\ \bar{\mathbf{q}} \end{Bmatrix} + \left[\begin{array}{c|c} C_b \omega_j^2 & 0 \\ \hline 0 & C_b \omega_j \end{array} \right]^{-1} \mathbf{A}^{-1} \tilde{\mathbf{F}}(t, \mathbf{x}, \dot{\mathbf{x}}, \dot{\theta})$$

In order to obtain the force vector $\tilde{F}(t, \mathbf{x}, \dot{\mathbf{x}})$ during numerical integrations, the state vector $(\dot{\bar{\mathbf{x}}}_b, \dot{\mathbf{q}}, \bar{\mathbf{x}}_b, \mathbf{q})$ in the condensed coordinate should be converted to physical coordinate $(\dot{\mathbf{x}}, \dot{\boldsymbol{\theta}}, \mathbf{x}, \boldsymbol{\theta})$ at each time segment.

Step 3: Initial Guess of Generation Production

The initial state vector for shooting is consist of two different domains such as physical coordinate and modal coordinate. In physical coordinate, position and velocity of rotor at nonlinear bearing locations, $\bar{\mathbf{x}}_b, \dot{\bar{\mathbf{x}}}_b$ are randomly produced guesses within the clearance of each bearing. In addition to this, modal coordinate state vector $\bar{\mathbf{q}}, \dot{\bar{\mathbf{q}}}$ is also randomly generated, but it has a post process, which reorders $\bar{\mathbf{q}}$ elements associated with higher modes to be decremented.

Step 4: Begin Shooting-CMS Procedure

Using a group of initial guess, shooting and continuation with CMS can begin the solution search procedure.

Numerical Example 1: Turbocharger Supported by FRBs

Model Description

A turbocharger is a very popular rotor-bearing application for down-sized automotive engines; it collects exhaust gas to compress intake air and supplies the high pressurized air to the engine combustor. Automotive turbochargers normally run in very high speeds condition (e.g, 150krpm to 350 krpm) that is far beyond first critical speed so that limit cycles and various nonlinear oscillations are assumed to be observed in operations. This study employs a set of turbocharger parameters used in Ref. [55] and Fig. 56 depicts the schematic of the turbocharger rotor. In order to model the single-stage turbocharger, a 14-station Euler beam with the lumped masses and inertias is built based on the mechanical parameters in Table 14 and Table 15. Fig. 57 depicts the finite element rotor model. Since the reference did not provide FRB parameters, a set of FRB parameters is employed from other reference [41]; the bearing diameter is not aligned to the shaft diameter, the values are modified proportionally to the shaft diameter. Table 16 shows the FRB parameters used in this study.

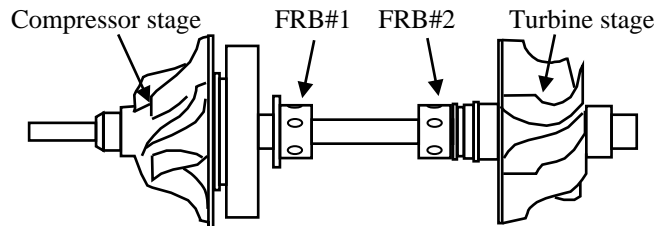


Fig. 56. Schematics of turbocharger rotor model in Ref. [55]

Table 14. Parameters of the rotor shaft

#	Length [mm]	Inner Shaft			Outer Shaft		
		Diameter [mm]	Density [kg/m ³]	Young's modulus [GPa]	Diameter [mm]	Density [kg/m ³]	Young's modulus [GPa]
1	10.0	4.1	7800	200			
2	4.5	4.1	7800	200	6.0	2700	-
3	15.2	4.1	7800	200	10.0	2700	-
4	6.0	4.1	7800	200	25.0	2700	-
5	7.1	8.0	7800	200			
6	9.5	6.2	7800	200			
7	12.65	6.0	7800	200			
8	12.5	6.0	7800	200			
9	6.65	6.0	7800	200			
10	11.2	9.9	7800	200			
11	6.6	14.2	7800	200			
12	9.6	11.0	7800	200			
13	5.0	7.0	7800	200			
14	0.0	0.0	7800	200			

Table 15. Parameters of the rigid disks

	station #	Mass [kg]	Transverse Inertia moment I_T [kgm ²]	Polar inertia moment I_p [kgm ²]
Impeller	4	0.013328	1.2740×10^{-6}	2.1560×10^{-6}
Turbine	12	0.043414	3.1360×10^{-6}	5.8800×10^{-6}

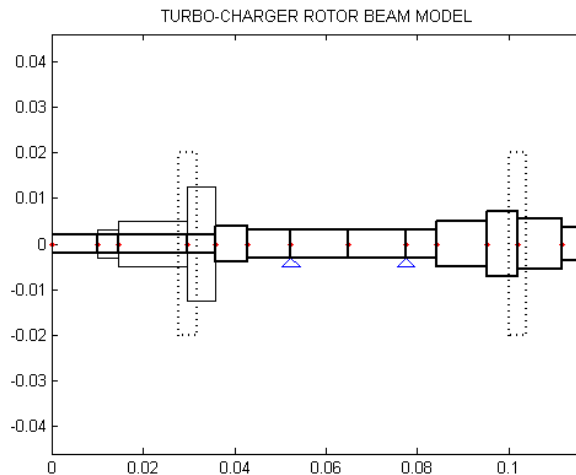


Fig. 57. F.E. Turbo-charger model with 14 stations

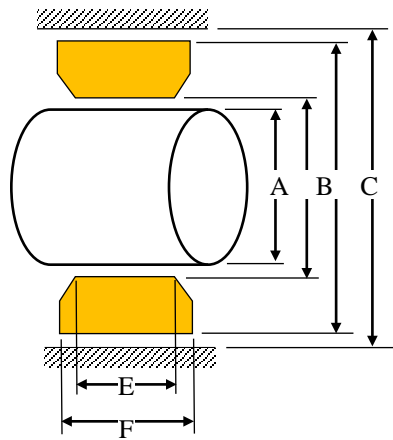


Fig. 58. Schematics of floating ring bearing

Table 16. Floating Ring Bearing Dimensions

	Parameter	mm
A	Journal diameter	6.000
B	Ring Inner Diameter	6.018
C	Ring Outer Diameter	9.239
D	Bearing Diameter	9.289
E	Inner Film Length	4.588
F	Outer Film Length	5.891

Response from Reduced System (Verification with Full DOF)

Instead of the full DOF turbocharger beam model, a reduced DOF model utilized in the numerical investigation. To rely on the reduced DOF model, a comparison with the results from full DOF is conducted; the reduced turbocharger beam retains 10 DOF out of 56 DOF for the beam elements, here, 4 DOF is associated to lateral and vertical movements of shaft at bearing positions, and the other 6 DOF exists in the modal coordinate. Besides, the nonlinear coordinates associated three ring movements (i.e., vertical, lateral and rotational) are remained at each bearing position. Hence, the reduced finite turbocharger model has total 16 DOF. The direct numerical integrations are performed with the two different DOF conditions (Full: 62 DOF vs. Reduced: 16 DOF). For the transient response, the dynamic differential equations are integrated using a

commercial software, MATLAB[®] routine ode15s, for 400 revolution periods, and the response was collected for last 100 revolutions; here, the spin speed is 30,000rpm. Fig. 59 shows the time transient numerical integration results from the two systems, and the result agrees well with each other. Other calculated results, not presented in this paper, confirm the reliability of the reduced system.

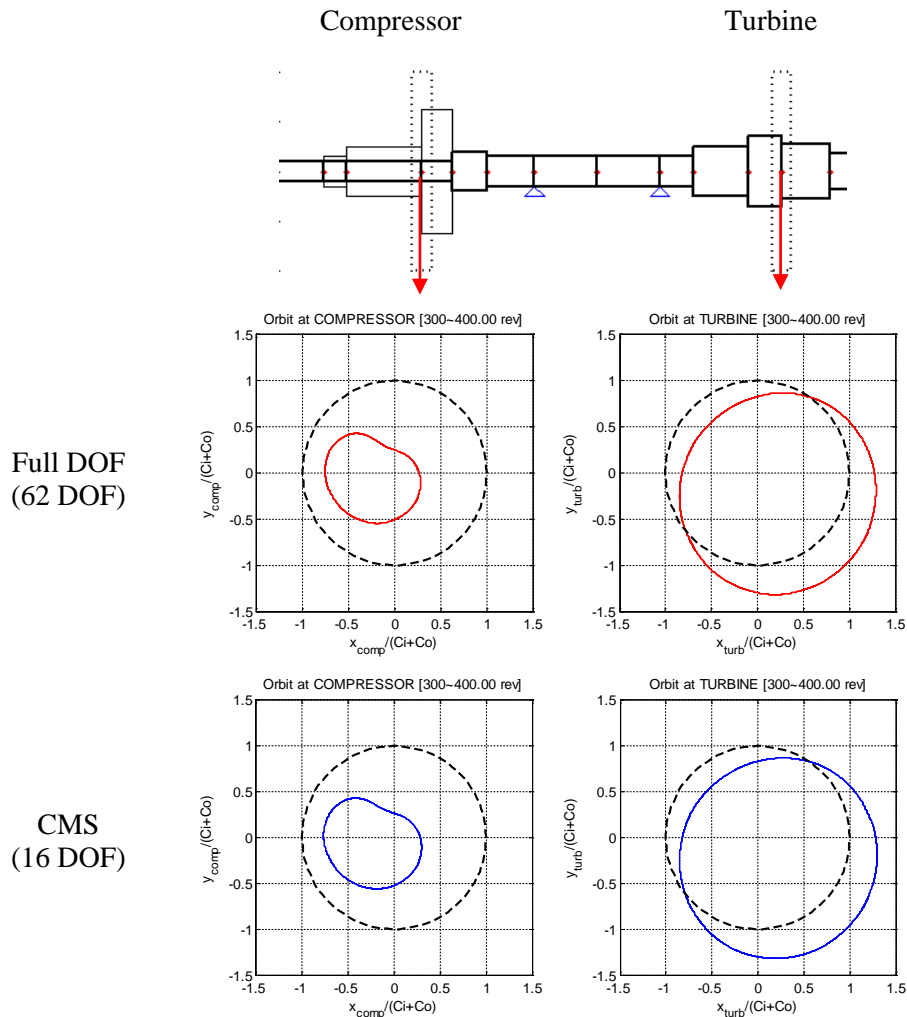


Fig. 59. Orbits comparison at compressor and turbine: Full DOF (62 DOF) vs. CMS (16 DOF)

Autonomous Shooting with CMS

Turbocharger rotors commonly combine with fully-/semi- floating ring bearings. As discussed in Chapter 3, self-excited nature in FRBs has strong nonlinearity, so various nonlinear behaviors are observed. In this study, the finite turbocharger model is assumed as fully balanced, so the structural vibrations incorporated with the nonlinear bearing force are to be focused; i.e. autonomous responses.

Fig. 60 shows the coexisting multiple steady state responses at compressor and turbine stages determined by the autonomous shooting method at a speed of 28 krpm with CMS. The stability of each response is determined using the Floquet theory; three periodic solutions (PS) are identified such as one unstable (PS 2) and two stables (PS 1 and PS 3). These results imply that the one unstable solutions (PS 2) will ultimately be attracted to one of the stable solutions (PS 1 or PS 3).

Bifurcations Results using Arc-Length Continuation with CMS

As shown in Fig. 61, the numerical continuation provides a bifurcation diagram, which presents non-dimensionalized maximum and minimum vertical positions of the shaft center at FRB #2 (i.e., \max/\min of $y_j C_o / (C_i + C_o)$) with respect to the bifurcation parameter (i.e., rpm) as in Fig. 61(a) and corresponding non-dimensionalized period of the limit cycle (i.e., τ/τ_s , where τ_s is spinning period 2π) as in Fig. 61(b). As the rotor speed increased, the equilibrium position (EP) loses its linear stability at Hopf bifurcation and turns to a periodic (limit cycle) response. The system has an N-S bifurcation after undergoing the Hopf bifurcation. After the first N-S bifurcation, the

response frequently undergoes another N-S bifurcations so that additional frequency components are removed or emerge at each N-S. When the orbit has a form of periodic response (i.e., closed orbit), the period of solution is disconnected from the previously found periodic solution as in Fig. 61(b). Fig. 62 depicts the coexistent periodic responses and their stability at 10,600 rpm.

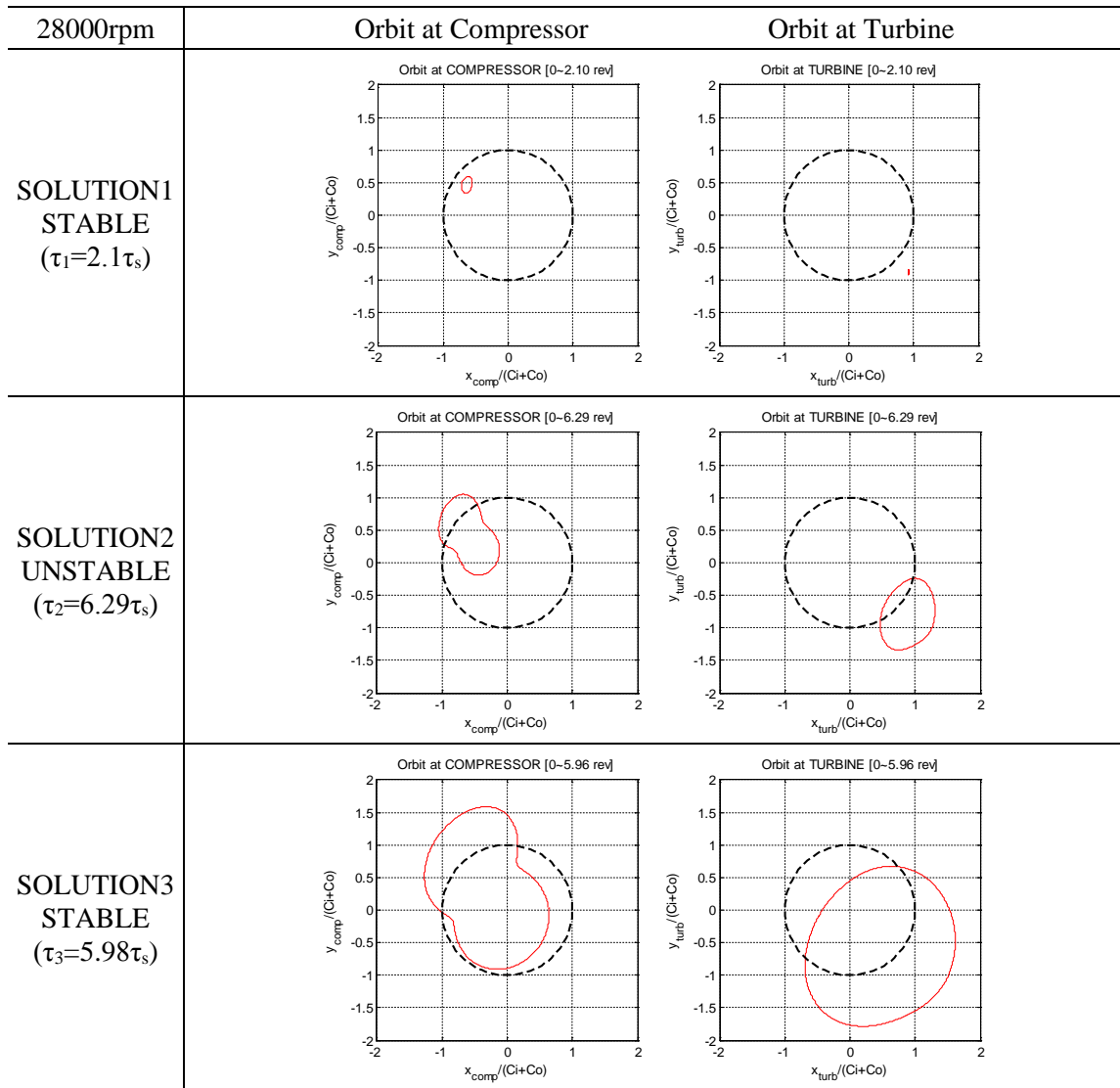


Fig. 60. Whirl Orbits at Compressor and Turbine

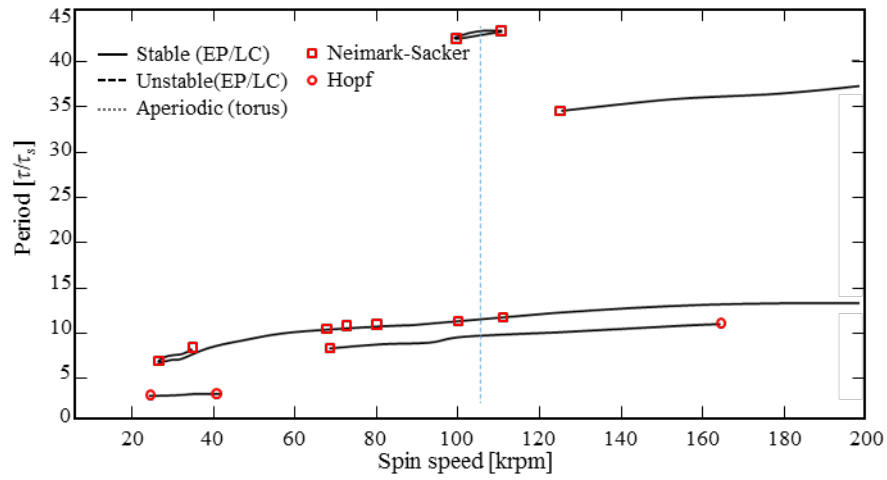
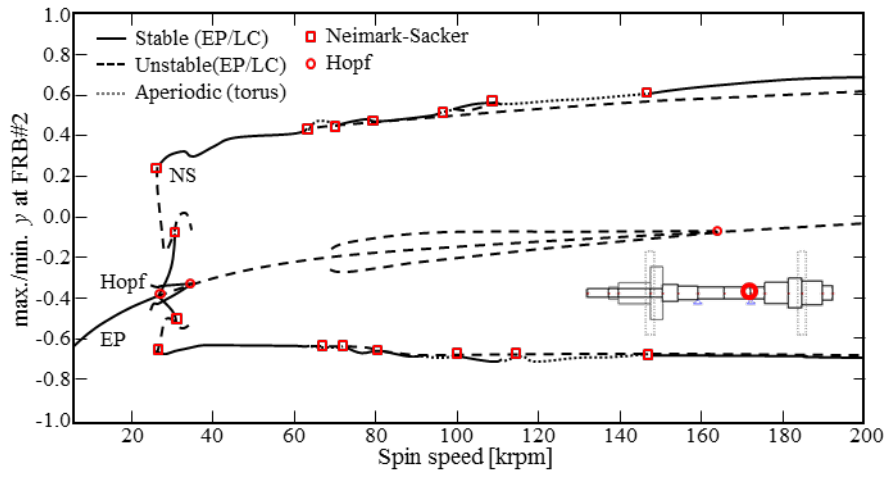


Fig. 61. Bifurcation diagram: maximum/minimum of vertical displacement at FRB #2

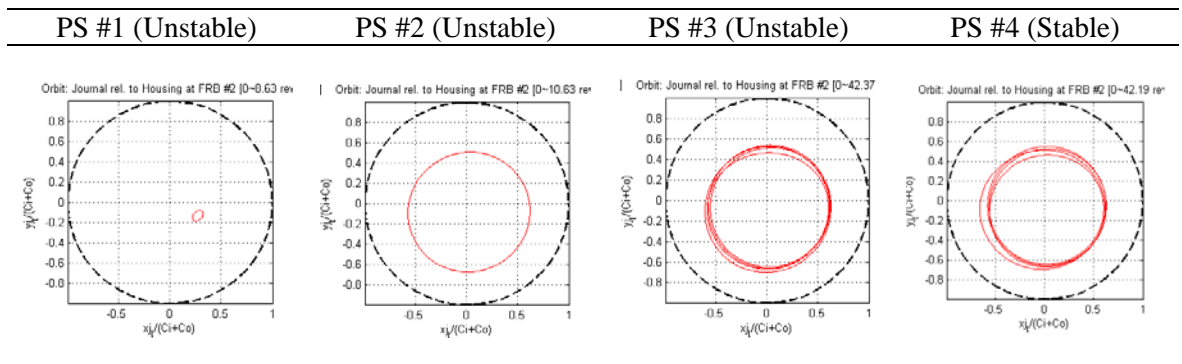


Fig. 62. Identified journal orbits (rel. to housing) at FRB #2 (106000rpm)

Jump between Multiple Responses Due to Base Excitation

Since multiple steady state responses can coexist at the same rpm, and the same imbalance amount; it may be speculated that one response state could potentially switch to the other if a disturbance is sufficiently strong to force the original state to jump out of its current basin of attraction (BOA). In reality, turbochargers are used in automobiles so that a sudden disturbance, for instance, speed bumps on roads, may induce response jumps in operation. It would be beneficial for developers/operators to anticipate the response uncertainty.

In order to simulate this phenomenon, an impulsive, vertical base excitation is applied to the two FRB housings over a very short period while the turbocharger is operating within one steady state orbits. Fig. 63 depicts the scenario of sudden bump to the turbocharger. The sudden base movements cause external force term to the outer film, and if the force is enough to escape the current BOA in phase space, the orbit may converge to another response state.

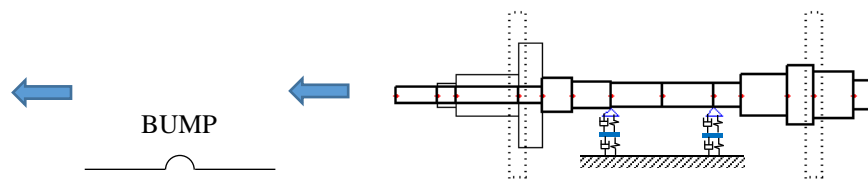


Fig. 63. Illustration of a sudden bump

The displacement of the FRB housing can be expressed with a characteristic frequency of base motion and its harmonics.

$$y_b(t) = Y_o \left\{ \frac{\tau_p}{T_f} + \sum_{n=1}^{\infty} \frac{2}{n\pi} \sin\left(\frac{n\pi\tau_p}{T_f}\right) \cos\left(\frac{2n\pi}{T_f}t\right) \right\} \quad (67)$$

Jump phenomenon between two stable responses was tested as shown in Fig. 64; blue colored orbits represent initial states before the bump and red colored orbits represent response states after the bump.

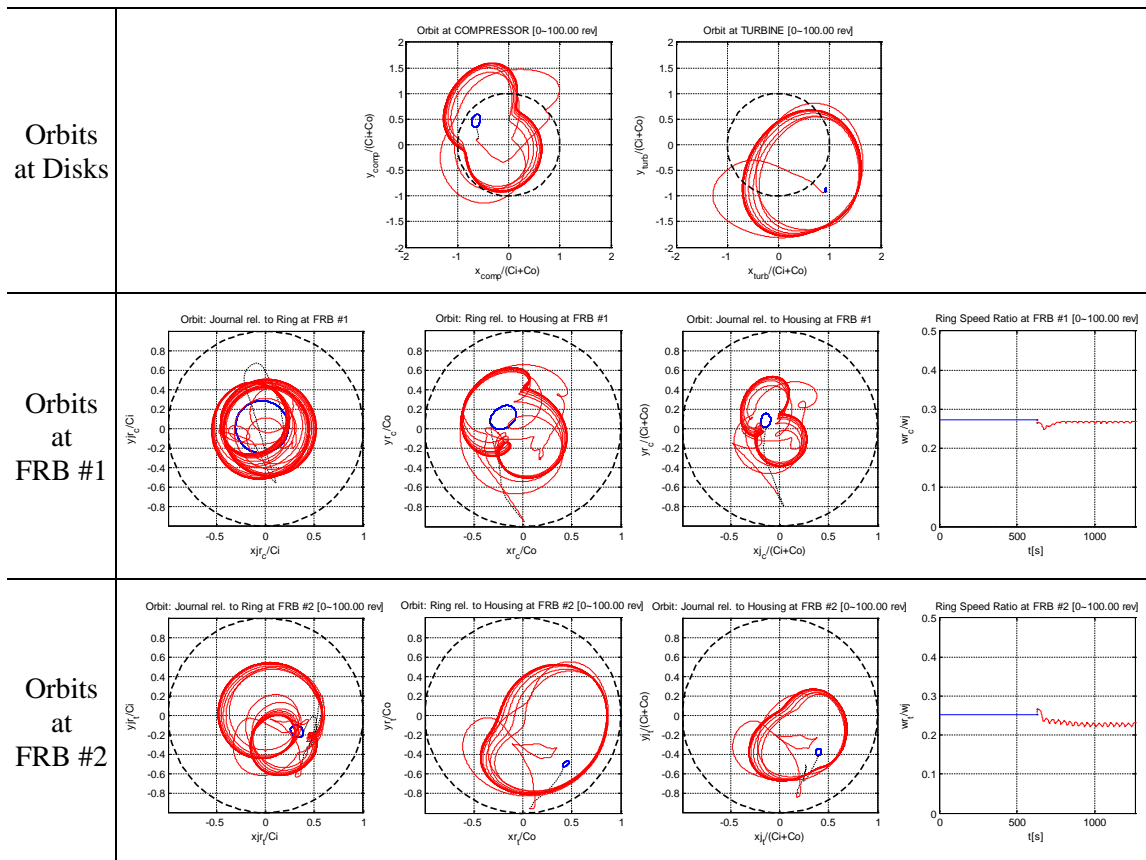


Fig. 64. Jump phenomenon between stable orbits: response before bump (blue) → response after bump (red)

Synchronization

In industry, engineers have observed oil/gas whirls due to the self-excited nonlinear characteristics of fluid film bearings. One useful treatment for the problem is that properly added intentional imbalance can quench the large sub-synchronous orbit, i.e., synchronization. A numerical investigation of the synchronization is conducted for the turbocharger supported by FRBs. The imbalance amount (e_{imb}) is added with various eccentricities on the compressor stage. Fig. 65 depicts the orbital motion and corresponding frequency spectrum at 30,000rpm for each e_{imb} amount. As the imbalance eccentricity increases, the limit cycle changes to $1\times$ synchronous at $e_{imb}=0.1C_o$, then it goes into a quasi-periodic response. As can be seen in Fig. 66, low frequency components are suddenly disappeared at $e_{imb}=0.1C_o$ and only the $\times 1$ frequency component is remained. The orbital motions in Fig. 67 also describe the sudden transition between the quasi-periodic at $e_{imb}=0.09C_o$ and the synchronous at $e_{imb}=0.1C_o$ due to synchronization effect.

Chaotic Motion in Turbo-Charger

From the previous study on rigid rotor supported by FRB, chaotic motion has occurred in case of low rates of the L/D ratio. The TC rotor was tested with the condition of 0.25 L/D ratio and $e_{imb}=0.1C_o$, as a results, chaotic motions are found near 20,000rpm. In Fig. 68, the chaotic orbits and ring speed ratio are plotted in Fig. 68 (a) and corresponding strange attractor are shown in Fig. 68 (b)

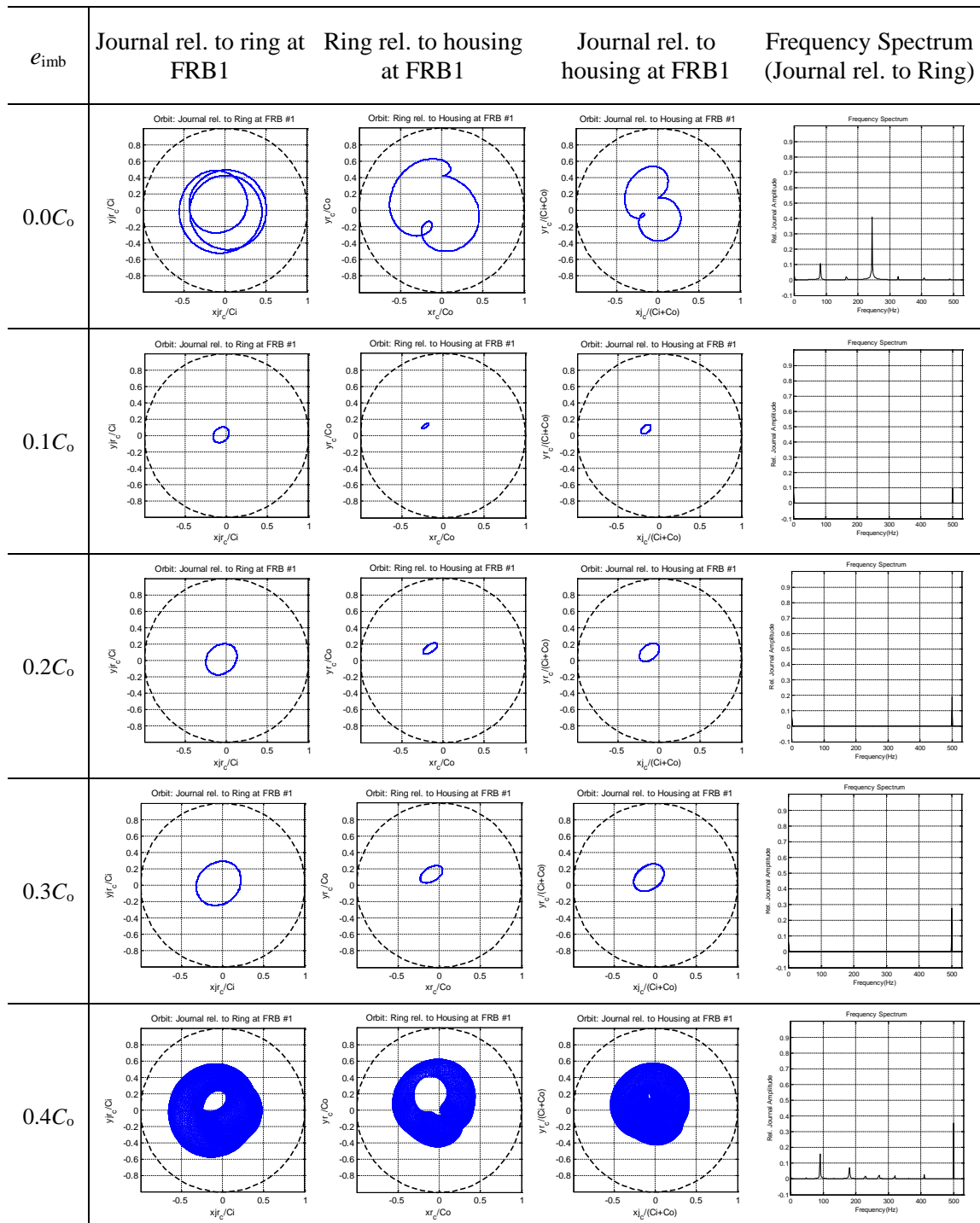


Fig. 65. Responses at FRB #1 with respect to different imbalance eccentricity (@ 30,000rpm)

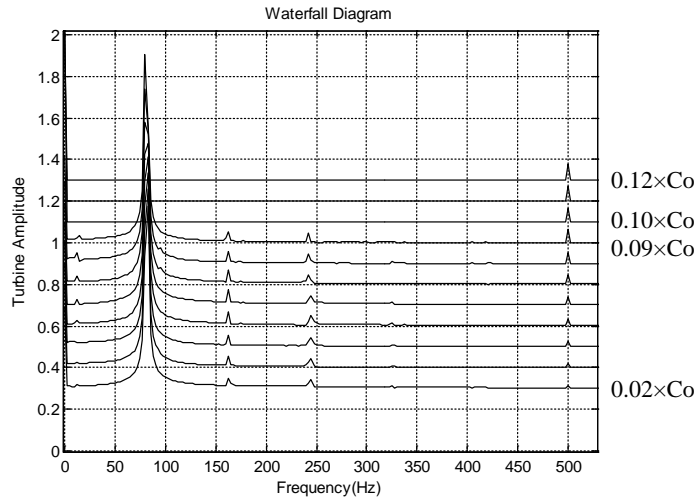


Fig. 66. Waterfall diagram w.r.t imbalance eccentricity (e_{imb} : $0.02C_o \sim 0.12C_o$)

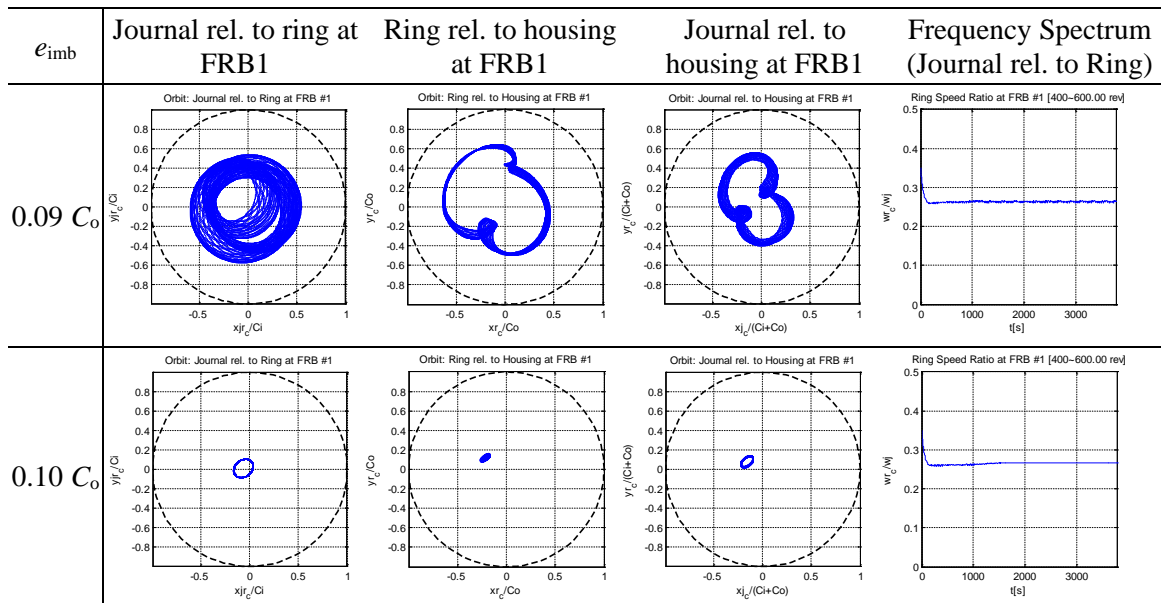
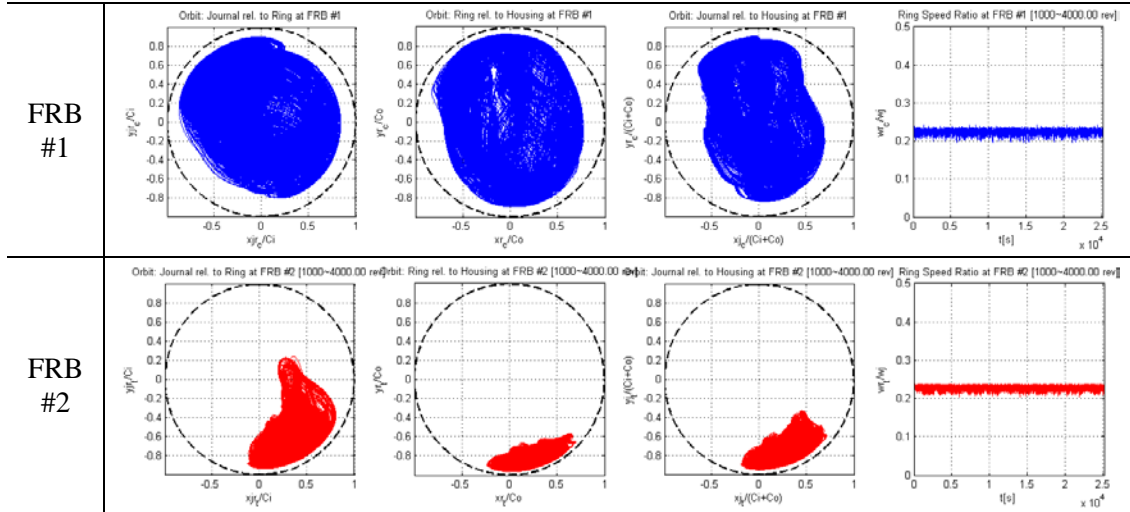


Fig. 67. Bifurcation onset from imbalance eccentricity (@ 30,000rpm)

(a) Orbits and Ring speed ratio: $1000\tau \sim 4000\tau$ spin period



(b) Strange Attractor: $1000\tau \sim 4000\tau$ spin period

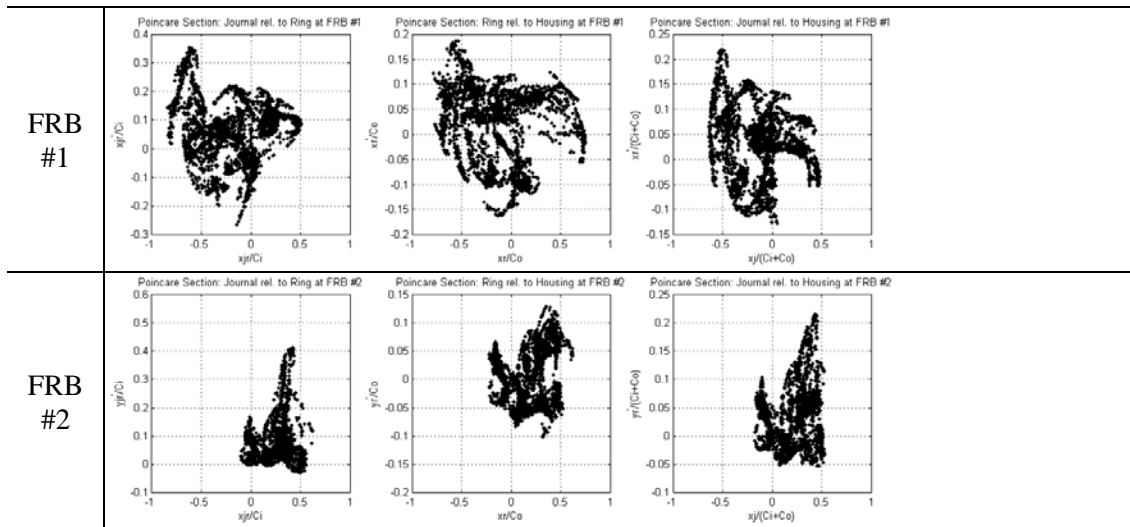


Fig. 68. Chaotic motion in Turbo-charger rotor model ($L/D=0.25$)

Numerical Example 2: Eight-Stage Compressor Supported by TPJBs

Model Description

In addition to the turbocharger rotor supported on FRBs, another industrial rotor model is considered. The geometry of the rotor model basically follows the eight-stage centrifugal compressor rotor model as shown in Fig. 69, which was introduced by Wilson and Barrett in Ref. [56]. The compressor rotor is modeled with a 35-station finite element beam and built based on the mechanical cross-sectional parameters in Table 17. Here, the added properties at nodes (i.e. weight, transverse moment of inertia and polar moment of inertia) has three times increased values than the original data to exaggerate nonlinear behaviors; according to the results of Chapter 3, it was shown that a heavily loaded rotor has higher possibility of various nonlinear responses such as sub-/super-synchronous, quasi-periodic, chaotic vibrations. The compressor is supported on two identical five-pad TPJBs and the TPJB specification is shown in Table 18. Since a TPJB is a highly stabilized bearing application, external excitations induced by imbalance on the fourth compressor disc (i.e. 16th node) are applied to have orbital motions in the system. Table 19 describes the imbalance distributions for the nonlinear study.

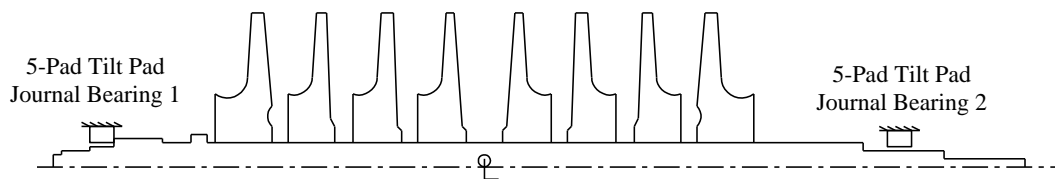


Fig. 69. Schematic of eight-stage compressor

Table 17. Sectional data of the eight-stage compressor

Station number	Length [m]	Outside diameter [m]	E*I [Nm ²]	Added polar moment of inertia [kgm ²]	Added transverse moment of inertia [kgm ²]	Added mass [kg]
1	0.0345	0.0698	0.1558×10 ⁶	0.0000	0.0000	217.8434
2	0.1712	0.1107	0.9843×10 ⁶	0.0000	0.0000	30.5823
3	0.0381	0.1270	1.7047×10 ⁶	0.0000	0.0000	38.7783
4	0.0434	0.1270	1.7047×10 ⁶	0.0000	0.0000	19.7489
5	0.0881	0.1651	4.8787×10 ⁶	0.0000	0.0000	41.8211
6	0.0544	0.1681	5.2231×10 ⁶	0.0000	0.0000	53.0737
7	0.0897	0.1580	4.0751×10 ⁶	0.0000	0.0000	51.8275
8	0.0864	0.1824	7.2319×10 ⁶	0.0000	0.0000	69.5893
9	0.0625	0.1702	5.4813×10 ⁶	0.0000	0.0000	63.1890
10	0.0787	0.1702	5.4813×10 ⁶	0.5415	0.2712	137.7147
11	0.0625	0.1702	5.4813×10 ⁶	0.0298	0.0156	61.1294
12	0.0787	0.1702	5.4813×10 ⁶	0.5415	0.2712	137.7147
13	0.0625	0.1702	5.4813×10 ⁶	0.0298	0.0156	61.1294
14	0.0787	0.1702	5.4813×10 ⁶	0.5415	0.2712	137.7147
15	0.0625	0.1702	5.4813×10 ⁶	0.0298	0.0156	61.1294
16	0.1600	0.1702	5.4813×10 ⁶	0.5415	0.2712	169.4969
17	0.1600	0.1702	5.4813×10 ⁶	0.0000	0.0000	125.0924
18	0.0721	0.1702	5.4813×10 ⁶	0.5415	0.2712	172.7563
19	0.0909	0.1702	5.4813×10 ⁶	0.0431	0.0238	72.1343
20	0.0721	0.1702	5.4813×10 ⁶	0.5415	0.2712	146.5431
21	0.0909	0.1702	5.4813×10 ⁶	0.0431	0.0237	72.1343
22	0.0721	0.1702	5.4813×10 ⁶	0.5415	0.2712	146.5431
23	0.0909	0.1702	5.4813×10 ⁶	0.0431	0.0238	72.1343
24	0.1273	0.1702	5.4813×10 ⁶	0.5415	0.2712	167.9352
25	0.0734	0.1702	5.4813×10 ⁶	0.1439	0.1062	105.0318
26	0.0587	0.1778	6.5432×10 ⁶	0.0000	0.0000	53.5920
27	0.0902	0.1681	5.2231×10 ⁶	0.0000	0.0000	58.4511
28	0.0544	0.1681	5.2231×10 ⁶	0.0000	0.0000	54.8367
29	0.0876	0.1651	4.8787×10 ⁶	0.0000	0.0000	52.8098
30	0.0434	0.1270	1.7047×10 ⁶	0.0000	0.0000	41.6933
31	0.0381	0.1270	1.7047×10 ⁶	0.0000	0.0000	18.1165
32	0.1445	0.1189	1.3086×10 ⁶	0.0000	0.0000	35.2563
33	0.0475	0.0950	0.5338×10 ⁶	0.0000	0.0000	44.9676
34	0.1400	0.0935	0.4993×10 ⁶	0.0000	0.0000	43.5297
35	0.0000	0.0935	0.4993×10 ⁶	0.0000	0.0000	25.4281

Table 18. TPJB specification and parameter ranges

Bearing Parameter	Value [unit]	Pad parameter	Value [unit]
Journal diameter (D)	0.1272 [m]	Num. of pads (arclength)	5 (60° , LOP)
Bearing length (L)	0.0636 [m]	Preload (m_p)	1/2, 2/3
Spin speed	1 ~ 20 [krpm]	Offset (α/β)	0.5, 0.6
Lubricant viscosity (μ)	7.0, 13.8, 27.0 [cP]	Bearing clearance (C_b)	101.6 [μm]
Pad thickness	12.7 [mm]	Pad clearance (C_p)	203.2 [μm]

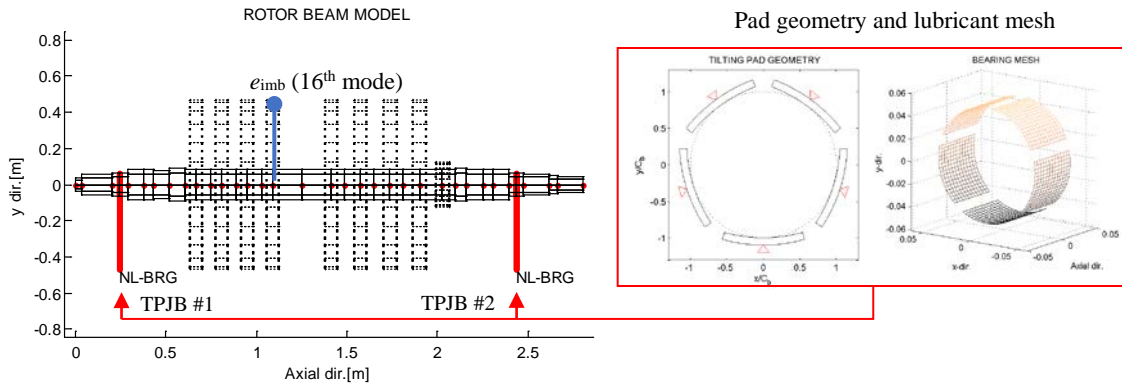


Fig. 70. F.E compressor model supported by two F.E TPJB at the ends

Table 19. Imbalance position and amounts in the eight-stage compressor

Position of imbalance	Amounts of imbalance on disc (e_{imb})
4 th disc (16 th node)	$0.0C_b \sim 0.4C_b$

Response from Reduced System (Verification with Full DOF)

Instead of the use of full DOF eight-stage compressor beam model, a reduced DOF model is utilized in the numerical investigation; here, component mode synthesis (CMS) is applied again to reduce this rotor model. The reduced compressor beam retains 12 DOF out of 140 DOF for the beam elements, here 4 DOF is associated to lateral and vertical movements of shaft at bearing positions, and the other 8 DOF exists in the modal coordinate. On the other hand, the nonlinear coordinates that associated to five pad rotational movements are entirely remained at each bearing position. Hence, the reduced finite compressor model has total 22 DOF. The direct numerical integrations are performed with the two different DOF conditions (Full: 150 DOF vs. Reduced: 22 DOF) to compare the result from each DOF condition. For the transient response, the dynamic differential equations are integrated using a commercial software, MATLAB® routine ode15s, for 300 revolution periods, and the response was collected for last 100 revolutions; here, three different unbalance condition such as no unbalance, small unbalance and large unbalance. Fig. 71, Fig. 72 and Fig. 73 show the time transient numerical integration results from the two DOF conditions; the results agree well with each other. Other calculated results, not presented in this paper, confirm the reliability of the reduced system.

Table 20. Coordinate values of equilibrium positions

Equilibrium Position	TPJB #1		TPJB #2	
	x_{brg1}/C_b	y_{brg1}/C_b	x_{brg2}/C_b	y_{brg2}/C_b
CMS (22 DOF)	0	-0.418	0	-0.400
FULL (150 DOF)	0	-0.418	0	-0.400

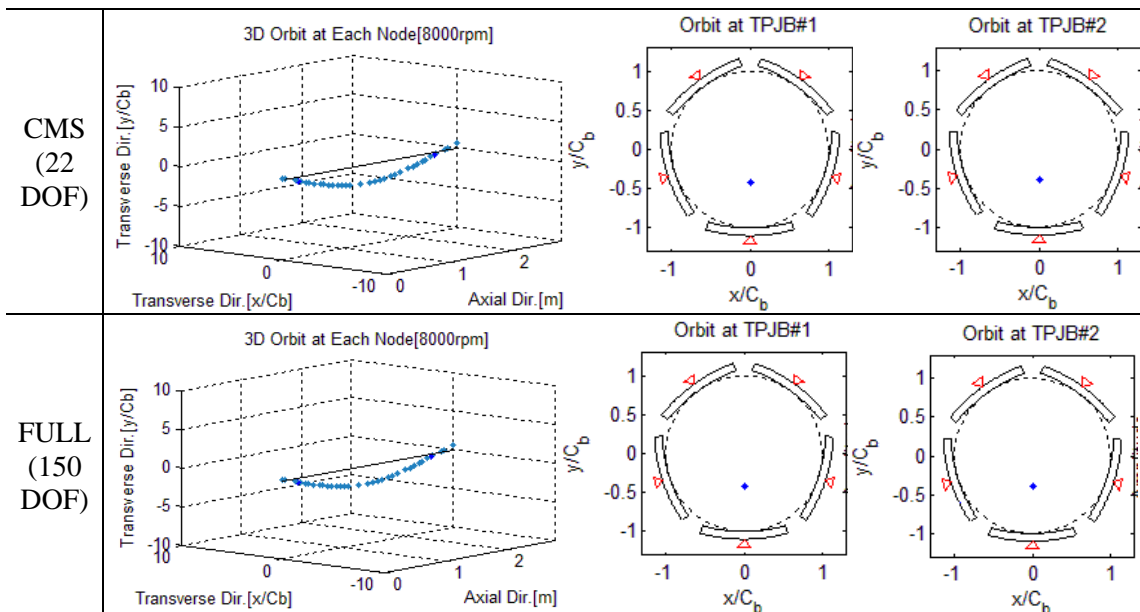


Fig. 71. Comparison of equilibrium positions between Reduced DOF and Full DOF: without unbalance (imbalance force to bearing load ratio: 0.00)

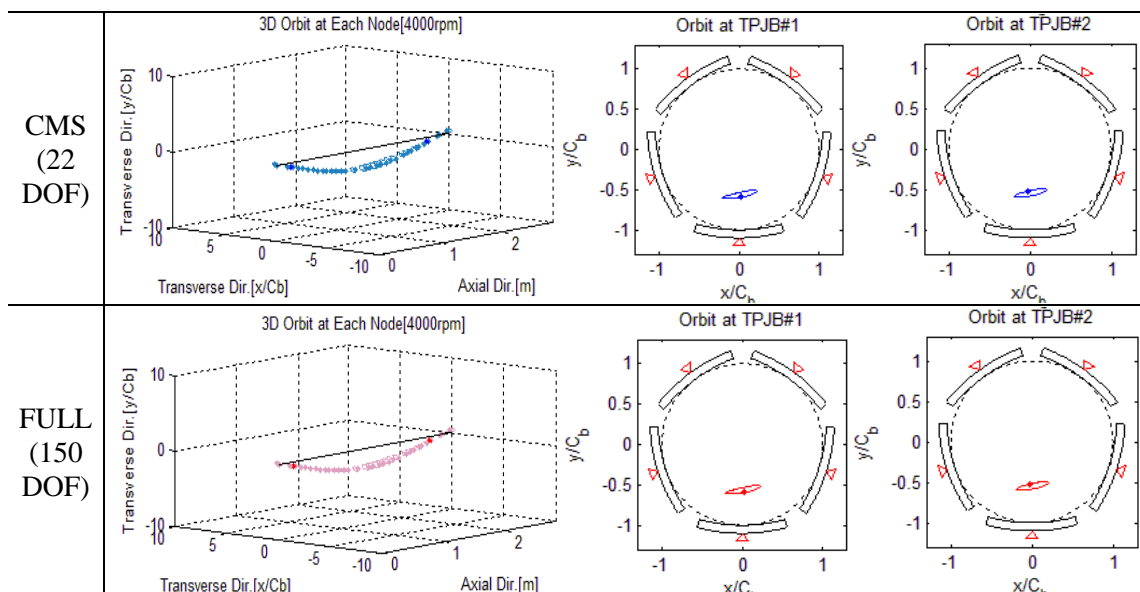


Fig. 72. Comparison of low eccentricity orbits between Reduced DOF and Full DOF: with small unbalance (imbalance force to bearing load ratio: 0.60)

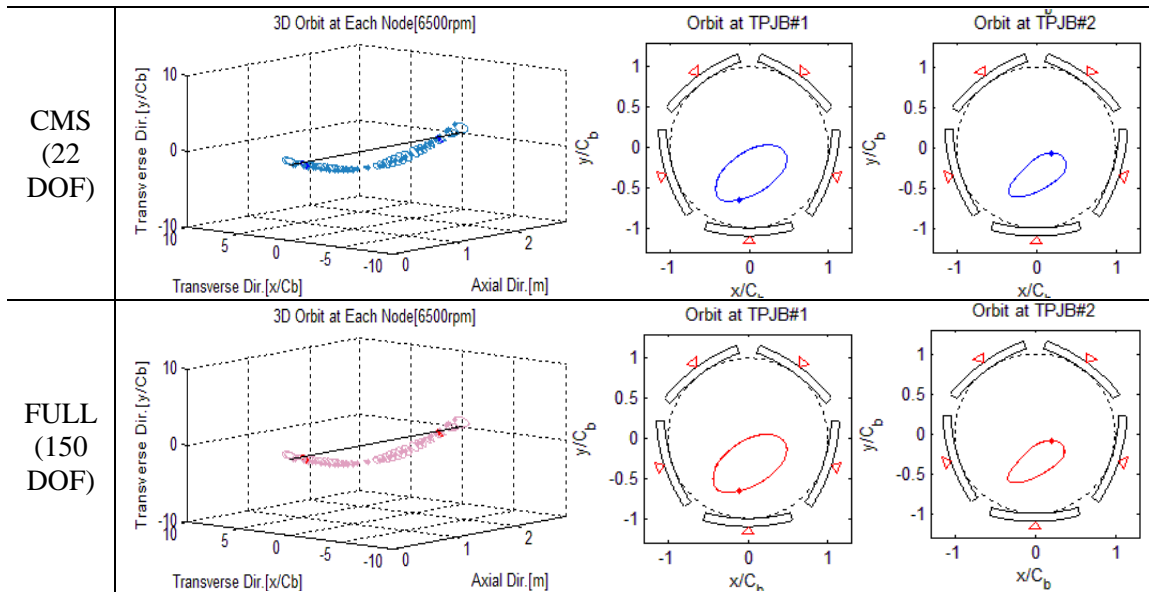


Fig. 73. Comparison of high eccentricity orbits between Reduced DOF and Full DOF: with large unbalance (imbalance force to bearing load ratio: 1.60)

Transient Numerical Integrations with CMS

Using the direct NI, bifurcation diagrams consisted of consecutive collections of Poincaré dots with regard to an operation control parameter can be obtained. Though the method is a kind of brute and incomplete sense of multiple responses and stability, it is useful as an instant tool to examine responses and rotordynamic bifurcations. For the transient responses, the dynamic differential equations are integrated using a commercial software, MATLAB[®] routine ode15s, for 300 revolution periods, and steady states is assumed to be achieved for last 100 revolutions and the data is collected for analysis. As can be seen in Fig. 74 and Fig. 75, bifurcation diagrams, which records the non-dimensional vertical journal motion, y/C_b , at each spin period (2π), show that synchronous, $1/2$ sub-synchronous and quasi-periodic/apperiodic responses as the spin speed increases.

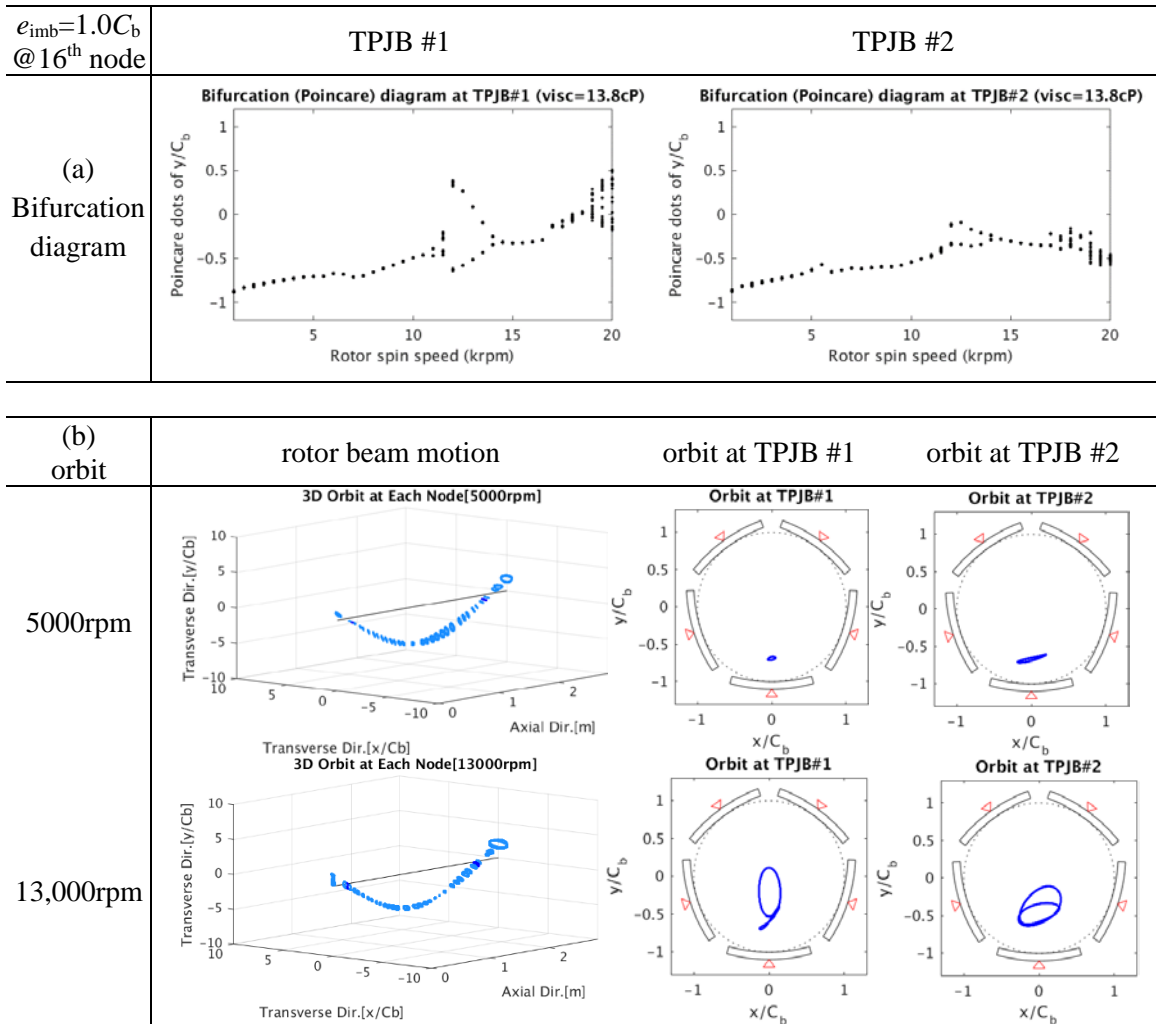


Fig. 74. Bifurcation diagrams wrt spin speed and orbits at specific rpms ($m_p=1/2$, $\alpha/\beta=0.5$)

Non-autonomous Shooting with CMS

Referring to the results from NI, the non-autonomous shooting method is applied in searching for $n\tau$ periodic responses (e.g. $1/2\times$, $1/3\times$, $1/4\times$, $2\times$, $3\times$, ...) at an operation condition (13,000rpm, $e_{imb}=1.5C_b@16^{th}$ node and $\mu=13.8cP$). As a result, three coexistent response states are identified as shown in Fig. 76: $1\times$ synchronous (stable), $1/2\times$ sub-synchronous (unstable) and $2\times$ super-synchronous (unstable) responses.

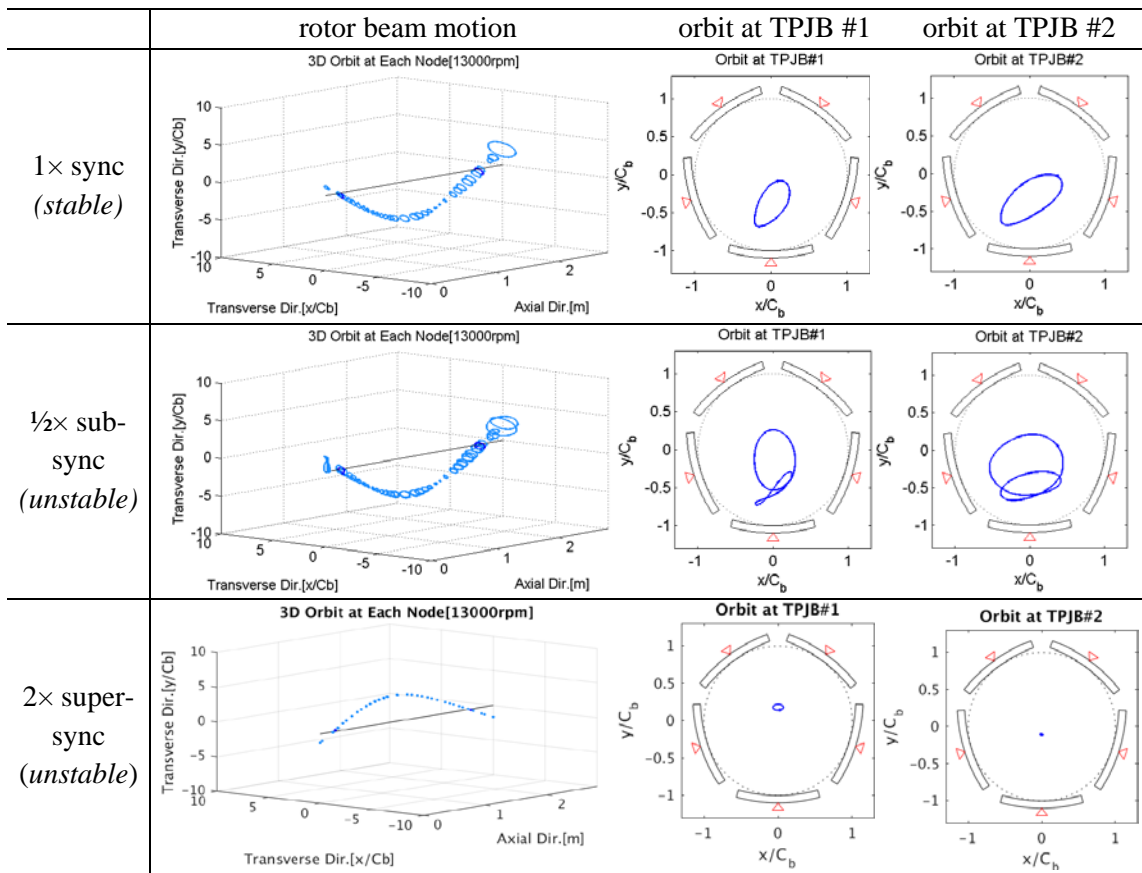


Fig. 76. Coexistent periodic responses at 13,000rpm ($e_{imb}=1.5C_b@16^{th}$ node and $\mu=13.8cP$, $m_p=1/2$, $\alpha/\beta=0.5$)

Bifurcations Results from Arc-Length Continuation with CMS

Control parameter: rotor spin speed ω [rad/sec]

The bifurcation diagrams are obtained by apply the method of non-autonomous, arc-length continuation. The control parameter of the numerical continuation is selected as the rotor revolution speed (*rev/min*), and it proceeds for each harmonic solution that is identified by the shooting method; here, the imbalance eccentricity on 4th disc (16th node) is set as $e_{imb}=1.5C_b$. To illustrate the results, the maximum and minimum values of the non-dimensional vertical displacements, y/C_b , of periodic solutions are plotted in Fig. 77.

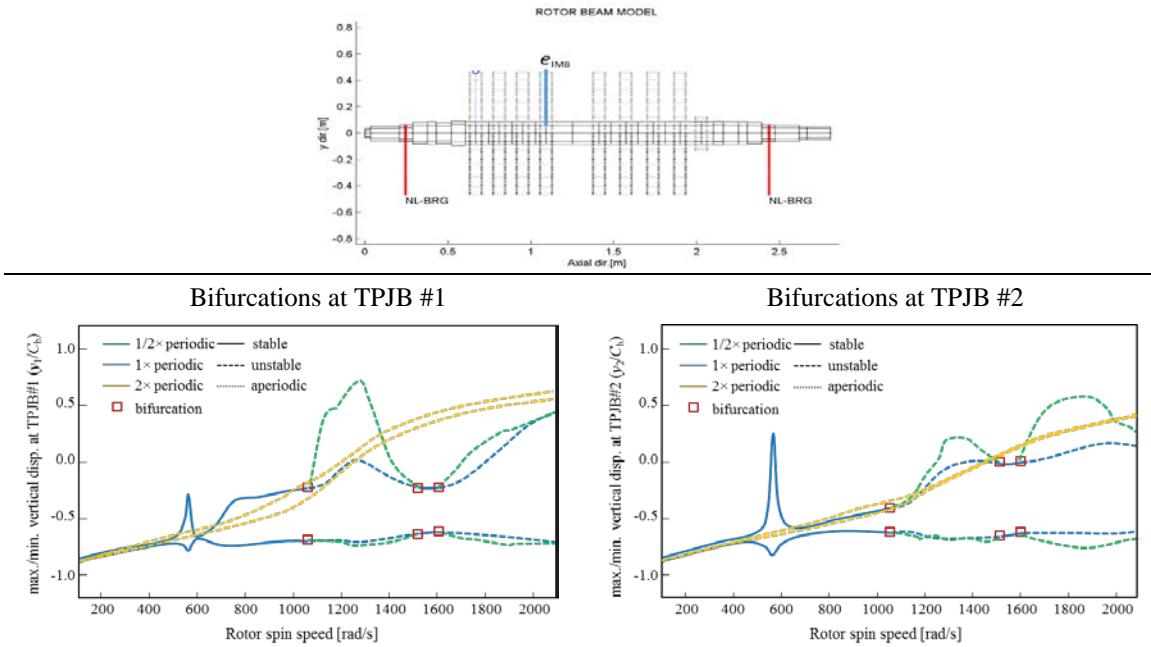


Fig. 77. Bifurcation diagrams with regard to spin speed (using continuation): $e_{imb}=1.5C_b$ (@ 16th node), $\mu=13.8cP$, $m_p=1/2$ and $\alpha/\beta=0.5$

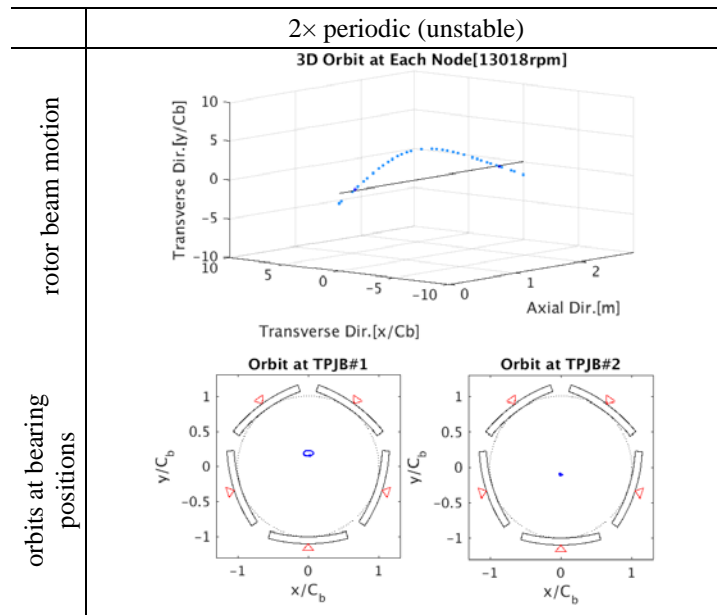
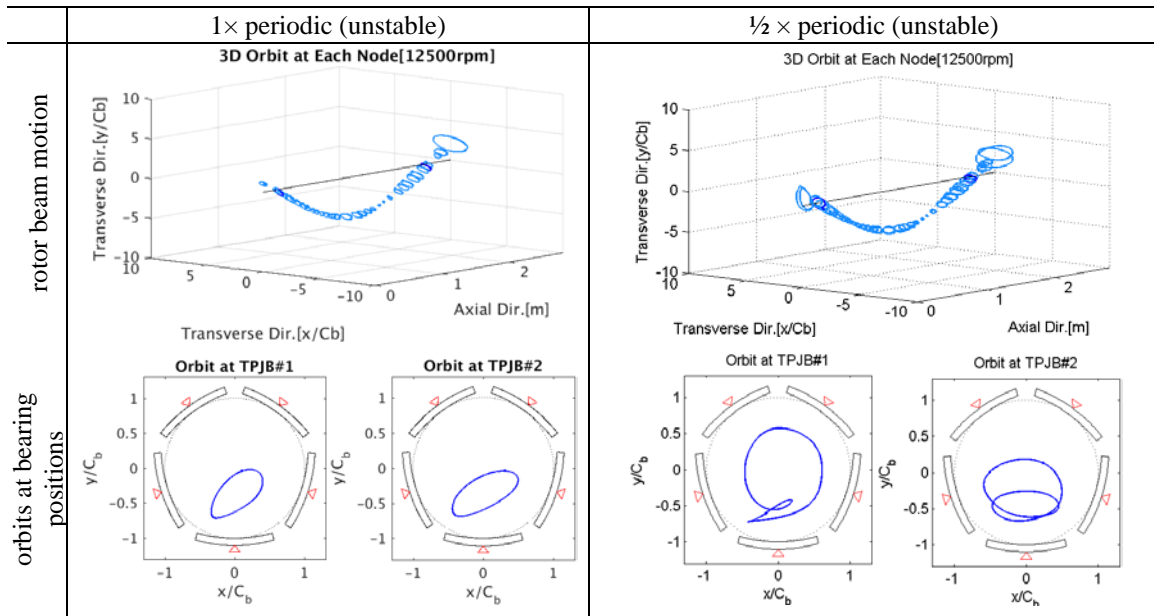


Fig. 78. Multiple response states at 1300 rad/sec with $e_{imb}=1.5C_b$ (@16th node)
 $\mu=13.8cP$, $m_p=1/2$ and $\alpha/\beta=0.5$

In low spin speeds, the journal maintains a stable $1\times$ synchronous response and it locates near the bearing clearance area. After undergoing a resonance near 550 rad/s, a critical bifurcation occurs at 1060 rad/s, which causes the $1\times$ synchronous response loses its stability and an unstable $1/2\times$ sub-synchronous response appeared; since all periodic solutions are unstable, quasi-periodic motion roles as an attractor of all motions. Both periodic solutions converge at 1550 rad/s, and then separate again at 1650 rad/s. Meanwhile, the $2\times$ super-synchronous response appears as unstable all along the operation condition; though it is unstable over the control parameter ranges, this result may explain that a rotor system with TPJB supports can shortly exhibit super-synchronous by any condition of disturbance during operations.

Control parameter: imbalance eccentricity (e_{imb})

The control parameter of the numerical continuation is selected as the amount of imbalance eccentricity on 4th disc. The maximum and minimum vertical displacements of journal, max./min. y_j/C_b , at each TPJB are plotted vs. the imbalance eccentricity on 4th disc in Fig. 79. The $1\times$ synchronous response is the primary form of unbalance response. The first emergence of the $1/2\times$ sub-synchronous response occurs near $0.75C_b$, and it initially appears as stable but it become unstable near $1.4C_b$; at the same condition, the other branch of $1/2\times$ sub-synchronous response emerged from the $1\times$ synchronous response. Then, all the periodic responses turn to unstable so that it can be assumed that quasi-periodic motion roles as an attractor of all motions. The unstable $1/2\times$ sub-synchronous response is eventually disappeared at $2.3C_b$ and $2.5C_b$, respectively. In case

of $2\times$ super-synchronous response, it appears as unstable all along the operation condition. Fig. 80 represents an example of multiple response states those are located at $e_{imb}=2.0C_b$.

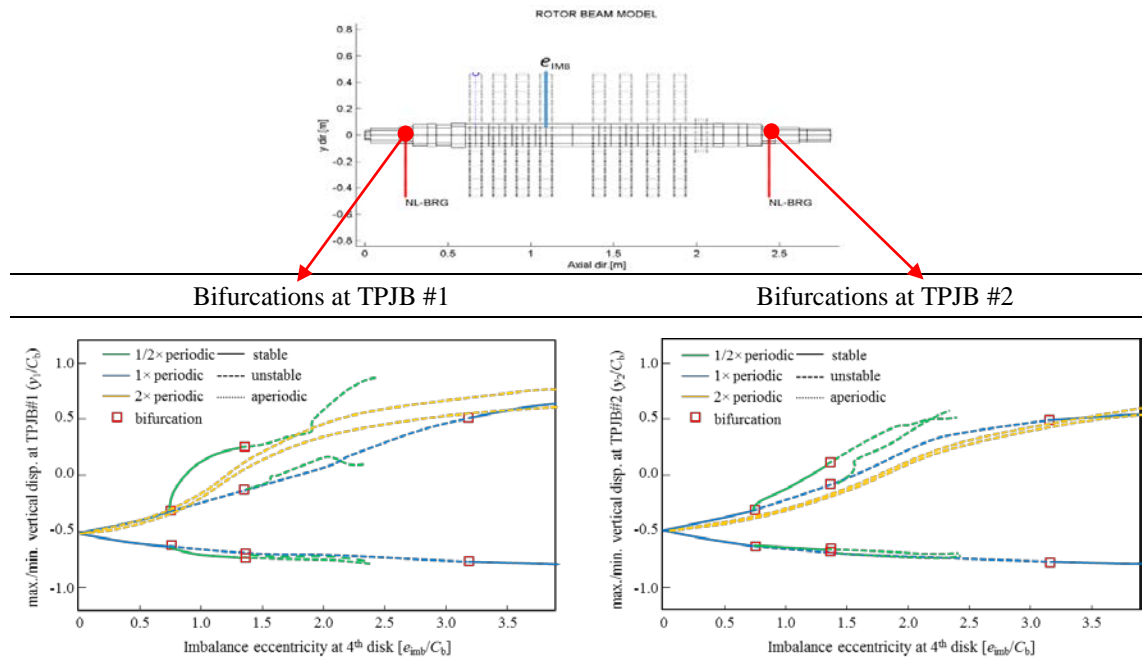


Fig. 79. Bifurcation diagrams with regard to imbalance eccentricity (13,000rpm, $\mu=13.8cP$, $m_p=1/2$ and $\alpha/\beta=0.5$)

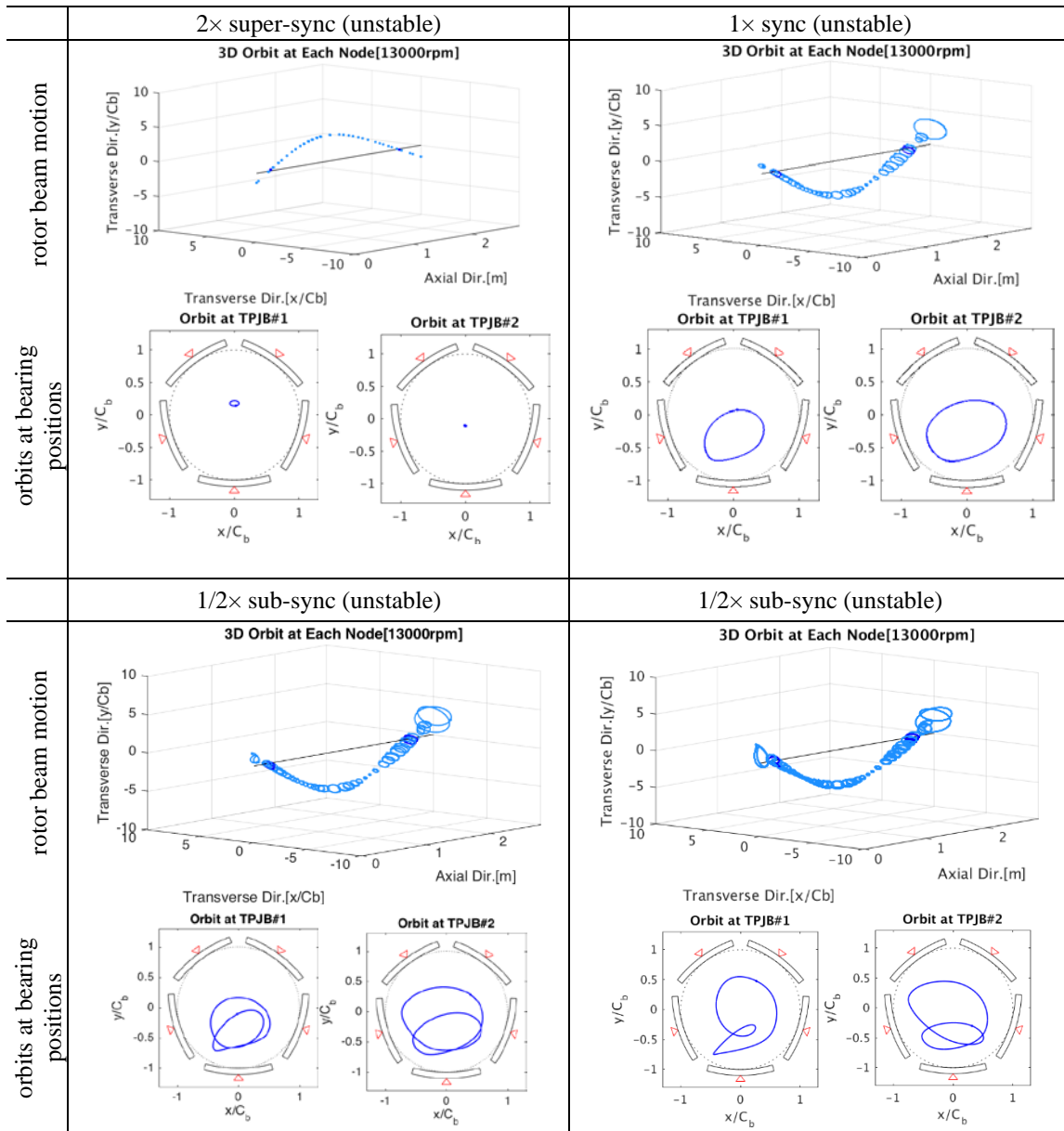


Fig. 80. Multiple response states at 13,000rpm and $e_{imb}=2.0C_b$ (@16th node), $\mu=13.8cP$, $m_p=1/2$ and $\alpha/\beta=0.5$

Effects of Pad Preload and Pivot Offset

In addition to the current pad preload and pivot offset parameters, i.e., case1: $m_p=1/2$, $\alpha/\beta=0.5$, three additional pad-pivot geometrical sets such as case 2: $m_p=2/3$, $\alpha/\beta=0.5$, case 3: $m_p=1/2$, $\alpha/\beta=0.6$ and case 4: $m_p=2/3$, $\alpha/\beta=0.6$, are chosen for investigating their effects on bifurcations of the eight-stage compressor.

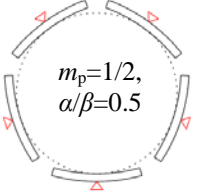
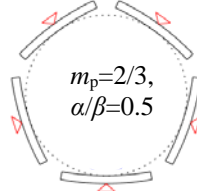
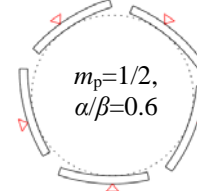
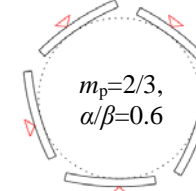
Fig. 81 (a), (b), (c) and (d) show the bifurcation diagrams obtained using the numerical continuations with regard to spin speed for each pad-pivot parameter set. In contrast, corresponding bifurcation diagrams using transient NI are represented in series of Fig. 82, and the results can provide for non-periodic responses. In case2 ($m_p=2/3$, $\alpha/\beta=0.5$) shown in Fig. 81 (b), it is seen that the subcritical type of bifurcation sudden jump to $1/2\times$ sub-synchronous near 1050 rad/s changes to supercritical type (i.e., sudden jump \rightarrow smooth transition), and sub-synchronous and quasi-periodic responses are remained. In case3 ($m_p=1/2$, $\alpha/\beta=0.6$) shown in Fig. 81 (c), notable changes are observed such that: 1) the $1/2$ sub-synchronous response is almost disappeared, 2) the overall responses persist relatively small dynamic eccentricity on their orbits, 3) quasi-periodic motions and N-S bifurcation onsets significantly reduced. In case4 ($m_p=2/3$, $\alpha/\beta=0.6$) shown in Fig. 81 (d), the overall bifurcation scenarios can be interpreted as combined result of case 2 and case 3, which shows sub-synchronous and quasi-periodic significantly suppressed.

In contrast, the bifurcation diagrams in Fig. 83 show the pad-pivot effects on nonlinear behaviors with standpoint of imbalance eccentricity as a control parameter; Fig. 84 shows the corresponding results of transient NI. These results distinguish the

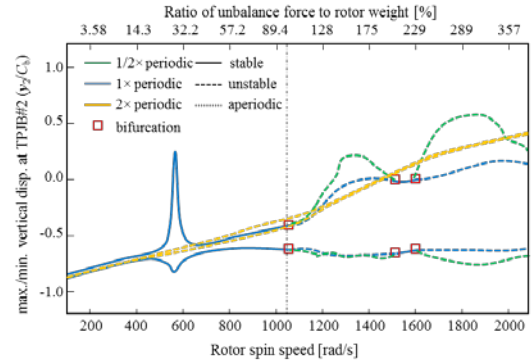
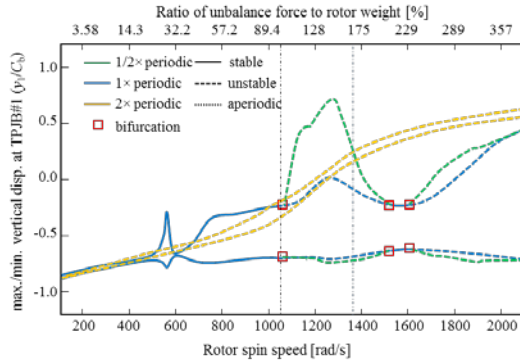
addressed effects in previous more clearly such that appearance of $\frac{1}{2}$ sub-synchronous and stability highly incorporates with the pad-pivot parameters. Table 21 describes the summary of their effects on bifurcations.

The results of pad-pivot parametric study is consistent with the TPJB-rigid rotor system such that the pivot location is major factor to determine system's whole response states and bifurcation scenario and the preload has effects on location and existence of sub-synchronous; here, $\frac{1}{2}\times$ sub-synchronous near $e_{imb}=0.7 \sim 2.5C_b$.

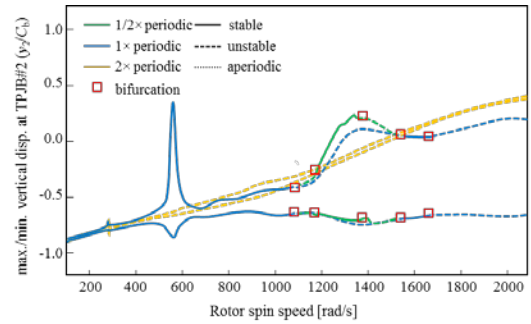
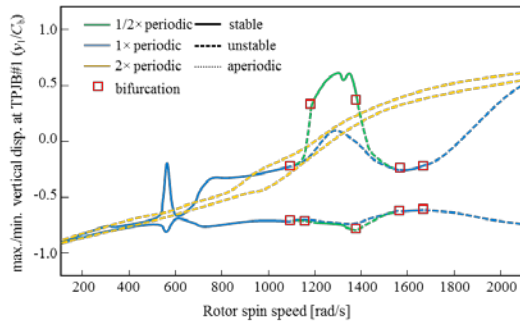
Table 21. Summary of pad preload (m_p) and pivot offset (α/β) effects on bifurcations

case 1	case 2	case 3	case 4
 <p>$m_p=1/2,$ $\alpha/\beta=0.5$</p>	 <p>$m_p=2/3,$ $\alpha/\beta=0.5$</p>	 <p>$m_p=1/2,$ $\alpha/\beta=0.6$</p>	 <p>$m_p=2/3,$ $\alpha/\beta=0.6$</p>
<ul style="list-style-type: none"> • sub-synchronous and quasi-periodic motions at high imbalance and spin speed 	<ul style="list-style-type: none"> • reduce sudden jump (i.e, subcritical bifurcations), but sub-synchronous and quasi-periodic responses are remained <p><i>Minor improvement</i></p>	<ul style="list-style-type: none"> • reduce overall amplitudes • almost disappeared sub-synchronous • significantly reduce quasi-periodic motions and N-S bifurcation onsets <p><i>Significant improvement</i></p>	<ul style="list-style-type: none"> • combined results of case 2 and case 3 • reduce sub-synchronous and quasi-periodic

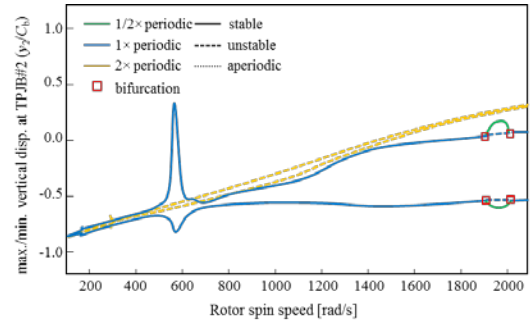
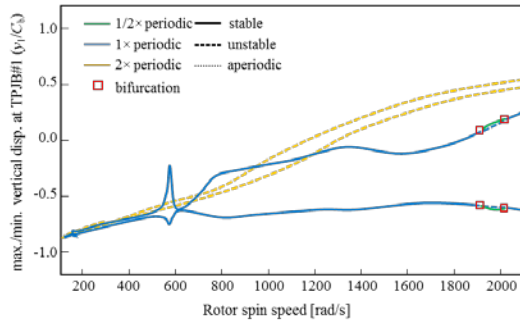
(a) $m_p=0.5, \alpha/\beta=0.5$



(b) $m_p=0.67, \alpha/\beta=0.5$



(c) $m_p=0.5, \alpha/\beta=0.6$



(d) $m_p=0.67, \alpha/\beta=0.6$

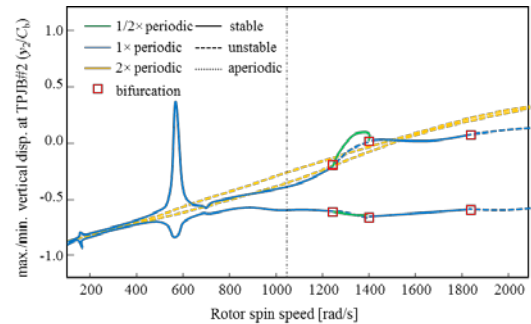
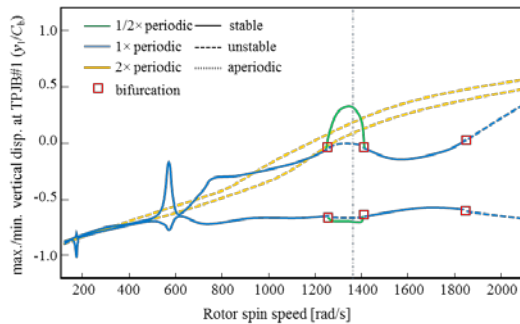


Fig. 81. Bifurcation diagrams with regard to spin speed (using continuation): (a) $m_p=0.5, \alpha/\beta=0.5$, (b) $m_p=0.67, \alpha/\beta=0.5$, (c) $m_p=0.5, \alpha/\beta=0.6$, (d) $m_p=0.67, \alpha/\beta=0.6$

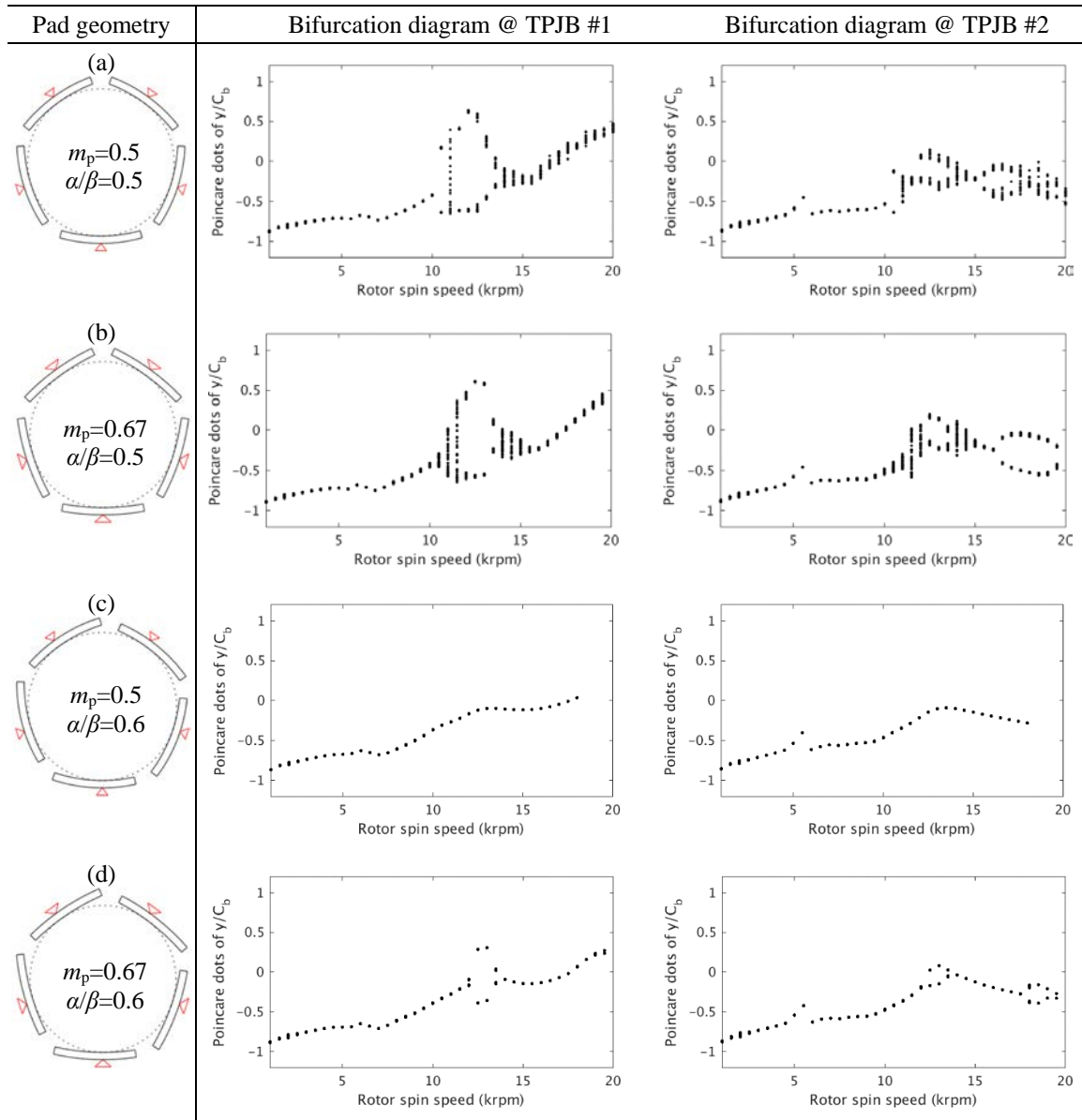
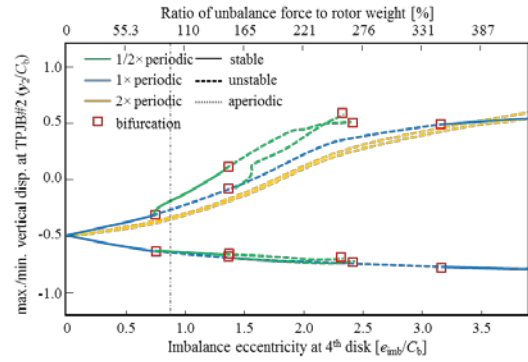
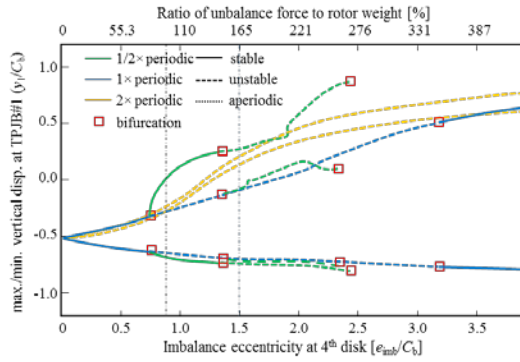
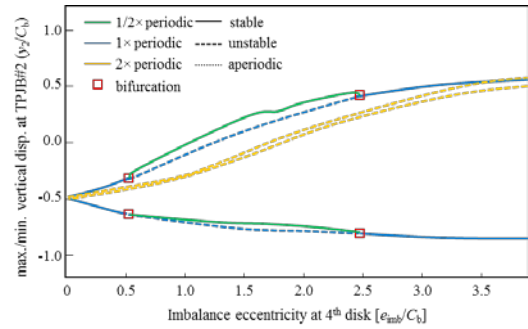
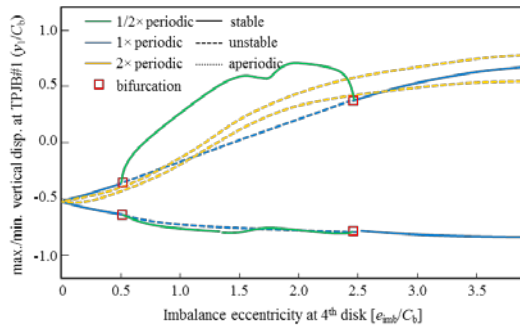


Fig. 82. Bifurcation diagrams with regard to spin speed (using transient NI): (a) $m_p=0.5$, $\alpha/\beta=0.5$, (b) $m_p=0.67$, $\alpha/\beta=0.5$, (c) $m_p=0.5$, $\alpha/\beta=0.6$, (d) $m_p=0.67$, $\alpha/\beta=0.6$

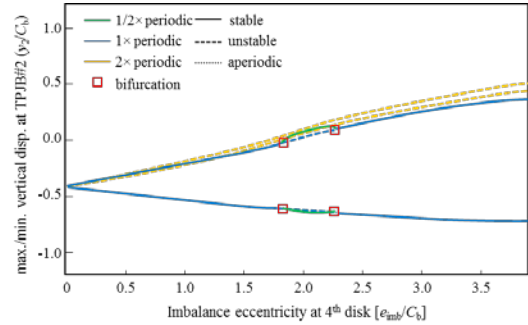
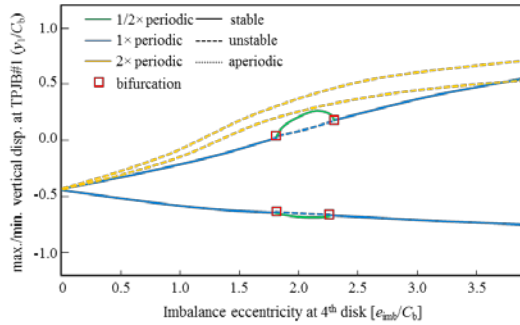
(a) $m_p=0.5, \alpha/\beta=0.5$



(b) $m_p=0.67, \alpha/\beta=0.5$



(c) $m_p=0.5, \alpha/\beta=0.6$



(d) $m_p=0.67, \alpha/\beta=0.6$

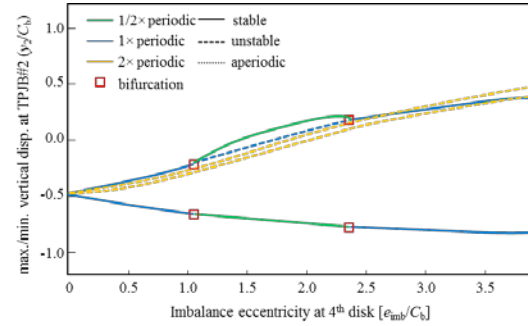
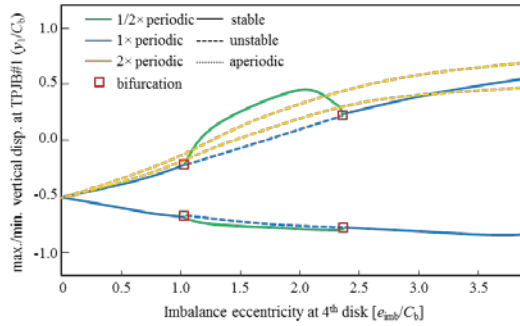


Fig. 83. Bifurcation diagrams with regard to imbalance eccentricity (using continuation):

(a) $m_p=0.5, \alpha/\beta=0.5$, (b) $m_p=0.67, \alpha/\beta=0.5$, (c) $m_p=0.5, \alpha/\beta=0.6$, (d) $m_p=0.67, \alpha/\beta=0.6$

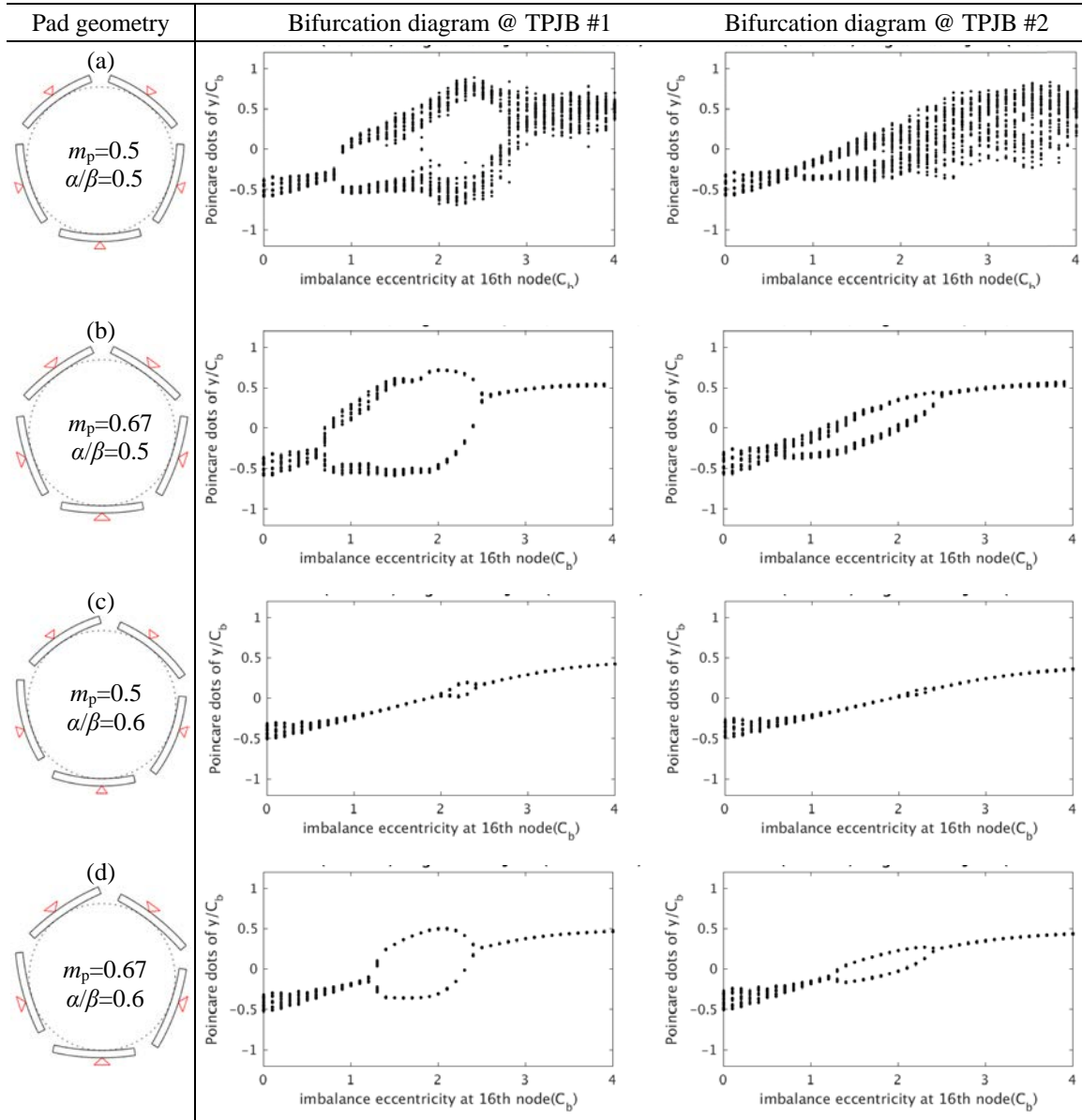


Fig. 84. Bifurcation diagrams with regard to imbalance eccentricity (using transient NI):
 (a) $m_p=0.5$, $\alpha/\beta=0.5$, (b) $m_p=0.67$, $\alpha/\beta=0.5$, (c) $m_p=0.5$, $\alpha/\beta=0.6$, (d) $m_p=0.67$, $\alpha/\beta=0.6$

Effects of Lubricant Viscosity

In addition to the current lubricant viscosity parameter, i.e., $\mu=13.8\text{cP}$, two additional viscosity values such as $\mu=27.0\text{cP}$ and 7.0cP , are applied for investigating lubricant effect on the eight-stage compressor; the oil is assumed an ISO VG 22 and a corresponding temperature is 45°C (@ $\mu=27.0\text{cP}$), 65°C (@ $\mu=13.8\text{cP}$) and 82°C (@ $\mu=7.0\text{cP}$), respectively.

Fig. 85 shows the bifurcation diagrams using the numerical continuation with regard to spin speed for each lubricant viscosity; here, $e_{\text{imb}}=1.5C_b$ and the supplemental diagrams using transient NI is shown in Fig. 86. The result with high viscosity, i.e., $\mu=27.0\text{cP}$ in Fig. 85 (a), shows stabilized responses overall operation ranges such that $1/2\times$ sub-synchronous responses are disappeared; only $1\times$ synchronous remained, so dynamic eccentricity is not drastically enlarged as the spin speed increases. In contrast, low viscosity, i.e., $\mu=7.0\text{cP}$ in Fig. 85 (c), loses the response stability in low rpm region, so it sooner get into quasi-periodic motions. The $1/2\times$ sub-synchronous is remained and appeared as unstable.

Fig. 87 shows the bifurcation diagrams using the numerical continuation with regard to imbalance eccentricity for each lubricant viscosity; here, $\text{rpm}=16\text{k}$ and Fig. 88 is corresponding results from transient NI. The results show similar manner with the previous approach such that low viscosity holds $1/2$ sub-sync; they are mostly unstable solutions, so quasi-periodic responses are dominant under high speed/high imbalance.

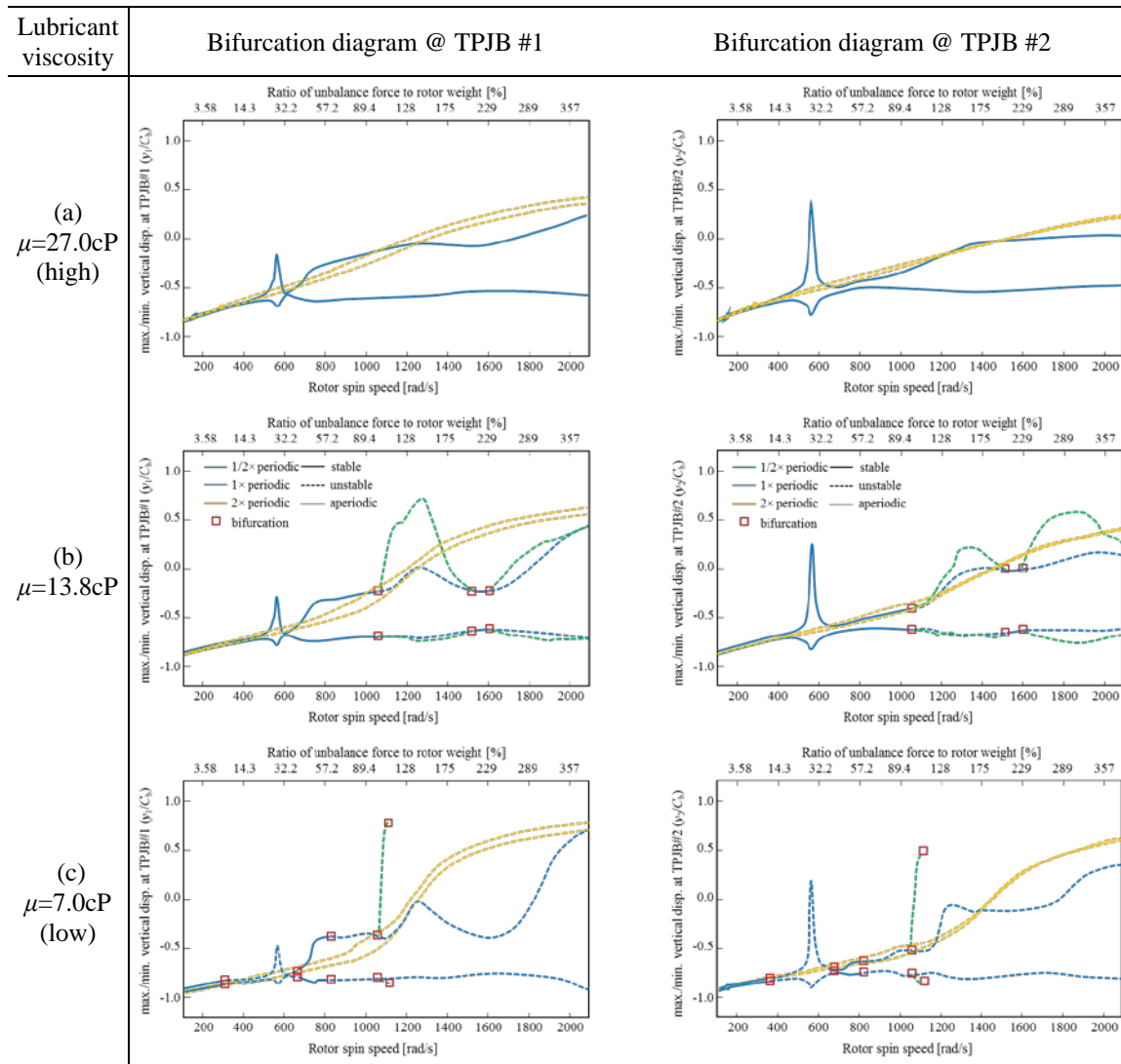


Fig. 85. Bifurcation diagrams with regard to spin speed (using continuation): (a) $\mu=27.0\text{cP}$, (b) $\mu=13.8\text{cP}$, (c) $\mu=7.0\text{cP}$

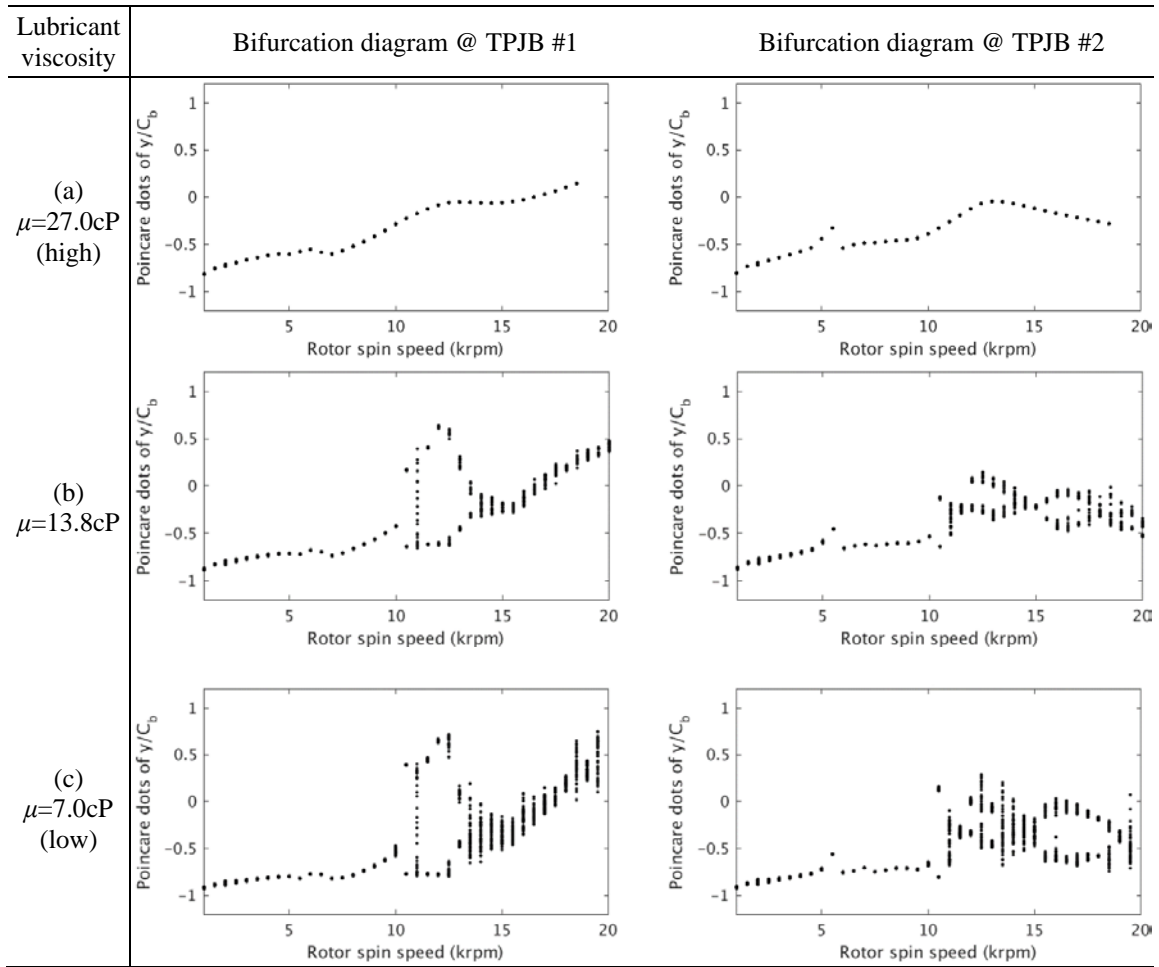


Fig. 86. Bifurcation diagrams with regard to spin speed (using transient NI): (a) $\mu=27.0\text{cP}$, (b) $\mu=13.8\text{cP}$, (c) $\mu=7.0\text{cP}$

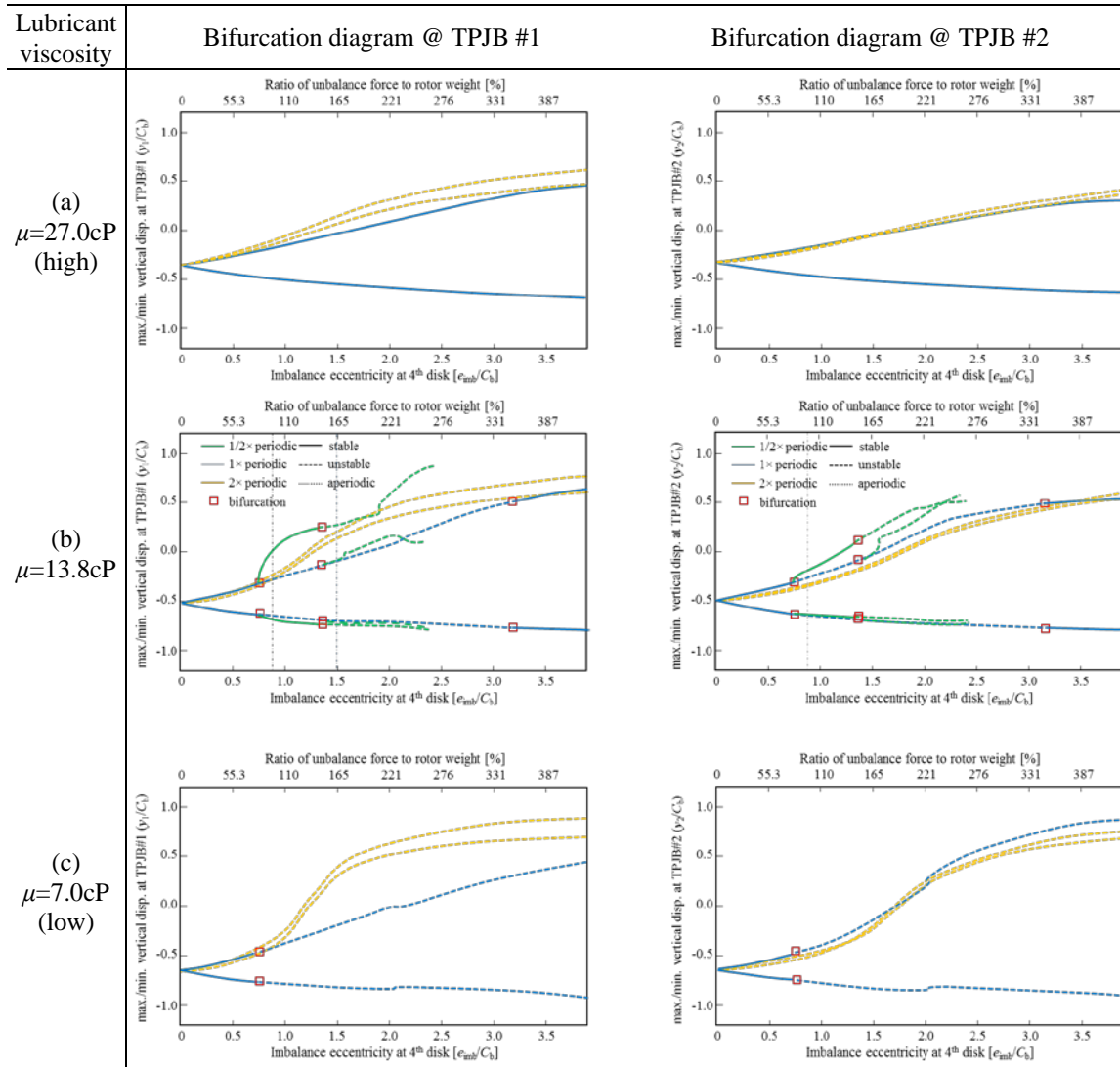


Fig. 87. Bifurcation diagrams with regard to imbalance eccentricity (using continuation):
 (a) $\mu=27.0\text{cP}$, (b) $\mu=13.8\text{cP}$, (c) $\mu=7.0\text{cP}$

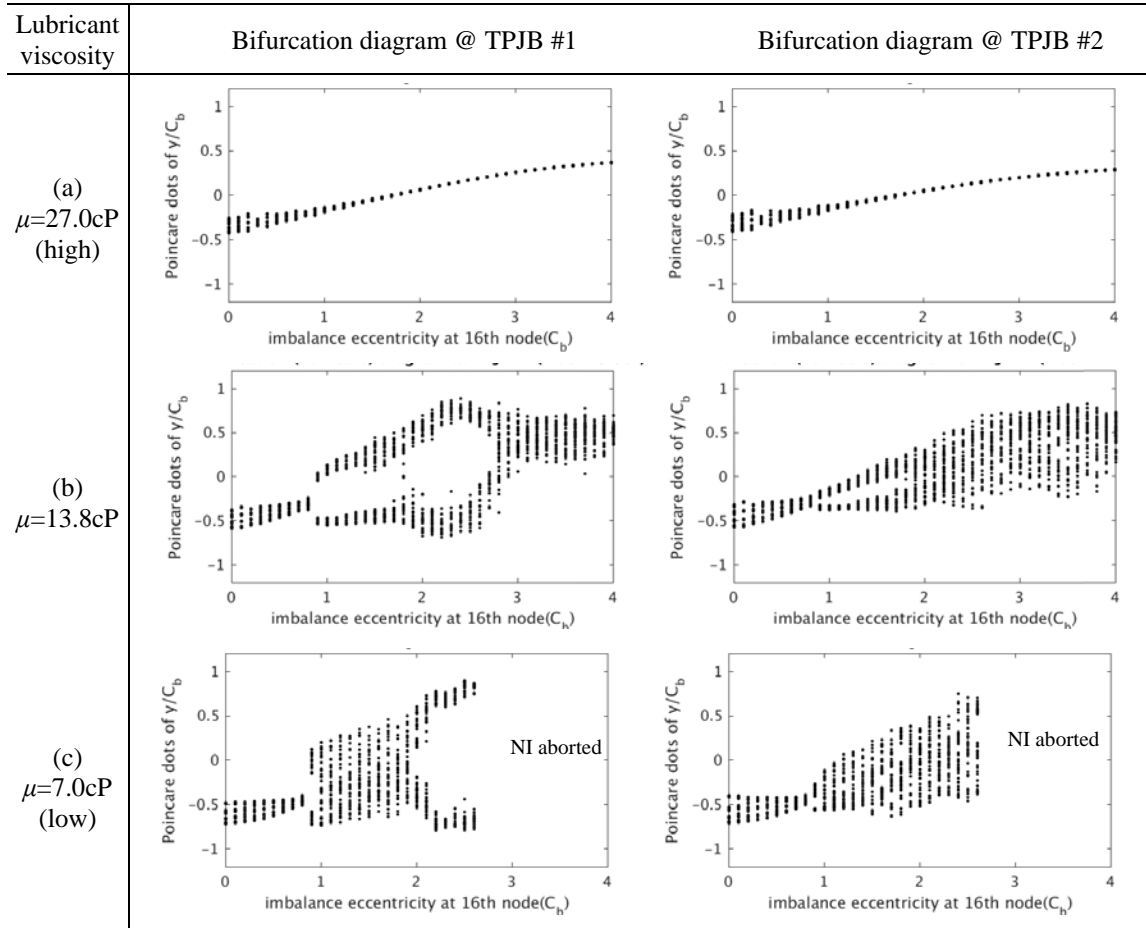


Fig. 88. Bifurcation diagrams with regard to imbalance eccentricity (using transient NI):
(a) $\mu=27.0\text{cP}$, (b) $\mu=13.8\text{cP}$, (c) $\mu=7.0\text{cP}$

CHAPTER IV

CONCLUSIONS AND RECOMMENDATIONS

Conclusions

Nonlinear response, stability and bifurcations of rotor systems supported by nonlinear fluid film bearings such as floating ring bearings (FRBs) and tilting pad journal bearings (TPJBs) were studied using the improved shooting and continuation methods along with the conventional numerical investigation approaches (e.g. transient numerical integrations, Lyapunov exponents, etc). The employment of mathematical deflation and the parallel computing provided that the numerical algorithms could incorporate with the finite element bearing models, while other related research has utilized the approximated bearing models. The use of the finite element bearing models promised to construct complex bearing geometry and to provide accurate oil pressure distributions.

In the dissertation, there were four discussions addressed regarding 1) nonlinear response and bifurcations of a rigid rotor supported by FRBs, 2) effects of a thermo-hydrodynamic (THD) FRB model on rotordynamic bifurcations, 3) nonlinear response and bifurcations of a rigid rotor supported by TPJBs, 4) applications to general, complex, multi-mass rotor beam models. The specific contributions and results are the followings:

Rigid rotor supported by floating ring bearings

- 1) The bifurcation type of response highly depends on bearing length to diameter (L/D) ratio; shorten L/D ratio tends to have subcritical type of primary Hopf bifurcation, but higher L/D ratio has supercritical type of Hopf and then undergoes several secondary Hopf bifurcations, i.e. Neimark-Sacker.
- 2) It was confirmed that two coexistent steady state responses can jump to each other in the identical operation condition upon a sudden base excitation. This has an important consequence for machinery that encounters sudden base motions, since response amplitude and ring rotational speed can drastically jump at the event.
- 3) Chaotic motions were quantitatively confirmed for a non-autonomous case, with low L/D ratio in the FRB-rotor system. A positive LE component and strange attractor confirmed the characteristics in explicit and implicit manners.
- 4) In order to quench/reduce the sub-synchronous oil whirls, synchronization through an intended unbalance was studied. Numerical investigation for determining imbalance eccentricity and position achieved significant amplitude reductions.
- 5) Comparison between the results from the finite bearing model and short bearing model for L/D=0.5 exhibited significant differences of bifurcation onsets in high speed condition over 120krpm.

Effect of thermo-hydrodynamic (THD) FRB model on bifurcations

- 1) In the model, the temperature distributions of the inner and outer lubricant layers and ring cross section area were kept updated for a certain time segment (i.e. $\Delta t \approx \tau_R/30$). The solution of the shooting and the continuation should consent its periodicity for temperature distributions in the FRB components as well as for dynamics states of the journal and ring.
- 2) In the autonomous case, the obtained THD periodic solutions and THD bifurcation diagrams showed that the lubricant supply temperature delays the onset of a Hopf bifurcation with increasing speed. However, it adversely widens the speed range over which a sudden jump from a benign limit cycle to a large limit cycle may occur. In general, the THD bifurcation curves are seen to be more sensitive with regard to changes in speed and supply temperature than the isothermal responses.
- 3) In the non-autonomous case, the simulation results with large unbalance has confirmed that the bifurcation event to the oil whirls further delayed due to the synchronization. The quenching effect extends the stable regions in high spinning speeds; however, it also brings the bifurcations and the multiple response states in low speed areas. The stability of the $1/2\times$ sub-synchronous and the quasi-periodic responses in the low speed ranges highly depends on the lubricant temperature. The comparison with the isothermal case in the low speed ranges shows that the bifurcation onsets generally agree well with each other due to the small dynamic eccentricities.

Rigid rotor supported by tilting pad journal bearings

- 1) Results of successive numerical integrations with regards to spin speed vs. unbalance force, *Loci of bifurcations* of the TPJB-rigid rotor were obtained. If the bearing gets heavily loaded and highly unbalanced, the response exhibited non-synchronous and aperiodic motions other than the classical oil whirls; for instance, when $W=19.6\text{kN}$ and $\text{rpm}=15\text{k}$, the system showed various responses in the consecutive forms of $1\tau \rightarrow 2\tau \rightarrow 4\tau \rightarrow$ quasi-periodic/aperiodic as accumulating unbalance force on the disc
- 2) Results of the non-autonomous shooting/continuation algorithms discovered nonlinear nature of TPJB; in particular, when the unbalance force to bearing load ratio (F_u/W) became 5 to 8, the system located under many numbers of coexistent response states due to multiple onsets of saddle node bifurcations from $\frac{1}{2}$ sub-synchronous responses.
- 3) A parametric study with pad-pivot geometry confirmed that the pivot location significantly influences nonlinear aspects such that periodic doubling bifurcations and high vibration states are significantly suppressed by locating the pivot point a little after the mid-plane of the pads (i.e., $\alpha/\beta > 0.5$). On the other hand, the pad preload steers onsets of stable high amplitude $\frac{1}{2}$ sub-synchronous responses.
- 4) It has confirmed that lubricant viscosity has a major role to determine overall response behaviors such that higher viscosity (i.e., viscid) tend to suppress appearance of sub-synchronous responses and lower viscosity tends to get

into quasi-periodic motion. Lyapunov exponents can explicitly differentiate n -periodic-, quasi-periodic, chaotic responses in TPJBs.

Extension of study to flexible, multi-mass rotor systems

- 1) The improved shooting and continuation methods were combined with the model reduction technique, i.e., Component Mode Synthesis (CMS), to deal with general, flexible, multi-mass rotor system (i.e., large order system): two examples of industrial rotors such as a turbocharger with FRBs and an eight-stage compressor with TPJBs were studied.
- 2) The finite element 14-station turbocharger system that has total 62 DOF was reduced to 16 DOF with the aid of CMS. Multiple response states and bifurcation diagrams were obtained using the autonomous shooting-CMS method. The jump phenomenon between coexistent stable responses at an identical operation condition had simulated with a pulse type excitation that depicted a sudden bump on the road. Intended imbalance mass on a rotor/disk, here, $e_{imb}=0.1C_o$ on compressor stage, exhibited the significant reduction of the oil whip type orbit to the synchronous orbit in small dynamic eccentricity at 30krpm; it was a good example of synchronization. Chaos was observed in turbocharger when the L/D ratio of FRB became low rates, for instance, below 0.25, under unbalance response.
- 3) The finite element 35-station eight-stage compressor system that has total 150 DOF was reduced to 22 DOF with the aid of CMS. The non-autonomous

shooting/continuation-CMS methods applied independently for $n\tau$ period, and $1\times$ synchronous, $\frac{1}{2}\times$ sub-synchronous and $2\times$ super-synchronous responses are identified. A parametric study with pad-pivot geometry confirmed that the pivot location plays the main role to determine appearances of sub-synchronous and quasi-periodic responses in the larger order system. In contrast, the amount of preload had influence on stability of the responses at high speed ranges. It was reconfirmed that the higher lubricant viscosity greatly suppressed the emergence of sub-synchronous and quasi-periodic responses.

Recommendations for Further work

Development of a thermo-hydrodynamic (THD) TPJB model

With the use of the THD-FRB model, it was discovered that how the thermal condition in FRB components influences the bifurcation in a FRB-rotor system. As an extension of this work, the development of a THD TPJB model would be recommendable, since many of modern turbomachinery install various types of TPJBs. The finite element based TPJB models should consider the energy equation and thermal conduction equation to calculate thermal property change in 1) shaft to lubricant layers, 2) lubricant layers on pads and 3) pads to pivots. The steady state THD solution procedure would also be utilized for identify the thermal condition in TPJB components.

Extension of nonlinear bearing applications

The introduced improved shooting/continuation methods proved the efficiency and adaptability for analysis of finite element based general, complex nonlinear bearing models. The incorporation of the algorithms with extended bearing applications such as squeeze film dampers (SFDs), SFDs in series with TPJBs, pressure dam, offset bearing, seals, etc. would provide original contributions to nonlinear dynamics study of rotor-bearing systems.

High fidelity finite element bearing models

The use of high fidelity bearing models to the shooting/continuation would be able to specify a detailed source of nonlinear nature in fluid film bearings. In other words, modeling of thermo-hydrodynamic fluid elements, thermo-elastic (i.e. deformable) solid elements, fluid inertia components and bifurcation study with the finite element model would provide information of key factors of nonlinear behaviors of hydrodynamic bearings; with engineer's stand point, this would give useful treatments when they encounter an instability.

Nonlinear phenomena due to accumulated unbalance distributions

Many of industrial turbomachinery are required to consistently operate in years. Over a period of time, however, the rotor machinery may develop an unbalance condition due to various aspects came from turbine blade erosion/defects, couplings, misalignment and generator bowing. A numerical study regarding nonlinear phenomena

due to evenly or unevenly accumulated unbalance distributions on rotors/discs would give a useful reference for long-term operations.

Development of an algorithm to quench/reduce of large oil whirls (i.e. synchronization)

A numerical algorithm to identify optimal position and amount of unbalance force for quenching a large orbit in a rotor system would be useful reference those who involved in shop/field rotor-balancing.

Development of new/improved algorithm for identifying coexistent solutions

Harmonic balance method, trigonometric collocation method, and shooting method, etc. have been using in identifying multiple response states in nonlinear rotordynamic systems. It would be meaningful to develop a new/improved algorithm other than the conventional approaches. In that sense, Genetic algorithm (GA) recently has been utilized as a nonlinear dynamic solver while it is usually employed in optimal design study. A preliminary work for “a modified GA for nonlinear rotordynamic system” is described Appendix C.

Analytical investigation for routes to chaos of rotor systems

Chaos can be categorized as a non-periodic steady-state solutions arising in a deterministic dynamic system that exhibits a sensitive dependence on initial conditions. In the current study, the determinations of chaotic motions in the rotor-bearing systems were evaluated in four separate approaches such as Lyapunov exponents, strange

attractor, bifurcation diagram, and frequency spectrum. In addition to this, the investigation of the transition routes to chaos can be another important aspect to understand nonlinear stability of the rotor-bearing systems. A route to chaos can be occurred in various ways such as the period-doubling sequence or the intermittency mechanisms or quasi-periodic sequence or blue-sky catastrophe, etc.[37]. Identification of a chaos route and parametric study with a control parameter would shed light on nonlinear causality of the bounded solution from an equilibrium point or a periodic solution or a quasiperiodic solution. Besides, analytical predictions of chaos occurrence can also be recommendable; for instance, the use of Melnikov's criterion, which derives a function to describe the first order distance between perturbed stable and unperturbed manifolds, can provide a global analysis of the heteroclinic or the homoclinic bifurcations.

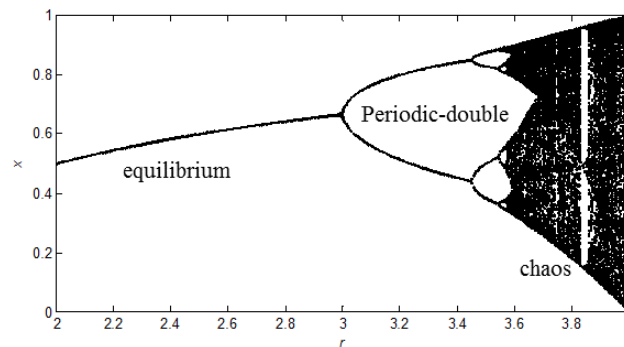


Fig. 89. The period-double route to chaos in a Logistics map function

Development of a test rig and experimental study

So far, analytical and numerical methods have been provided the nonlinear phenomena in rotor-bearing systems. However, the simulations always face a challenge to verify the validity of results so that test data from an open literatures or a test rig would be an inevitable step for further work. Furthermore, the experiment results may provide another important but missed parameters (e.g. friction, rub, etc.) in the numerical modeling of rotor-bearing system.

In order to construct a test rig, a set of equipment such as a DC motor, rotor, stator, pedestal, concrete foundation, lubricating system, coupling, gearbox, eddy-current transducers, control box, data acquisition-analysis system, etc. should be considered and assembled for experimental purposes.

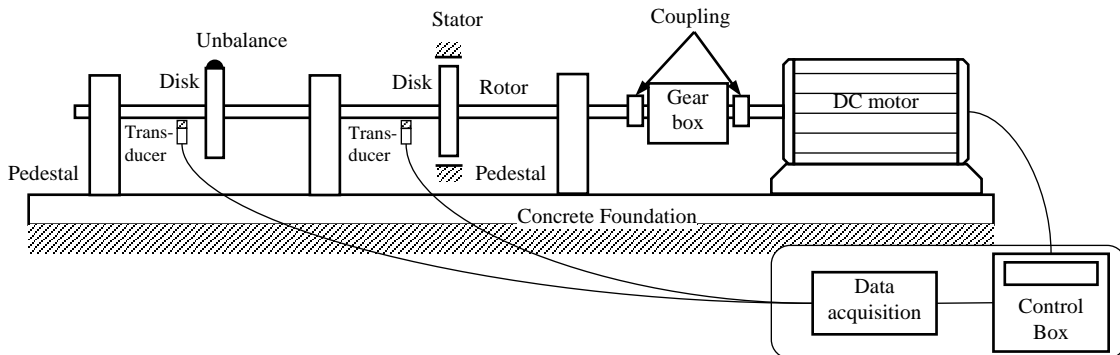


Fig. 90. An example of a rotor-bearing test rig

REFERENCES

- [1] Muszynska, A. "Whirl and whip—rotor/bearing stability problems." *Journal of Sound and Vibration* 110, no. 3 (1986): 443-462.
- [2] Muszynska, A. "Stability of whirl and whip in rotor/bearing systems." *Journal of Sound and Vibration* 127, no. 1 (1988): 49-64.
- [3] Hollis, P., and Taylor, D. L. "Hopf bifurcation to limit cycles in fluid film bearings." *Journal of Tribology* 108, no. 2 (1986): 184-189.
- [4] Adiletta, G., Guido, A. R. and Rossi, C. "Chaotic motions of a rigid rotor in short journal bearings." *Nonlinear Dynamics* 10, no. 3 (1996): 251-269.
- [5] Zhao, J. Y., and Hahn, E. J. "Subharmonic, quasi-periodic and chaotic motions of a rigid rotor supported by an eccentric squeeze film damper." *Proceedings of the Institution of Mechanical Engineers, Part C: Journal of Mechanical Engineering Science* 207, no. 6 (1993): 383-392.
- [6] Abu-Mahfouz, I, and Adams, M. L. "Numerical study of some nonlinear dynamics of a rotor supported on a three-pad tilting pad journal bearing (TPJB)." *Journal of Vibration and Acoustics* 127, no. 3 (2005): 262-272.
- [7] Childs, D. W. *Turbomachinery Rotordynamics: Phenomena, Modeling, and Analysis*. John Wiley & Sons, 1993.
- [8] Childs, D. W., and Hale, K. "A test apparatus and facility to identify the rotordynamic coefficients of high-speed hydrostatic bearings." *Journal of Tribology* 116, no. 2 (1994): 337-343.
- [9] Nguyen-Schäfer, H. *Rotordynamics of automotive turbochargers*, Springer, 2012

- [10] Tanaka, M., and Hori, Y. "Stability characteristics of floating bush bearings." *Journal of Lubrication Technology* 94.3 (1972) 248-259.
- [11] Bonello, P. "Transient modal analysis of the non-linear dynamics of a turbocharger on floating ring bearings." *Proceedings of the Institution of Mechanical Engineers, Part J: Journal of Engineering Tribology* 223.1 (2009) 79- 93.
- [12] Holt, C., San Andrés, L., Sahay, S., Tang, P., La Rue, G., and Gjika, K., "Test response and nonlinear analysis of a turbocharger supported on floating ring bearings." *Journal of Vibration and Acoustics* 127.2 (2005) 107-115.
- [13] Tian, L., Wang, W. J., and Peng, Z. J. "Nonlinear effects of unbalance in the rotor-floating ring bearing system of turbochargers." *Mechanical Systems and Signal Processing* 34 (2013) 298-320.
- [14] Schweizer, B. "Oil whirl, oil whip and whirl/whip synchronization occurring in rotor systems with full-floating ring bearings." *Nonlinear Dynamics* 57.4 (2009) 509-532.
- [15] Kim, Y. B., and Noah, S. T. "Bifurcation analysis for a modified Jeffcott rotor with bearing clearances." *Nonlinear Dynamics* 1, no. 3 (1990): 221-241.
- [16] Kim, Y. B., and Noah, S. T. "Response and bifurcation analysis of a MDOF rotor system with a strong nonlinearity." *Nonlinear Dynamics* 2, no. 3 (1991): 215-234.
- [17] Von Groll, G., and Ewins, D. J. "The harmonic balance method with arc-length continuation in rotor/stator contact problems." *Journal of Sound and Vibration* 241, no. 2 (2001): 223-233.

- [18] Nataraj, C., and Nelson, H. D. "Periodic solutions in rotor dynamic systems with nonlinear supports: a general approach." *Journal of Vibration, Acoustics, Stress and Reliability in Design* 11 (1989) 187-193.
- [19] Jean, A. N., and Nelson, H. D. "Periodic response investigation of large order non-linear rotordynamic systems using collocation." *Journal of Sound and Vibration* 143.3 (1990) 473-489.
- [20] Sundararajan, P., and Noah, S. T. "Dynamics of forced nonlinear systems using Shooting/arc-length Continuation method-application to rotor systems." *Journal of Vibration and Acoustics* 119.1 (1997) 9-20.
- [21] Sundararajan, P., and Noah, S. T. "An algorithm for response and stability of large order non-linear systems —application to rotor systems." *Journal of Sound and Vibration* 214.4 (1998) 695-723.
- [22] Chu, F., and Tang, Y. "Stability and non-linear responses of a rotor-bearing system with pedestal looseness." *Journal of Sound and Vibration* 241, no. 5 (2001): 879-893.
- [23] Kirk, R. G., and Gunter, E. J. "Short bearing analysis applied to rotor dynamics — part I: theory." *Journal of Tribology* 98.1 (1976) 47-56.
- [24] Childs, D. W., Moes, H., and Van Leeuwen, H. "Journal bearing impedance descriptions for rotordynamic applications." *Journal of Tribology* 99.2 (1977) 198-210.
- [25] Boyaci, A., Seemann, W., and Proppe, C. "Bifurcation analysis of a turbocharger rotor supported by floating ring bearings." *IUTAM Symposium on Emerging Trends in Rotor Dynamics*. Springer Netherlands (2011) 335-347.

- [26] Boyaci, A., Hartmut, H., Seemann, W., Proppe, C., and J. Wauer. "Analytical bifurcation analysis of a rotor supported by floating ring bearings." *Nonlinear Dynamics* 57, no. 4 (2009) 497-507.
- [27] Lund, J. W. "Stability and damped critical speeds of a flexible rotor in fluid-film bearings." *Journal of Engineering for Industry* 96, no. 2 (1974): 509-517.
- [28] Gadangi, R. K., Palazzolo, A. B., and Kim, J. "Transient analysis of plain and tilt pad journal bearings including fluid film temperature effects." *Journal of Tribology* 118, no. 2 (1996): 423-430.
- [29] Gadangi, R. K., and Palazzolo, A. B. "Transient analysis of tilt pad journal bearings including effects of pad flexibility and fluid film temperature." *Journal of Tribology* 117, no. 2 (1995): 302-307.
- [30] Suh, J., and Palazzolo, A. B. "Three-Dimensional Thermohydrodynamic Morton Effect Simulation—Part I: Theoretical Model." *Journal of Tribology* 136, no. 3 (2014): 031706.
- [31] Brown, K. M., and Gearhart, W. B. "Deflation techniques for the calculation of further solutions of a nonlinear system." *Numerische mathematik* 16.4 (1971) 334-342.
- [32] Ojika, T., Satoshi, W., and Taketomo, M. "Deflation algorithm for the multiple roots of a system of nonlinear equations." *Journal of Mathematical Analysis and Applications* 96.2 (1983) 463-479.
- [33] Kalantonis, V. S., Perdios, E. A., Perdious, A. E., Ragos, O., and Vrahatis, M.N. "Deflation techniques for the determination of periodic solutions of a certain period." *Astrophysics and Space Science* 288.4 (2003) 489-497.

- [34] Wang, Z., Jin X., Zhou, Q., Ai, X., Keer, L. M., and Wang, Q. "An Efficient Numerical Method With a Parallel Computational Strategy for Solving Arbitrarily Shaped Inclusions in Elastoplastic Contact Problems." *Journal of Tribology* 135, no. 3 (2013): 031401.
- [35] Mongkolkeha, A., Ruimi, A. and Palazzolo, A.B. "Modal reduction technique for predicting onset of chaotic behavior due to lateral vibrations in drillstrings." *Journal of Vibration and Acoustics* 137.2 (2015) 021003.
- [36] Mondy, R.E. "The diagnosing and corrective actions taken to reduce the effects of steam whirl in a general electric D-11 steam turbine." *International Symposium for Stability Control of Rotating Machinery ISCORMA-3*, Cleveland (2005) 19-23
- [37] Nayfeh, A. H., and Balachandran, B. *Applied Nonlinear Dynamics: Analytical, Computational and Experimental Methods*. John Wiley & Sons, 2008.
- [38] Mees, A. I. *Dynamics of Feedback Systems*. John Wiley & Sons, Inc., 1981.
- [39] Tian, L., Wang, W. J., and Peng, Z. J. "Dynamic behaviours of a full floating ring bearing supported turbocharger rotor with engine excitation." *Journal of Sound and Vibration* 330.20 (2011) 4851-4874.
- [40] Clarke, D. M., Fall, C., Hayden, G. N., and Wilkinson, T. S. "A steady-state model of a floating ring bearing, including thermal effects." *Journal of Tribology* 114, no. 1 (1992): 141-149.
- [41] San Andres, L., and Kerth, J. "Thermal effects on the performance of floating ring bearings for turbochargers." *Proceedings of the Institution of Mechanical Engineers, Part J: Journal of Engineering Tribology* 218, no. 5 (2004): 437-450.

- [42] Bellen, A., "The collocation method for the numerical approximation of the periodic solutions of functional differential equations." *Computing* 23, no.1 (1979):55-66.
- [43] Pagano, S., Rocca, E., Russo, M., and Russo, R. "Dynamic behaviour of tilting-pad journal bearings." *Proceedings of the Institution of Mechanical Engineers, Part J: Journal of Engineering Tribology* 209, no. 4 (1995): 275-285.
- [44] Brancati, R., Rocca, E., and Russo, R. "Non-linear stability analysis of a rigid rotor on tilting pad journal bearings." *Tribology International* 29, no. 7 (1996): 571-578.
- [45] Cao, J., Dimond, T., and Allaire, P., "Nonlinear modeling of tilting-pad bearings with application to a flexible rotor analysis." *In ASME 2013 International Design Engineering Technical Conferences and Computers and Information in Engineering Conference*, pp. V008T13A059-V008T13A059. American Society of Mechanical Engineers, 2013.
- [46] Amamou, A., and Chouchane, M. "Nonlinear stability analysis of long hydrodynamic journal bearings using numerical continuation." *Mechanism and Machine Theory* 72 (2014): 17-24.
- [47] Someya, T., Mitsui, J., Esaki, J., Saito, S., Kanemitsu, Y., Iwatsubo, T., Tanaka, M., Hisa, S., Fujikawa, T., and Kanki, H. *Journal-Bearing Databook*. Edited by Someya. Springer Science & Business Media, 2013.
- [48] Foiles, W. C., Allaire, P. E., and Gunter, E. J. "Review: rotor balancing." *Shock and Vibration* 5, no. 5-6 (1998): 325-336.
- [49] Sundararajan, P. "Response and Stability of Nonlinear Rotor Bearing Systems." PhD diss., Texas A&M University, 1996.

- [50] Glasgow, D. A., and Nelson, H. D. "Stability analysis of rotor-bearing systems using component mode synthesis." *Journal of Mechanical Design* 102, no. 2 (1980): 352-359.
- [51] Nelson, H. D., and Meacham, W. L. "Transient analysis of rotor-bearing systems using component mode synthesis." In *ASME 1981 International Gas Turbine Conference and Products Show*, pp. V004T13A009-V004T13A009. American Society of Mechanical Engineers, 1981.
- [52] Nelson, H. D., Meacham, W.L., Fleming, D. P., and Kascak A.F. "Nonlinear analysis of rotor-bearing systems using component mode synthesis." In *ASME 1982 International Gas Turbine Conference and Exhibit*, pp. V005T13A027-V005T13A027. American Society of Mechanical Engineers, 1982.
- [53] Craig, R. R., and Chang, C. J., "Substructure coupling for dynamic analysis and testing," NASA CR-2781, 1977.
- [54] Craig, R. R., and Chang, C. J. "Free-interface methods of substructure coupling for dynamic analysis." *AIAA Journal* 14, no. 11 (1976): 1633-1635.
- [55] Rübél, J. "Vibrations in Nonlinear Rotordynamics - Modelling, Simulation, and Analysis." PhD diss., the University of Heidelberg, 2009
- [56] Wilson, B. W., and Barrett, L. E. "The Effects of Eigenvalues-Dependent Tilt Pad Journal Bearings on the Stability of Rotor Bearing Systems." Report No. UVA/43092/MAE85/321, University of Virginia, Charlottesville, VA. 1985.

APPENDIX A

COMPUTATIONAL EFFICIENCY OF DEFLATION ALGORITHM AND PARALLEL COMPUTING

The efficiency of deflation and parallel computing is examined by solving a nonlinear dynamic problem with nine dynamic state elements; three multiple roots exists at a specific parameter set. Four different combinations of the two acceleration techniques are arranged as in the following table,

Table A.1. Application sets of the numerical acceleration techniques

	set #1	set #2	set #3	set #4
Deflation	off	on	off	on
Parallel computing	off	off	on	on

Intel xeon 2.5GHz, E5-2670V2 processors of Ada system at Texas A&M University supercomputing center is utilized as the computation platform, and MATLAB[®] 2015a is the program language of the shooting algorithm. Two different multiple core sets, 6 cores and 12 cores, are applied for overviewing efficiency of the parallel computing. The numbers of generated initial guess for the shooting method are 40, 80, and 120, and the solution procedures are repeated 5 times to average the execution time. As can be seen in Fig. A.1-1 and Table A.1-2, the applications of the both techniques can eventually accelerate 5 to 8 times faster than the conventional

shooting with 6 cores of CPU and 12 to 15 times with 12 cores of CPU. The shooting method utilizes both the techniques, and arc-length continuation only employs parallel computing since it is a path-following of a current solution.

Table A.1. Computation time with the numerical acceleration techniques

6 Cores	w/o deflation	w deflation	w/o deflation	w deflation
	w/o parallel	w/o parallel	w parallel	w parallel
40 shoots	564 sec	288 sec	117 sec	69.2 sec
80 shoots	1128 sec	631 sec	330 sec	228 sec
120 shoots	1911 sec	865 sec	558 sec	376 sec
12 Cores	w/o deflation	w deflation	w/o deflation	w deflation
	w/o parallel	w/o parallel	w parallel	w parallel
40 shoots	562 sec	288 sec	77.2 sec	43.6 sec
80 shoots	1124 sec	622 sec	151 sec	87.5 sec
120 shoots	1902 sec	857 sec	236 sec	126 sec

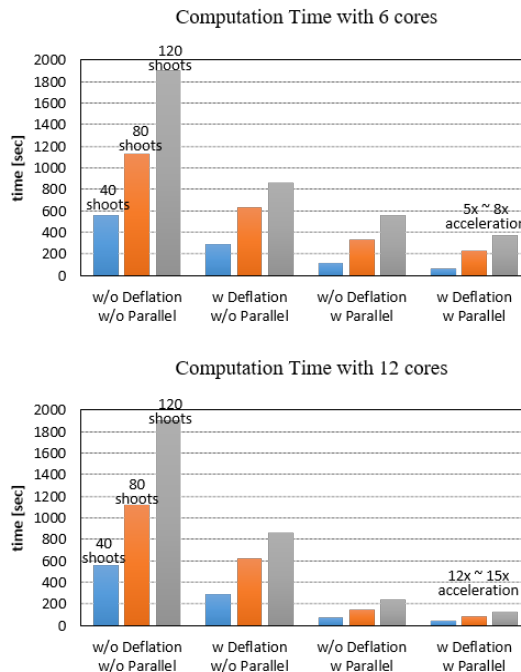


Fig. A.2. Computation time of shooting method for solving a three-multiple root nonlinear equation problem with acceleration techniques

APPENDIX B

AUTONOMOUS SHOOTING/CONTINUATION TO A COMPLEX, MULTI-MASS ROTOR SUPPORTED ON FIXED PAD JOURNAL BEARING

Finite element fixed pad journal bearing

The eight-stage compressor is supported by fixed pad journal bearings that have the following description:

Table B.1. Parameters of fixed pad journal bearing

5 pads	Pad arc length 60 degrees
viscosity = 0.0134 Ns/m ²	shaft diameter = 0.127 m
bearing length = 0.127m	radial clearance=0.0106 ×10 ⁻³
Pivot offset = 0.5	preloads = 0.0, 0.5, 0.75

Different amount ($M_p=0.0, 0.5, 0.75$) are applied for case study with bearing preloads such as relation between the preloads and rotor stabilities including bifurcation.

Shooting and Continuation

The shooting and the arc-length continuation algorithms have applied to the compressor rotor system, the bearing has 0.75 preloads. Fig. B.1. depicts the bifurcation diagram of orbit maximum and minimum displacement in y -direction and corresponding response period. It is shown that system has sub-critical Hopf bifurcation near 8100 rpm and then approximate 1/2 sub-synchronous whirl orbit is emerged (Figs. B.2 and B.3).

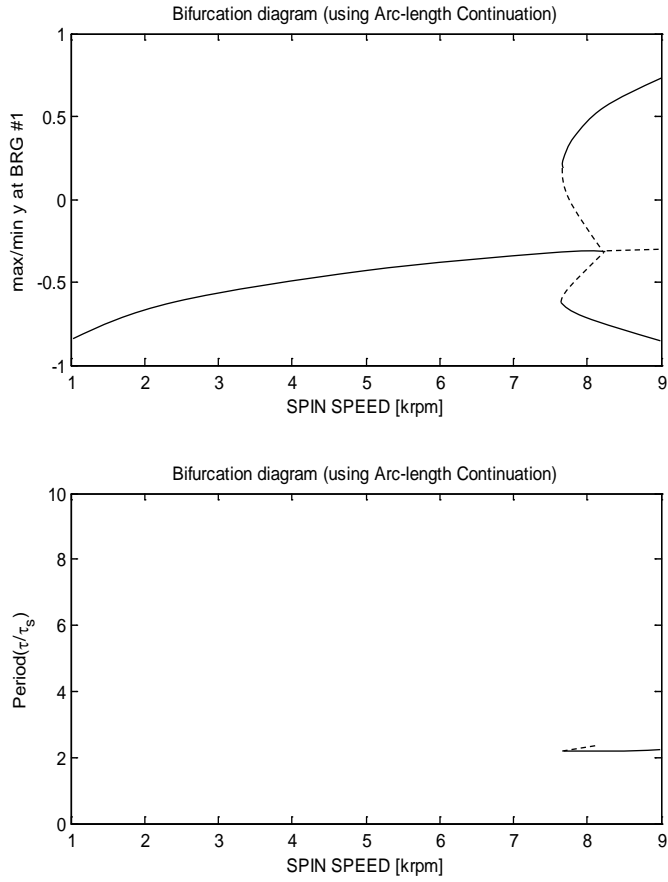


Fig. B.1. Orbital motion of multiple response at 7700rpm ($M_p=0.75$)

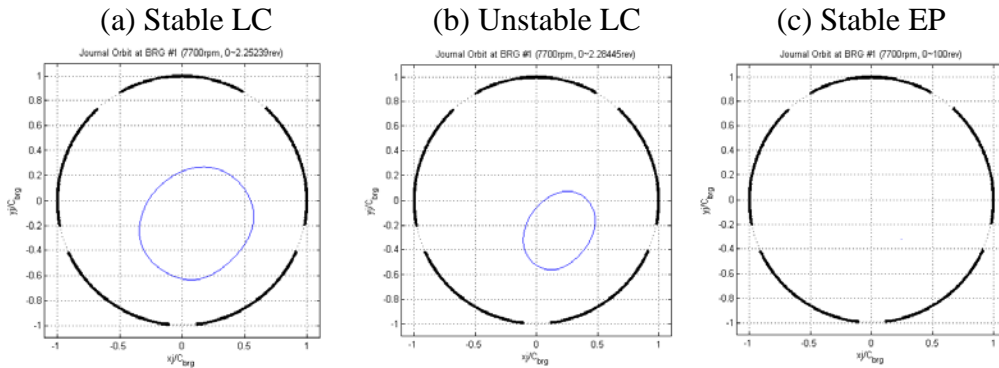
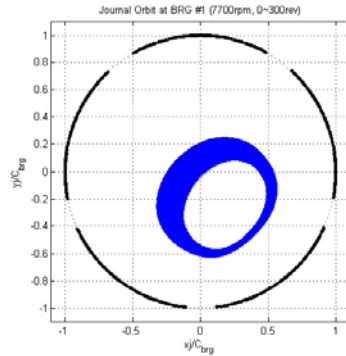


Fig. B.2. Orbital motion of multiple response at 7700rpm ($M_p=0.75$)

(a) Attraction to stable LC



(b) Attraction to stable EP

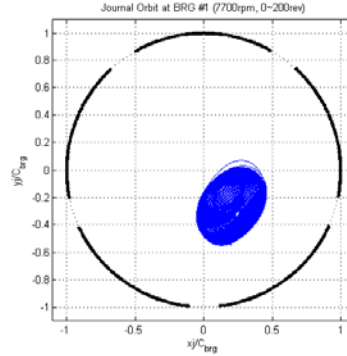


Fig. B.3. Attraction from unstable response to stable response

Multiple response state of the compressor supported by fixed pad bearing has studied with respect to different pad preloads (M_p). The shooting and arc-length continuation applied to the rotor system with three different bearing preloads condition (i.e., $M_p = 0.0, 0.5, 0.75$). The bifurcation diagrams from the results show that bearing preload has a relation with Hopf bifurcation of the system. In the Fig. B.4, preload increases system stability so that instability onset speed has increased along with amount of preload, and it also changes Hopf bifurcation types from super-critical to sub-critical (Table B.2). Figure B.4 (c) clearly show that multiple response can exist near the bifurcation point.

Table B.2. Fixed pad bearing characteristics in eight stage compressor w.r.t. pad preload

Pad preload (M_p)	Instability onset speed (Jump from EP to LC)	Multiple steady state response region	Hopf type
0.0	5740 rpm	-	super-critical
0.5	6530 rpm	6520 ~ 6530 rpm	sub-critical
0.75	8100 rpm	7660 ~ 8100 rpm	sub-critical

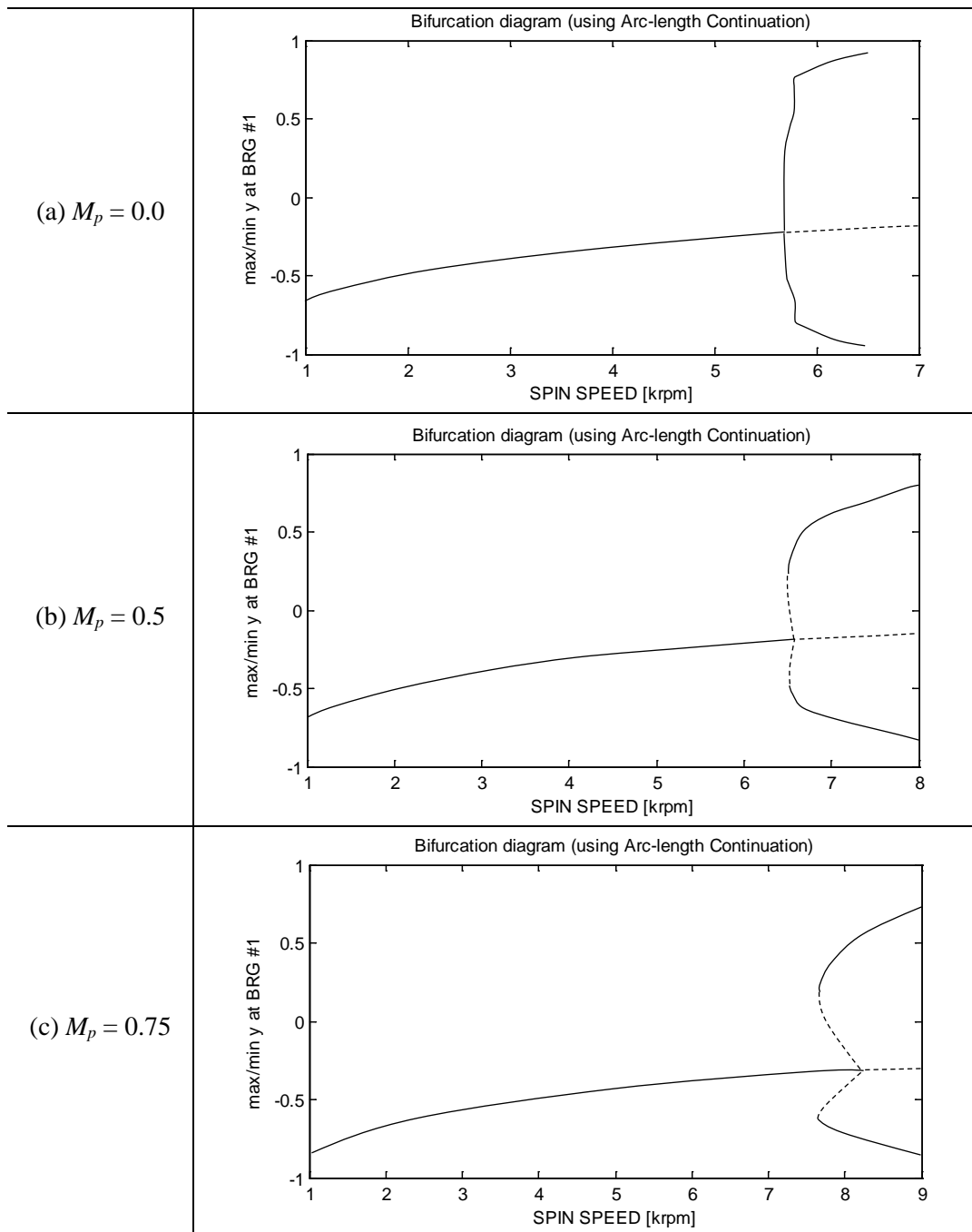


Fig. B.4. Transition of Hopf bifurcation (Super \rightarrow Sub-critical) due to bearing pad preload (M_p)

Jump phenomenon at same speed

From the bifurcation diagram of $M_p=0.75$ case, there is a region that multiple steady state response coexist. A simulation which depicts sudden house impact when response is located in the equilibrium position shows that orbit jump to the other steady state response (Fig. B.5). It is shown that the orbit first attracted an unstable limit cycle but it eventually converges to the stable limit cycle. Thus, in this case, operator may observe two amplitude jumps sequentially after the sudden impact. Similar jump phenomenon may be occurred the multiple steady state coexistence region.

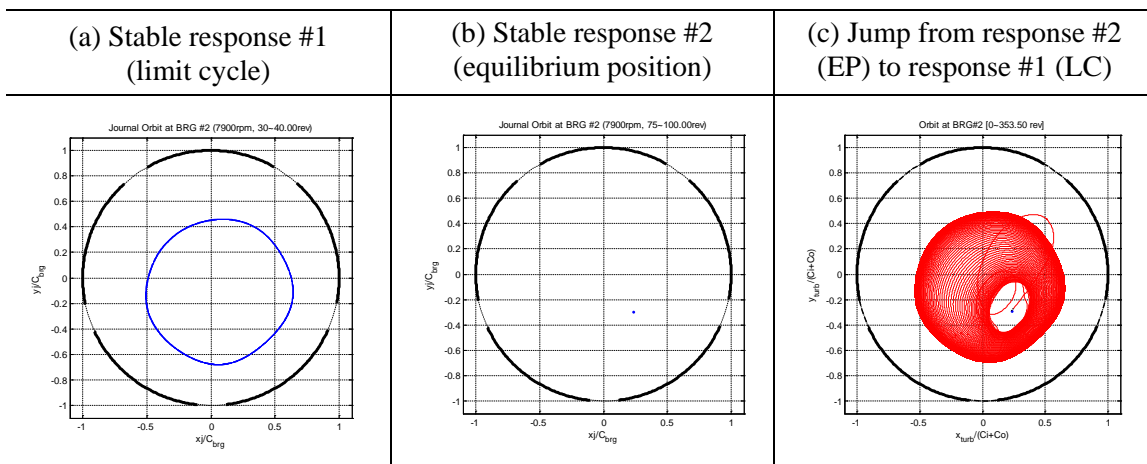


Fig. B.5. Jump between two stable response (EP to LC) at 7900rpm ($M_p=0.75$)

Synchronization

Synchronization for the compressor rotor model is studied. Prior to determine imbalance position and amount, the transient numerical integrations apply to obtain three dimensional rotor beam motion at 8000rpm, which represents the data collected between 390 ~ 400 revolution periods (See Fig. B.6).

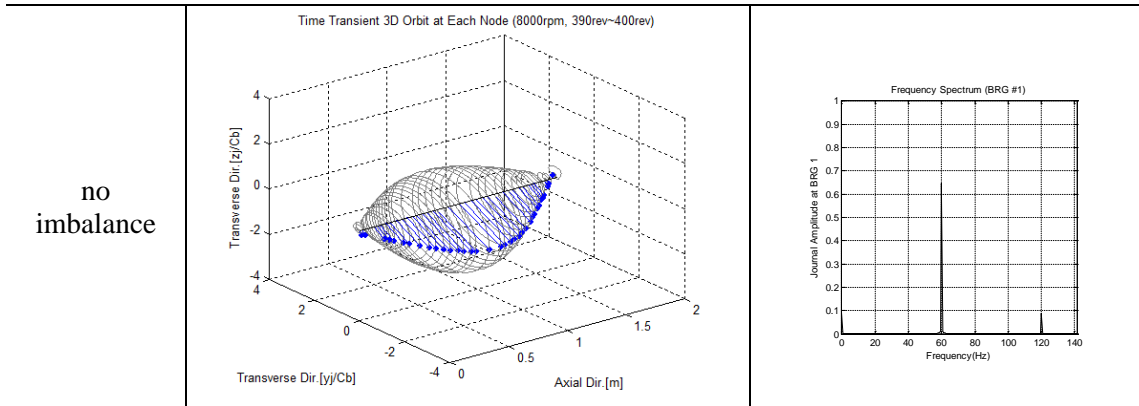


Fig. B.6. (a) 3D orbits from time transient numerical integration at 8000 rpm (no imbalance, 390-400rev), (b) Frequency spectrum of bearing #1

In order to identify an appropriate position of imbalance for synchronization, various position and amount of imbalance are tested with transient numerical integration method as shown in Table B.3. and Fig. B.7. From the results, middle of the rotor is assumed to be most influential position for imbalance.

Table B.3. Run cases for synchronization

Station # (imbalance position)	imbalance eccentricity (e_{imb}), ratio of unbalance force to weight of the rotor(n)	phase angles
#17 (center)	$e_{imb} = 2.0C_b, n=0.64$	$0^\circ, 45^\circ, 90^\circ$
	$e_{imb} = 3.0C_b, n=0.96$	
	$e_{imb} = 4.0C_b, n=1.28$	
#7(first stage), #28(last stage)	$e_{imb} = 2.0C_b, n=0.64$	$0^\circ, 45^\circ, 90^\circ$
	$e_{imb} = 3.0C_b, n=0.96$	
	$e_{imb} = 4.0C_b, n=1.28$	

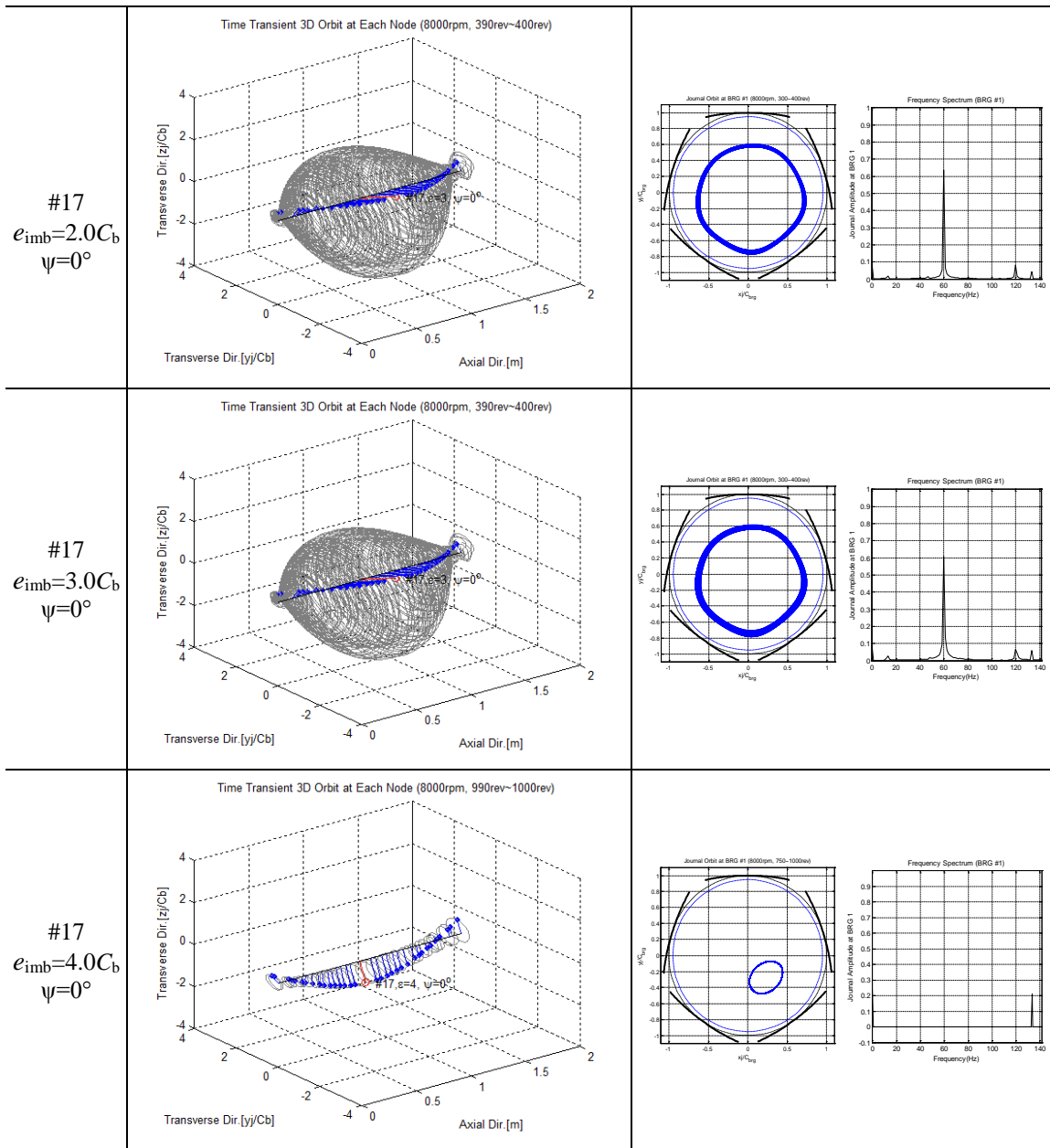


Fig. B.7. Responses with different imbalance amounts on 17th node (using transient numerical integrations)

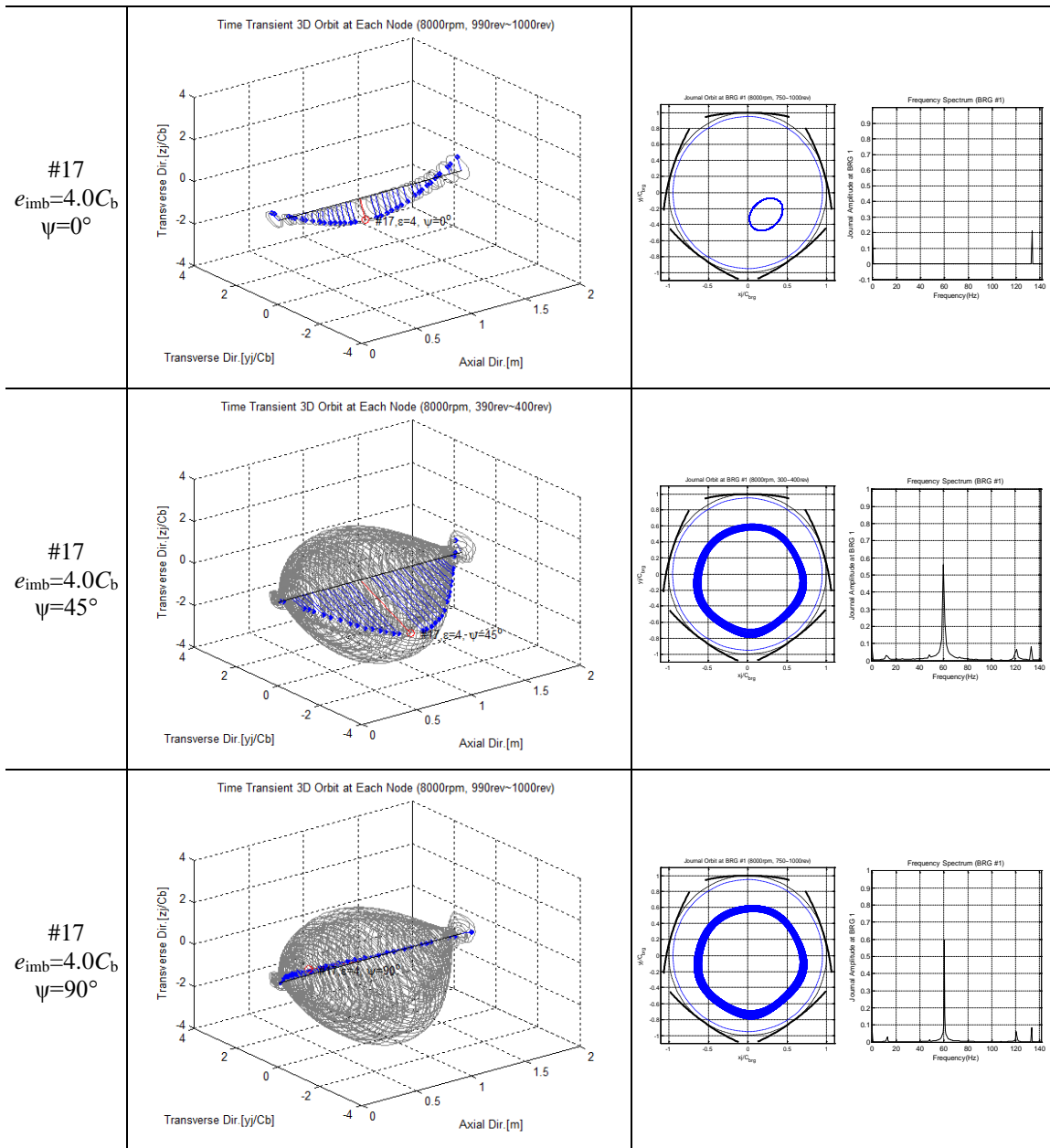


Fig. B.8. Responses with different phase angles on 17th node (using transient numerical integrations)

Synchronous response from Shooting

Shooting method is also utilized to identify synchronous response under unbalance force. As a result, Shooting found an initial condition for stable synchronous response which could not be obtained from numerical integration method. From this result, better amount of imbalance force ($e_{imb}=4C_b \rightarrow e_{imb}=3C_b$) are identified. In future, Shooting-Genetic combined algorithm will be developed to provide optimal position and amount of imbalance force for synchronization.

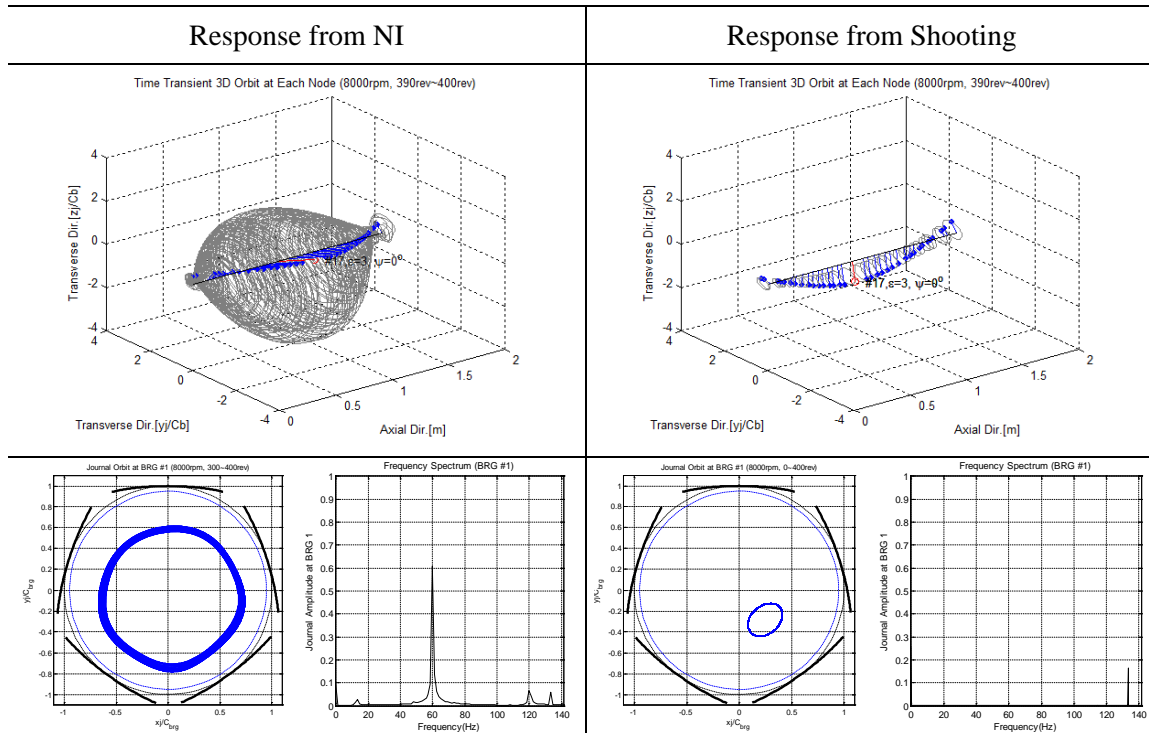


Fig. B.9. Synchronization result obtained from Shooting method.

APPENDIX C

DEVELOPMENT OF A DIRECT SOLUTION SEARCH SOLVER FOR NONLINEAR OSCILLATIONS BASED ON GENETIC ALGORITHM

Generic algorithm (GA) is a method for solving both constrained and unconstrained optimization problems based on a natural selection process that mimics biological evolution. The algorithm repeatedly modifies a population of individual solutions. At each step, the genetic algorithm randomly selects individuals from the current population and uses them as parents to produce the children for the next generation. Over successive generations, the population "evolves" toward an optimal solution. In the case of rotordynamics, this may correspond as follows,

Table C.1. Genetic algorithm creatures vs. Correspondences for rotor-dynamics

Creatures		Rotor-dynamics
Population	\Leftrightarrow	State vector
Genetic objectives	\Leftrightarrow	Min $\ x(0) - x(T)\ $

Moreover, crossover reproduction process is not appropriate for the state vector GA. This may be explained that the crossover of two different equilibrium points (EPs) doesn't make improvement or another EP. Instead of crossover, random reproduction will be applied to maintain diversity of possible solution. The following flow chart in Fig. C.1. represents a genetic process for multiple steady state responses for nonlinear dynamic system.

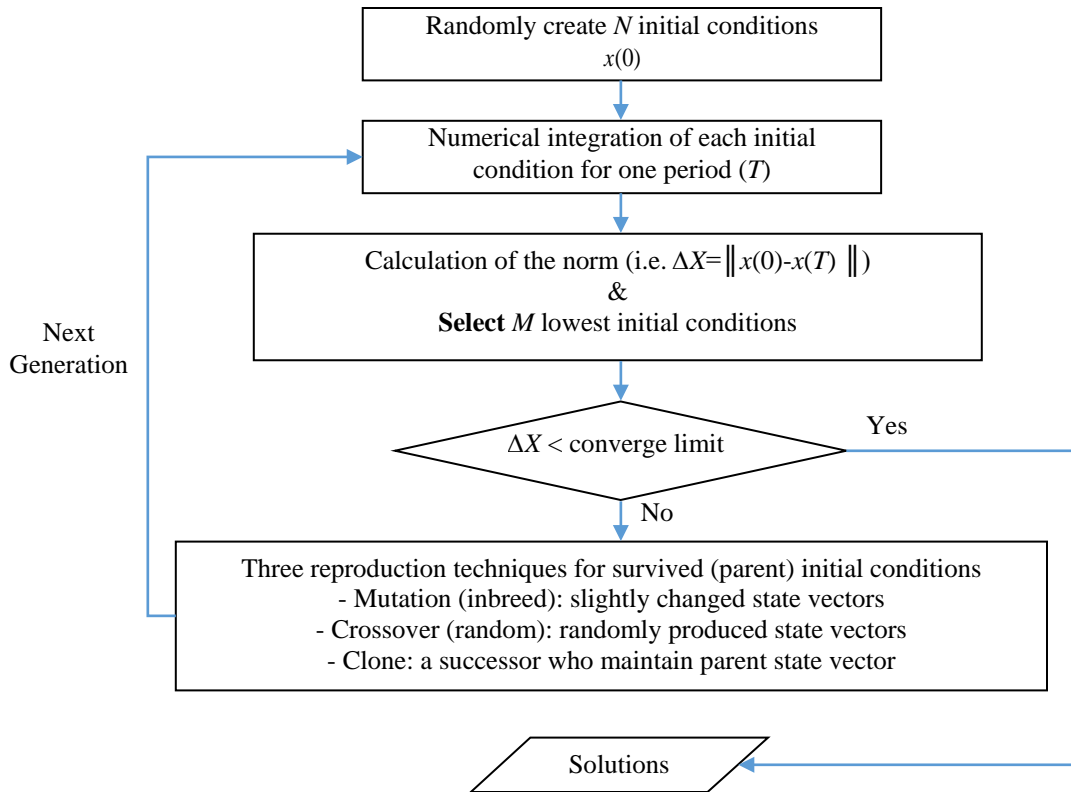


Fig. C.1. Flow chart of genetic process

Duffing System (Non-autonomous)

For a trial test, relatively simple nonlinear dynamic equation such as a Duffing system is tested. As a result, though the GA missed two initial conditions compared to the shooting method (Table C.2 and Fig. C.2), GA also could find all possible orbits in the system.

$$x'' + 2\xi x' + x + \varepsilon x^3 = \delta_{sl} \cos(\omega_R \tau) \quad (C 1)$$

$$x' = y \quad (C 2)$$

$$\xi = .005, \omega_R = 3.2, \varepsilon = .5, \delta_{sl} = .5 \quad (C 3)$$

Table C.2. Coexistent solutions identified by Genetic algorithm vs. Shooting method

		Genetic Algorithm	Shooting Method	Note
Harmonic solution ($\tau=T_R$)	i	(-0.054119 0.000599)	(-0.054118 0.000599)	response 1
	ii	(-0.054107 0.000593)	(-0.054106 0.000593)	response 1
Sub-harmonic solution ($\tau=1/3T_R$)	iii	-	(0.400286 0.402331)	response 2
	iv	-	(-0.607937 0.232897)	
	v	(0.037171 -0.610530)	(0.037034 -0.610908)	response 3
	vi	(-0.516674 0.445559)	(-0.516940 0.445090)	
	vii	(0.529551 0.219957)	(0.529795 0.219361)	

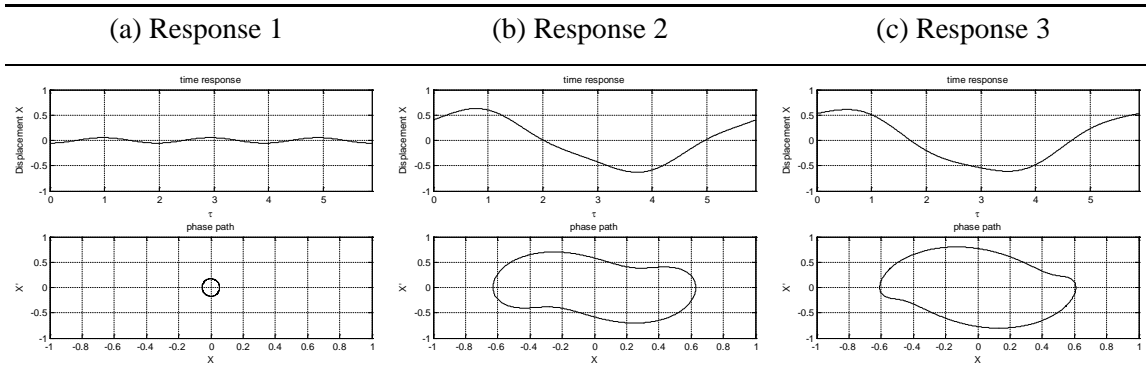


Fig. C.2. Time events and phase portraits of solutions

Van Der Pol system (Autonomous)

To solve an autonomous system, the Genetic algorithm treats the response period (T) as one more unknown parameter, and the other process is same as the non-autonomous system. As a result, GA could find two (stable) responses and missed one (unstable) response compared to the Shooting method (Table C.3. and Fig C.3).

$$x'' + x + \varepsilon h(x, y) = 0 \tag{C 4}$$

where, $h(x, y) = (-31.83x' + 51.89x'^3 - 11.84x'^5 + 0.566x'^7) / 1000$

$$\varepsilon = 5$$

Table C.3. Coexistent solutions identified by Genetic algorithm vs. Shooting method

		Genetic Algorithm	Shooting Method	Note
Limit cycles	i	$x_0 = [-0.29775 \ -0.94243]$ $T_0 = 1.00122$	$x_0 = [-0.418664 \ 0.924055]$ $T_0 = 1.00126$	response 1
	ii	$x_0 = [-5.30223 \ 0.02069]$ $T_0 = 1.12177$	$x_0 = [-1.520554 \ 4.001426]$ $T_0 = 1.12178$	response 2
	iii	-	$x_0 = [-0.260788 \ 2.410471]$ $T_0 = 1.00634$	response 3

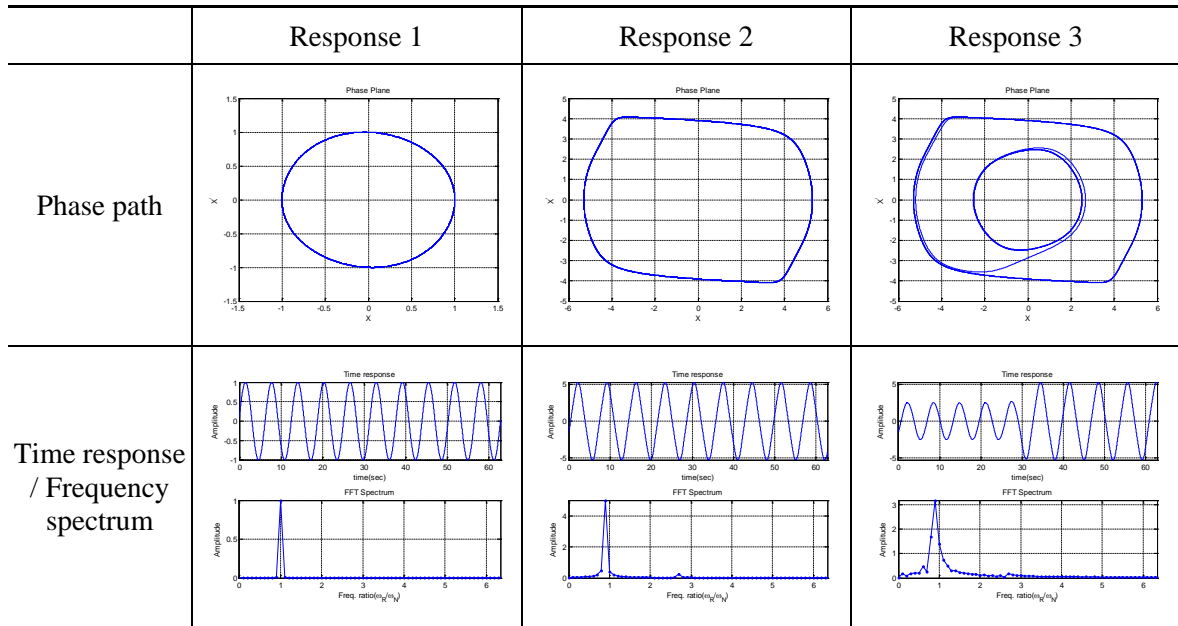


Fig. C.3. Phase paths, time events, and frequency spectra of solutions

Genetic Algorithm to Floating Ring Bearing System

Genetic algorithm code has been developing to solve the floating ring bearing system introduced in Chapter 3. The cross-over reproduction process in the GA approach now uses two-states vector while single DOF systems such as Duffing and Van Der Pols has one. This process slightly increased convergence rate to find steady state responses. It is shown that the reproduction process highly affects the efficiency of the solution search.

First, current version of GA code has applied to autonomous FRB system at 36 krpm and 140 krpm. As a result, a single response of the journal and ring is identified as shown in Fig C.4. In contrast, two different limit cycles are identified at 65krpm by GA. Current version of the GA is not faster than the shooting method, but one big advantage of the GA is able to find multiple solutions independently and simultaneously.

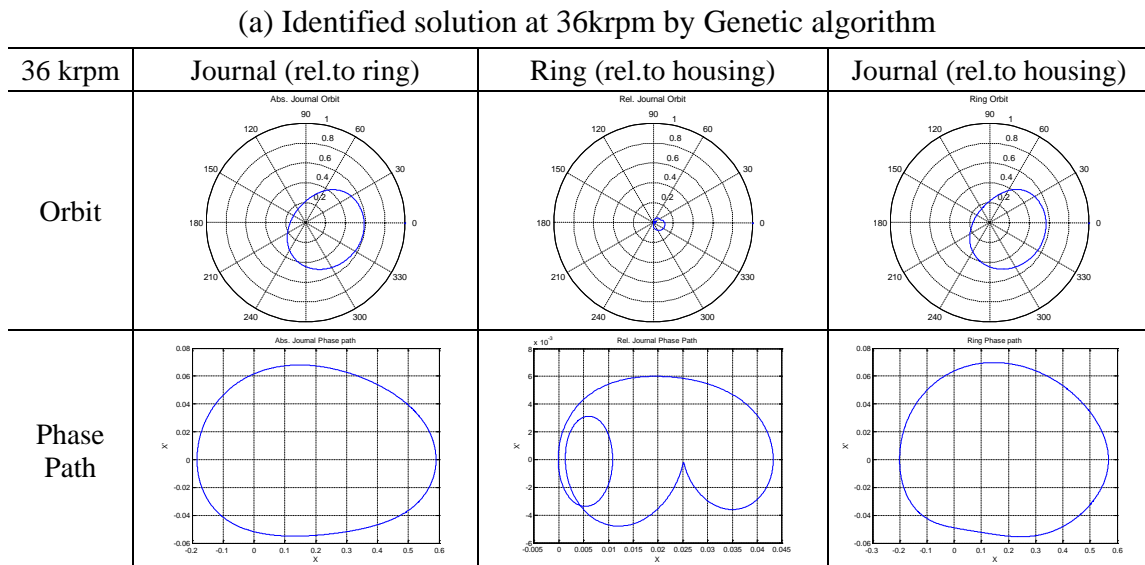


Fig. C.4. Solution identified by Genetic algorithm: (a) 36 krpm, (b) 140 krpm

(b) Identified solution at 140krpm by Genetic algorithm

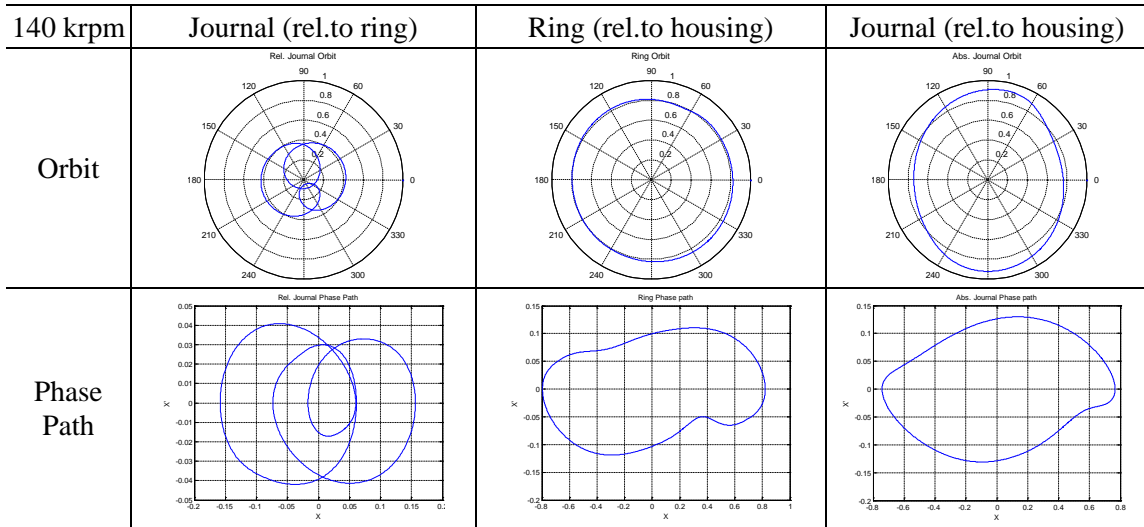
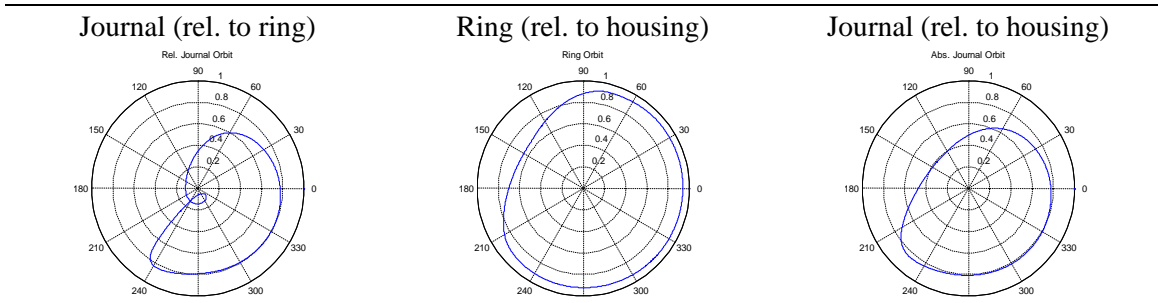


Fig. C.4. Continued

Each limit cycle is the result of revolutions; Figure C.6 (a) and (b) show the revolution of response generation by generation.

(a) Limit cycle #1



(b) Limit cycle #2

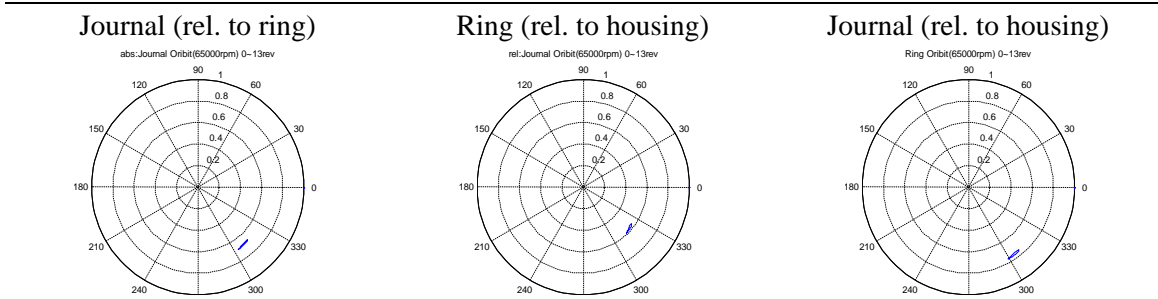
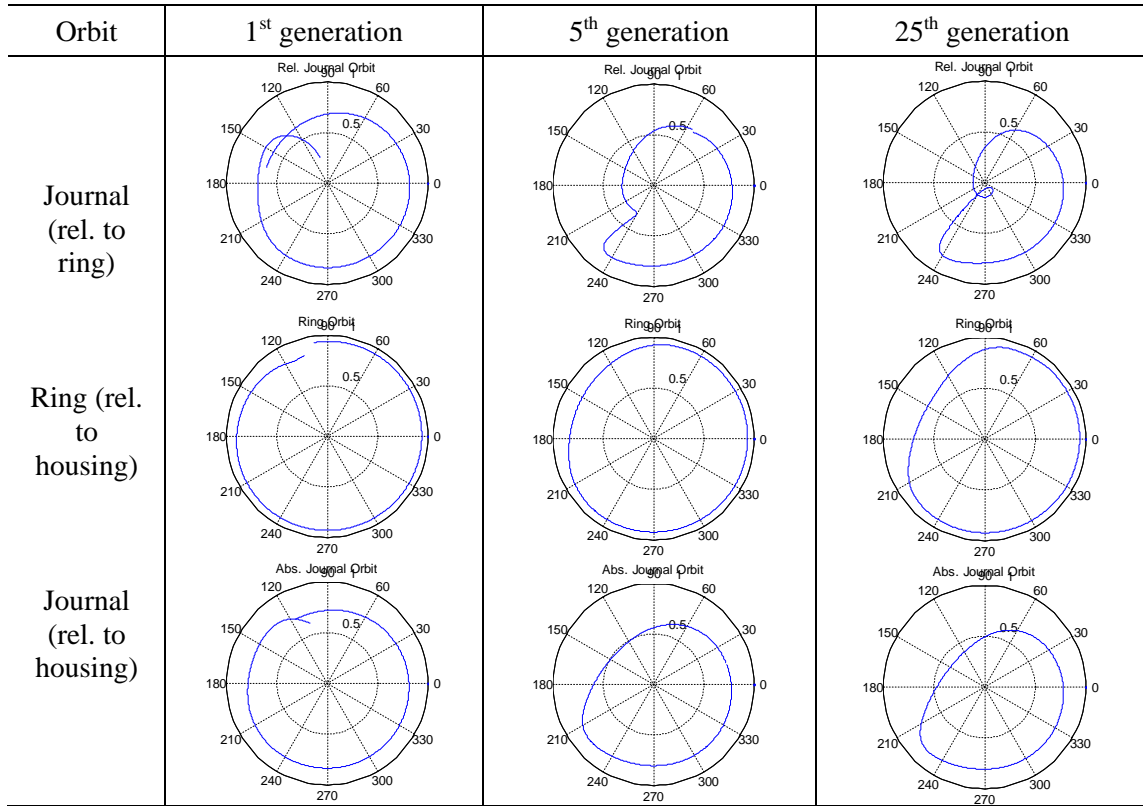


Fig. C.5. Multiple response states (two stable limit cycles) identified by GA

(a) Limit cycle #1: Orbit Changed by Generation



(b) Limit cycle #2: Phase Path Changed by Generation

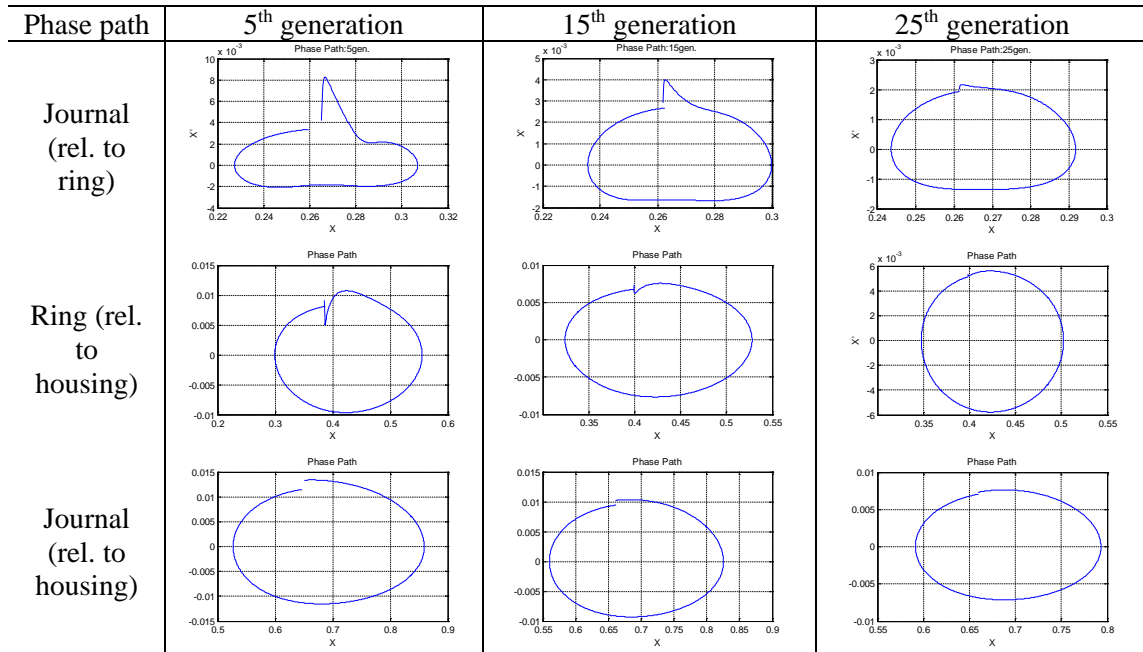


Fig. C.6. Revolution of the responses by Genetic algorithm

APPENDIX D

FORMULATIONS OF FLUID FILM FORCE BASED ON INFINITELY SHORT BEARING APPROXIMATION

$$\begin{Bmatrix} f_x \\ f_y \end{Bmatrix} = - \frac{\left[(x-2y')^2 + (y+2x')^2 \right]^{1/2}}{1-x^2-y^2} \begin{Bmatrix} 3xV(x, y, \alpha) - \sin \alpha G(x, y, \alpha) - 2 \cos \alpha S(x, y, \alpha) \\ 3xV(x, y, \alpha) + \cos \alpha G(x, y, \alpha) - 2 \sin \alpha S(x, y, \alpha) \end{Bmatrix}$$

where,

$$\alpha = \text{atan} \left(\frac{y+2x'}{x-2y'} \right) - \frac{\pi}{2} \text{sign} \left(\frac{y+2x'}{x-2y'} \right) - \frac{\pi}{2} \text{sign}(y+2x')$$

$$V(x, y, \alpha) = \frac{2 + (y \cos \alpha - x \sin \alpha) G(x, y, \alpha)}{1-x^2-y^2}$$

$$S(x, y, \alpha) = \frac{x \cos \alpha + y \sin \alpha}{1 - (x \cos \alpha + y \sin \alpha)^2}, \quad G(x, y, \alpha) = \frac{2}{(1-x^2-y^2)^5} \left[\frac{\pi}{2} + \text{atan} \frac{y \cos \alpha - x \sin \alpha}{(1-x^2-y^2)^5} \right]$$